DISS. ETH NO. 17183

Experimental and numerical investigation of the catalytic partial oxidation of methane to synthesis gas for power generation applications

A dissertation submitted to

ETH ZURICH

for the degree of

Doctor of Sciences

Presented by

ADRIAN SCHNEIDER

Diplom Maschineningenieur, ETH Zurich

born 28.09.1977

citizen of
Buchholterberg Bern

Accepted on recommendation of

Prof. Dr. K. Boulouchos, examiner
Dr. I. Mantzaras, co-examiner
Prof. Dr. G. Groppi, co-examiner

Zurich 2007

Meiner Familie

Acknowledgements

Table of contents

Kurzfassung

Gegenstand der vorliegenden Arbeit ist die Untersuchung der katalytischen partiellen Oxidation (CPO) für Gasturbinenanwendungen. Kombinierte experimentelle und numerische Untersuchungen der CPO von Methan zu Synthesegas (H_2, CO) über Rhodiumkatalysatoren wurden unter Hochdruck von bis zu 10 bar ausgeführt.

Die hohe Reaktivität des erzeugten Wasserstoffs und der stabile Betrieb des CPO-Reaktors selbst ermöglichen im Betrieb von Gasturbinen zur Stromerzeugung eine weitere Senkung der NO_x-Emissionen, den zuverlässigen Betrieb mit Brennstoffen niedrigen Brennwerts und neuartige Brennverfahren mit grosser Abgasrezirkulation für effiziente Kraftwerke mit CO_2-Abtrennung.

In einer optisch zugänglichen katalytischen Kanalströmungsbrennkammer wurden die optischen Messverfahren Raman Spektroskopie und Laser-induzierte Fluoreszenz (LIF) von Formaldehyd benutzt, um Informationen über die katalytische und die Gasphasenchemie zu erhalten. Die per spontaner Ramanstreuung gemessenen transversalen Konzentrationsprofile aller Hauptspezies erlaubten Rückschlüsse auf die katalytische Reaktivität, während per LIF die Flammform und -position gemessen wurden, die die Gasphasenreaktivität charakterisierten.

Durch Vergleiche von Messungen und 2-D CFD Simulationen wurden ein detaillierter katalytischer und ein detaillierter Gasphasen Reaktionsmechanismus validiert. Experimente mit kleinen Gasturbinen-Honigwaben-Katalysatoren haben gezeigt, dass die Mechanismen auch unter Bedingungen eines kommerziellen Einsatzes in Gasturbinen mit kurzen Reaktorverweilzeiten gute Resultate liefern. Das Zündverhalten dieser CPO-Katalysatoren konnte durch den hetero-/homogenen Reaktionsmechanismus in transienten Simulationen nachvollzogen werden. Die Zünd-Lösch-Hysterese konnte durch eine Verschiebung von teilweiser zu vollständiger Oxidation bei niedrigen Einlasstemperaturen erklärt werden. Trotz des chemischen Effekts der H_2O-Verdünnung wurden Zündtemperaturen und Zündgeschwindigkeit nicht beeinflusst.

Der Einfluss der Betriebsparameter wie Stöchiometrie, Verdünnung mit H_2O und CO_2, Einlass- und Oberflächentemperatur, Druck, Verweilzeit, Edelmetallbeladung, Katalysatorträgermaterial und Katalysatorgeometrie wurde analysiert; hierfür wurden zusätzlich nulldimensionale Modelle idealer Reaktoren herangezogen.

Mit hoher Selektivität konnte Synthesegas produziert werden, wobei die katalytischen Zündtemperaturen trotz der Abgasverdünnung im Rahmen von Kompressorausgangs-

temperaturen lagen. Auch bei Temperaturen über 200 K unter den Zündtemperaturen sind die CPO-Reaktoren nicht erloschen, was auf eine ausgeprägte Hysterese bei der Methan CPO hinweist.

Der Oberflächenreaktionsmechanismus gab den CH_4- und O_2-Verbrauch gut wieder. Es kam zu einer nur leichten Übergewichtung von totaler über teilweise Oxidation. Im vorderen Teil des Reaktors traten vollständige und teilweise Oxidation parallel auf, deren Verhältnis sich mit Abnahme der O_2-Konzentration in Richtung teilweiser Oxidation verschob. In den hinteren Teilen des Katalysators traten Dampfreformierung von CH_4 und die Wassergas-Shift-Reaktion auf, was den dortigen H_2O-Verbrauch und die anhaltende CO_2-Produktion begründete. Es handelt sich somit um eine Kombination von direkter und indirekter Synthesegasproduktion.

Die Verdünnung mit H_2O erzeugte zusätzliche O(s) und OH(s) Radikale, was die H_2-Selektivität und der CH_4-Umsatz erhöhte, die CO-Selektivität jedoch reduzierte. Durch die H_2O-Verdünnung sanken die Oberflächentemperaturen, was sich in der Folge positiv auf die Katalysatorlebensdauer auswirkt.

CO_2-Verdünnung hatte unter den untersuchten Bedingungen keinen chemischen Einfluss, da Oxy- und Dampfreformierung im Vergleich zur CO_2-Reformierung die signifikant schnelleren Reaktionen waren.

Die verschiedenen Katalysatorträger wirkten sich vor allem durch ihre unterschiedliche Edelmetalldispersion in der Reihenfolge α-Al_2O_3, ZrO_2, Ce-ZrO_2 aus. Ein höherer Dispersionswert führte zu einer niedrigeren katalytischen Zündtemperatur, zu einer höheren Synthesegasausbeute und zu niedrigeren Katalysatortemperaturen. Es konnte gezeigt werden, dass die Aktivierung von Koreaktanden durch das Trägermaterial und der OH(s) Übertritt vom Trägermaterial auf das Edellmetall vernachlässigt werden konnten.

Der Einfluss des Drucks auf den katalytischen Reaktionsweg war gering. Der Gasphasenmechanismus reproduzierte bei Drücken unter 10 bar die Flammgeschwindigkeit, ab 10 bar wurde sie jedoch unterschätzt. Das für die Anwendung wichtigste Resultat ist die zuverlässige Vorhersage der Zündverzugszeit in der Gasphase durch den hetero-/homogenen Reaktionsmechanismus, die für den sicheren Betrieb von CPO-Brennkammern relevant ist.

Beim Reaktordesign ist das durch nicht equilibrierte Reaktionen bedingte Auftreten von superadiabatischen Gas- und Oberflächentemperaturen zu berücksichtigen.

Abstract

The present work addresses the catalytic partial oxidation (CPO) of methane to synthesis gas, with particular emphasis on power generation applications. A combined experimental and numerical investigation of methane partial oxidation to synthesis gas (H_2, CO) over rhodium-based catalysts has been carried out at pressures of up to 10 bar.

The reactivity of the produced hydrogen and the suitably-low light-off temperatures of the CPO reactor, greatly facilitate operation of power generation gas turbines with reduced NO_x emissions, stable operation with low calorific value fuels, and new combustion strategies for efficient CO_2 capture. Those strategies utilize CPO of methane with oxygen (separated from air) and large exhaust gas recycle (H_2O and CO_2).

An optically accessible catalytic channel-flow reactor was used to carry out Raman spectroscopy of major gas-phase species and laser induced fluorescence (LIF) of formaldehyde, in order to gain fundamental information on the catalytic and gas-phase chemical pathways. Transverse concentration profiles measured by the spontaneous Raman scattering technique determined the catalytic reactivity, while the LIF provided flame shapes and anchoring positions that, in turn, characterized the gaseous reactivity.

Comparison between measurements and 2-D CFD computations, led to the validation of detailed catalytic and gas-phase reaction mechanisms.

Experiments in a subscale gas-turbine honeycomb catalytic reactor have shown that the foregoing reaction mechanisms were also appropriate under gas-turbine relevant conditions with short reactant residence times. The light-off behavior of the subscale honeycomb reactor was reproduced by transient 2-D CFD computations. Ignition and extinction in CPO was studied. It was shown that, despite the chemical impact of the H_2O diluent during the transient catalytic ignition event, the light-off times themselves were largely unaffected by the exhaust gas dilution. The extended ignition/extinction hysteresis of the CPO reactor was due to a shift from partial to total oxidation (and hence to higher exothermicity) with decreasing reactor inlet temperature.

The influence of different operating conditions such as stoichiometry, dilution with H_2O and CO_2, inlet and surface temperatures, pressure, residence time, noble metal loading, catalyst support und geometry were quantified. Those studies were facilitated with additional computations in ideal, zero-dimensional reactor models.

Synthesis gas has been produced with high selectivity. Despite the high exhaust gas dilution, the catalytic light-off occurred at temperatures well-within the range of compressor outlet temperatures. Vigorous burning was sustained at inlet temperatures at least 200 K lower than the light-off temperature, indicating an extended ignition/extinction hysteresis during CPO of methane.

The surface reaction mechanism captured the CH_4 and O_2 consumption; however, a slight overprediction of the total over the partial oxidation route was evident. In the upstream sections of the reactor total and partial oxidation occurred in parallel, with the latter growing to more importance as oxygen consumption increased. Farther downstream, H_2O-reforming and water-gas-shift reactions became important. Synthesis gas production appeared, therefore, to be controlled by both the direct and the indirect reaction pathways.

The H_2O dilution provided additional O(s) and OH(s) surface radicals, which resulted in increased H_2 selectivity and CH_4 conversion and in decreased CO selectivity. With H_2O dilution, lower catalyst temperatures could be obtained, which was beneficial for an extended catalyst/reactor lifetime.

CO_2 dilution had no significant chemical impact (dry reforming) under the investigated conditions due to the presence of the significantly faster oxy- and steam-reforming reactions.

The primary effect of different catalyst supports was the resulting different noble metal dispersion, increasing in the order α-Al_2O_3, ZrO_2, and Ce-ZrO_2. Higher dispersion led to lower light-off temperatures, higher synthesis gas yields and lower catalyst temperatures. It was shown that, under the present high H_2O dilution, the H_2O activation on support sites and the inverse spillover of OH(s) from the support to the noble metal sites could be neglected. This allowed for a successful numerical modeling of different supports through the use of a single parameter, the noble metal dispersion.

The effect of pressure on the catalytic reaction pathway was altogether small.

Flame propagation characteristics (flame speeds) were reproduced well by the gas phase reaction mechanism at pressures of up to 8 bar; however, at higher pressures the flame speeds were underpredicted. Nonetheless, the gas-phase ignition delay times, which were crucial parameters for safe CPO burner operation, were captured well at all pressures by the employed hetero-/homogeneous reaction schemes.

The issue of superadiabatic surface temperatures, caused by reaction non-equilibration, was shown to be an important for CPO reactor design.

Nomenclature

B	ratio of active to geometrical surface area
c_p, c	specific heat of gas at constant pressure, specific heat of solid
D_{km}	mixture-average diffusion coefficient of kth species, cm/s
D_k^T	thermal diffusion coefficient of kth species, cm/s
h	total enthalpy of gaseous mixture
h_k, h_k^o	total and chemical enthalpy of k-th species
K_g	total number of gas-phase species
L, L_c, L_u	total reactor length, coated length, uncoated length, cm
Le	Lewis number (thermal over species diffusivity)
M_s	total number of surface species
p	pressure
$\dot{q}_{acc}$, $\dot{q}_{gen}$	accumulation and heat generation
$\dot{q}_{rad}$, $\dot{q}_{cond}$, $\dot{q}_{conv}$	radiative, conductive and convective heat transfer
R	universal gas constant
Re	Reynolds number
r_h	channel hydraulic radius, cm
$\dot{s}_k$	catalytic molar production rate of kth species, gmol/cm^2 s
S_k	selectivity of kth species
S/V	surface-to-volume ratio
t	time
T	temperature, K
T_o, T_{eq}	reference temperature, adiabatic equilibrium temperature
u, U_{IN}	axial velocity component, inlet axial velocity
U_{IN}	inlet axial velocity, cm/s
v	radial velocity component
V	Reactor volume, cm^3
$\vec{V}_k$	diffusion velocity vector of kth gaseous species, cm/s
W_k, $\overline{W}$	species molecular weight, average molecular weight, g/mol
x	streamwise coordinates
X_k, Y_k	gas-phase species mole and mass fraction

x	streamwise coordinate
y, r	cartesian and cylindrical transverse coordinate

Greek Symbols

α	thermal diffusivity ($\lambda/\rho c$)
Γ	surface site density, mol/cm^2
δ , δ_c	channel solid wall thickness, catalyst thickness, cm
ε	surface emissivity
θ_m	surface coverage of m-th species
λ	thermal conductivity
λ_g , λ_s	thermal conductivity of gas and solid, W/cm K
μ	viscosity
ρ	density, g/cm^3
φ	fuel-to-air equivalence ratio
$\dot{\omega}_k$	gas-phase molar production rate of k-th species

Subscripts

ig	ignition
IN, OUT	inlet, outlet
FeCr, ZrO$_2$	solid materials
g, s	gas, solid
k, m	indices for gas-phase and surface species
σ_m	surface species site occupancy
τ	reactor residence time
W	wall
x, r	streamwise and radial components

Abbreviations

CPO	catalytic partial oxidation
EGR	exhaust gas recycle
GHSV	gas hourly space velocity
SPSR	surface perfectly stirred reactor

I   Introduction

I.1   Motivation

The driving force for the investigation of methane (the main constituent of natural gas) catalytic partial oxidation (CPO) over rhodium is the potential of this combustion methodology to very low emissions. Hydrogen addition to hydrocarbon fuels can stabilize combustion at lower flame temperatures, leading to reduced NO_x formation. The required hydrogen can be produced on-site by a CPO reactor.

New zero-emissions power generation processes aiming at mitigating both NO_x and CO_2 employ large exhaust gas recycle (EGR). They particularly profit by the use of CPO as the first stage of a "catalytic-rich, gaseous-lean combustion" process. Therein, the fuel is partially oxidized with a fraction of oxidizer, coming from the compressor of the gas-turbine, in the catalytic-rich stage. The hot, H_2-containing product gases are subsequently burned in a conventional gas-phase combustor with the remaining oxidizer. This process facilitates combustion of CH_4/O_2 mixtures highly diluted with exhaust gas; due to the lack of N_2, CO_2 can easily be captured from the exhaust for sequestration.

I.2   Objectives

The main objectives are:

− to validate the heterogeneous and homogeneous reaction schemes at gas-turbine relevant conditions (pressure, surface and gas temperatures and stoichiometry)

− to assess the effect of exhaust gas dilution (H_2O, CO_2) on the synthesis gas yields and selectivities

− to investigate the effect of pressure on the heterogeneous and homogeneous reaction pathways

− to study the light-off (catalytic ignition) and extinction during methane CPO with large EGR, in light of the stringent demands imposed by gas-turbines

− to search for appropriate rhodium-based supported catalysts that meet the light-off requirements and selectivity needs of power generation applications.

I.3   Method of Approach

To address the foregoing issues, a combined experimental and numerical approach has been adopted.

I.3.1   Experimental

CPO test have been carried out in two high-pressure catalytic reactors. Both reactors were fed with accurately-measured amounts of CH_4/O_2 and superheated steam. The flows were laminar in both reactors. Supported rhodium catalysts have been applied by spraying and were characterized with surface science analysis (BET, chemisorption, surface Raman).

An optically accessible channel-flow reactor with a channel gap of 7 mm allowed for Raman spectroscopy of all major species (CH_4, O_2, H_2, CO, H_2O, CO_2) and for laser induced fluorescence (LIF) of the trace formaldehyde. The measured transverse concentration profiles of major species were used to assess the catalytic processes. LIF detected the onset of homogenous ignition as well as the flame shape and position. Details of this reactor along with the laser diagnostics and main findings are reported in Sections II.3 and V.2.3/4.

A subscale gas-turbine honeycomb reactor with individual channel hydraulic diameters of 1.2 mm was used, in conjunction with gas-chromatography exhaust analysis, to investigate steady and transient CPO at industrially-relevant short contact times (~8 ms). Details are given in Section III.2.

Different catalyst supports within the honeycomb and the channel-flow reactor were investigated. The key findings of this work are reported in Section V.

I.3.2   Numerical

For simulations of all stationary experiments, a steady full-elliptic 2-D laminar CFD code has been used. This code included detailed hetero-/homogeneous chemistry and realistic transport including thermal diffusion for the light species.

While the energy wall boundary conditions in the case of the optical accessible reactor were directly provided by surface temperature measurements (Section V.3.2) the simulations of the honeycomb reactor necessitated the solution of an energy equation for the solid (Section III.3.1).

For the transient light-off simulations, the quasi-steady approach for the gas-phase was invoked within a full elliptic 2-D laminar code. This approach was valid due to the short characteristic gas diffusion and convection times compared to the solid heat-conduction times (Section IV.3.1.).

For extensive parametric studies, ideal zero-dimensional models (e.g. the Surface Perfectly Stirred Reactor and the Batch Reactor) have been used (Section IV.3.4).

The heterogeneous chemistry was represented by the detailed surface reaction mechanism for CPO over supported rhodium of Deutschmann [1, Schwiedernoch et al., 2003] including 38 reactions and 12 surface species.

The C2 gas-phase chemistry of Warnatz [2, Warnatz et al., 1996] was used. This scheme employed 164 reactions and 34 species. The catalytic and gas-phase schemes are described in Section IV.3.3 and listed in Appendices B and C.

I.4   Outline

The four parts (Sections II to V) of this thesis are journal publications, thus they can be read independently.

In part II, the reaction schemes are validated with experimental data obtained in the optically accessible reactor. The influence of high exhaust gas dilution (H_2O, CO_2) and pressure (4 to 10 bar) on the hetero-/homogeneous reaction pathways is analyzed.

Part III deals with steady-state CPO in the short contact time honeycomb reactor at 5 bar. Next to the effect of H_2O/CO_2 dilution on conversion and synthesis gas selectivities, the extinction hysteresis and the thermal management are addressed.

Part IV deals with the transient catalyst light-off and the controlling chemical and physical parameters. Furthermore, the ignition/extinction hysteresis is studied in detail. On the numerical side, a transient code was employed.

Part V deals with the effect of different supports on the activity and selectivity of the Rh-based catalysts. The key parameter(s) needed to model the impact of support are identified.

I.5   Conclusions

The hetero-/homogeneous reaction schemes for CPO of CH_4 over rhodium have been validated at pressures up to 10 bar with large H_2O and CO_2 dilution in the feed.

An increase in pressure from 4 to 10 bar had only a minor impact on the heterogeneous methane conversion and synthesis gas selectivites.

Addition of large amounts H_2O (up to 46.3% vol.) enhanced the CH_4 conversion and H_2 selectivity and decreased the CO selectivity. The effect of CO_2 dilution (dry reforming) was negligible due to the presence of oxygen and large amounts of H_2O.

The employed gas-phase reaction scheme captured the onset of homogeneous ignition.

The heterogeneous reaction scheme reproduced steady experiments in a short contact time reactor with large H_2O and CO_2 dilution. The H_2O addition lowered the surface temperatures and thus facilitated thermal management, which was of importance in practical systems.

Light-off temperatures and ignition modes were also captured by the numerical model. The light-off times were controlled by total oxidation and not by partial oxidation or reforming reactions, the key reaction being $CO(s) + O(s) \rightarrow CO_2(s)$.

The different behavior of catalysts with α-Al_2O_3, ZrO_2 and Ce-ZrO_2 supports was explained by their different noble metal dispersion. Due to the high activity of the rhodium along with the high concentrations of co-reactants, inverse spillover from the support to the noble metal sites could be neglected at the present conditions with large EGR dilution.

II Laser induced fluorescence of formaldehyde and Raman measurements of major species during partial catalytic oxidation of methane with large H$_2$O and CO$_2$ dilution at pressures up to 10 bar

A paper written by Adrian Schneider, John Mantzaras, Rolf Bombach, Sabine Schenker, Niclas Tylli and Peter Jansohn; presented at the 31st International Symposium on Combustion, August 6 - 11, 2006, University of Heidelberg, Germany.

Abstract

The catalytic partial oxidation (CPO) of CH$_4$/O$_2$ mixtures diluted with large amounts of H$_2$O and CO$_2$ (up to 43% and 21% vol., respectively) was investigated experimentally and numerically in the pressure range 4 bar $\leq p \leq$ 10 bar. Experiments were carried out in an optically accessible channel-flow catalytic reactor coated with Rh/ZrO$_2$, and included planar laser induced fluorescence (LIF) of formaldehyde for the assessment of homogeneous (gas-phase) ignition and one-dimensional spontaneous Raman of all major gas-phase species for the evaluation of the heterogeneous (catalytic) processes. Simulations were performed with a full elliptic model that included detailed heterogeneous and homogeneous chemical reaction schemes. Over the reactor length with negligible gas-phase participation, the employed heterogeneous reaction scheme provided good agreement to the measured methane consumption and synthesis gas yields, overpredicting mildly the total over the partial oxidation route. It was shown that the added water provided a source of O(s) and OH(s) surface radicals that enhanced the methane conversion and H$_2$ yields and reduced the CO yields. Moreover, the addition of CO$_2$ had a negligible chemical effect on the aforementioned parameters. An increase in pressure from 4 to 10 bar had a minor impact on the methane conversion and hydrogen selectivity. The employed gaseous scheme reproduced the LIF-measured onset of homogeneous ignition, although it underpredicted the extent of the formaldehyde zone ahead of the flame and the flame propagation characteristics at the highest investigated pressure (10 bar).

II.1 Introduction

The catalytic partial oxidation (CPO) of methane to synthesis gas can be accomplished autothermally and selectively at millisecond contact times over noble metals [3, Hickman and Schmidt, 1993; 4, Deutschmann and Schmidt, 1998], rendering this process particularly

attractive for on-board fuel reforming in many practical devices such as fuel-cells [5, Chaniotis and Poulikakos, 2004], internal combustion engines [6, Allgeier et al., 2004] and natural-gas-fired turbines [7, Castaldi et al., 2005]. In the last two applications, a fraction of the hydrocarbon fuel undergoes CPO and the produced synthesis gas allows for enhanced stability of the follow-up flame. To advance these new combustion technologies, Appel et al. [8, Appel et al., 2005] have recently investigated CPO of CH_4/air over Rh/ZrO_2 at a moderate pressure of 6 bar. Therein, in situ 1-D Raman measurements of gas-phase species concentrations were used, in conjunction with detailed simulations, to elucidate the underlying hetero-/homogeneous processes.

In the last years, the CPO of natural-gas/air mixtures diluted with large recycled exhaust gas has received increased attention in power generation. One such example is the advanced zero emissions power process [9, Griffin et al., 2004], wherein the recycled H_2O and CO_2 comprise up to 80% of the feed. The addition of water is beneficial in many CPO-based chemical processes: it facilitates the autothermal reforming of methane [10, Bharadwaj and Schmidt, 1994; 11, Appel, 2002] and ethanol [12, Deluga et al., 2004], and it suppresses the formation of olefins in the reforming of higher hydrocarbons [13, Dreyer et al., 2005]. Understanding the impact of large H_2O/CO_2 dilution on the hetero-/homogeneous processes during CPO of methane (the main component of natural gas) is of paramount importance for power systems with exhaust recirculation.

The present study undertakes an experimental and numerical investigation of methane CPO with large H_2O and CO_2 dilution (up to 43% and 21% vol., respectively) that is relevant to power generation cycles. High-pressure experiments (up to 10 bar) were carried out in an optically accessible reactor. In situ 1-D Raman measurements of major species concentrations were used to assess the heterogeneous processes and planar laser induced fluorescence (LIF) of formaldehyde monitored gaseous combustion. The main objectives were to investigate the impact of H_2O and CO_2 on the methane consumption and product selectivities at power-generation-relevant conditions, to establish an experimental technique for the assessment of homogeneous ignition during CPO, and to provide validated hetero-/homogeneous chemical reaction schemes at high pressures.

II.2 Experimental

II.2.1 Test rig and catalyst preparation

Experiments were carried out in an optically accessible catalytic channel-flow reactor, positioned inside a high-pressure cylindrical tank (Fig. II.1). The reactor comprised two non-porous Si[SiC] ceramic plates (300 mm long, 104 mm wide, placed 7 mm apart) and two 3-mm-thick quartz windows. A Rh/ZrO_2 coating (2% wt. Rh) was applied to the inner Si[SiC] surfaces. The surface temperatures were monitored by thermocouples (twelve for each plate) arranged along the *x-y* symmetry plane and embedded 0.9 mm beneath the catalyst through holes eroded from the outer Si[SiC] surfaces. Two 350-mm-long and 35-mm-thick quartz windows on the high-pressure tank maintained optical access from both reactor sides. Two additional quartz windows, one at the rear flange of the tank and the other (not shown in Fig. II.1) at the reactor exit, provided a further streamwise optical access for the LIF excitation beam. Details of the reactor/tank have been provided elsewhere [8, Appel et al., 2005; 14, Reinke et al., 2005; 15, Reinke et al., 2004].

Pure oxygen was used in the feed with nitrogen added as balance. Superheated steam was supplied by an AWTEC-DLR steam-generator. The O_2, N_2 (and CO_2 when applicable) flows were mixed and then electrically preheated. Room-temperature CH_4 and superheated steam were injected downstream; the feed achieved a good degree of premixedness in two sequential static mixers and a 30-mm-long packing of 2-mm-diameter ceramic spheres. The mixture was finally driven into the reactor through a 50-mm-long inert honeycomb. A thermocouple positioned at the downstream end of the honeycomb provided the inlet temperature of the feed.

The catalyst preparation involved incipient wetness impregnation of the ZrO_2 support with a $Rh(NO_3)_3$ solution. The impregnated catalyst powder was calcined at 600°C for 5 h. A slurry created from the catalyst powder and a solvent mixture was sprayed on the Si[SiC] plates, yielding a 12-μm-thick coating. The coated Si[SiC] plates were subsequently calcined at 600°C for 1 h. BET (N_2 physisorption) and CO chemisorption were used to assess the total and active surface areas, respectively. The deduced ratio of the active to geometrical area in the tested samples was 4.5. Post-combustion X-ray photoelectron spectroscopy (XPS) analysis indicated that bulk elements (e.g. Si) did not diffuse to the surface. The catalyst was reduced in a heated (400°C) flow of H_2/N_2 before each combustion test.

II.2.2 Laser diagnostics

The Raman/LIF set-up is depicted in Fig. II.1. A traversable mirror directed the frequency-doubled 532 nm radiation of an Nd:YAG pulsed laser (Quantel YG981E20-CL, 380 mJ pulse energy, 12 ns pulse) to the Raman or to the LIF set-up. In the Raman experiments, the 532 nm beam was temporally stretched to 34 ns using a partially reflecting mirror and an optical delay line for the transmitted radiation (Fig. II.1). This allowed for efficient use of the entire pulse energy without window damage or dielectric gas breakdown. The temporally-stretched and expanded (25 mm diameter) beam was focused through the tank and reactor side-windows into a vertical line (~0.3 mm thick) by an f_1 = 150 mm cylindrical lens. The focal line spanned the 7-mm transverse gap and was laterally offset (z = 15 mm) to increase the light collection angle and minimize thermal beam steering [14, Reinke et al., 2005; 16, Appel et al., 2002]. Two f_2 = 300 mm spherical lenses focused the scattered light to the entrance slit of a 25 cm imaging spectrograph (Chromex-250i). The dispersed light was recorded on an intensified CCD camera (Princeton Instruments MAX-1024HQ, 1024x254 pixels). To increase the spatial resolution, only the upper channel half-height was recorded. Each image comprised 630x254 pixels that corresponded to wavelength and transverse (y) distance, respectively. The 3.5 mm half-height was resolved with 200 pixels, which were further binned to 84 pixels. A holographic notch-filter (Kaiser HNPF-532.0-1.5) and a colored glass filter were placed before the spectrograph slit to attenuate the scattered Rayleigh signal and the stray laser light. The spectral dispersion extended up to 4500 cm^{-1}, allowing observation of all major species. Given the steady operating conditions, 2000 images were averaged to increase the signal-to-noise ratio. The effective Raman cross-sections were evaluated by recording the signals of several pressurized CH_4, N_2/H_2 and CO_2 containing mixtures, air, and the actual feed mixture. Those tests also quantified the cross-talk between the CO_2/O_2 and CO/N_2. Spectroscopic data for the CH_4, H_2O, CO_2 and CO Raman cross-sections were obtained from Refs. [17, Steiner, 2002; 18, Eisenberg, 1995; 19, Schaefer et al., 1991]. Measurements were acquired at 14 mm $\leq x \leq$ 168 mm by traversing axially an optical table that supported both sending and collecting optics (Fig. II.1). Raman data closer than 0.3 mm to the upper wall were discarded due to low signal-to-noise ratio.

At fuel-rich conditions, planar LIF of OH is not amenable due to the associated sub-ppm levels [8, Appel et al., 2005]. Formaldehyde LIF was thus introduced, whereby the 532 nm radiation pumped a tuneable dye laser (Quantel TDL90 NBP2UVT3) filled with pyridine-1 dye. Its frequency-doubled radiation at 352 nm was transformed into a slightly

diverging laser sheet (propagating counterflow along the *x-y* symmetry plane, Fig. II.1) by a telescopic system. The broadband fluorescence was collected at 90° with an intensified CCD camera (LaVision-IRO with 1392x1024 pixels, recorded with a binning of 2x2). The collection optics included achromatic lenses and filters that provided spectral detection between 410 and 480 nm. Zones of 110x7 mm^2 were recorded on a 696x44 pixel section, and the camera was traversed axially to map the entire reactor extent. Uncertainties in the broadband emission of formaldehyde and the significant laser radiation absorption along its propagation path (given the large amounts of CH_2O) precluded quantification of the LIF signals. The present study reports the first direct measurements of homogeneous ignition in CPO using CH_2O-LIF. In catalytic systems, this technique has only been used to measure the pure heterogeneous production of formaldehyde in the oxidation of methanol over Pt [20, Kang et al., 1996] at low temperatures (140°C).

Figure II.1
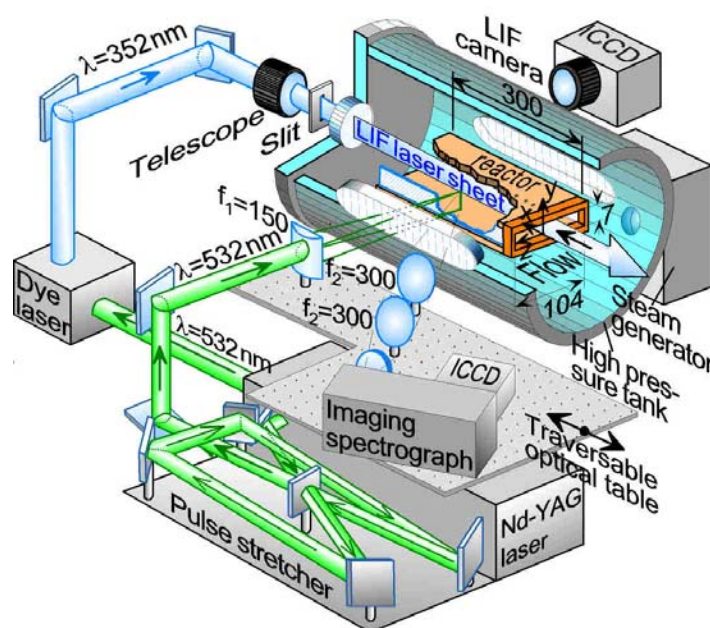
Schematic of the reactor and the Raman/LIF set-up.

II.3 Numerical

A full elliptic 2-D CFD code [16, Appel et al., 2002; 21, Dogwiler et al., 1999] provided the simulation platform. It included the multi-step heterogeneous scheme of Deutschmann (Schwiedernoch et al. [1, Schwiedernoch et al., 2003]), comprising 38 reactions, 12 surface and 6 gaseous species. The impact of added radical (OH, H, O) adsorption/desorption reactions [22, Deutschmann et al., 2000] (not included in the original scheme [19]) on

homogeneous ignition was minimal. For gas-phase chemistry, the C_2/H/O mechanism of Warnatz et al. [2, Warnatz et al., 1996] (164 reversible reactions and 34 species, with appropriate pressure dependencies for 6 reactions) was employed. Transport was modeled with mixture-average diffusion including thermal diffusion for the light species, using the CHEMKIN database [23, Kee et al., 1996]. Gaseous and surface chemical reaction rates were evaluated with CHEMKIN [24, Kee et al., 1996] and Surface-CHEMKIN [25, Coltrin et al., 1996], respectively. Gas-phase and surface thermochemical data were included in the provided mechanisms.

Uniform properties for the temperature, the axial velocity and the species mass fractions were used at the inlet. Fitted curves through the twelve thermocouple measurements of each plate provided the interfacial energy boundary conditions at $y = 0$ and 7 mm, respectively. No-slip conditions for both velocity components were applied at the channel walls and zero-Neumann conditions at the outlet. An orthogonal staggered mesh of 480x84 points (over the 300 and 7 mm dimensions, respectively) was sufficient to produce a grid-independent solution.

II.4 Results and discussion

The experimental conditions are provided in Table 1. The minimum flow rate requirements of the steam-generator placed a lower limit to the inlet Reynolds numbers, which ranged from 2500 to 2650 (based on the 13.1 mm channel hydraulic diameter). The flow could be treated as laminar since recent turbulent catalytic combustion studies [26, Appel et al., 2005] have shown that the strong flow laminarization induced by the heat transfer from the hot walls guaranteed laminar flow conditions even at considerably higher inlet Reynolds numbers.

Table II.1

Experimental conditions[a]

Case	p	φ	T_{IN}	U_{IN}	CH_4	H_2O	CO_2
1	4	2.5	457	1.72	20	42	-
2	6	4.0	566	1.62	29	38	-
3	8	2.5	569	1.07	20	43	20
4	10	2.5	553	0.82	21	42	21
5	10	4.0	549	0.93	30	37	-

[a]inlet properties (p in bar, T_{IN} in K, U_{IN} in m/s) and %vol. feed composition. Case 1 has also 22% vol. CO. O_2 is deduced from the equivalence ratio (φ) and the balance is N_2.

II.4.1 Heterogeneous processes

Comparisons between Raman-measured and predicted species transverse profiles are illustrated in Figs. II.2 to II.4. For clarity, up to 20 of the total 84 measuring points are provided over the experimentally resolved extent $0 \leq y \leq 3.2$ mm. The measurement accuracy was $\pm 3\%$ for species compositions $\geq 10\%$ vol. and $\pm 10\%$ for compositions as low as 0.5% vol.; concentrations less than 0.5% vol. entailed larger measurement uncertainties. The resulting C/H/O element balances along the channel were reproduced within 5%. Figure II.5 provides the computed streamwise profiles of the average (over the 7 mm channel height) species mole fractions and the thermocouple-measured upper and lower wall temperatures for Cases 2 and 5. The temperature differences between the two walls were within 25 K. Emphasis is placed on the pure H_2O dilution cases since, as shown next, CO_2 had a minor chemical impact.

Homogeneous ignition was attained in all cases of Table 1 as evidenced by the formaldehyde LIF (see forthcoming Fig. II.8). Streamwise profiles of the computed catalytic and gas-phase species production rates (the latter integrated over the 7 mm channel-height) are provided in Fig. II.6 for Cases 2 and 5. Gas-phase chemistry was negligible at $x \leq 120$ mm (Case 2) and $x \leq 86$ mm (Case 5), wherein its contribution was less than ~5% of the catalytic pathway. Similarly, in Case 4 the computations indicated negligible gas-phase contribution for $x \leq 80$ mm. Those axial extents corresponded to the first four transverse

profiles of Fig. II.2 and the first three profiles of Figs. II.3 and II.4. The predicted onset of homogeneous ignition (defined in Section II.4.4 by the formaldehyde rise) was located ~20 mm farther downstream of the aforementioned onset of appreciable gas-phase contribution.

Figure II.2
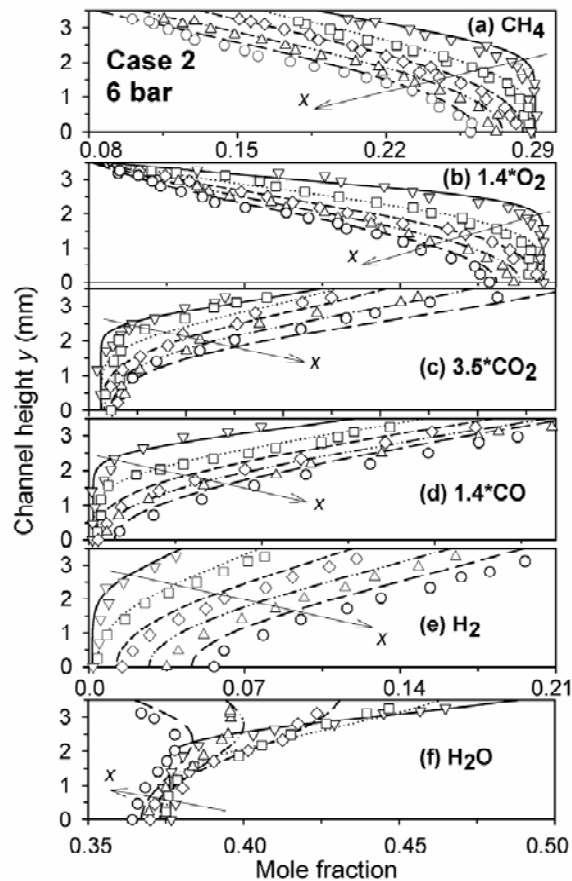
Predicted (lines) and measured (symbols) profiles of species mole-fraction for Case 2: x=14mm (solid-lines, lower-triangles), x=48mm (dotted-lines, squares), x=88mm (short-dashed-lines, diamonds), x=128mm (double-dotted-dashed lines, upper-triangles), x=168mm (long-dashed-lines, circles). The wall is at $y = 3.5$ mm and the symmetry plane at $y = 0$.

As further discussed in Section II.4.4, the predicted homogeneous ignition distances (x_{ig}) were in general agreement with the LIF measurements, suggesting that the above-computed reactor extent with negligible gas-phase contribution was realistic. Over this extent, comparisons between measured and predicted methane mole fractions indicated relative differences of up to 4% (see Figs. II.2a, II.3a, II.4a), which were well-within the experimental uncertainty. Larger differences were only evidenced at the last streamwise distance of Figs. II.3 and II.4

due to the influence of gas-phase combustion and the associated slower predicted flame propagation (see Section II.4.4).

Figure II.3
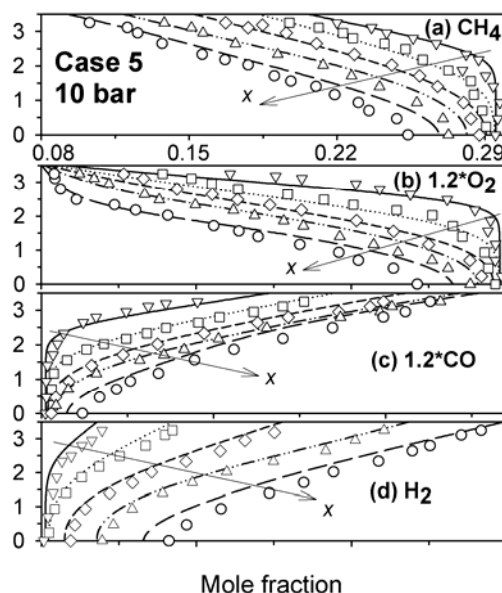
Measured and predicted species profiles for Case 5. The notation follows Fig. II.2.

Figure II.4
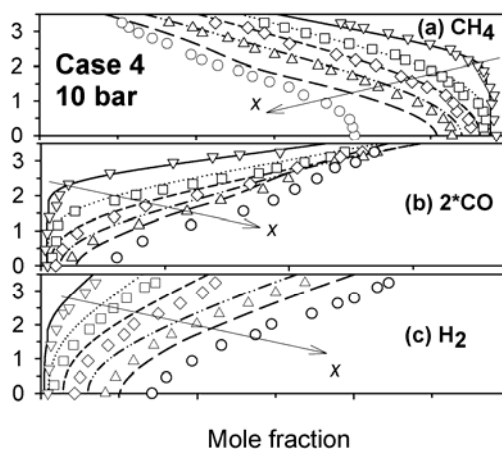
Measured and predicted species profiles for Case 4. The notation follows Fig. II.2.

In the H_2O dilution cases, the partial oxidation products (CO and H_2) were somewhat underpredicted (Figs. II.2(d, e), II.3(c,d)). On the other hand, the total oxidation products (CO_2 and H_2O) were slightly overpredicted as shown in Fig. II.2 (CO_2 and H_2O are not provided in Fig. II.3, however, the same trends were also observed there). Thus, the employed heterogeneous reaction scheme favored slightly the partial over the total oxidation route and this behavior was in qualitative agreement with earlier CH_4/air CPO experiments without dilution [8, Appel et al., 2005]. Comparisons between measurements and predictions

have also attested the aptness of the employed heterogeneous scheme in the presence of CO_2 dilution and further revealed the same small overprediction of the partial over the total oxidation route (see Fig. II.4, the first three CO and H_2 profiles). Having established the overall applicability of the employed heterogeneous reaction scheme in the presence of large H_2O and CO_2 dilution, the following numerical analysis in Sections II.4.2 and II.4.3 elucidates the underlying catalytic processes.

II.4.2 Production of synthesis gas

The O_2 profiles in Figs. II.2 and II.3 indicated a mass-transport-limited catalytic conversion (manifested by the very low O_2 levels at the wall). In the upstream regions of minimal gas-phase pathway participation, there was always O_2 available (Figs. II.2b, II.3b). In the first ~3 cm of the reactor, the O_2/CH_4 catalytic destruction ratio ranged between one and two (Fig. II.6), demonstrating a strong contribution of complete oxidation ($CH_4+2O_2{\rightarrow}2H_2O+CO_2$) in addition to CPO ($2CH_4+O_2{\rightarrow}4H_2+2CO$). Farther downstream, the destruction rate of CH_4 overtook that of O_2, and the molar ratio H_2/CO approached two at the end of the catalytically-dominant zones (Fig. II.5a). The total oxidation at the upstream locations resulted in very steep transverse wall gradients of H_2O and CO_2 (see the first two profiles in Fig. II.2(c, f)).

Water was catalytically produced at $x \leq 100$ mm (Fig. II.6a) and $x \leq 92$ mm (Fig. II.6b). Farther downstream, the catalyst turned to a sink of H_2O due to steam reforming ($CH_4+H_2O{\rightarrow}CO+3H_2$). Moreover, even well-downstream the onset of homogeneous ignition ($x > x_{ig}$), the catalytic pathway continued to play a pivotal role (Fig. II.6); therein, the catalyst consumed CH_4 and H_2O, while it produced H_2, CO and CO_2. This was a result of heterogeneously-catalyzed steam reforming, which was responsible for H_2/CO molar ratios approaching three at the reactor exit (Fig. II.5a). The catalytic production of CO_2 was due to the water gas shift reaction $CO+H_2O{\rightarrow}CO_2+H_2$. The aforementioned catalytic production or destruction of the major species was also affirmed experimentally by the sign of the Raman-measured transverse gradients near the wall (Figs. II.2 to II.4). The pure catalytic methane conversion (before the onset of appreciable gas-phase contribution) was as high as 17%, with a hydrogen selectivity (based on the stoichiometry of the partial oxidation reaction) of up to 85%. For a given methane conversion, an increase in pressure from 4 to 10 bar decreased the hydrogen selectivity by a factor of ~1.50 to ~1.15. However, this effect reflected the lower surface temperatures of the higher-pressure cases (Fig. II.5). Computations at a constant mass throughput and wall temperature (from 900 to 1100 K) have

shown that an increase in pressure from 4 to 10 bar decreased only mildly the methane conversion and had practically no impact on the hydrogen selectivity. Those findings were in agreement with lower-pressure experiments (1.4 to 5.5. bar [27, Dietz and Schmidt, 1995]) of CH_4/air CPO without dilution.

Figure II.5
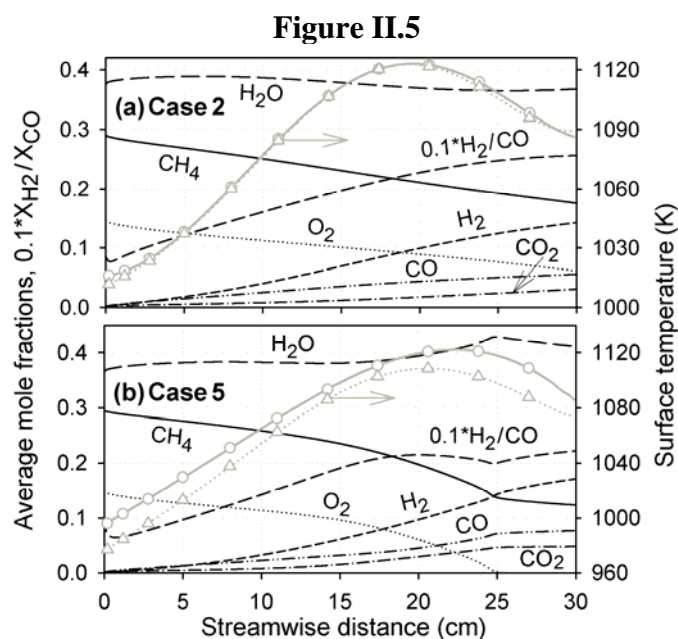
Computed streamwise profiles of *y*-averaged species mole fractions. Streamwise profiles of wall temperatures (gray lines) fitted through the thermocouple measurements (circles: upper wall, triangles: lower wall). The sharp bends at $x \approx 25$ cm in (b) are associated with the end of flame (Fig. II.8(5b)).

For the present high surface temperatures (Fig. II.5), coking was not an issue: post-combustion catalyst examination indicated no visible carbon deposition. While it is understood that non-visible carbon deposition can still influence the catalytic activity, the steady reactor performance suggested that surface carbon did not lead to catalyst deactivation over the timescales of testing.

Figure II.6
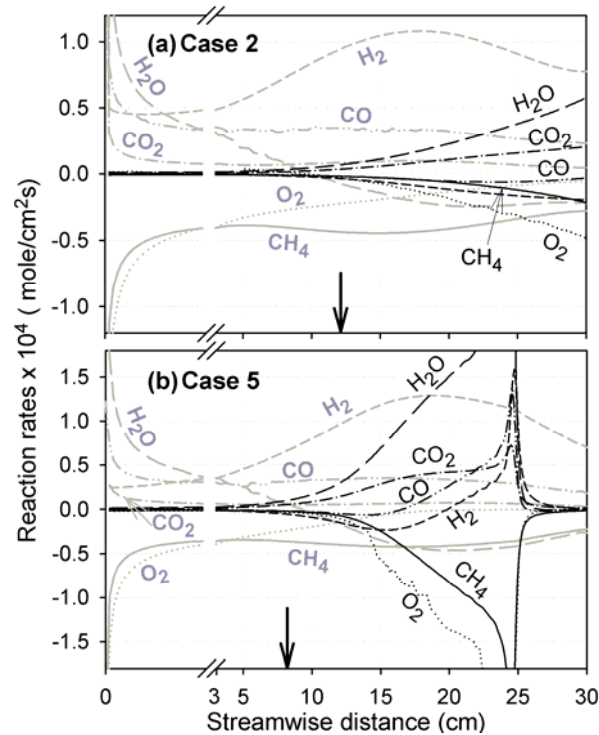
Computed species production rates (gray lines: catalytic, black lines: gaseous). For clarity, the initial 3 cm are expanded. The thick arrows indicate the position where gas-phase contribution becomes appreciable.

II.4.3 Effect of H₂O and CO₂ dilution on synthesis gas

The impact of water on the synthesis gas yields was investigated numerically by replacing the diluent H_2O with a fictitious species H_2O^* that had the same thermodynamic and transport properties as H_2O but did not participate in any reaction. H_2O^* simulated only the incoming diluent whereas the catalytic and gaseous pathways were still allowed to generate H_2O. The surface coverage of Case 2 with H_2O and H_2O^* dilution is presented in Fig. II.7. The addition of H_2O increased the $H_2O(s)$ coverage due to partial equilibration of the H_2O adsorption/desorption reactions. The higher $H_2O(s)$ coverage, in turn, enhanced the $OH(s)$ and $O(s)$ coverage (Fig. II.7). The reduced impact of the $H(s)$-consuming reactions $H(s)+O(s)=OH(s)+Rh(s)$ (due to the increased $OH(s)/O(s)$ ratio of the H_2O- compared to the H_2O^*-dilution) and $H(s)+OH(s)=H_2O(s)+Rh(s)$ (due to the corresponding increase in the $H_2O(s)/OH(s)$ ratio) led to a ~20% increase in $H(s)$ for the former case (Fig. II.7) that, in turn, promoted the H_2-producing desorption reaction $2H(s)\rightarrow H_2+2Rh(s)$. The addition of H_2O also caused a significant drop in $C(s)$ (Fig. II.7) since the higher $O(s)$ coverage accelerated the $C(s)$-depleting reaction $C(s)+O(s)=CO(s)+Rh(s)$. The higher amounts of $O(s)$ favored

CO(s)+O(s)=CO_2(s)+Rh(s) against CO(s)→CO+Rh(s), thus reducing the yields of CO and increasing those of CO_2. When H_2O was replaced by H_2O^*, computations over the extent with negligible gas-phase contribution have shown a 10% decrease in CH_4 conversion, a 21% drop in H_2 yields and a 6% increase in CO yields. This effect of H_2O dilution is consistent with autothermal CPO experiments [10, Bharadwaj and Schmidt, 1994]; the current computations have provided a first identification of the surface pathways responsible for this behavior.

Figure II.7
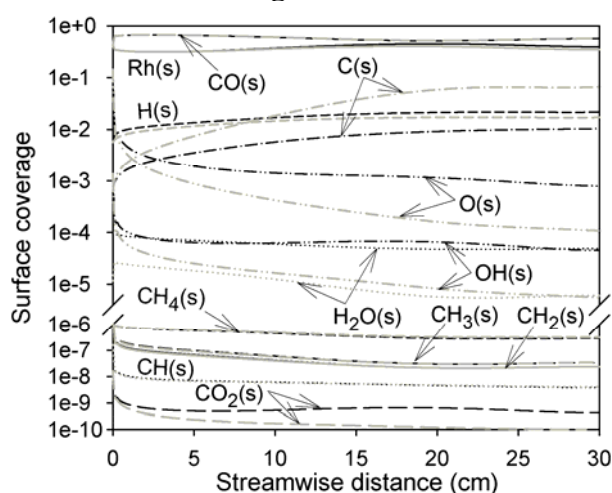
Surface coverage for Case 2 (black lines) and for the same case with diluent chemically inert H_2O^* (gray lines).

The effect of CO_2 dilution was investigated similarly through a fictitious species CO_2^*. The computations revealed that neither the CH_4 conversion nor the H_2/CO yields were affected by the presence of CO_2. When CO_2 was replaced by CO_2^*, the main change was a drop in CO_2(s) by a factor of five; however CO_2(s) was already too low (Fig. II.7) to significantly affect the other surface species.

II.4.4 Homogeneous ignition

The onset of homogeneous ignition is a safety concern in CPO-based high-pressure systems (e.g. turbines). Comparisons between LIF-measured and predicted CH_2O distributions are illustrated in Fig. II.8. Case 1 was specifically included so as to investigate homogeneous ignition at a much higher CO/H_2 ratio. The predicted levels of formaldehyde ranged from 1000 to 4100 ppmv. The flame shapes exhibited small asymmetries due to differences

between the two channel wall temperatures (see Fig. II.5). The onset of homogeneous ignition (x_{ig}), shown with the green arrows in Fig. II.8, was defined in both measurements and predictions by the location where the formaldehyde levels rose to 5% of their maximum flame value. There was an overall good agreement between the measured and predicted x_{ig} (within 5% for Cases 1, 4 and 5 and within 20% for Cases 2 and 3).

Figure II.8
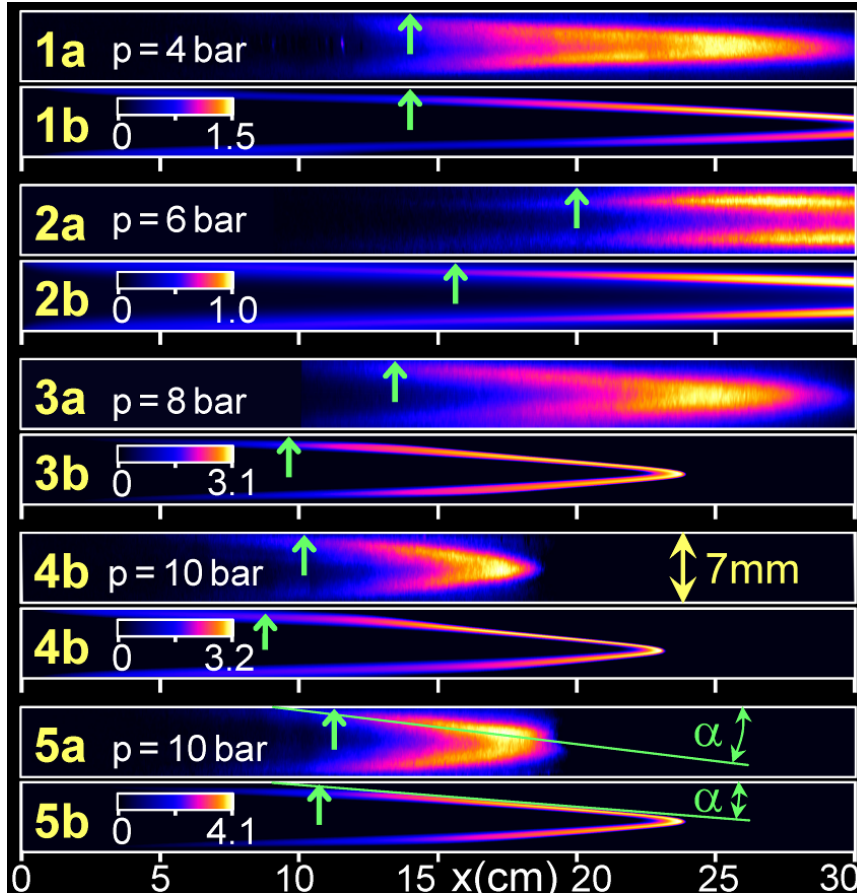
(a) LIF-measured, and (b) numerically predicted distributions of CH_2O for the five cases of Table II.1. The color bars provide the CH_2O in ppmv x 10^{-3}.

Despite the good homogenous ignition predictions, there were differences in the spatial distribution of formaldehyde. The predicted formaldehyde was concentrated in thin reaction zones, whereas the measurements indicated a broader distribution in the pre-flame region. The latter was not an experimental artifact as evidenced by the following analysis. Tuning the excitation wavelength off-resonance revealed no significant background signal contribution. This was not surprising, since broadband fluorescing poly-aromatic-hydrocarbons (PAH) were only formed downstream the end of the flame at the reactor exhaust (as visibly seen and also as attested by LIF measurements in the exhaust at shallow optical collection angles). An elongation by a factor of two of the apparent

formaldehyde zone has been reported in LIF measurements of non-preheated, atmospheric-pressure stoichiometric and slightly rich methane/air flames due to the exaggerated signal contribution of the colder (and hence higher density) zones upstream of the flame and due to quenching variations [28, Shin et al., 2001]. However, this effect is diminished in the present experiments due to mixture preheat, moderate flame temperatures (up to 1620 K at the channel center), and small changes of the gas composition (due to the substantially fuel-rich mixtures and the large H_2O dilution). Formaldehyde is known to form upstream of the flame front [28, Shin et al., 2001], however, it appears that the employed reaction scheme underestimates the contribution of those zones. Sensitivity analysis has further indicated that homogeneous ignition was affected by the H_2 and CO adsorption/desorption steps, as they determined the composition of the ignitable gaseous mixture. The small differences between Raman measurements and predictions could induce a ~3% difference in x_{ig}. This chemistry coupling has nevertheless exemplified the importance of the present combined hetero-/homogeneous investigations.

The measured flame sweep angles (denoted by α in Fig. II.8(5)) were reproduced well by the predictions only at pressures up to 8 bar. In Cases 4 and 5 (10 bar), the measured flame lengths were noticeably shorter than the predicted ones, suggesting that the employed gas-phase scheme underpredicted the propagation characteristics (laminar flame speeds) at those mixture compositions and pressures. However, in practical CPO systems the main requirement on the gas-phase scheme is to capture ignition delay (i.e. x_{ig}) and not propagation characteristics. Despite some apparent deficiencies of the employed reaction scheme, the present study has shown that it can reproduce the key safety issue of homogeneous ignition.

II.5 Conclusions

The partial catalytic oxidation of $CH_4/O_2/H_2O/CO_2/N_2$ mixtures over Rh/ZrO_2 was investigated experimentally with in situ, 1-D Raman and CH_2O planar LIF measurements. Numerical simulations have shown that the employed homogeneous reaction scheme, despite deficiencies in the extent of the formaldehyde zone and its propagation characteristics at 10 bar, reproduced well the onset of homogeneous ignition. The heterogeneous reaction scheme provided good agreement to the synthesis gas yields overpredicting slightly the total over the partial oxidation routes. The addition of H_2O increased the CH_4 conversion and H_2 yields and decreased the CO yields, due to a corresponding enhancement in the O(s) and OH(s) surface coverage. An increase in pressure from 4 to 10 bar had a minor effect on the methane conversion and hydrogen selectivity, while the addition of CO_2 had a minimal chemical impact.

III Experimental and numerical investigation of the catalytic partial oxidation of CH$_4$/O$_2$ mixtures diluted with H$_2$O and CO$_2$ in a short contact time reactor

A paper written by Adrian Schneider, John Mantzaras and Peter Jansohn; published in Chemical Engineering Science, 61:4634-4649, 2006.

Abstract

The catalytic partial oxidation (CPO) of fuel-rich CH$_4$/O$_2$ mixtures, heavily diluted with H$_2$O and CO$_2$ (46.3% and 23.1% volumetric feed composition, respectively), was investigated experimentally and numerically at 5 bar. Experiments were carried out in an ~8 ms residence time prototype gas-turbine honeycomb reactor coated with a Rh/ZrO$_2$ catalyst and included temperature measurements along the reactor and exhaust gas analysis. Simulations with detailed hetero-/homogeneous chemical reaction schemes were performed using a steady, full elliptic 2-D code for both the gas and solid phases. The employed catalytic reaction scheme overpredicted mildly the impact of the total over the partial oxidation route and this effect was more pronounced at lower reactor inlet temperatures ($<$ 523 K). The contribution of the various chemical pathways to the synthesis gas yields and selectivities has been elucidated. It was shown that the addition of water provided a source of surface oxygen and hydroxyl radicals, which in turn enhanced the CH$_4$ conversion and H$_2$ selectivity and reduced the CO selectivity. On the other hand, the addition of CO$_2$ had a minor impact on the aforementioned parameters. The increase in the H$_2$/CO product ratio with water dilution is highly desirable in new power generation processes with large exhaust gas recycle, which utilize the "catalytic rich combustion" methodology (the partial oxidation products stabilize a post-catalyst flame). At steady operation the catalyst surface temperatures exceeded by 200 K the adiabatic equilibrium temperature and standard (passive) heat transfer mechanisms in the solid were shown to be ineffective in providing proper reactor thermal management. Catalytic ignition was achieved at 670 K, however, the strong ignition/extinction hysterisis allowed for sustained steady CPO at inlet temperatures as low as 473 K.

III.1 Introduction

The catalytic partial oxidation (CPO) of methane to synthesis gas over noble metals has received increased attention in the last years [1, Schwiedernoch et al., 2003; 3, Hickman and

Schmidt, 1993; 4, Deutschmann and Schmidt, 1998; 29, Aghalayam et al., 2003; 30, Bodke et al., 1998; 31, Bruno et al., 2005] due to its key role in the efficient conversion of natural gas to synthetic liquid fuels and hydrogen. CPO can be accomplished autothermally and selectively in very short contact times over Pt- or Rh-based catalysts [3, Hickman and Schmidt, 1993; 4, Deutschmann and Schmidt, 1998; 32, Goralski Jr and Schmidt, 1999]. This allows for small reactor sizes that, in turn, render the process particularly attractive for on-board fuel reforming in many practical systems such as microreactors [33, Norton and Vlachos, 2005], fuel-cells [5, Chaniotis and Poulikakos, 2004], internal combustion engines [6, Allgeier et al., 2004] and large natural-gas-fuelled turbines of power generation systems [7, Castaldi et al., 2005].

The adopted approach in gas-turbines, denoted as "catalytic rich combustion", involves mixing of the entire fuel stream with part of the air stream and subsequent partial oxidation of the resulting fuel-rich mixture in a catalytic reactor. The hot combustion products (synthesis gas, complete oxidation products and unconverted reactants) are rapidly mixed with the remaining air and stabilize a post-catalyst fuel-lean gaseous flame. "Catalytic rich combustion" has two main advantages in comparison to the conventional catalytically stabilized thermal combustion (CST) that utilizes fuel-lean mixtures for both the catalytic and gas-phase reaction zones [34, Carroni et al., 2002; 35, Beebe et al., 2000]. The first is the lower catalyst light-off temperature due to the fact that noble metals are more active in the oxidation of fuel-rich rather than of fuel-lean hydrocarbon/air mixtures [36, Veser et al., 1999]. The second is the enhanced stability of the follow-up flame due to the highly reactive hydrogen contained in the synthesis gas. To advance the understanding of "catalytic rich combustion", [8, Appel et al., 2005] have recently investigated the partial oxidation of methane (main constituent of natural gas) in air over Rh/ZrO_2 at 6 bar. Therein, in situ laser-based measurements of major and minor species concentrations over the boundary layer of a channel-flow catalytic reactor were used, in conjunction with detailed numerical predictions, to elucidate the underlying heterogeneous (catalytic) and homogeneous (gas-phase) reaction pathways. A first application of the validated numerical model to a prototype gas turbine reactor was also reported in the last reference.

The standard "catalytic rich combustion" involves fuel-rich catalytic and fuel-lean gaseous combustion of natural gas in pure air. In the last years, however, technologies for the efficient combustion of natural-gas and air (or pure oxygen) diluted with large amounts of recycled exhaust gas (H_2O and CO_2) are under intense investigation. One such example is the advanced zero emissions approach [9, Griffin et al., 2004], which aims at mitigating both NO_x

and CO_2 in power plants. Therein nitrogen is separated from air, such that the natural gas is combusted at modest temperatures (up to 1500 K) in a stream of oxygen and recycled exhaust gas with the latter comprising up to 80% vol. of the feed. Combustion in pure oxygen rather than air circumvents the formation of NO_x. In addition, the absence of N_2 in the exhaust products allows for an easy separation of the non-recycled CO_2 from H_2O (e.g. via condensation), thus facilitating the sequestration or further disposal of CO_2. Pure gas-phase combustion of such heavily diluted mixtures at those temperatures is particularly challenging, rendering "catalytic rich combustion" a viable alternative. Understanding the impact of large H_2O and CO_2 dilution on the catalytic reaction pathways controlling the synthesis gas production is of paramount importance for the new power generation processes. Validated catalytic and gas-phase kinetics are indispensable input in multidimensional numerical codes needed for reactor design.

Steam addition is widely used in the autothermal catalytic reforming of methane for the chemical production of hydrogen e.g. [10, Bharadwaj and Schmidt, 1994; 37, Klein et al., 2001]. Moreover, steam facilitates the autothermal reforming of ethanol [12, Deluga et al., 2004] and suppresses the formation of olefins in the reforming of higher hydrocarbons [13, Dreyer et al., 2005]. The previous works refer to short-contact-time (~ms) reactors, except in Bharadwaj and Schmidt (1994) with corresponding times of 0.1-0.5 sec. On the other hand, dry (CO_2) reforming of methane is a long-contact-time (1-2 s) industrial process, which is used for the adjustment of the CO/H_2 ratio at the exit of a steam reformer and for the synthesis of alcohols, dimethylether and acetic acid. Dry reforming of methane over Rh-supported catalysts has been investigated by [38, Bitter et al., 1998; 39, Ferreira-Aparicio et al., 1998] and [40, Wang and Ruckenstein, 2000], while mechanistic aspects of this reaction have been reported in [41, Efstathiou et al., 1996; 42, Mark and Maier, 1996] and [43, Richardson et al., 2003]. The role of CO_2 reforming at the short contact times of interest to CPO is still under debate. Very few studies addressed dry reforming of methane at millisecond-long contact times [44, Basile et al., 1998].

The CPO of methane in gas turbines is differentiated in many ways from that employed in chemical processes. Nearly complete conversion of methane is sought in the latter, whereas in the former a ~50% conversion suffices given the post-catalyst gaseous combustion zone. Moreover, the presence of large CO_2 (in addition to H_2O) dilution in gas-turbines raises the issue of CO_2 reforming impacting the synthesis gas production. The optimization of the H_2 and CO selectivities is also not a controlling issue; CO is converted to CO_2 and the amount of hydrogen produced should only suffice for the stabilization of

follow-up gaseous combustion zone. On the other hand, in gas-turbines there are stringent catalyst light-off requirements (~670 K or less) at gas hourly spatial velocities (GHSV) of at least 10^6 h^{-1}.

The influence of large H_2O and CO_2 dilution on the CPO processes pertinent to gas-turbines has not been hitherto elaborated. The present study undertakes an experimental and numerical investigation of methane CPO with large H_2O and CO_2 dilution (CH_4/O_2 and H_2O/CO_2 volumetric ratios of two with 69.4% vol. exhaust gas). Steady and transient experiments have been carried out at 5 bar in a short contact time (residence times ~8 ms) prototype gas-turbine honeycomb catalytic reactor coated with ZrO_2-supported rhodium (1% weight). Gas analyzers and gas chromatography provided the exhaust composition whereas thermocouples monitored the inlet, outlet, and reactor temperature. The steady experiments were simulated with a single-channel model based on a full elliptic 2-D numerical code that included elementary hetero-/homogeneous chemical reaction schemes, detailed transport, and heat conduction in the solid. The main objectives were to elucidate the impact of H_2O and CO_2 addition on the steady CPO processes, to assess the applicability of existing catalytic reaction schemes, and to identify the chemical pathways responsible for methane consumption and synthesis gas production. Particular objectives were to address key thermal management requirements at steady reactor performance and to investigate the catalytic ignition characteristics in light of the corresponding stringent requirements of gas turbines.

III.2 Experimental

III.2.1 High pressure reactor

The test rig consisted of a prototype gas-turbine honeycomb catalytic reactor (Fig. III.1a, III.1b), which was positioned inside a high-pressure tank (Fig. III.1a), and a steam-generator supplying superheated steam (Fig. III.1c). The reactor itself has also been used in earlier complete oxidation studies of fuel-lean CH_4/air mixtures over Pt at turbine-relevant conditions [45, Carroni et al., 2003]. It comprised a 35 mm inner-diameter and 1.5 mm thick steel tube, whereby alternating flat and corrugated 50-μm-thick FeCr-alloy foils created a honeycomb structure (see detail in Fig. III.1b) with trapezoidal channels of hydraulic diameter $d_h = 1.2$ mm. The reactor had a total length $L = 75$ mm and was mounted inside a well-insulated (using a 30 mm thick fiber ceramic material) cylindrical steel frame. The first and last honeycomb sections with lengths $L_u = 10$ mm were catalytically inactive, whereas the central length $L_c = 55$ mm (Fig. III.1a) was coated with a Rh/ZrO_2 catalyst

according to the procedure outlined in Section III.2.4. The inlet, outlet and reactor temperatures were monitored with five 50-µm-thick K-type (Ni/Cr-Ni/Al) sheathed thermocouples. Four of the carrying wires were driven counterflow inside the reactor through

Figure III.1
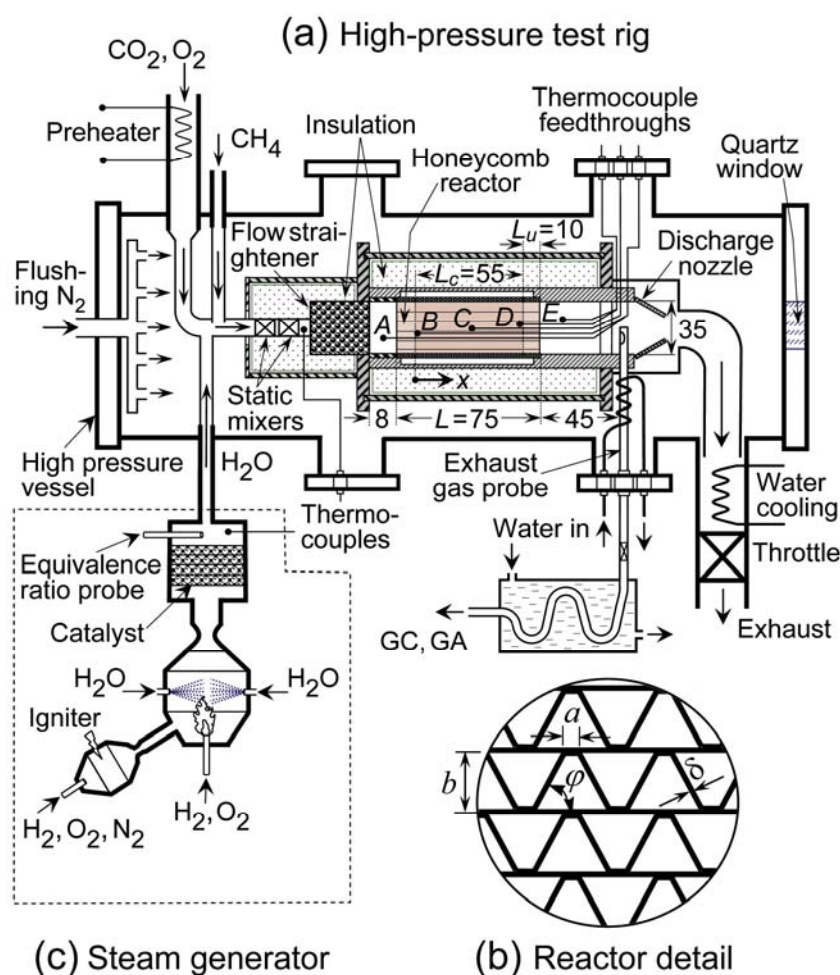
(a) High-pressure test rig, (b) detail of the honeycomb reactor, and c) steam generator. All distances are in mm. In (b) $a/b = 0.2$, $\varphi = 68°$ and $\delta = 50$ µm.

four honeycomb channels so as to position the thermocouple beads at $x = $ -15, 0, 27 and 55 mm ($x = 0$ denotes the beginning of the Rh-coated section); a fifth thermocouple at $x = 75$ mm monitored the outlet temperature. The three thermocouples inside the honeycomb (B, C and D in Fig. III.1a) provided neither the true surface nor the mean gas temperature but rather a weighted average, which was only indicative of the local steady reactor temperature. Nonetheless, those measurements were well-suited for the determination of light-off, wherein the inlet temperature was ramped at a rate of +2 K per minute until a vigorous steady burning state could be reached.

High-pressure bottles provided technical-grade CH_4 (> 99.5%), CO_2, and O_2. The flows were regulated and measured with three Brooks mass-flow controllers, leading to equivalence ratio accuracies better than ±0.5%. The CO_2 and O_2 flows were preheated by a 3 kW resistive heater to temperatures up to 720 K and then mixed with superheated steam (see Fig. III.1a and Section III.2.2). Room-temperature methane was injected farther downstream. The resulting $CH_4/O_2/CO_2/H_2O$ mixture passed through two sequential static mixers (Sulzer SMV) and a 40-mm long packing of ceramic spheres (2-mm in diameter) that straightened the flow. Those units were thermally insulated with a ceramic fiber material (Fig. III.1a). A K-type thermocouple positioned immediately after the static mixers monitored the gas temperature, which was used as a feedback to control the amount of CO_2/O_2 preheat and the degree of steam superheat. The honeycomb was located 8 mm downstream of the flow straightener and was mounted inside a 2.5 mm thick and 35 mm internal-diameter support steel tube. To minimize the heat losses, only the first and last 2 mm of the honeycomb contacted the steel tube; in the remaining length, a 1-mm-thick annular air-cushion was provided. Finally, the support tube ended in a discharge nozzle that directed the combustion products first to an exhaust pipe and then to a water-cooled outlet of the high-pressure tank.

The high pressure tank that housed the reactor was a stainless-steel cylindrical structure with a length of 1.8 m and an internal diameter of 0.28 m; the same casing also housed an optically accessible channel-flow catalytic reactor of earlier fundamental kinetic studies [14, Reinke et al., 2005; 15, Reinke et al., 2004; 46, Reinke et al., 2002; 47, Appel et al., 2005a]. A continuous flow of flushing nitrogen removed any unwanted combustion products from the free volume between the vessel and the reactor assembly (Fig. III.1a). Visual inspection of the reactor was achieved via a quartz window at the rear flange (Fig. III.1a) and two 300x35 mm quartz windows at the tank sides (not shown in Fig. III.1). Finally, the thermocouples, the gas sampling probe and its associated water cooling lines (see Section III.2.3) were driven inside the tank through high-pressure feedthroughs positioned on four dedicated flanges.

Radiation corrections were not required for the outlet thermocouple (*E*) measurements since the wall temperature at the reactor exit exceeded the mean gas outlet temperature ($T_{OUT} = T_E$) by less than 20 K (see forthcoming Fig. III.3). Moreover, T_{OUT} was at the most 15 K higher than the surface temperature of the surrounding metal support tube due to the good thermal insulation; this was attested by traversing radially the outlet thermocouple *E*. On the other hand, radiation corrections were applied to the inlet thermocouple (*A*) that had a

direct view to the hot catalyst entry. The corrections amounted to less than 8 K given the particular levels of gas inlet and maximum catalyst temperature (shown in Table III.1 and Fig. III.3). The corrected inlet temperatures (T_{IN}) were also consistent with the temperatures measured after the static mixers (~10 K lower). Overall, the absolute accuracy of the gas temperature measurements was ±10 K for the hot outlet and ±6 K for the inlet.

Table III.1

Experimental conditions[a]

Case	p (bar)	U_{IN} (m/s)	T_{IN} (K)	Re_{IN}
1	5	5.1	623	590
2	5	4.7	573	637
3	5	4.3	523	689
4	5	3.9	473	755

[a]pressure, inlet velocity, temperature and Reynolds number. The inlet volumetric compositions for all cases are: 20.4% CH_4, 10.2% O_2, 46.3% H_2O and 23.1% CO_2.

III.2.2 Steam generator

The steam generator (Fig. III.1c) provided superheated steam at flow rates of 0.9-20 g/s and temperatures of 473-1273 K. Such high mass flow rates could not be supplied by common electric-heater-based systems; therefore, the heat of H_2/O_2 combustion was used to vaporize known amounts of added liquid water. The device consisted of a combustion chamber, a gas/water supply and an electronic control unit. The combustion chamber was designed by DLR [48, Beer and Willms, 1993] and comprised three modules: the hot gas igniter, the main combustion chamber and the catalytic converter. In the former module a small amount of $H_2/O_2/N_2$ was ignited by conventional spark plugs. The resulting hot exhaust gases were then flushed into the main chamber to ignite a central H_2/O_2 flame, which was stabilized by the recirculation zone of a sudden geometric expansion. A continuous spray injection of demineralized liquid water controlled the amount of steam and the reactor temperature. A follow-up Ni-Pd catalyst packing converted any escaping H_2 and O_2 to H_2O. To avoid hydrogen breakthrough, the central burner was operated slightly fuel-lean ($0.98 \leq \varphi < 1$). An equivalence-ratio probe (similar to those used in automotive engines) positioned at the downstream end of the catalytic converter monitored the O_2 content and determined the

degree of steam purity. Step-motor-controlled needle valves regulated the liquid water and the gaseous flows of the main combustor; a Micro-Motion-Elite sensor and Brooks meters measured the liquid water and the gaseous mass flows, respectively. Finally, a thermocouple positioned at the downstream end of the catalytic converter provided the steam temperature.

III.2.3 Gas analysis

A fraction of the exhaust gas was sampled with a probe positioned 45 mm downstream the reactor exit (Fig. III.1a). The probe consisted of a water-cooled Si-coated steel tube so as to mitigate catalytic and gas-phase reactions in the sampled gas. The steam was further condensed in a serpentine-type heat exchanger (water-cooled) outside the high pressure tank. The dried gases entered a rack of gas analyzers (GA) and the sample port of a gas chromatograph (GC). Water removal was necessary for the proper operation of both analysis instruments. However, the compositions of the actual wet gas products could still be determined by carrying out element balances.

Hartmann and Braun gas analyzers (Uras-10E for CO, Magnos-6G for O_2 and Caldos-5G for H_2) were used for continuous gas analysis; their operating principle was based on NDIR for CO, paramagnetism for O_2 and thermal conductivity for H_2. The accuracy of the measurements (determined with calibration gas mixtures) was particularly good for CO (0.3% relative error for 10-14% vol. CO in the dry gas) and that of O_2 was still good despite the associated low levels (20% relative error for ~1% vol. O_2). However, the presence of gases with thermal conductivities largely different than that of reference N_2 (e.g. CH_4 and CO_2) resulted in larger inaccuracies for the H_2 levels (20% relative error for typical ~30% vol. H_2 in the dry gas); this effect was partly compensated by calibrating the device with simulated exhaust gas compositions. More detailed analysis was carried out with an HP-6890++ GC equipped with porous polymer and molecular siever columns and a thermal conductivity sensor. The carrier gas was helium and the analysis was discontinuous with one measurement every 8 min. Integration was performed with the HP ChemStation software, while a spreadsheet was used to calculate the final compositions. The GC allowed measurements of all key species. The porous polymer column separated CO_2 before the gas entered the molecular sieve. The GC has been tested against a selection of different calibration gas mixtures. Even though the hydrogen signals were weak due to the choice of He as carrier gas, for the present substantial levels (~30% vol. H_2) the accuracy was good (relative error for H_2 ~4%). The relative error in the measurements of CH_4, CO_2 and CO was 4-5% and that of O_2 was 60%. For the short GC runtimes, higher hydrocarbons could not be detected; however,

the element balances have shown that their contribution –if any– was within the experimental uncertainty. The GC measurements will be used in the ensuing analysis while the GA data will provide an additional control for the CO and O_2 compositions.

III.2.4 Catalyst preparation and operating conditions

The catalyst of the present investigation was 1%Rh (wt.) on ZrO_2, prepared by incipient wetness impregnation of the ZrO_2 support with a $Rh(NO_3)_3$ solution. The impregnated catalyst powder was calcined at 1120 K for 10 hr. A slurry prepared from the powder and a solvent mixture was sprayed on FeCr-alloy foils. The coated foils were calcined at 920 K for 5 hrs and the measured catalytic layer thickness was $\delta_c \approx 12$ μm. In the inactive front and rear sections ($L_u = 10$ mm) of the FeCr-alloy foils, a 12 μm ZrO_2 layer without rhodium was applied. The total and active areas of both fresh and used Rh-coated FeCr-alloy foils were measured with BET (N_2-physisorption) and CO-chemisorption, respectively. In addition, the surface composition was determined with X-ray photoelectron spectroscopy (XPS); XPS provided information on the oxidation state of the detected species and also showed that Fe or Cr did not diffuse in the surface. Finally, surface Raman spectroscopy was used to determine the crystal structure of the support. The detailed catalyst characterization is outside the scope of this work and is reported elsewhere [49, Eriksson et al., 2006]; in the following, only information relevant to the current investigation will be presented.

The experimental conditions for the 1%Rh/ZrO_2 catalyst are provided in Table 1. The pressure was 5 bar, the inlet temperatures (T_{IN}) ranged from 473 to 623 K and the inlet velocities increased with rising T_{IN} so as to maintain the same mass throughput. The gas hourly space velocity (GHSV) was in all cases 8×10^5 hr^{-1} and the computed residence times in the catalytic section (accounting for the flow acceleration due to heating) ranged from 7 ms (Case 1) to 7.8 ms (Case 4). The equivalence ratio was $\varphi = 4$ and the dilution comprised 46.3% H_2O and 23.1% CO_2 per volume. Before each combustion run, the catalyst was reduced in a heated (673 K) H_2/N_2 flow for 15 min.

III.3 Numerical

Numerical simulations were carried out with a steady, two-dimensional, elliptic numerical code that included detailed hetero-/homogeneous chemistry, transport and heat transfer in the solid. Given the good thermal insulation and the uniform reactor entry properties, a single-channel modeling approach has been adopted. A representative trapezoidal channel

with a length $L = 75$ mm was modeled as an equivalent cylindrical channel with a hydraulic radius $r_h = 0.6$ mm.   This was a reasonable simplification for the channel geometry of Fig. III.1a.   The parameters $a/b = 0.2$ and $\varphi \approx 68°$ yielded friction factors $f \cdot Re$ and Nusselt numbers Nu_H (constant heat transfer case) within 6% and 15% of the corresponding values of a cylindrical duct [50, Shah and London, 1978], thus suggesting a rather weak three-dimensionality of the flow.   After all, post-combustion examination of the reactor has indicated that the individual trapezoidal channel cross section was not maintained constant since the flat and corrugated FeCr-alloy foils were not welded to each other.   Moreover, the 2-D modeling rendered the computations with detailed chemistry feasible.   A 2-D flow model has also been successfully applied to the fuel-lean combustion of CH_4/air over Pt in a similar honeycomb reactor [45, Carroni et al., 2003].

III.3.1 Numerical model and boundary conditions

A steady laminar flow with elementary heterogeneous and homogeneous chemical reaction schemes in its full elliptic, cylindrical-coordinate formulation was modeled.   The gas-phase and surface species governing equations have been provided elsewhere [21, Dogwiler et al., 1999; 45, Carroni et al., 2003] and are not repeated here.   The species diffusion velocities $\vec{V}_k$ were computed using mixture-average plus thermal diffusion for the light species H and H_2 [51, Kee et al., 1996a]:

$$\vec{V}_k = -(D_{km} / Y_k)\nabla Y_k + (D_k^T / \rho Y_k T)\, \nabla T\,, \quad k = 1,..,K_g. \tag{1}$$

A 2-D approach was also adopted for the solid substrate (thickness $\delta/2 + \delta_c = 37$ mm), thus extending the earlier 1-D solid model [45, Carroni et al., 2003]. Solution was obtained for the steady solid heat conduction:

$$\lambda_s(r)\frac{\partial^2 T_W}{\partial x^2} + \frac{1}{r}\frac{\partial}{\partial r}\left[r\lambda_s(r)\frac{\partial T_W}{\partial r}\right] = 0\,, \tag{2}$$

with $\lambda_s(r) = 0.4$ $Wm^{-1}K^{-1}$ for $r_h < r \leq r_h + \delta_c$ (ZrO_2 porous washcoat) and $\lambda_s(r) = 16$ $Wm^{-1}K^{-1}$ for $r_h + \delta_c < r < r_h + \delta_c + \delta/2$ (FeCr-alloy).

The interfacial energy boundary condition ($r = r_h$) was:

$$\dot{q}_{rad} - (\lambda_g\,\partial T_W/\partial r)_{r = r_{h-}} + (\lambda_s\,\partial T_W/\partial r)_{r = r_{h+}} + B\sum_{k=1}^{K_g}\left(\dot{s}_k h_k W_k\right)_{r = r_h} = 0\,. \tag{3}$$

The term $\dot{q}_{rad}$ accounted for the radiation exchange of each differential cylindrical surface element with all other differential surface elements as well as with the channel entry and outlet. The gas-phase species interfacial boundary conditions were:

$$(\rho Y_k V_{k,r})_{r=r_h} + B \dot{s}_k W_k = 0, \quad k = 1,.., K_g, \tag{4}$$

with $\dot{s}_k = 0$ over the inactive channel length. The factor B denoted the ratio of the active to the geometrical surface area and was determined by the CO chemisorption tests. Those tests revealed an active area of 25.9 m^2/gr-Rh for the used catalysts; with known size, weight and noble metal content of the analyzed samples, the latter value yielded $B = 4.5$. The fresh samples had a considerably higher value ($B = 17.4$) as they comprised both high-surface-area tetragonal phase and low-surface-area monoclinic ZrO_2 phase (detected with surface Raman). On the other hand, the used samples comprised mainly low-surface-area monoclinic phase. The value $B = 4.5$ was maintained in successive combustion runs and was, therefore, used in the simulations. Intraphase species diffusion was not considered because the catalyst layer was only 12 μm thick and was applied on a non-porous FeCr-alloy.

Radiative boundary conditions were applied at the reactor inlet and outlet:

$$\lambda_s(r)\partial T_W / \partial x = \varepsilon\sigma \left[T_W^4(x) - T_{IN}^4 \right] \qquad \text{at } x = -L_u, \quad r_h < r \leq r_h + \delta_c + \delta/2$$

$$-\lambda_s(r)\partial T_W / \partial x = \varepsilon\sigma \left[T_W^4(x) - T_{rad,OUT}^4 \right] \quad \text{at } x = L_c + L_u, \quad r_h < r \leq r_h + \delta_c + \delta/2. \tag{5}$$

A surface emissivity $\varepsilon = 0.3$ was used for the coated surfaces. The radiation exchange temperature $T_{rad,OUT}$ was taken 15 K lower than the mean gas outlet temperature, considering the somewhat colder support tube enclosure as discussed in Section III.2.1. It will be shown, however, that radiation effects were altogether minimal (Section III.4.3). Finally, the outer channel walls were treated as adiabatic ($\partial T_W / \partial r = 0$ at $r = r_h + \delta_c + \delta/2$) so as to account for the adjacent honeycomb channels.

Uniform profiles for the axial velocity (deduced from the measured inlet temperature and mass flow rates), the species mass fractions and the temperature were specified at the inlet. The 8 mm gap between the flow straightener and the honeycomb entry created only a very thin boundary layer (less than 0.4 mm since the Reynolds numbers in the 35 mm diameter support tube exceeded 15000), hence justifying the consideration of a representative constant inlet velocity for all channels. At the axis of symmetry ($r = 0$) and the channel outlet ($x = L_c + L_u$) zero-Neumann boundary conditions were used for all thermoscalars and the axial velocity, while the radial velocity was set to zero. No-slip has been applied for both velocity components at $r = r_h$.

The governing equations were discretized with a finite volume scheme and the solution was obtained iteratively using a SIMPLER [52, Patankar, 1980] method for the pressure-velocity field. Details on the solution algorithm and the treatment of the hetero-/homogeneous coupling have been provided elsewhere [21, Dogwiler et al., 1999; 53, Mantzaras et al., 2000; 54, Appel et al., 2002]. An orthogonal staggered grid of 220x24 points in x and r, respectively, (75 mm x 0.6 mm) with finer x-spacing closer to the beginning of the catalyst section and r-spacing closer to the wall was sufficient to produce a grid-independent solution. The solid was discretized with 220x20 points (75 mm x 0.037 mm).

III.3.2 Chemical Kinetics

The elementary heterogeneous chemical reaction scheme of Deutschmann [1, Schwiedernoch et al., 2003] was used to describe the partial oxidation of methane over rhodium. The scheme consisted of 38 reactions, 12 surface and 6 gas-phase species (see Table 2). The mechanism has been augmented by four radical adsorption/desorption reactions (S7-S9 and S42) in order to properly account for the potential onset of homogeneous ignition [55, Mantzaras et al., 2000]. Unity sticking coefficients were used in S7-S9 and literature values for the kinetic parameters of S42 [3, Hickman and Schmidt, 1993]. Fundamental kinetic studies in an optically accessible reactor have shown [47, Appel et al., 2005a] that the aforementioned catalytic scheme reproduced the methane conversion and synthesis gas yields in CPO of CH_4/air (without exhaust gas dilution), at least over the reactor extent were oxygen was still available. In the present studies a small oxygen breakthrough was always assured.

The C_2/H/O gas-phase scheme of Warnatz et al. (1996) was used to assess the impact of homogeneous chemistry. This scheme has reproduced homogeneous ignition characteristics in CPO of CH_4/air over Rh [47, Appel et al., 2005a]. Simulations of the present experiments have clearly indicated that the homogeneous reaction pathway was negligible. The gas-phase contribution was also negligible over the 45-mm-long gap separating the reactor exit and the sampling probe as demonstrated by additional plug-flow-reactor simulations. The minimal gas-phase contribution was further attested experimentally: turning the cooling water of the sampling probe off, resulted in only 3% relative rise of the GC-measured hydrogen volumetric composition, despite the fact that the residence time in the visibly-hot part of the probe was about ten times longer than that of the reactor.

Table III.2

Catalytic reaction scheme[a]

Adsorption reactions		A (γ)	b	E
S1.	$CH_4 + Rh(s) \rightarrow CH_4(s)$	0.008	0.0	0.0
S2.	$O_2 + 2Rh(s) \rightarrow 2O(s)$	0.01	0.0	0.0
S3.	$H_2 + 2Rh(s) \rightarrow 2H(s)$	0.01	0.0	0.0
S4.	$H_2O + Rh(s) \rightarrow H_2O(s)$	0.01	0.0	0.0
S5.	$CO_2 + Rh(s) \rightarrow CO_2(s)$	10^{-5}	0.0	0.0
S6.	$CO + Rh(s) \rightarrow CO(s)$	0.5	0.0	0.0
S7.	$H + Rh(s) \rightarrow H(s)$	1.0	0.0	0.0
S8.	$O + Rh(s) \rightarrow O(s)$	1.0	0.0	0.0
S9.	$OH + Rh(s) \rightarrow OH(s)$	1.0	0.0	0.0

Surface reactions				
S10.	$H(s) + O(s) \rightarrow OH(s) + Rh(s)$	5.0×10^{22}	0.0	83.7
S11.	$OH(s) + Rh(s) \rightarrow H(s) + O(s)$	3.0×10^{20}	0.0	37.7
S12.	$H(s) + OH(s) \rightarrow H_2O(s) + Rh(s)$	3.0×10^{20}	0.0	33.5
S13.	$H_2O(s) + Rh(s) \rightarrow H(s) + OH(s)$	5.0×10^{22}	0.0	106.4
S14.	$OH(s) + OH(s) \rightarrow H_2O(s) + O(s)$	3.0×10^{21}	0.0	100.8
S15.	$H_2O(s) + O(s) \rightarrow OH(s) + OH(s)$	3.0×10^{21}	0.0	224.2
S16.	$C(s) + O(s) \rightarrow CO(s) + Rh(s)$	3.0×10^{22}	0.0	97.9
S17.	$CO(s) + Rh(s) \rightarrow C(s) + O(s)$	2.5×10^{21}	0.0	169.0
S18.	$CO(s) + O(s) \rightarrow CO_2(s) + Rh(s)$	1.4×10^{20}	0.0	121.6
S19.	$CO_2(s) + Rh(s) \rightarrow CO(s) + O(s)$	3.0×10^{21}	0.0	115.3
S20.	$CH_4(s) + Rh(s) \rightarrow CH_3(s) + H(s)$	3.7×10^{21}	0.0	61.0
S21.	$CH_3(s) + H(s) \rightarrow CH_4(s) + Rh(s)$	3.7×10^{21}	0.0	51.0
S22.	$CH_3(s) + Rh(s) \rightarrow CH_2(s) + H(s)$	3.7×10^{24}	0.0	103.0
S23.	$CH_2(s) + H(s) \rightarrow CH_3(s) + Rh(s)$	3.7×10^{21}	0.0	44.0
S24.	$CH_2(s) + Rh(s) \rightarrow CH(s) + H(s)$	3.7×10^{24}	0.0	100.0
S25.	$CH(s) + H(s) \rightarrow CH_2(s) + Rh(s)$	3.7×10^{21}	0.0	68.0
S26.	$CH(s) + Rh(s) \rightarrow C(s) + H(s)$	3.7×10^{21}	0.0	21.0
S27.	$C(s) + H(s) \rightarrow CH(s) + Rh(s)$	3.7×10^{21}	0.0	172.8
S28.	$CH_4(s) + O(s) \rightarrow CH_3(s) + OH(s)$	1.7×10^{24}	0.0	80.3
S29.	$CH_3(s) + OH(s) \rightarrow CH_4(s) + O(s)$	3.7×10^{21}	0.0	24.3
S30.	$CH_3(s) + O(s) \rightarrow CH_2(s) + OH(s)$	3.7×10^{24}	0.0	120.3
S31.	$CH_2(s) + OH(s) \rightarrow CH_3(s) + O(s)$	3.7×10^{21}	0.0	15.1
S32.	$CH_2(s) + O(s) \rightarrow CH(s) + OH(s)$	3.7×10^{24}	0.0	158.4
S33.	$CH(s) + OH(s) \rightarrow CH_2(s) + O(s)$	3.7×10^{21}	0.0	36.8
S34.	$CH(s) + O(s) \rightarrow C(s) + OH(s)$	3.7×10^{21}	0.0	30.1
S35.	$C(s) + OH(s) \rightarrow CH(s) + O(s)$	3.7×10^{21}	0.0	145.5

Desorption reactions				
S36.	$2H(s) \rightarrow H_2 + 2Rh(s)$	3.0×10^{21}	0.0	77.8
S37.	$2O(s) \rightarrow O_2 + 2Rh(s)$	1.3×10^{22}	0.0	$355.2-280\theta_O$
S38.	$H_2O(s) \rightarrow H_2O + Rh(s)$	3.0×10^{13}	0.0	45.0
S39.	$CO(s) \rightarrow CO + Rh(s)$	3.5×10^{13}	0.0	$133.4-15\theta_{CO}$
S40.	$CO_2(s) \rightarrow CO_2 + Rh(s)$	1.0×10^{13}	0.0	21.7
S41.	$CH_4(s) \rightarrow CH_4 + Rh(s)$	1.0×10^{13}	0.0	25.1
S42.	$OH(s) \rightarrow OH + Rh(s)$	8.1×10^{11}	0.0	142.2

[a]from Schwiedernoch et al. (2003). In all surface and desorption reactions, the reaction rate coefficient is $k = AT^b exp(-E/RT)$. S10 to S35 comprise thirteen pairs of forward and backward reactions. Units: A (mol-cm-sec), E (kJ/mol). In the adsorption reactions, A denotes a sticking coefficient (γ). The suffix (s) designates a surface species. The surface site density is 2.72×10^{-9} mol/cm^2.

Therefore, the inclusion of gas-phase chemistry and of the additional four catalytic reactions did not impact the following simulations.

The CHEMKIN database was used to evaluate transport properties [51, Kee et al., 1996a]. Thermodynamic data for the gas-phase species were included in the chemical scheme [2, Warnatz et al., 1996]. Finally, surface and gas-phase reaction rates were evaluated with SURFACE CHEMKIN [25, Coltrin et al., 1996] and CHEMKIN [56, Kee et al., 1996b], respectively.

III.4 *Results and discussion*

III.4.1 Catalytic ignition

Even though steady CPO constitutes the main topic of this work, it is worthwhile to demonstrate that the examined catalyst meets light-off requirements at turbine-relevant conditions, i.e. catalytic ignition at inlet temperatures as low as 670 K and realistically high space velocities ($\sim 10^6\,hr^{-1}$). In certain processes with exhaust gas recycle, such as the advanced zero emissions approach of Griffin et al. (2004), the ignition requirements may be less stringent since the inlet temperatures can provisionally reach 850 K. Table 3 provides the measured light-off temperatures of four representative catalysts with different Rh-loadings and supports, selected from a larger number of screened catalysts. Details of the catalyst screening at the present operating conditions are provided in Eriksson et al., 2005a, whereas at lower H_2O dilutions (10% vol.) and GHSV ($10^5\,h^{-1}$) in Eriksson et al., 2005b. The mass throughput in the ignition tests of Table 3 was the same as in the steady experiments of Table 1. Increasing the inlet temperature to T_{ig} caused an abrupt transition to vigorous steady combustion with measured outlet reactor temperatures in excess of 1000 K. The 1%Rh/ZrO_2 catalyst of the present study (No. 2 in Table 3) was promising for gas turbines ($T_{ig} = 670$ K). The other catalysts of Table 3 were only included to give a perspective on the ignition capabilities of the chosen catalyst.

Table III.3

Catalytic ignition experiments[a]

Catalyst	Rh (% wt.)	Support	T_{ig} (K)
1	0.5	ZrO_2	700
2	1	ZrO_2	670
3	1	$Ce-ZrO_2$	655
4	1	$Ce_{0.9}La_{0.1}O_2$	710

[a]ignition temperature for various catalysts.

Upon ignition, the inlet temperature could be further reduced by as much as 200 K while still maintaining high steady fuel conversion and reactor exothermicity. This is illustrated in Fig. III.2, which provides the measured continuous time history of the inlet and outlet temperature and the discontinuous GC-deduced outlet composition (on a dry basis). Reduction of T_{IN} by 200 K led to a drop of T_{OUT} by only 45 K and to a moderate decline of CH_4 conversion and synthesis gas yields (e.g. decrease in H_2 content from 36% to 30% vol.). Nonetheless, the outlet temperatures and hydrogen concentrations were still maintained to high levels for the subsequent gaseous combustion. It is noted that the observed large hysterisis in the catalytic ignition/extinction characteristics was beneficial for low part-load and idle turbine operation (compressor discharge temperatures typically ~100 K lower than the corresponding full-load values). Such extended hysterisis is not typical in fuel-lean methane catalytic combustion and this behavior deserves future investigation. The steady conditions of Table 1 were obtained by igniting the catalyst at $T_{IN} = 670$ K and then reducing accordingly the inlet temperature. In a similar fashion, the numerical solution of Case 1 was used as an initial guess to obtain converged ignited solutions for the lower inlet temperature Cases 2-4. It is finally noted that the GC-measured CO mole fractions of Fig. III.2 were reproduced within 0.5% by the GA measurements; the corresponding agreement in the largely depleted O_2 was 25%.

III.4.2 Comparisons between measurements and predictions

Axial profiles of the predicted wall temperature (T_W), the average (over the radial distance r_h) gas temperature (T_{gas}), and the average methane and hydrogen mole fractions are depicted in Fig. III.3 for Cases 1 and 4. In the same figure, the measured temperatures at positions *A* through *E* (Fig. III.1a) and the measured mole fractions (wet gas) of CH_4 and H_2 in the

exhaust are provided along with the calculated adiabatic equilibrium temperature and species mole fractions. The measured and predicted major species mole fractions and temperatures (the latter at $x = 55$ mm) are summarized in Table 4 for all cases. The measured wet composition in Table 4 was assessed by carrying out balances for the C, H and O elements. Two linearly independent element conservation equations were constructed that provided two independent wet compositions. The small relative deviation (less than 3%) of the independently assessed compositions attested the accuracy of the measurements.

Figure III.2
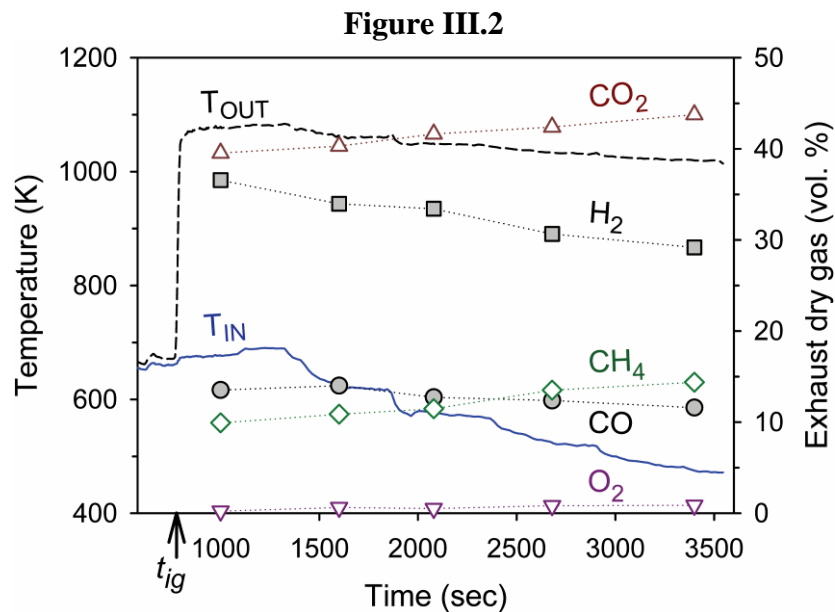
Time histories of measured inlet (T_{IN}, solid lines) and outlet (T_{OUT}, dashed lines) temperatures and GC-measured dry-gas exhaust compositions. CO_2: open upper triangles, H_2: filled squares, CH_4 open diamonds; CO: filled circles; O_2: open lower triangles. The time $t = t_{ig}$ corresponds to catalytic ignition.

The chemical scheme underpredicted somewhat the methane conversion and overpredicted the extent of the complete over the partial oxidation route; the latter was manifested by the lower predicted synthesis gas and higher complete oxidation products. The relative deviations between measured and predicted mole fractions increased with decreasing inlet temperature but were maintained within 20%. Nonetheless, the lower inlet temperature Cases 3 and 4 were marginally interesting for steady gas-turbine operation and, in particular, for approaches with large exhaust gas recycle. The temperature comparisons in Fig. III.3a were especially encouraging at $x = 27$ and 55 mm: the thermocouple measurements were bounded by T_W and T_{gas} (see also Table III.4), in accordance to the anticipated behavior discussed in Section III.2.1, suggesting that the numerical model realistically reproduced the

temperature evolution along the reactor. On the other hand, the particularly good agreement between measured and predicted temperatures in the lower T_{IN} case (Fig. III.3b) at $x = 55$ mm reflected to some extent the counteracting effects of lower predicted CH_4 conversion and higher selectivity to complete oxidation products. The analysis in the following sections will focus on the higher inlet temperature Case 1.

Table III.4

Comparison between experiments and simulations[a]

Case	CH_4 (%)		O_2 (%)		H_2 (%)		CO (%)		H_2O (%)		CO_2 (%)		T (K)	
	Exp.	Sim.	Exp.	Sim.	Exp.	Sim.	Exp.	Sim.	Exp.	Sim.	Exp.	Sim.	Exp.	Sim.
	Dry	Dry	Dry	Dry	Dry	Dry	Dry	Dry	Dry	Dry	Dry	Dry	T_D	T_W
	Wet	*Wet*	*Wet*	*Wet*	*Wet*	*Wet*	*Wet*	*Wet*	*Wet*	*Wet*	*Wet*	*Wet*		T_{gas}
1	12.8	13.1	0.3	1.5	33.3	31.3	14.3	13.8	-	-	39.4	40.4	1054	1062
	7.4	*7.4*	*0.1*	*0.8*	*19.3*	*17.7*	*8.3*	*7.8*	*42.0*	*43.5*	*22.8*	*22.8*		*1054*
2	13.6	14.7	0.5	1.6	31.6	28.7	13.5	13.7	-	-	40.9	41.3	1041	1048
	7.7	*8.1*	*0.3*	*0.9*	*17.9*	*15.8*	*7.6*	*7.5*	*43.2*	*44.8*	*23.2*	*22.8*		*1037*
3	14.8	16.4	0.9	1.7	29.6	26.1	12.5	13.4	-	-	42.2	42.4	1028	1035
	8.3	*8.8*	*0.5*	*0.9*	*16.5*	*14.3*	*7.0*	*7.2*	*44.2*	*46.0*	*23.6*	*22.9*		*1019*
4	16.1	18.1	1.3	1.9	27.9	23.4	12.2	13.1	-	-	42.5	43.5	1020	1021
	8.9	*9.5*	*0.7*	*1.0*	*15.5*	*12.7*	*6.7*	*6.9*	*44.6*	*47.2*	*23.5*	*23.0*		*1001*

[a] volumetric exit compositions (%, on dry and wet basis) and temperature at the end of the catalytically active section (position D in Fig. III.1, $x = 55$ mm).

Figure III.3
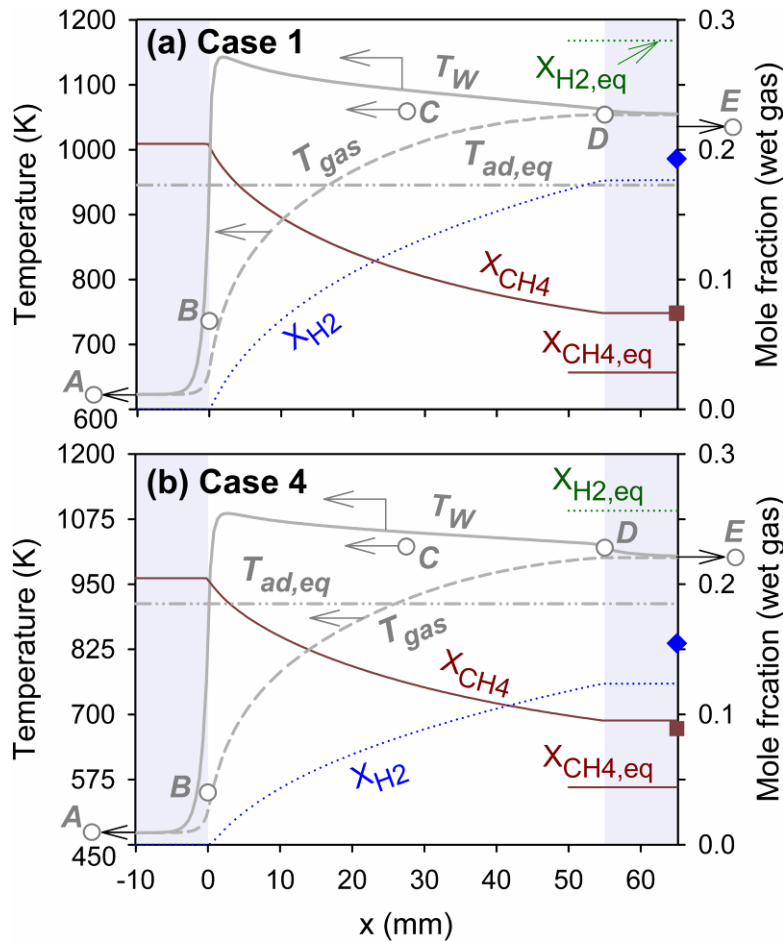
Axial profiles of temperature and species for: a) Case 1 and b) Case 4. Predictions: wall temperature T_W (solid gray lines), mean gas temperature T_{gas} (dashed gray lines), mean CH$_4$ mole fraction (solid lines), mean hydrogen mole fraction (dotted lines). Adiabatic equilibrium calculations are also provided for the gas temperature and the mole fractions of CH$_4$ and H$_2$ ($T_{ad,eq}$, $X_{CH4,eq}$ and $X_{H2,eq}$, respectively). Measurements: temperature (open circles), outlet H$_2$ mole fraction (filled diamond), outlet CH$_4$ mass fraction (filled square). The shaded areas denote the inactive reactor length.

III.4.3 Steady reactor temperature

Since the magnitude and spatial distribution of the reactor temperature is of prime importance in practical systems, the sensitivity of those quantities to the various modes of solid-phase heat transfer is established next. The energy balance for each differential solid cylindrical element (length Δx and thickness $\delta_c + \delta/2$) is provided in Fig. III.4, while the 2-D temperature distribution in both solid and gas is illustrated in Fig. III.5a (Case 1). The latter

indicated very small radial gradients in the solid (temperature differences of less than 0.4 K over the 37 μm thickness) at steady operation. In Fig. III.4, $\dot{q}_{cond}$ accounted for both the radial and the (integrated across the twenty radial solid-phase volumes) axial heat conduction, $\dot{q}_{gen}$ represented the chemical heat release at the surface, and $\dot{q}_{conv}$ denoted the convective heat loss to the gas. The heat generation peaked nearly at the start of the coated section (the light-off distance was practically zero) due to complete oxidation reactions as will be further discussed in Section III.4.4. Radiation was negligible, with only a minor net radiative heat transfer from the initial hot ~3 mm catalytic section to the adjacent ~3 mm inactive section. Repeating the computations with $\varepsilon = 0$ reproduced the same surface temperatures.

Figure III.4
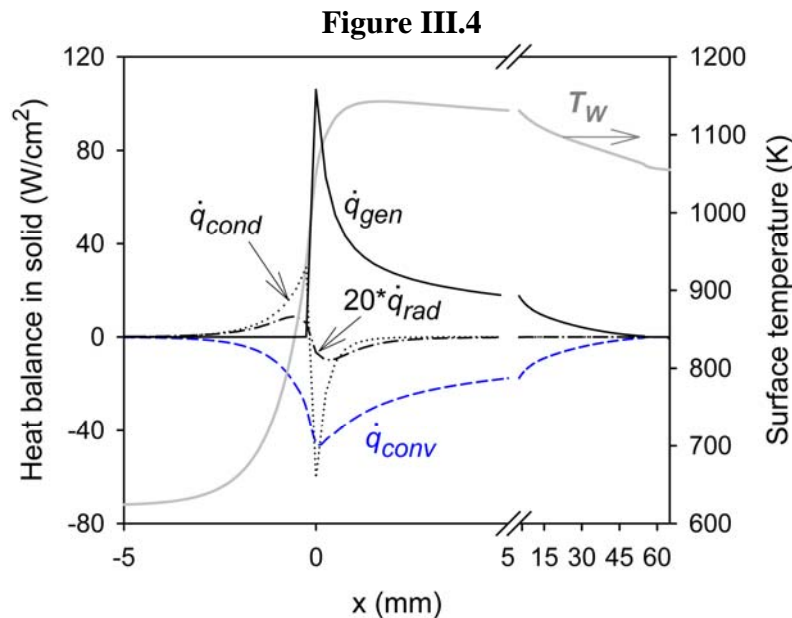
Heat balance in the solid for Case 1. Surface heat generation: solid lines; convection: dashed lines; conduction: dotted lines; radiation: dashed-dotted lines. For clarity, the radiation term is multiplied by 20. The solid gray line provides the wall temperature.

The insignificance of $\dot{q}_{rad}$ was a direct consequence of the negligible light-off distance that resulted in wall temperatures differing by less than 86 K over the entire length $x > 0$ (see Fig. III.3). Contrary to fuel-rich combustion, in fuel-lean applications the light-off distance can be considerably longer due to blocking of the catalyst by surface oxygen [21, Dogwiler et al., 1999; 45, Carroni et al., 2003] leading to appreciable temperature differences along the catalytic wall (> 500 K). In those cases, despite the small associated geometrical view factors, radiation exchange can aid light-off by transferring heat from the hotter rear channel surfaces to the colder entry. Heat conduction ($\dot{q}_{cond}$) was also important around -3 mm $< x < 3$ mm (Fig. III.4) wherein the wall temperature differences were appreciable.

Although $\dot{q}_{cond}$ was far larger than $\dot{q}_{rad}$, its overall impact was weak. Computations without heat conduction yielded peak wall temperatures only 20 K higher at $x \approx 0$ and practically the same T_W profiles at $x > 3$ mm. Similarly, an increase of the FeCr-alloy thickness by factor of five resulted in a drop of the predicted peak wall temperature by only 15 K and did not affect

Figure III.5
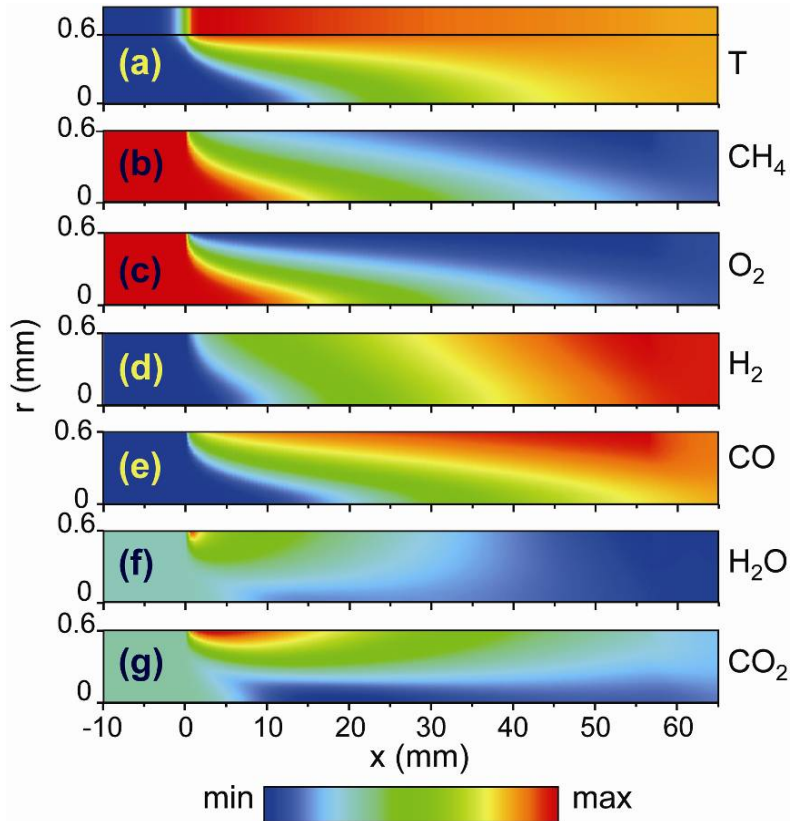
Computed 2-D distributions of the temperature and species mole fractions for Case 1 of Table 1. The minimum and maximum levels of the color bar are: (a) T: 623 K to 1123 K, (b) CH_4: 0.061 to 0.204, c) O_2: 0.001 to 0.103, d) H_2: 0.0 to 0.184, e) CO: 0.0 to 0.090, f) H_2O: 0.432 to 0.528 and g) CO_2: 0.219 to 0.260. The centerline is located at $r = 0$ and the gas-solid interface at $r = 0.6$ mm; the catalytically active section spans the range $0 \le x \le 55$ mm. The temperature inside the solid (0.6 mm $< r < 0.637$ mm) is also shown in (a) on an expanded radial scale.

T_W at $x > 3$ mm. In contrast, heat conduction to the front section of the reactor can be essential in fuel-lean combustion [21, Dogwiler et al., 1999]. Overall, the temperature profiles of Fig. III.3 reflected predominantly the impact of chemical kinetics and fluid mechanical transport rather than that of heat-transfer mechanisms in the solid.

The predicted wall temperatures in Fig. III.3a exceeded the corresponding adiabatic equilibrium temperature ($T_{ad,eq}$) for $x > 0$ while the mean gas temperatures exceeded $T_{ad,eq}$ for $x > 17$ mm ($x > 26$ mm in Fig. III.3b); the thermocouple measurements also attested the aforementioned superadiabaticity. Superadiabatic surface temperatures are known to arise when a limiting reactant exhibits diffusional imbalance, e.g. in hydrogen-lean or methane-lean (fuels with Lewis numbers $Le < 1$) catalytic complete oxidation [54, Appel et al., 2002; 57, Pfefferle and Pfefferle, 1986; 58, Appel et al., 2005b]. In CPO, however, superadiabatic temperatures were a result of product non-equilibration due to short convective time scales and the presence of multiple reaction pathways. Contrary to complete combustion with one dominant pathway, in CPO there were multiple routes that can be summarized with the following global steps:

$$CH_4 + 2O_2 = CO_2 + 2H_2O \qquad \text{(complete oxidation)} \qquad \text{(R1)}$$
$$2CH_4 + O_2 = 2CO + 4H_2 \qquad \text{(partial oxidation)} \qquad \text{(R2)}$$
$$CH_4 + H_2O = CO + 3H_2 \qquad \text{(steam reforming)} \qquad \text{(R3)}$$
$$CO + H_2O = CO_2 + H_2 \qquad \text{(water gas shift)} \qquad \text{(R4)}$$
$$CH_4 + CO_2 = 2CO + 2H_2 \qquad \text{(CO}_2 \text{ reforming)} \qquad \text{(R5)}$$
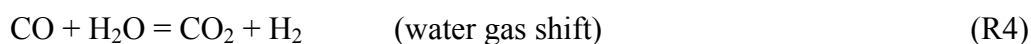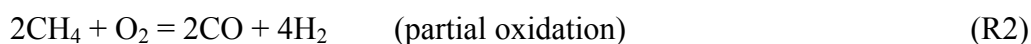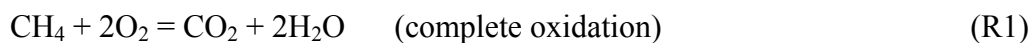
The reaction rate of endothermic steam reforming (R3) was slow compared to the faster exothermic oxidation steps (R1, R2) leading to non-equilibration at very short contact times. This could be readily seen by comparing the adiabatic equilibrium hydrogen mole fraction with the computed or measured values along the reactor length (Fig. III.3). The origin of the superadiabatic mean gas temperatures at $x > 17$ mm (Case 1) was a result of the local chemical energy (averaged over r_h) being lower than the adiabatic equilibrium value; this, in turn, led to higher sensible energies and hence to superadiabatic gas temperatures.

The calculated wall temperatures exceeded $T_{ad,eq}$ by as much as 200 K; nevertheless, the absolute surface temperatures were maintained below 1150 K and could be thus tolerated by the catalyst and the reactor structure. Replacing the exhaust gas dilution with N_2 resulted in T_W up to 1220 K due to the lower heat capacity of the gaseous mixture and the weaker moderating impact of endothermic steam reforming. Safe operation ($T_W < 1150$ K) of CPO-based reactors without or with reduced exhaust gas recycle necessitated proper thermal management such as passive reactor cooling with alternately-coated honeycomb structures, similar to that adopted in fuel-lean combustion [45, Carroni et al., 2003]. Therein, only every second channel of the honeycomb was coated so that the flow in the uncoated channels cooled the reactor walls.

Figure III.6
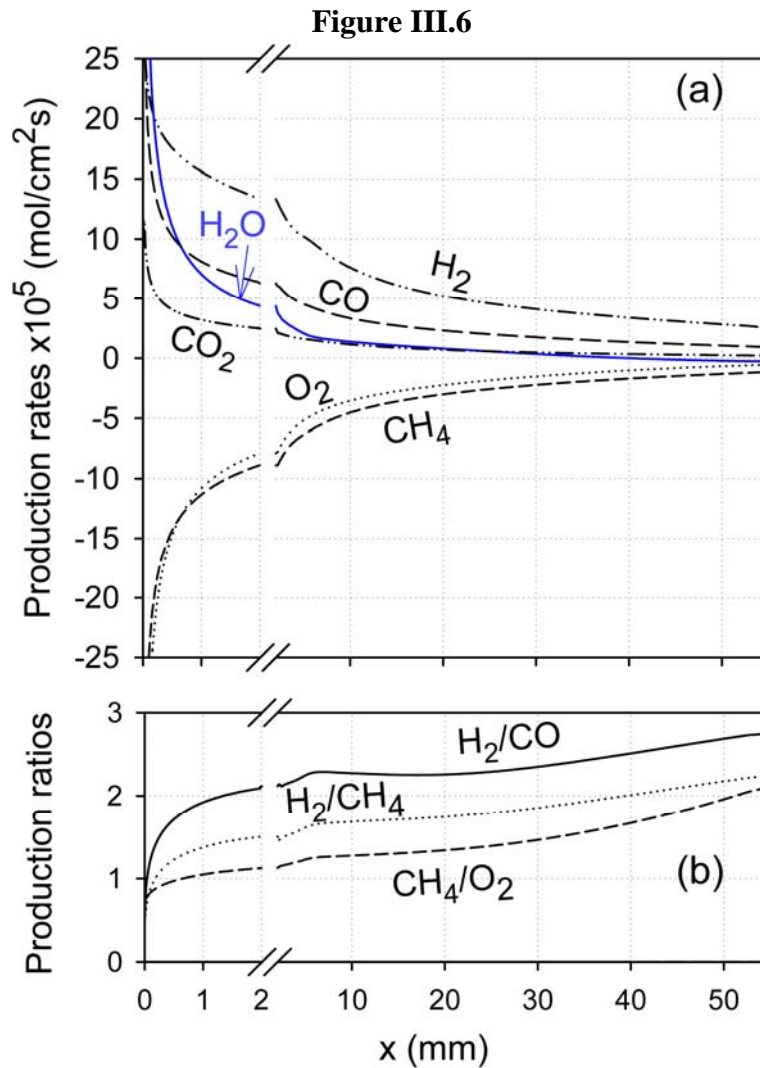
Computed axial profiles (Case 1) of: (a) molar species catalytic production (or destruction) rates, and (b) rate-ratios for selected pairs of species (in H_2/CH_4, the absolute value is given). For clarity, the first 2 mm are expanded.

The requirement for accurate modeling of transport and catalytic chemistry should not be understated in very short contact time applications: an artificial reduction of the wall temperature by 40 K decreased the computed hydrogen yields (dry basis) by a factor of two. Moreover, the entropic consistency of the catalytic reaction schemes, a necessary requirement to reproduce equilibrium [59, Mhadeshwar et al., 2003], deserves special attention. For very short contact time reactors, this requirement may be relaxed; however, entropic consistency is essential for longer residence times when products approach equilibration. In conclusion, the results of this section have exemplified the importance of an accurate transport/chemical model for the assessment of the reactor temperature. The employed model reproduced well the measured reactor temperatures and exit compositions (at least for the higher inlet temperature Cases 1 and 2) and could thus be used for elaborate reactor design. In CPO with large exhaust recirculation the attained superadiabatic temperatures were within acceptable

limits (< 1150 K); however, key issue at lower dilutions (or operation in air) was the thermal management of the reactor. The latter could not be meaningfully controlled with heat transfer mechanisms in the solid-phase.

For the conditions run in this study, no visible carbon deposits were observed in the reactor. While it is understood that non-visible carbon deposition can influence catalytic activity, the steady reactor performance at the investigated conditions suggested that surface carbon did not drive catalyst deactivation over the timescales of testing.

Figure III.7
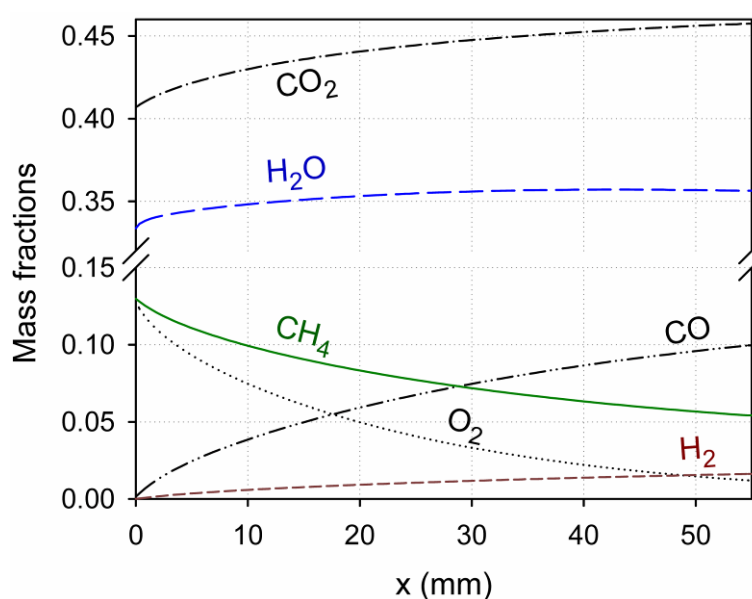
Computed axial profiles of radially-averaged species mass fractions for Case 1.

III.4.4 Synthesis gas production

The processes along the channel are described in this section using the simulations of Case 1. The impact of H_2O and CO_2 dilution on the synthesis gas yields will be elaborated in Section III.4.5. Computed 2-D distributions of the temperature and major species mole fractions are presented in Fig. III.5 for Case 1. The underlying physicochemical processes are investigated with the aid of Fig. III.5, Fig. III.6 (axial profiles of species molar catalytic production/destruction rates and selected rate-ratios) and Fig. III.7 (axial profiles of radially-averaged species mass fractions). Mass rather than mole fractions were used in Fig. III.7, so as to appropriately describe the species spatial evolution in the presence of non-equimolar reactions (R2, R3 and R5). This resulted in exit H_2O mole fractions lower than those of the inlet (Fig. III.5f) despite the increase in water mass throughput (Fig. III.7).

The peak in the H_2O and CO_2 mole fractions (Fig. III.5f and III.5g) at $x \approx 0$ and the accompanying peaks in the production rates of those species (Fig. III.6a) were indicative of complete oxidation (R1) at the beginning of the catalyst. This reaction became mass-transport-limited already at $x \approx 0$ (manifested in Fig. III.5c by the nearly zero levels of the deficient O_2 reactant at $r = 0.6$ mm), leading to the high peak wall temperatures discussed in Section III.4.3. The CH_4/O_2 destruction ratio was 0.78 at $x = 0$ (Fig. III.6b), demonstrating a non-negligible partial oxidation (R2) contribution. Partial oxidation products were readily formed at $x \approx 0$ (Fig. III.5d and III.5e). Over the length 2 mm $< x <$ 25 mm, the H_2/CO production ratio was ~2.2, the CH_4/O_2 destruction ratio was ~1.2 and the H_2/CH_4 destruction/production absolute ratio was ~1.6 (Fig. III.6b), pointing to the significance of both R1 and R2; in this zone oxygen was still available in the gas (Fig. III.7) to accommodate the oxidation reactions. At $x >$ 39 mm, where O_2 was largely depleted (Figs. III.7 and III.5c), there was a shift from production to destruction of H_2O (Fig. III.6a). Steam reforming (R3) was considerable at those downstream parts, as also manifested by the increase of the H_2/CO production ratio to nearly three at the end of the catalyst. The continuous drop of the wall temperature along the reactor (Figs. III.5a and III.3a) concurred to the importance of this endothermic step. Water gas shift (R4) was also present at $x >$ 39 mm and contributed to further enhancing the H_2/CO and H_2/CH_4 ratios (Fig. III.6b). It is noted that the capacity of the employed reaction scheme [1, Schwiedernoch et al., 2003] to accommodate steam reforming and water gas shift reactions has been demonstrated by additional computations with pure CH_4/H_2O or CO/H_2O incoming mixtures. On the other hand, CO_2 reforming (R5) had no contribution to the synthesis gas production, as will be further elaborated in Section III.4.5. It is finally pointed out that the large diffusivity of hydrogen yielded mole fraction distributions with a considerably higher radial uniformity compared to that of the other species (Fig. III.5d).

The predicted methane conversion (deduced from Fig. III.7) was 58.6%, a value acceptable for "catalytic rich combustion" with a post-catalyst flame zone. The water mass throughput increased along the reactor ($Y_{H2O,IN} = 0.332$ and $Y_{H2O,OUT} = 0.357$, see Fig. III.7) despite the contribution of steam reforming and water gas shift reactions farther downstream. There was simply insufficient residence time at the given temperatures for the slow endothermic steam reforming to further increase the consumption of water and methane. The former species played a key role in the hydrogen yields as will be elaborated in Section III.4.5. The predicted wet gas outlet H_2 and CO mole (mass) fractions in Case 1 were

0.177 (0.016) and 0.078 (0.099), respectively. The partial oxidation product selectivities, defined as:

$$S_{H2} = \frac{0.5\,Y_{H2}/W_{H2}}{(Y_{CH4,IN} - Y_{CH4,OUT})/W_{CH4}} \qquad \text{and} \tag{6}$$

$$S_{CO} = \frac{Y_{CO}/W_{CO}}{(Y_{CH4,IN} - Y_{CH4,OUT})/W_{CH4}} . \tag{7}$$

For Case 1, $S_{H2} = 0.84$ and $S_{CO} = 0.74$. The definition of Eq. (6) is based on hydrogen produced from methane and it is maintained herein, despite the added H_2 production from H_2O. Table III.5 summarizes the CH_4 conversions and H_2 and CO selectivities for all cases.

Table III.5

Selectivities and fractional methane conversion [a]

Case	T_{IN} (K)	CH_4 conversion		CO selectivity		H_2 selectivity	
		Exp.	Sim.	Exp.	Sim.	Exp.	Sim.
1	623	0.58	0.59	0.81	0.74	0.94	0.84
2	573	0.57	0.55	0.75	0.75	0.89	0.80
3	523	0.54	0.52	0.71	0.76	0.85	0.76
4	473	0.51	0.49	0.72	0.76	0.84	0.71

[a]comparison of experiments and simulations for the cases of Table 1. The selectivities are defined according to Eqs. (6) and (7).

III.4.5 Impact of H_2O and CO_2 on synthesis gas production

To identify the impact of water on the synthesis gas yields and product selectivities, additional predictions have been carried out with the diluent H_2O replaced by a fictitious species H_2O* that had the same thermodynamic and transport properties as H_2O but did not participate in any reaction. H_2O* simulated only the incoming diluent whereas the catalytic pathway was still allowed to create combustion-generated H_2O. The wall temperature profile of Fig. III.3a was imposed as energy boundary condition in the computations with H_2O* so as to isolate the chemical effects of dilution. The surface coverage for the standard Case 1 (H_2O dilution) and for the corresponding case with H_2O* dilution is shown in Fig. III.8. The axial profiles of radially-averaged major species mass fractions are presented in Fig. III.9 for the H_2O* dilution. To facilitate the ensuing comparisons, the profiles of Case 1 (Fig. III.7) are

also repeated in Fig. III.9. A reaction flux analysis is provided in Fig. III.10 for Case 1, referring to the position $x = 10.8$ mm. Even though the reaction flux depends on the selected position, the graph of Fig. III.10 suffices for the following discussion. Finally, a sensitivity analysis (SA) was carried out using the surface perfectly stirred reactor (SPSR) package of CHEMKIN [60, Moffat et al., 1993] at conditions (residence time, surface temperature and surface-to-volume ratio) that reproduced the methane conversions and synthesis gas yields of Case 1. The normalized sensitivity coefficients of H_2 and CO are given in Fig. III.11 for the fifteen most significant reactions.

Figure III.8
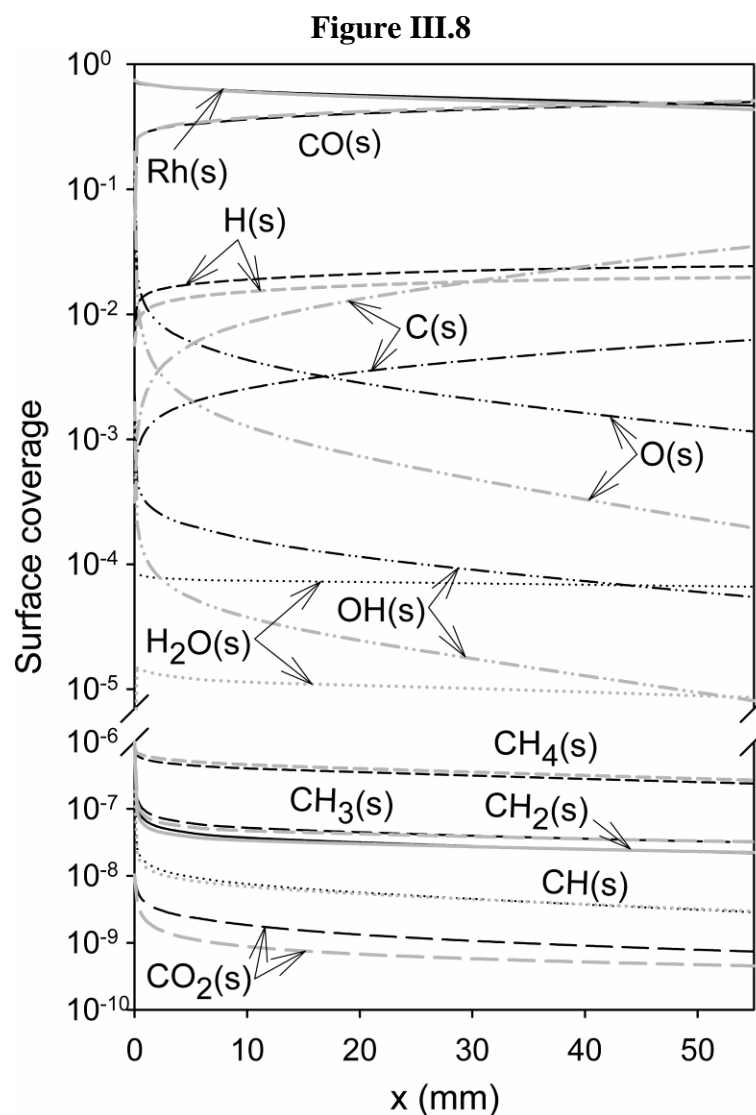
Surface coverage for Case 1 (black lines) and for the same case when the inlet 46.3% H_2O replaced by equal amount of chemically inert H_2O^* (gray lines).

The presence of steam in the feed augmented the $H_2O(s)$ coverage by almost an order of magnitude (Fig. III.8) due to the near equilibration of the H_2O adsorption/desorption

reactions (see magnitudes of S4 and S38 in Fig. III.10). The increase in $H_2O(s)$ also enhanced the $O(s)$ coverage especially at the downstream locations were O_2 was largely depleted (Fig. III.5c). The comparisons of Fig. III.8 revealed a factor of six increase of $O(s)$ for the H_2O-diluted case at $x = 55$ mm. The elevated $O(s)$, which was a result of the faster net S14-S15 and slower net S10-S11 (see Fig. 10) of the H_2O-dilution compared to the H_2O*-dilution, led to an enhanced methane depletion (Fig. III.9) according to the surface oxidation route $S28 \rightarrow S30 \rightarrow S32 \rightarrow S34$ $(CH_4(s) \rightarrow CH_3(s) \rightarrow CH_2(s) \rightarrow CH(s)$, see Fig. III.10). This route was also responsible for the augmented $OH(s)$ coverage of the H_2O-diluted case (by a factor of seven at $x = 55$ mm, see Fig. III.8) that, in turn, fed the $O(s)$ production cycle. Subsequently, the intermediates $CH_4(s)$, $CH_3(s)$, $CH_2(s)$ and $CH(s)$ led via the net of S20-S21, S22-S23, S24-S25 and S26-S27 to $H(s)$. The reduced impact of the $H(s)$-consuming net reactions S10-S11 (due to the increased $OH(s)/O(s)$ ratio of the H_2O- compared to the H_2O*-dilution) and S12-S13 (due to the corresponding increase in the $H_2O(s)/OH(s)$ ratio) resulted in a ~25% rise of $H(s)$ for the former case (Fig. III.8) that, in

Figure III.9
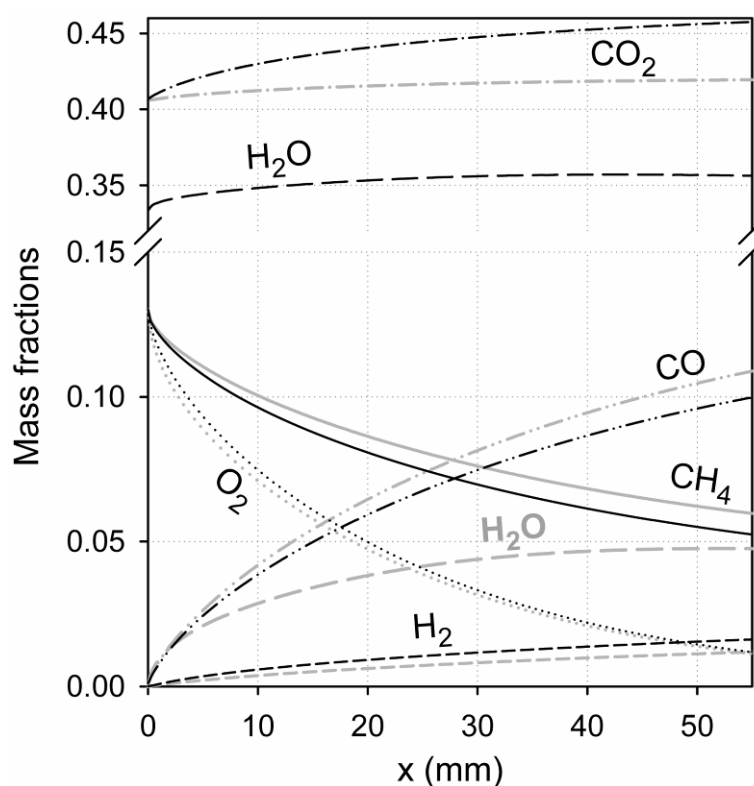
Computed axial profiles of radially-averaged species mass fractions for Case 1
(black lines) and corresponding profiles when the inlet water content of Case 1 is
replaced by equal amount of chemically inert H_2O* (gray lines).

Figure III.10

Reaction flux diagram (mol/cm^{2}s) for Case 1 at $x = 10.8$ mm. The reaction numbering follows Table 2. Only fluxes greater than 10^{-6} mol/cm^{2}s are shown.

turn, promoted the H$_2$-producing desorption reaction S36. When H$_2$O was replaced by H$_2$O* the comparisons in Fig. 9 revealed a decrease in both methane conversion (from 58.6% to 54.1%) and hydrogen exit mass fractions (from 0.016 to 0.012). The SA of Fig. III.11a has identified the importance of the H$_2$O adsorption/desorption reactions (S4, S38) and of the competing steps S36/S3 (net producing H$_2$) and S10/S11, S12/S13 (net oxidizing H(s)).

The addition of steam caused a significant drop in C(s) (Fig. III.8) since the higher O(s) coverage accelerated the C(s)-depleting reaction S16-S17. The higher amounts of O(s) also favored the complete oxidation CO(s)+O(s) $\rightarrow$ CO$_2$(s)+Rh(s) (net of S18-S19) against the CO-producing desorption S39 (see Fig. III.10), thus reducing the yields of CO and increasing those of CO$_2$ (Fig. III.9). When H$_2$O was replaced by H$_2$O*, the CO exit mass fractions increased from 0.099 to 0.109. The SA of Fig. III.11b indicated the strong impact of the competing steps S18 (eventually leading to CO$_2$) and S39/S6 (net producing CO). The selectivities for the H$_2$O*-dilution, computed from Eqs. (13) and (14), were $S_{H2} = 0.67$ and $S_{CO} = 0.87$. Therefore, the presence of 46.3% H$_2$O increased the H$_2$ selectivity by 25% and reduced the CO selectivity by 15%. Within the context of gas-turbine "catalytic rich

Figure III.11

Normalized sensitivity coefficients for: a) H_2 and b) CO computed in a surface perfectly stirred reactor. The fifteen most significant reactions are shown.

combustion", the increase in hydrogen selectivity is particularly beneficial for the stabilization of the post-catalyst flame. The increase in H_2 and drop in CO selectivity with increasing water dilution (up to the 46% H_2O levels of the present study) is in good agreement with CPO studies in short-contact-time reactors [37, Klein et al., 2001]. Although quantitative comparisons with the previous work cannot be made due to their different operating conditions (p = 1 bar, CH_4/O_2 inlet molar ratio of 1.8 and CH_4 conversion > 95%), it is worth mentioning that their measured CO selectivity at 46% H_2O dilution was ~70% (compared to our 72-81%, see Table 5) and their H_2/CO molar ratio was ~2.9 (compared to our ~2.3, see Table III.4).

The impact of CO_2 dilution was investigated in a similar fashion by introducing a fictitious species CO_2*. The computations revealed that neither the CH_4 conversion nor the H_2 and CO selectivities were affected by this change. When CO_2 was replaced by CO_2*, the only noticeable change was a drop in the $CO_2(s)$ coverage by up to a factor of two; nonetheless, the $CO_2(s)$ coverage was too low (Fig. III.8) to meaningfully affect the other surface species. Alternately, the rate of S19 (the backward of the CO(s) surface oxidation reaction S18) was very slow to appreciably alter the fluxes of Fig. III.10. Therefore, CO_2 had a minor chemical impact and CO_2 reforming (R5) was not significant. On the other hand, for pure dry reforming [44, Basile et al., 1998] reported appreciable CH_4 and CO_2 conversions

($> 30\%$) at conditions similar to those of the present study (temperature 1023 K, residence time 12 ms and CH_4/CO_2 ratio of 1). This difference is attributed to the fact that in the presence of $H_2O/O_2/CO_2$, H_2O or O_2 reforming reactions of methane are appreciably faster than CO_2 reforming [42, Mark and Maier, 1996]. Finally, both H_2O^* and CO_2^* dilution cases were computed anew by removing the prescribed wall temperature boundary condition. The resulting wall temperature profile of the CO_2^* dilution was the same as that of Fig. III.3a whereas the H_2O^* dilution yielded slightly higher peak wall temperatures (by 11 K) and exit H_2 compositions (by 1.6%). In that, thermal effects did not alter the findings of this section regarding the controlling chemical pathways.

As a final point, the impact of key parameters (H_2O dilution, residence time and inlet temperature) on the synthesis gas selectivities has been investigated with extensive SPSR parametric studies. Figure III.12 provides the H_2/CO molar ratio as a function of SPSR residence time for: a) the base Case 1 and two additional conditions with: b) increased inlet temperature, $T_{IN} = 823$ K, and c) the H_2O and CO_2 dilution replaced by 69.4% vol. N_2. Lines (a) and (c) in Fig. III.12 reveal the significant impact of water addition in increasing the H_2/CO ratio, lines (a) and (b) point to the benefit of higher inlet temperature in accelerating the endothermic steam reforming and, finally, all three lines indicate a more pronounced impact of the residence time for the wet rather than for the dry mixtures due to the increased importance of the slow endothermic steam reforming. Graphs such as those of Fig. III.12 are particularly useful for defining basic reactor requirements before a detail design is pursued.

Figure III.12
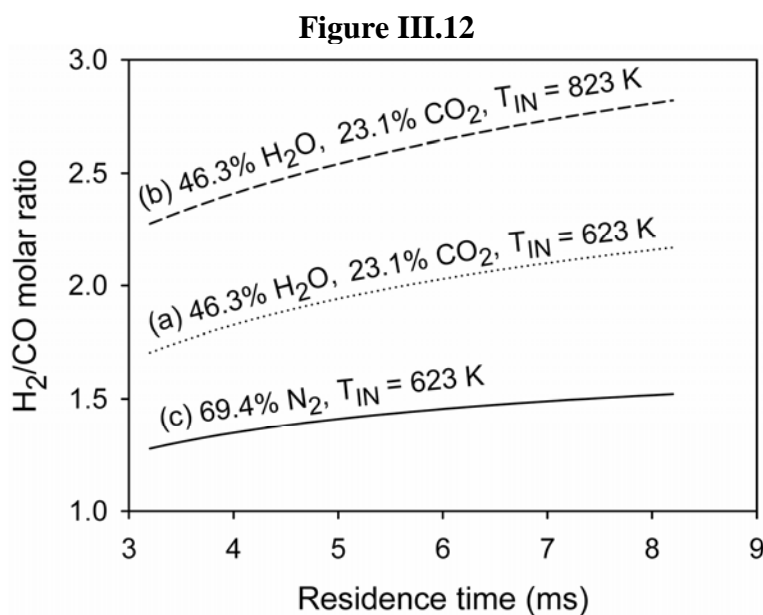
Molar ratio H_2/CO in a surface perfectly stirred reactor as a function of residence time for: a) Case 1, b) inlet species composition as in Case 1 and inlet temperature $T_{IN} = 823$ K, and c) CH_4 and O_2 compositions as in Case 1 but with 69.4% vol. N_2 dilution.

III.5 Conclusions

The catalytic partial oxidation (CPO) of methane to synthesis gas over Rh/ZrO_2 has been investigated experimentally and numerically in a short contact time (~8 ms) prototype gas-turbine reactor operated at 5 bar. The CH_4/O_2 mixture was diluted with exhaust gas (46.3% H_2O and 23.1% CO_2 vol. in the feed). The impact of large H_2O and CO_2 dilution on the H_2 and CO selectivities and CH_4 conversion was assessed and reactor thermal management issues were discussed. The following were the key conclusions of this study.

1) Catalytic ignition was achieved at the gas-turbine-relevant inlet temperature of 670 K and, owing to a strong hysterisis in the catalytic ignition/extinction characteristics, steady combustion could be subsequently maintained at inlet temperatures as low as 473 K.

2) The employed catalytic reaction scheme reproduced the measured temperatures along the reactor as well as the measured exit composition, overpredicting mildly the impact of the total over the partial oxidation route. The overprediction was more pronounced at lower inlet temperatures.

3) The reactor thermal management was an important issue in practical reactors. The surface temperatures exceeded by as much as 200 K the adiabatic equilibrium temperature due to

the short residence times and the multiple reaction pathways that included complete and total oxidation, steam reforming and water gas shift. It was shown that thermal management approaches solely based on heat transfer mechanisms in the solid substrate were inadequate in controlling the surface temperatures.

4) The presence of H_2O provided a source for surface oxygen and hydroxyl-radicals, $O(s)$ and $OH(s)$, which in turn resulted in higher methane conversion, higher H_2 and lower CO selectivity. This was highly desirable for CPO-based turbine reactors as hydrogen can aid the stabilization of the post-catalyst gaseous combustion zone. The higher hydrogen selectivities were attributed to the more favorable competition of hydrogen desorption ($2H(s) \rightarrow 2Rh(s)+H_2$) over surface oxidation ($H(s)+O(s) \rightarrow Rh(s)+OH(s)$ and $H(s)+OH(s) \rightarrow Rh(s)+H_2O(s)$). On the other hand, the CO selectivity decreased due to the promotion of its surface oxidation ($CO(s)+O(s) \rightarrow Rh(s)+CO_2(s)$).

5) The addition of CO_2 had a minor impact on the CH_4 conversion and the H_2 or CO selectivity during CPO with large H_2O dilution. Therefore, CO_2 reforming is not important in short contact time gas-turbine reactors with exhaust recirculation.

IV Ignition and extinction in catalytic partial oxidation of methane-oxygen mixtures with large H_2O and CO_2 dilution

A paper written by Adrian Schneider, John Mantzaras and Sara Eriksson, published in Combustion Science and Technology.

Abstract

The ignition and extinction in catalytic partial oxidation (CPO) of CH_4/O_2 mixtures with large exhaust gas dilution (46.3% H_2O and 23.1% CO_2 vol.) has been investigated experimentally and numerically at 5 bar. Experiments were carried out in a short contact time Rh-coated honeycomb reactor and included temperature measurements along the reactor and exhaust gas analysis. Numerical predictions were performed with a 2-D transient elliptic code that included detailed chemical reaction schemes and relevant heat transfer mechanisms in the solid. The employed heterogeneous reaction scheme reproduced the measured minimum inlet temperatures required for catalytic ignition (light-off), the elapsed times for the propagation of the reaction front, and the steady-state exhaust gas compositions at an equivalence ratio $\varphi = 4.0$. The chemical impact of the added H_2O, although important already at the early light-off stages, was minimal on the ignition delay times because the latter were dominated by total oxidation and not by partial oxidation or reforming reactions. The key reaction controlling catalytic ignition was the surface oxidation of CO to CO_2, which was the main exothermic heat release step in the induction zone. Measurements and predictions indicated that vigorous combustion could be sustained at inlet temperatures at least as low as 473 K and 298 K in CPO with and without exhaust gas dilution, respectively. The extended stability limits of CPO combustion were due to a shift from partial to total oxidation products, and hence to higher exothermicity, with decreasing inlet temperature. The key parameter controlling extinction was the CO(s) coverage, which increased near extinction and led to catalyst poisoning. Finally, operation at non-optimal stoichiometries ($\varphi = 2.5$) was shown to be beneficial in CPO of power generation systems with large exhaust dilution, due to the moderating effect of dilution on the maximum reactor temperature.

IV.1 Introduction

The catalytic partial oxidation (CPO) of natural gas to synthesis gas has attracted increased attention in gas turbines of power generation systems [9, Griffin et al., 2004; 61, Karim et al., 2002]. The adopted approach, referred to as "catalytic rich combustion", entails CPO of natural gas with part of the air stream (at suitably fuel-rich stoichiometries) in a short contact time reactor. Only a fraction of the fuel is converted in the CPO reactor, while the products (mainly synthesis gas and unconverted methane) are subsequently mixed with the remaining air to stabilize a post-catalyst fuel-lean homogeneous combustion zone. The aforementioned methodology has a number of advantages compared to the conventional fuel-lean catalytically stabilized combustion [34, Carroni et al., 2002], the two most prominent ones being the lower catalyst light-off temperature [36, Veser et al., 1999] and the enhanced stability of the follow-up flame due to the CPO-produced hydrogen [9, Griffin et al., 2004]. Even though "catalytic rich combustion" usually applies to natural-gas/air mixtures, the use of large exhaust gas recycle (EGR) in the feed is under investigation for new power generation cycles. Such an example is the advanced zero-emissions power cycle [62, Griffin et al., 2005] that aims at mitigating both NO_x and CO_2 emissions. Therein natural gas is combusted at moderate temperatures (up to 1500 K) in a stream comprising oxygen (separated from air) and large EGR (up to 80% vol.). Combustion in pure oxygen negates the formation of NO_x, while the lack of nitrogen in the flue gases allows for an efficient separation of CO_2 from H_2O (e.g. via condensation) thus facilitating the subsequent sequestration of CO_2.

Due to its key role in the chemical industry, CPO of methane (the main constituent of natural gas) has been intensely studied during the last years, with emphasis on understanding the heterogeneous kinetics over Pt and Rh surfaces and the synthesis gas yields in short contact time reactors [1, Schwiedernoch et al., 2003; 3, Hickman and Schmidt, 1993; 4, Deutschmann and Schmidt, 1998; 29, Aghalayam et al., 2003; 30, Bodke et al., 1998]. The CPO processes in power generation are, nonetheless, differentiated from those of the chemical industry. A fractional fuel conversion is sufficient in the former, whereas complete conversion is desired in the latter. In addition, the optimization of product yields and selectivities is not an overriding issue in power generation since CO is ultimately converted to CO_2 and the amount of hydrogen should simply suffice for the stabilization of the follow-up flame. Conversely, in gas turbines there are stringent catalyst light-off requirements (~700 K or less) at gas hourly space velocities (GHSV) of ~10^6 h^{-1}. To advance the understanding of

"catalytic rich combustion", [47, Appel et al., 2005a] have recently studied the underlying heterogeneous processes in CPO of CH_4/air over Rh/ZrO_2 at 6 bar by applying laser-based in situ Raman measurements of major gas-phase species concentrations over the catalyst boundary layer. In the same study, the validated kinetic schemes were also used to simulate the steady operation of a prototype subscale gas turbine reactor. More recently, [63, Schneider et al., 2007] investigated the hetero-/homogeneous kinetics in CPO of methane with large EGR in the pressure range of 4 to 10 bar by employing Raman measurements of major species concentrations and laser induced fluorescence (LIF) of formaldehyde. The steady performance of a subscale gas turbine reactor and the chemical impact of large H_2O and CO_2 dilution on the synthesis gas yields and selectivities were further addressed in [64, Schneider et al., 2006].

Dynamic performance in gas-turbine-related CPO has not been elaborated in the past. Light-off, in particular, is crucial given the strict limitations in reactor inlet temperature. Extinction is also a key issue, especially for low part-load and idle turbine operation. Recent experiments have reported an extended hysteresis in the ignition/extinction characteristics of methane CPO with EGR [64, Schneider et al., 2006]. Similarly, strong hysteresis has been observed in CPO of methane, landfill gas, and diesel fuels with air [65, Smith et al., 2006a]. The reason for this behavior, which is in marked contrast to fuel-lean catalytic combustion, has not yet received proper attention.

Transient models are of great interest for the description of dynamic operation in practical catalytic systems and also for the fundamental investigation of kinetically-driven dynamic oscillatory phenomena [66, Imbihl and Ertl, 1995]. Given the typically long characteristic solid substrate heat-up time compared to the corresponding chemical, convective and gas diffusive time scales, the quasisteady assumption for the gas-phase is usually invoked. This is the preferred approach in demanding (even when simplified surface chemistry is used) 2-D transient channel simulations [67, Sinha et al., 1985; 68, Hayes and Kolaczkowski, 1997]. The quasisteady approximation has also been applied in continuum 2-D models for the entire honeycomb structure [69, Schwiedernoch et al., 2002; 70, Zygourakis and Aris, 1983]; these models are of great interest for practical systems with non-adiabatic operation and non-uniform inlet properties, but they do not resolve the details in the solid wall of each channel and they require careful assessment of effective continuum properties for the solid structure. Transient simulations for both the solid and gas phases, with the added complexity of detailed surface chemistry, have only been reported with 1-D models using lumped heat and mass transport coefficients [71, Kramer et al., 2002]. Despite

the computational efficiency of 1-D approaches, 2-D models have the advantage of accurately describing the interphase transport and the gas-phase chemical processes; the latter are strongly dependent on the cross-flow distribution of species and temperature and can become increasingly important at high-pressures [72, Mantzaras, 2006]. For methane CPO, in particular, 1-D transient modeling has been carried out in [73, Veser and Frauhammer, 2000] for Pt catalysts and 2-D continuum modeling in [1, Schwiedernoch et al., 2003] for Rh catalysts; both studies employed detailed surface reaction mechanisms. Transient 2-D models with detailed chemistry have not yet been reported for single catalytic channels.

An experimental and numerical study of methane CPO is undertaken in the present work, with emphasis on light-off and extinction. Light-off has been investigated in CPO with large EGR (up to 75% vol.) whereas extinction has been studied in CPO with and without EGR. Transient and steady experiments have been carried out at pressures of 5 and 3 bar in a short contact time (~10 ms) subscale gas-turbine catalytic reactor coated with Rh/ZrO_2. The exhaust composition was monitored with gas chromatography, while the inlet, outlet, and reactor temperatures were measured with thermocouples. An elliptic 2-D transient model for a single channel has been developed, which included detailed hetero-/homogeneous chemical reaction schemes and all relevant heat transfer mechanisms in the solid. The main objectives were to validate the aptness of heterogeneous reaction mechanisms during ignition/extinction in CPO of methane with large EGR, to identify the chemical pathways controlling catalytic ignition and extinction, and to understand the origin of the extended extinction limits of short contact time reactors. Particular objectives were to address design issues for transient performance in CPO reactors with large EGR.

The high-pressure test rig and the numerical methodology are introduced first. Comparisons between measured and predicted ignition characteristics in CPO of $CH_4/O_2/H_2O/CO_2$ mixtures are then presented and the chemical pathways controlling light-off are identified. The extinction in CPO of $CH_4/O_2/H_2O/CO_2$ and $CH_4/O_2/N_2$ mixtures is finally elaborated and the key chemical pathways affecting extinction are elucidated.

IV.2 Experimental

IV.2.1 High pressure test rig

The short contact time honeycomb catalytic reactor was a subscale unit of a prototype CPO burner developed for large gas turbines [9, Griffin et al., 2004] and formed a liner inside a high-pressure tank (Fig. IV.1(a)). The same reactor type has also been used in earlier

Table IV.1

Experimental conditions[a]

Case	Type	φ	p (bar)	U_{IN} (m/s)	T_{IN} (K)	CH_4 (%)	O_2 (%)	H_2O (%)	CO_2 (%)	N_2 (%)	Catalyst Rh wt%	B[b]
1	Ign.	4.0	5	5.6	680	20.4	10.2	46.3	23.1	-	1.0	4.5
2	Ext.	4.0	5	5.1	623	20.4	10.2	46.3	23.1	-	1.0	4.5
3	Ext.	4.0	5	4.7	573	20.4	10.2	46.3	23.1	-	1.0	4.5
4	Ext.	4.0	5	4.3	523	20.4	10.2	46.3	23.1	-	1.0	4.5
5	Ext.	4.0	5	3.9	473	20.4	10.2	46.3	23.1	-	1.0	4.5
6	Ign.	4.0	5	6.0	730	20.4	10.2	46.3	23.1	-	0.5	3.0
7	Ext.	4.0	5	5.1	623	20.4	10.2	46.3	23.1	-	0.5	3.0
8	Ext.	4.0	5	4.3	523	20.4	10.2	46.3	23.1	-	0.5	3.0
9	Ext.	4.0	5	3.9	473	20.4	10.2	46.3	23.1	-	0.5	3.0
10	Ign.	2.5	5	5.5	725	13.9	11.1	50.0	25.0	-	1.0	4.5
11	Ext.	4.0	3	5.4	552	27.7	13.9	-	-	58.4	1.0	4.5
12	Ext.	4.0	3	4.5	470	27.7	13.9	-	-	58.4	1.0	4.5
13	Ext.	4.0	3	4.0	414	27.7	13.9	-	-	58.4	1.0	4.5
14	Ext.	4.0	3	2.9	298	27.7	13.9	-	-	58.4	1.0	4.5

[a]test type (ignition, extinction-related), equivalence ratio, pressure, inlet conditions and volumetric composition, rhodium loading in catalyst, ratio of active-to-geometrical surface area.

[b]the ratio B (active to geometrical area) corresponds to a catalyst dispersion of 25.9 m^2/g-Rh for the 1% wt Rh loading and to 34.5 m^2/g-Rh for the 0.5% wt Rh loading.

heterogeneous studies of methane, which included total oxidation over Pd [45, Carroni et al., 2003] and partial oxidation over Rh/ZrO_2 [64, Schneider et al., 2006].

It comprised a 35 mm inner-diameter, 75 mm long and 1.5 mm thick steel tube, wherein alternating flat and corrugated FeCr-alloy foils (with thickness $\delta = 50\ \mu m$) created a honeycomb structure. The cross section of each channel was trapezoidal with rounded

Figure IV.1
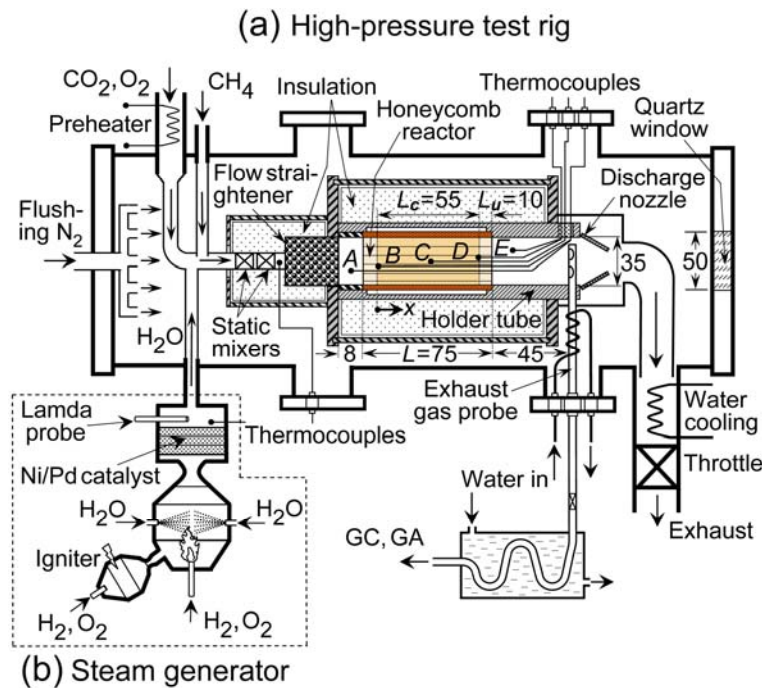
(a) High-pressure catalytic partial oxidation test rig, configured for operation with simulated exhaust gas recycle, (b) steam generator. All distances are in mm.

corners and the equivalent hydraulic radius was $r_h = 0.6$ mm. The reactor was mounted inside a well-insulated (using a 30-mm-thick fiber ceramic material) cylindrical steel frame. Only the central reactor extent ($L_c = 55$ mm) was coated with a catalyst, while the end-sections (each with a length $L_u = 10$ mm) were catalytically inactive (see Fig. IV.1(a)). The inlet, outlet and reactor temperatures were monitored with five 50-μm-thick K-type (Ni/Cr-Ni/Al) sheathed thermocouples (designated as A to E in Fig IV.1(a)). The thermocouple beads were positioned at $x = -15, 0, 27, 55$ and 75 mm, with $x = 0$ denoting the beginning of the catalytic section. The 0.8-mm-thick carrying wires of thermocouples A to D were driven into the reactor counterflow, through four honeycomb channels (Fig. IV.1(a)). The three thermocouples inside the honeycomb structure (B, C and D) provided neither the true catalyst surface temperature nor the mean gas temperature but rather a weighted average, which was only indicative of the local reactor temperature. Of the two measured true local gas temperatures (A, E), radiation corrections (amounting up to 8 K) have only been applied to the inlet thermocouple (A) that had a direct view to the hot catalyst entry; no such corrections were necessary for the outlet thermocouple (E) due to the small differences between the exit gas and rear reactor wall temperatures (~20°C). The absolute accuracy of the gas temperature measurements was ±10 K for the hot outlet and ±6 K for the inlet.

To simulate EGR, a dedicated steam-generator supplied superheated steam (Fig. IV.1(b)). Details of this unit have been provided elsewhere [64, Schneider et al., 2006] and only a brief description is given below. The device comprised a spark-ignited H_2/O_2 preburner, whose combustion products ignited a main H_2/O_2 burner. The latter was operated slightly fuel-lean ($\varphi \approx 0.99$), so as to avoid potential hydrogen breakthrough, by using the feedback control of a lambda probe similar to that used in automotive systems. The combustion heat was in turn used to vaporize accurately-measured amounts of demineralized liquid water. The degree of superheat and the amount of steam could be independently controlled (up to 1000°C and 20 g/s, respectively). Finally, a Ni/Pd-coated foam positioned downstream of the main burner served as safety backup to convert any escaping hydrogen and to assure a high degree of steam purity.

For the CPO tests of CH_4/O_2 with EGR, high-pressure bottles supplied CO_2, O_2 and technical-grade CH_4 (> 99.5%) Three Brooks mass flow-meters regulated the corresponding flows, leading to equivalence ratio accuracies better than ±0.5%. The CO_2 and O_2 flows were preheated by a 3 kW resistive heater and then mixed with superheated steam and room-temperature methane in two sequential static mixers (Fig. IV.1(a)). A follow-up 40-mm-long packing of 2-mm-diameter ceramic spheres straightened the flow. A K-type thermocouple positioned downstream of the static mixers monitored the gas temperature, which was in turn used as a feedback to control the level of CO_2/O_2 preheat and the degree of steam superheat for a desired mixture temperature at the reactor inlet. For the CPO tests with $CH_4/O_2/N_2$ mixtures (without EGR), nitrogen was supplied by high-pressure bottles and regulated by a Brooks mass flow-meter; the N_2 and O_2 gases were preheated in the aforementioned resistive heater and finally mixed with methane before entering the reactor.

The honeycomb structure was affixed 8 mm downstream of the flow straightener and was mounted inside a 2.5 mm thick and 35 mm internal diameter steel holder tube. To further minimize heat losses, only the first and last 2 mm of the reactor contacted the holder tube, while in the remaining length a 1-mm-thick annular air-cushion was available. The holder tube ended at a discharge nozzle that directed the flue gases first to an exhaust pipe and then to a water-cooled outlet of the high pressure tank.

The high pressure tank that housed the reactor was a stainless-steel cylindrical structure with a length of 1.8 m and an internal diameter of 0.28 m. The same tank has also accommodated an optically accessible catalytic reactor in earlier hetero-/homogeneous kinetic studies [14, Reinke et al., 2005; 15, Reinke et al., 2004; 47, Appel et al., 2005a; 63, Schneider et al., 2007]. For safety reasons, the exhaust gases were diluted with flushing nitrogen that

flowed continuously in the free volume between the high-pressure tank and the reactor. Visual inspection of the reactor assembly was achieved via a 50 mm diameter quartz window at the rear flange of the tank (Fig. IV.1(a)) and two 350 mm long and 50 mm high quartz windows at the tank sides (not shown in Fig. IV.1(a)). The gas sampling probe with its associated water cooling lines (see discussion in next section) and the thermocouple wires were driven inside the tank through high-pressure fittings mounted on four flanges.

The experimental conditions are provided in Table IV.1. Cases 1 to 9 referred to CPO of CH_4/O_2 with 69.4% vol. EGR dilution (46.3% H_2O and 23.1% CO_2) and a CH_4 to O_2 equivalence ratio of four; in Case 10 the EGR dilution was 75% vol. and $\varphi = 2.5$. Cases 11 to 14 referred to CPO of $CH_4/O_2/N_2$ mixtures with an O_2 to N_2 molar ratio of 0.24. In Cases 1 to 9 the pressure was 5 bar and the mass throughput ($\rho_{IN}U_{IN}$) was maintained constant. The CPO tests without EGR (Cases 11 to 14) were carried out at 3 bar, again at a constant mass throughput. Laminar flows were established in all cases, with incoming Reynolds numbers less than 580 in each individual channel of the honeycomb. The computed residence times (accounting for flow acceleration due to heating) ranged from 8.8 to 11.9 ms. The gas hourly space velocity (ratio of the incoming volumetric flow rate, at standard conditions, to the volume of the coated reactor section) was 7.4×10^5 h^{-1} in Cases 1 to 9, 6.9×10^5 h^{-1} in Case 10 and 5.2×10^5 h^{-1} in Cases 11 to 14, which were realistically high for gas-turbine CPO systems. Light-off tests were carried out only for CPO with EGR, in Cases 1, 6 and 10. Therein, the inlet mixture compositions were first established in the reactor at inlet temperatures (T_{IN}) about 100 K lower than those of Table IV.1. The inlet temperatures were then ramped at a rate of +10 K/min so as to reach the value required to achieve catalytic ignition. Once light-off was achieved and steady operation was reached in Cases 1 and 6, extinction was subsequently investigated by reducing the inlet temperatures at a rate of 10 K/min. At certain inlet temperatures, steady states were established for periods as long as 15 min to accommodate gas-analysis measurements. Of those steady states, Cases 2 to 5 (pertaining to Case 1) and Cases 7 to 9 (pertaining to Case 6) will be presented herein. In the $CH_4/O_2/N_2$ extinction studies (Cases 11 to14), steady combustion was first established at the conditions of Case 1; the steam generator was then turned off, nitrogen was added, and the corresponding CH_4, O_2 and N_2 flows were adjusted to achieve the composition of Table IV.1. Finally, data acquisition, reactor operation and safety control were achieved with dedicated software running on a PC at 1 Hz. This frequency was still sufficient for the ignition studies, characterized by light-off times of up to 10 sec.

IV.2.2 Gas analysis

Gas analysis was carried out in all steady cases; gas compositions could not be resolved over the short ignition events. Part of the exhaust gas was sampled with a water-cooled, silica-coated steel probe, which was positioned 45 mm downstream of the honeycomb (Fig. IV.1(a)). The steam of the sampled gas was condensed in a water-cooled serpentine heat exchanger outside the tank. The dried gases entered a rack of gas analyzers (GA) and also the sample port of a gas chromatograph (GC). Removal of the steam was necessary for the proper operation of both analysis instruments. Nonetheless, the compositions of the actual wet gas products could still be determined by calculating the element balances.

The Hartmann and Braun gas analyzers Uras-10E for CO (NDIR), Magnos-6G for O_2 (paramagnetic) and Caldos-5G for H_2 (thermal-conductivity-based) were used in a continuous mode. The accuracy of the GA measurements has been determined with calibration gas mixtures and was particularly good for CO (0.3% relative error for typical 10-14% vol. CO in the dry gas), while the O_2 accuracy was still acceptable despite the scarce amounts of this compound (20% relative error for ~1% vol. O_2). The presence of flue gases with thermal conductivities considerably different than that of the reference nitrogen (e.g. CH_4 and CO_2) resulted in larger inaccuracies for hydrogen (20% relative error for typical 25-30% vol. H_2 in the dry gas). This effect has been partly compensated by calibrating the device with simulated exhaust gas mixtures. In parallel to the GA measurements, more detailed analysis was carried out in an HP-6890++ GC equipped with porous polymer and molecular sieve columns and a thermal conductivity sensor. The GC further allowed for measurements of CH_4, CO_2 and N_2. The porous polymer column separated CO_2 before the gas entered the molecular sieve. Helium was the carrier gas, while the analysis was discontinuous with one measurement every 8 min. The GC has been tested against a selection of different calibration gas mixtures. Even though the hydrogen signals were weak due to the choice of helium as carrier gas, for the substantial H_2 amounts of the present work the accuracy was good (relative error for H_2 ~4%). The relative error in the GC measurements of the other species was less than 5% for CH_4, CO_2, CO and N_2, increasing up to 50% for the scarce O_2. In the forthcoming sections only the GC measurements will be presented; the GA data have provided an additional (and successful) control, mainly for the CO and O_2 compositions.

IV.2.3 Catalyst preparation and characterization

The ZrO_2 support material was calcined at 1073 K for 5 h. The catalyst contained 1% wt Rh (0.5% wt in Cases 6 to 9) and was prepared by incipient wetness impregnation of the ZrO_2 support with aqueous solutions of $Rh(NO_3)_3$. The impregnated supports were dried at 383 K, followed by calcination at 873 K for 5 h. A slurry of the catalyst powder was then sprayed into the FeCr-alloy foils and the coated structures were further calcined at 873 K for 1 h. Four successive layers were applied, resulting in a catalyst thickness $\delta_c = 4.6$ μm. Before each combustion run, the catalyst was reduced in a 673 K flow of H_2/N_2 for 20 min.

The total and active areas of both fresh and used FeCr-alloy foils were measured with BET (N_2-physisorption) and H_2-chemisorption. Hydrogen chemisorption analysis was performed on a Quantachrome Autosorb-1C to determine the noble metal dispersion. The hydrogen adsorption measurements were carried out at 195 K and the data analysis considered a H_2:Rh stoichiometry of 1:2. The metal dispersion was calculated according to the dual isotherm method. The ratio of active-to-geometrical surface area (B), which was deduced from the chemisorption-measured catalyst dispersion, was a parameter needed in the numerical model (see Table IV.1 and footnote (b)). Supplementary surface science measurements were also made (surface Raman and X-ray photoelectron spectroscopy to identify the crystal structure and oxidation state of the surface species, respectively), but they were of limited interest for the present study; details of the surface science measurements have been reported elsewhere .

IV.3 NUMERICAL

Given the good thermal insulation and the uniform properties at the front face of the honeycomb (see also discussion in section "Boundary conditions and method of solution"), a single-channel model has been constructed. A representative channel was treated as a tube with inner radius $r_h = 0.6$ mm. This was a reasonable simplification given the lack of prevailing secondary flows (straight channels having trapezoidal cross sections with rounded corners), as also reported in [64, Schneider et al., 2006]. A full elliptic 2-D quasisteady model was employed for the reactive gas flow. On the other hand, the spatial dimensionality of the solid was dictated by characteristic time considerations. The characteristic time for axial convection was, as discussed in the experimental section, $t_{g,x} \sim (9\text{-}12)\text{x}10^{-3}$ s while for radial gas diffusion the characteristic time (r_h^2/α_g) was $t_{g,r} \sim (5\text{-}20)\text{x}10^{-3}$ s (using gas

properties in the range 680 to 1180 K). The corresponding times for solid heat conduction, axial (L^2/α_{FeCr}) and radial [$(\delta/2)^2/\alpha_{FeCr} + \delta_c^2/\alpha_{ZrO2}$], were $t_{s,x} \sim (1.6\text{-}2.4)\text{x}10^3$ s and $t_{s,r} \sim (0.3\text{-}0.4) \text{ x}10^{-3}$ s, respectively (using the solid properties of Table IV.2, in the provided temperature ranges). Since the equilibration of the gas required times at least as long as $t_{g,r}$, the significantly faster radial solid heat conduction could not be resolved within the gas-phase quasisteady assumption. This condition was typical to many practical systems, whereby the high pressures led to elongated gas diffusion times. Thus, a 1-D approach for the solid has been adopted. A step of 50 ms, sufficiently long for gas-phase equilibration, was used for time integration.

Table IV.2

Properties of solid[a]

Material	T (K)	λ (W/mK)	ρ (kg/m^3)	c (J/kgK)[b]
FeCr	680	16	7200	615
FeCr	1100	16	7200	940
ZrO$_2$[c]	680	0.45	3560	590
ZrO$_2$	1100	0.52	3540	695

[a] thermal conductivity, density, heat capacity at two selected temperatures.

[b] in the range 600-1200 K, $c_{FeCr} = b_0 + b_1T + b_2T^2$, $b_0 = 580$, $b_1 = 0.394$ and $b_2 = 6.57\text{x}10^{-4}$.

[c] the properties of ZrO$_2$ have been corrected for porosity (37%, assessed from the physisorption tests).

IV.3.1 Governing equations

For a quasisteady laminar channel-flow with hetero-/homogeneous reactions, the governing equations in cylindrical coordinates become:

Continuity:

$$\frac{\partial(\rho u)}{\partial x} + \frac{1}{r}\frac{\partial(r\rho v)}{\partial r} = 0 . \tag{1}$$

Axial momentum:

$$\frac{\partial(\rho uu)}{\partial x}+\frac{1}{r}\frac{\partial(r\rho vu)}{\partial r}=-\frac{\partial p}{\partial x}+\frac{\partial}{\partial x}\left[2\mu\frac{\partial u}{\partial x}-\frac{2}{3}\mu\left(\frac{\partial u}{\partial x}+\frac{1}{r}\frac{\partial(rv)}{\partial r}\right)\right]+$$

$$+\frac{1}{r}\frac{\partial}{\partial r}\left[\mu r\left(\frac{\partial u}{\partial r}+\frac{\partial v}{\partial x}\right)\right].$$

(2)

Radial momentum:

$$\frac{\partial(\rho uv)}{\partial x}+\frac{1}{r}\frac{\partial(r\rho vv)}{\partial r}=-\frac{\partial p}{\partial r}+\frac{\partial}{\partial x}\left[\mu\left(\frac{\partial v}{\partial x}+\frac{\partial u}{\partial r}\right)\right]+\frac{\partial}{\partial r}\left[2\mu\frac{\partial v}{\partial r}-\frac{2}{3}\mu\left(\frac{\partial u}{\partial x}+\frac{1}{r}\frac{\partial(rv)}{\partial r}\right)\right]+$$

$$+\frac{2\mu}{r}\left(\frac{\partial v}{\partial r}-\frac{v}{r}\right).$$

(3)

Total enthalpy:

$$\frac{\partial(\rho uh)}{\partial x}+\frac{\partial(r\rho vh)}{\partial r}=\frac{\partial}{\partial x}\left(\lambda_g\frac{\partial T}{\partial x}-\rho\sum_{k=1}^{K_g}Y_k h_k V_{k,x}\right)+\frac{1}{r}\frac{\partial}{\partial r}\left(r\lambda_g\frac{\partial T}{\partial r}-r\rho\sum_{k=1}^{K_g}Y_k h_k V_{k,r}\right)$$

(4)

Gas-phase species:

$$\frac{\partial(\rho uY_k)}{\partial x}+\frac{1}{r}\frac{\partial(r\rho vY_k)}{\partial r}=-\frac{\partial}{\partial x}\left(\rho Y_k V_{k,x}\right)-\frac{1}{r}\frac{\partial}{\partial r}\left(r\rho Y_k V_{k,r}\right)+\dot{\omega}_k W_k,\quad k=1,..,K_g.$$

(5)

Surface species coverage:

$$\frac{\partial\theta_m}{\partial t}=\sigma_m\frac{\dot{s}_m}{\Gamma},\quad m=1,..,M_s.$$

(6)

The left side of Eqs. (6) was not a true transient term and its inclusion merely facilitated convergence to steady state. The diffusion velocities were computed using mixture-average plus thermal diffusion for the light species [51, Kee et al., 1996a]:

$$\vec{V}_k=-(D_{km}/Y_k)\nabla Y_k+(D_k^T/\rho Y_k T)\nabla T,\quad k=1,..,K_g.$$

(7)

Finally, the ideal gas and caloric state laws were:

$$p=\frac{\rho RT}{\overline{W}}\text{ and }h_k=h_k^\circ(T_o)+\int_{T_o}^{T}c_{p,k}dT,\text{ with }h=\sum_{k=1}^{K_g}Y_k h_k,\quad k=1,..,K_g.$$

(8)

The time-dependent energy balance for the 1-D solid was:

$$\left[\rho_{\text{FeCr}}\frac{\partial(c_{\text{FeCr}}T_W)}{\partial t}-\lambda_{\text{FeCr}}\frac{\partial^2 T_W}{\partial x^2}\right]\frac{\delta}{2}-\left[\dot{q}_{\text{rad}}-\lambda_g\frac{\partial T}{\partial r}\bigg|_{r=r_h-}+B\sum_{k=1}^{K_g}\left(\dot{s}_k h_k W_k\right)_{r=r_h}\right]\left(\frac{2r_h}{2r_h+\delta/2}\right)=0$$

(9)

The solid thickness in Eq. (9) corresponded to half of the FeCr-alloy ($\delta/2 = 25$ μm) due to the consideration of adjacent channels. The thinner catalyst layer ($\delta_c = 4.6$ μm) was neglected since its thermal conductivity and thermal inertia ($\rho_{ZrO2} c_{ZrO2} \delta_c$) were at least an order of magnitude lower than those of the FeCr-alloy, irrespective of temperature. For the FeCr-alloy, a temperature-dependent heat capacity was considered (see footnote (b) of Table IV.2); the thermal conductivity was taken constant at its 300 K value of 16 W/mK, given the lack of specific literature data and the weak temperature dependence of similar alloys [74, Touloukian et al., 1970]. The net received radiant heat flux ($\dot{q}_{rad}$ in Eq. (9)) accounted for the radiation exchange of each differential cylindrical surface element with all other differential surface elements as well as with the channel entry and outlet, and was modeled by the net radiation method for diffuse-gray areas [75, Siegel and Howell, 1981]. Details of the radiation model have been provided elsewhere [76, Karagiannidis et al., 2007]. The emissivities of all differential channel elements were equal to $\varepsilon = 0.6$, while the inlet and the outlet sections were treated as black bodies ($\varepsilon = 1.0$). The radiation exchange temperatures for the entry and outlet were considered equal to the corresponding mean gas temperatures. It will be shown, however, that radiation effects were altogether minimal.

IV.3.2 Boundary conditions and method of solution

The gas-phase species interfacial boundary conditions were:

$$(\rho Y_k V_{k,r})_{r=r_h-} + B \dot{s}_k W_k = 0, \quad k = 1,.., K_g, \tag{10}$$

with $\dot{s}_k = 0$ over the inactive channel length. The factor B in Eqs. (9) and (10) was the ratio of the active to the geometrical surface area and has been determined by H_2 chemisorption. Those tests provided the active areas in m^2/gr-Rh for the used catalysts; with known size, weight and noble metal content of the analyzed samples, the values of B could be calculated (see Table IV.1). It is noted that the fresh samples had considerably higher measured B factors as they comprised both high-surface-area tetragonal phase and low-surface-area monoclinic ZrO_2 phase (detected with surface Raman measurements), while the used samples comprised only monoclinic phase . The B values of the used samples were maintained in successive combustion runs and were, therefore, employed in the ensuing simulations (in all cases of Table IV.1 the catalysts had already been exposed to combustion environments at

foregoing runs). Intraphase species diffusion was not considered since the catalyst layer was only 4.6 μm thick and was applied on a non-porous FeCr-alloy.

Radiative boundary conditions were applied at the reactor inlet and outlet:

$$\lambda_{FeCr} \, \partial T_W / \partial x = \varepsilon \sigma \left[T_W^4(x) - T_{IN}^4 \right] \qquad \text{at } x = -L_u$$

$$-\lambda_{FeCr} \, \partial T_W / \partial x = \varepsilon \sigma \left[T_W^4(x) - T_{OUT}^4 \right] \text{ at } x = L_c + L_u. \tag{11}$$

Uniform profiles for the axial velocity, the species mass fractions and the temperature were specified at the inlet. The 8 mm gap between the flow straightener and the honeycomb entry created only a very thin boundary layer (less than 0.4 mm thick, since the Reynolds numbers in the 35 mm diameter holder tube exceeded 15,000), thus justifying the consideration of a single representative channel with a constant inlet velocity. Moreover, the adiabaticity of the honeycomb reactor was attested by the gas analysis and temperature measurements; the differences between the inlet and outlet total enthalpies corresponded to equivalent temperature differences of less than 15 K. It is worth mentioning that, apart from the good thermal insulation, the adiabaticity was aided by the particularly large (for laboratory-scale tests) honeycomb diameter (35 mm) that resulted in a low external surface-to-volume ratio. At the symmetry axis ($r = 0$) and the outlet ($x = L_c + L_u$) zero-Neumann boundary conditions were applied for all thermoscalars and the axial velocity, while the radial velocity was set to zero. Finally, no-slip conditions were used for both velocity components at $r = r_h$.

The coupled set of flow and solid equations (Eqs. (1) to (6) and Eq. (9)) were solved simultaneously. A finite volume scheme was adopted for the spatial discretization of the flow equations and solution was obtained with a SIMPLER method for the pressure-velocity field [52, Patankar, 1980]; details on the quasisteady flow solution have been provided elsewhere [21, Dogwiler et al., 1999; 53, Mantzaras et al., 2000; 54, Appel et al., 2002]. For the transient solid equation, a second order accurate, fully implicit scheme was constructed by using a quadratic backward time discretization [77, Ferziger and Petric, 1999]. At a given time step, the coupled flow and solid phases were solved iteratively such that at convergence the solid temperature did not vary by more than 10^{-4} K. An orthogonal staggered grid of 220x24 points in x and r, respectively, (75 mm x 0.6 mm) with finer axial spacing towards the start of the catalytic section and radial spacing closer to the wall, was sufficient to produce a grid-independent solution; the axial discretizations in the solid and gas were the same (220 points). For time integration, the step was $\Delta t = 50$ ms. Simulations of selected cases with steps of 35, 40 and 70 ms were in good agreement with the $\Delta t = 50$ ms results. The CPU time for a 10-sec-long integration was ~15 h on a 2.6 GHz Opteron processor when gas

chemistry was not included (otherwise the CPU time increased by a factor of four). Finally, a cluster of twenty same processors was used for elaborate parametric studies.

IV.3.3 Chemical kinetics

The detailed catalytic scheme of Deutschmann [1, Schwiedernoch et al., 2003] has been employed (38 reactions, 12 surface and 6 gaseous species, see Table IV.3). Earlier kinetic studies have shown [47, Appel et al., 2005a] that this scheme reproduced the measured methane conversion and synthesis gas yields in CPO of CH_4/air, at least over the reactor extent were oxygen was still available; in the experiments of Table IV.1, a small oxygen breakthrough was always assured. More recent kinetic studies [63, Schneider et al., 2007] have also attested the aptness of the catalytic scheme in CPO of methane with EGR at pressures of 4 to 10 bar.

For gas-phase chemistry, the C_2/H/O mechanism of [2, Warnatz et al., 1996] was used (164 reversible reactions and 34 species). This mechanism has reproduced homogeneous ignition characteristics in the aforementioned CPO studies without and with EGR [47, Appel et al., 2005a; 63, Schneider et al., 2007]. Selected simulations have shown that, for the present moderate pressures, the homogeneous reaction pathway was negligible not only during the transient light-off event but also during the steady operation where the surface temperatures were the highest (for the latter see also discussion in [64, Schneider et al., 2006]). Gas phase chemistry was also negligible over the 45-mm-long gap separating the reactor exit and the sampling probe (Fig. IV.1(a)), as shown by additional steady plug-flow reactor simulations. The minimal impact of gaseous chemistry was also demonstrated experimentally: when the cooling water of the sampling probe was turned off, the relative increase in the measured hydrogen composition was only 3%, despite the fact that the residence time in the visibly-hot part of the probe was about ten times longer than that inside the reactor.

Transport properties were evaluated using the CHEMKIN database [51, Kee et al., 1996a]. Gas-phase thermodynamic data were included in the provided scheme [2, Warnatz et al., 1996]. Finally, surface and gas-phase reaction rates (the latter were excluded from the ensuing computations) were evaluated with SURFACE CHEMKIN [25, Coltrin et al., 1996] and CHEMKIN [56, Kee et al., 1996b], respectively.

Table IV.3

Heterogeneous reaction scheme[a]

Adsorption reactions	$A\,(\gamma)$	b	E
S1. $CH_4 + Rh(s) \rightarrow CH_4(s)$	0.008	0.0	0.0
S2. $O_2 + 2Rh(s) \rightarrow 2O(s)$	0.01	0.0	0.0
S3. $H_2 + 2Rh(s) \rightarrow 2H(s)$	0.01	0.0	0.0
S4. $H_2O + Rh(s) \rightarrow H_2O(s)$	0.1	0.0	0.0
S5. $CO_2 + Rh(s) \rightarrow CO_2(s)$	10^{-5}	0.0	0.0
S6. $CO + Rh(s) \rightarrow CO(s)$	0.5	0.0	0.0

Surface reactions	$A\,(\gamma)$	b	E
S7. $H(s) + O(s) \rightarrow OH(s) + Rh(s)$	5.0×10^{22}	0.0	83.7
S8. $OH(s) + Rh(s) \rightarrow H(s) + O(s)$	3.0×10^{20}	0.0	37.7
S9. $H(s) + OH(s) \rightarrow H_2O(s) + Rh(s)$	3.0×10^{20}	0.0	33.5
S10. $H_2O(s) + Rh(s) \rightarrow H(s) + OH(s)$	5.0×10^{22}	0.0	106.4
S11. $OH(s) + OH(s) \rightarrow H_2O(s) + O(s)$	3.0×10^{21}	0.0	100.8
S12. $H_2O(s) + O(s) \rightarrow OH(s) + OH(s)$	3.0×10^{21}	0.0	224.2
S13. $C(s) + O(s) \rightarrow CO(s) + Rh(s)$	3.0×10^{22}	0.0	97.9
S14. $CO(s) + Rh(s) \rightarrow C(s) + O(s)$	2.5×10^{21} 0.0		169.0
S15. $CO(s) + O(s) \rightarrow CO_2(s) + Rh(s)$	1.4×10^{20} 0.0		121.6
S16. $CO_2(s) + Rh(s) \rightarrow CO(s) + O(s)$	3.0×10^{21} 0.0		115.3
S17. $CH_4(s) + Rh(s) \rightarrow CH_3(s) + H(s)$	3.7×10^{21} 0.0		61.0
S18. $CH_3(s) + H(s) \rightarrow CH_4(s) + Rh(s)$	3.7×10^{21} 0.0		51.0
S19. $CH_3(s) + Rh(s) \rightarrow CH_2(s) + H(s)$	3.7×10^{24} 0.0		103.0
S20. $CH_2(s) + H(s) \rightarrow CH_3(s) + Rh(s)$	3.7×10^{21} 0.0		44.0
S21. $CH_2(s) + Rh(s) \rightarrow CH(s) + H(s)$	3.7×10^{24} 0.0		100.0
S22. $CH(s) + H(s) \rightarrow CH_2(s) + Rh(s)$	3.7×10^{21} 0.0		68.0
S23. $CH(s) + Rh(s) \rightarrow C(s) + H(s)$	3.7×10^{21} 0.0		21.0
S24. $C(s) + H(s) \rightarrow CH(s) + Rh(s)$	3.7×10^{21} 0.0		172.8
S25. $CH_4(s) + O(s) \rightarrow CH_3(s) + OH(s)$	1.7×10^{24} 0.0		80.3
S26. $CH_3(s) + OH(s) \rightarrow CH_4(s) + O(s)$	3.7×10^{21} 0.0		24.3
S27. $CH_3(s) + O(s) \rightarrow CH_2(s) + OH(s)$	3.7×10^{24} 0.0		120.3
S28. $CH_2(s) + OH(s) \rightarrow CH_3(s) + O(s)$	3.7×10^{21} 0.0		15.1
S29. $CH_2(s) + O(s) \rightarrow CH(s) + OH(s)$	3.7×10^{24} 0.0		158.4
S30. $CH(s) + OH(s) \rightarrow CH_2(s) + O(s)$	3.7×10^{21} 0.0		36.8
S31. $CH(s) + O(s) \rightarrow C(s) + OH(s)$	3.7×10^{21} 0.0		30.1
S32. $C(s) + OH(s) \rightarrow CH(s) + O(s)$	3.7×10^{21} 0.0		145.5

Desorption reactions	$A\,(\gamma)$	b	E
S33. $2H(s) \rightarrow H_2 + 2Rh(s)$	3.0×10^{21} 0.0		77.8
S34. $2O(s) \rightarrow O_2 + 2Rh(s)$	1.3×10^{22}	0.0	$355.2-280\theta_O$
S35. $H_2O(s) \rightarrow H_2O + Rh(s)$	3.0×10^{13} 0.0		45.0
S36. $CO(s) \rightarrow CO + Rh(s)$	3.5×10^{13} 0.0		$133.4-15\theta_{CO}$
S37. $CO_2(s) \rightarrow CO_2 + Rh(s)$	1.0×10^{13} 0.0		21.7
S38. $CH_4(s) \rightarrow CH_4 + Rh(s)$	1.0×10^{13} 0.0		25.1

[a]Schwiedernoch et al. (2003). The reaction rate coefficient is $k = AT^b exp(-E/RT)$, A (mol-cm-sec) and E (kJ/mol). In the adsorption reactions, A denotes a sticking coefficient (γ). The suffix (s) designates a surface species. The surface site density is $\Gamma = 2.72\times10^{-9}\,mol/cm^2$.

IV.3.4 Ideal reactor modeling

In order to decouple the underlying chemical processes from reactor effects (e.g. properties of solid) additional computations have been carried out with ideal reactor models. Ignition delay times were computed in a constant pressure batch reactor. For this purpose, the homogeneous-reaction package SENKIN of CHEMKIN [78, Lutz et al., 1996] has been extended to include catalytic reactions. The governing equations were as follows:

Gas-phase species equation:

$$\rho \frac{dY_k}{dt} = (\dot{\omega}_k + \frac{S}{V} \dot{s}_k) W_k, \qquad k = 1,.., K_g. \tag{12}$$

Energy equation:

$$c_p \frac{dT}{dt} = -\frac{1}{\rho} \left[\sum_{k=1}^{K_g} h_k \dot{\omega}_k W_k + \frac{S}{V} \sum_{k=1}^{K_g+M_s} h_k \dot{s}_k W_k \right], \tag{13}$$

with *S* and *V* the reactor surface and volume, respectively. Equations (12), (13) and (6), supplemented by the gas laws of Eqs. (8), were solved subject to appropriate initial conditions.

Finally, the surface perfectly stirred reactor (SPSR) package of CHEMKIN [60, Moffat et al., 1993] facilitated the ignition/extinction studies:

Gas-phase species equations:

$$\frac{dY_k}{dt} = -\frac{1}{\tau}(Y_k - Y_{k,IN}) + \frac{1}{\rho}(\dot{\omega}_k + \frac{S}{V}\dot{s}_k)W_k, \qquad k = 1,.., K_g. \tag{14}$$

Energy equation:

$$c_p \frac{dT}{dt} = \frac{1}{\tau} \sum_{k=1}^{K_g} Y_{k,IN}(h_k - h_{k,IN}) - \frac{1}{\rho} \left[\sum_{k=1}^{K_g} h_k \dot{\omega}_k W_k + \frac{S}{V} \sum_{k=1}^{K_g+M_s} h_k \dot{s}_k W_k \right], \tag{15}$$

with τ the reactor residence time. The surface coverage and gas laws were given by Eqs. (6) and (8), respectively.

IV.4 Results and Discussion

IV.4.1 Catalytic ignition

Measured and predicted temporal profiles of temperature are provided in Fig. IV.2 for Case 1; predictions are shown for both the surface and the mean (radially-averaged) gas temperatures. Computed axial surface temperature profiles at selected time intervals are further given in

Fig. IV.3. During the ramping of the inlet temperature in the experiments, a small catalytic reactivity was always present for $T_{IN} > 600$ K, which resulted in measured reactor temperatures slightly higher than the corresponding T_{IN}. For consistency with the experiments, the initial solid temperature in the numerical model ($t = 0$ in Figs. IV.2 and IV.3) has been obtained by solving first a transient case at a lower inlet temperature ($T_{IN} = 670$ K) up to the time that yielded surface temperatures close to the measurements. It is, nonetheless, clarified that the small initial temperature excursions above $T_{IN} = 680$ K (less than 25 K at $t = 0$, as shown in Figs. IV.2 and IV.3) had a minimal impact on the subsequent time evolution of the ignition event.
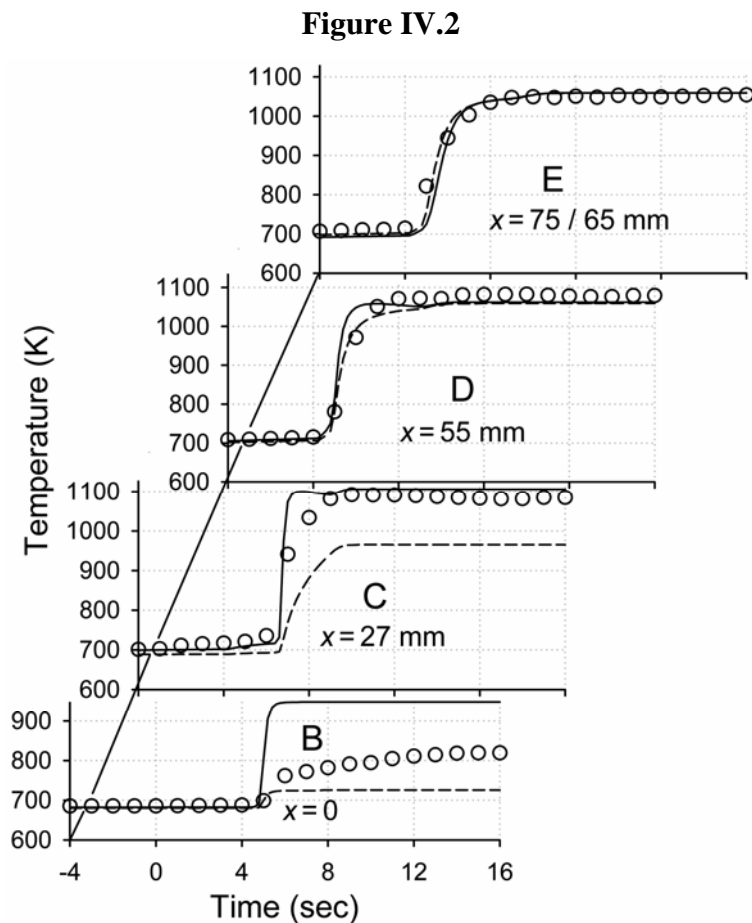
Figure IV.2

Predicted (lines) and measured (symbols) temperatures at axial positions B through E for Case 1. Predictions are given for the wall temperature (solid lines) and the mean gas temperature (dashed lines). At position E, the measurements refer to the mean gas temperature 10 mm downstream of the reactor ($x = 75$ mm), while the predictions refer to the mean gas temperature at the reactor exit ($x = 65$ mm).

Figure IV.3
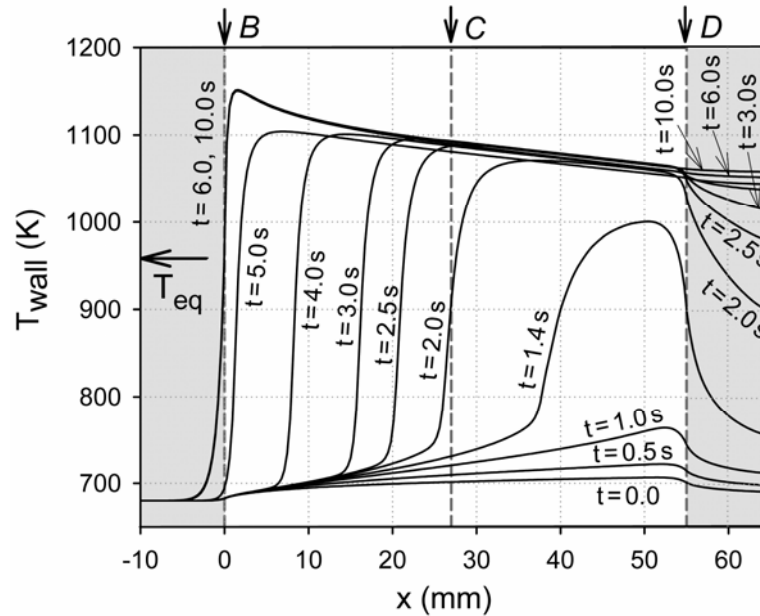
Predicted axial profiles of wall temperature at different times for Case 1. The shaded areas denote the non-catalytic part of the reactor. The vertical arrows at *B*, *C* and *D* indicate the thermocouple locations inside the reactor. The horizontal arrow marked T_{eq} denotes the adiabatic equilibrium temperature.

Figure IV.4
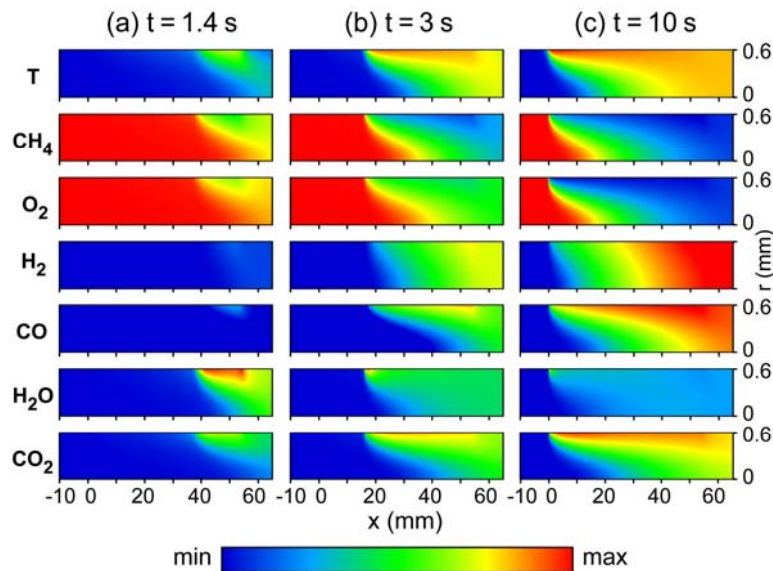
Predicted 2-D distributions of temperature and species mass fractions for Case 1 at three times: (a) 1.4 s, (b) 3.0 s, and (c) 10.0 s. The maximum and minimum levels of the color bar are: T: 681 K to 1146 K, CH_4: 0.039 to 0.131, O_2: 0.0 to 0.131, H_2: 0.0 to 0.0186, CO: 0.0 to 0.123, H_2O: 0.332 to 0.398, and CO_2: 0.406 to 0.478. The centerline is at $r = 0$ and the gas-solid interface at $r = 0.6$ mm. The catalytically active part of the reactor extents

The predictions reproduced well, at all four positions, the measured elapsed times for the onset of sharp temperature rise, the temporal extent of the main transient event, and also the final temperatures. At position E, the relevant predictions of Fig. IV.2 referred to the reactor exit ($x = 65$ mm); therein the channel walls were inert, leading to predicted mean gas temperatures higher than the corresponding surface temperatures during the period of sharp temperature rise. The measured temperatures at the late ignition stages ($t \geq 10$ s), where steady-state has been practically reached, were in good agreement with the predicted surface temperatures (Fig. IV.2). An exception was location B, with measurements in-between the predicted surface and mean gas temperatures. However, this can be attributed to the very steep spatial temperature gradients at position B (see Fig. IV.3): an effective repositioning of thermocouple B at $x = $ -0.3 mm could readily account for those differences. It is further noted that computations with $T_{IN} \leq 670$ K did not yield light-off (in the sense of a vigorous burning solution) for an integration period of up to 20 s, which was roughly threefold longer than the experimentally measured time needed to reach the steady-state wall temperature at $x \approx 0$ (see Figs. IV.2 and IV.3). This outcome was in good agreement with the experimentally assessed inlet temperature for ignition ($T_{IN} = 680$ K).

To facilitate the ensuing discussion, the main reaction pathways are summarized by the following global steps:

$CH_4 + 2O_2 = CO_2 + 2H_2O$ (total oxidation)   (R1)

$2CH_4 + O_2 = 2CO + 4H_2$ (partial oxidation)   (R2)

$CH_4 + H_2O = CO + 3H_2$ (steam reforming)   (R3)

$CO + H_2O = CO_2 + H_2$ (water gas shift)   (R4)

$CH_4 + CO_2 = 2CO + 2H_2$ (CO_2 reforming)   (R5)
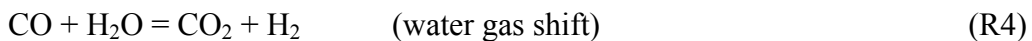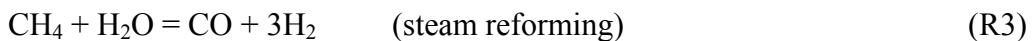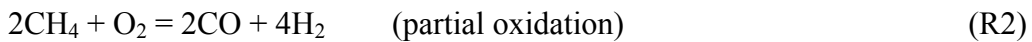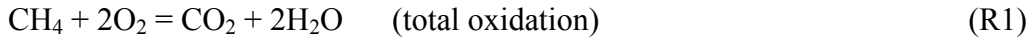
Mass rather than molar fractions will be preferably used thereafter, due to the presence of strongly non-equimolar reactions (R2, R3 and R5). The underlying chemical processes are discussed with the aid of Figs. IV.4 and IV.5 that provide, at three selected times, the 2-D maps of temperature and major species mass fractions, and the species net production rates and selected production rate ratios, respectively. Ignition was initiated at the rear of the channel as shown in Figs. IV.3 and IV.4(a). Total oxidation of methane dominated at early times as manifested by the sharp rise of H_2O, CO_2 and temperature in Fig. IV.4(a) and by the ~0.5 value of the CH_4:O_2 molar consumption ratio at the far upstream location of the reaction zone (see Fig. IV.5(a), $x \approx 36$ mm). H_2 and CO were not produced for $t < 1$ s, whereas at later times CO production commenced before that of H_2. At $t = 1.4$ s, both partial oxidation

products were produced (Fig. IV.5(a)), giving rise to the observed very low levels of H_2 and CO in Fig. IV.4(a). Following ignition, the reaction zone propagated upstream (Fig. IV.3) with an accompanying increase in peak surface temperature due to the gradual heat-up of the wall and the diminishing accumulation of heat in the solid mass. The peak temperature reached the front of the catalytically coated section at $t \approx 6$ s, while at $t \approx 10$ s steady-state had been practically achieved over the entire reactor length (Fig. IV.3). The wall and mean gas temperatures exceeded by as much as ~200 K the adiabatic equilibrium temperature ($T_{eq} = 959$ K, see Figs. IV.3 and IV.2), a condition typical in CPO reactors with residence times of a few milliseconds [64, Schneider et al., 2006; 73, Veser and Frauhammer, 2000].

The approach to steady state is also illustrated in Fig. IV.6(a), providing the predicted mean (radially-averaged) outlet species mass fractions versus time (black lines) and the corresponding GC steady-state measurements (the latter obtained at $t > 5$ min). The agreement between the measured and predicted outlet compositions was particularly good for all species; using the measured outlet species mass fractions and temperature, the calculated total enthalpy was within 0.4% of the corresponding inlet value (which was equivalent to a temperature differential of 15 K) and the C/H/O element balances were within 0.5%. For $t > 1.6$ s, H_2 and CO were formed at the upstream locations of the reaction zone mainly by the CPO reaction (R2) as manifested by the ~2:1 production ratio of H_2:CO (Fig. IV.5(b,c)). It is clarified that, as time progressed, the CO and H_2 formed increasingly closer to the front of the reaction zone. As in matter of fact, for $t > 2$ s both total and partial oxidation products were formed at the reaction zone front. This is illustrated by the CH_4:O_2 ratios in Fig. IV.5(b,c), which increased at the tip of the reaction zone from 0.55 ($t = 3$ s) to 0.88 ($t = 10$ s) indicating the growing contribution of the CPO reaction. This behavior was differentiated from earlier CH_4/air CPO studies without EGR [1, Schwiedernoch et al., 2003], where only total oxidation has been reported at the upstream reactor positions.

As the temperature of the catalyst increased, H_2 and CO were also produced farther downstream by the slower endothermic steam reforming (R3); this was manifested by the corresponding streamwise increase in the H_2:CO production ratio to values above 2.0 (Fig. 5(b,c)) and by the corresponding drop in surface temperature (Fig. IV.3). The surface temperatures had reached high enough levels for appreciable steam reforming particularly at $t > 5.2$ s, as seen by the sudden increase (decrease) in the H_2 (H_2O) profile of Fig. IV.6(a). At $t > 6$ s, water gas shift (R4) started playing a modest role at the far downstream positions: this was evidenced by the continuing small production of CO_2 and the corresponding rise of the H_2:CO ratio at the far end of the active channel section ($x > 50$ mm, Fig. IV.5(c)).

Figure IV.5
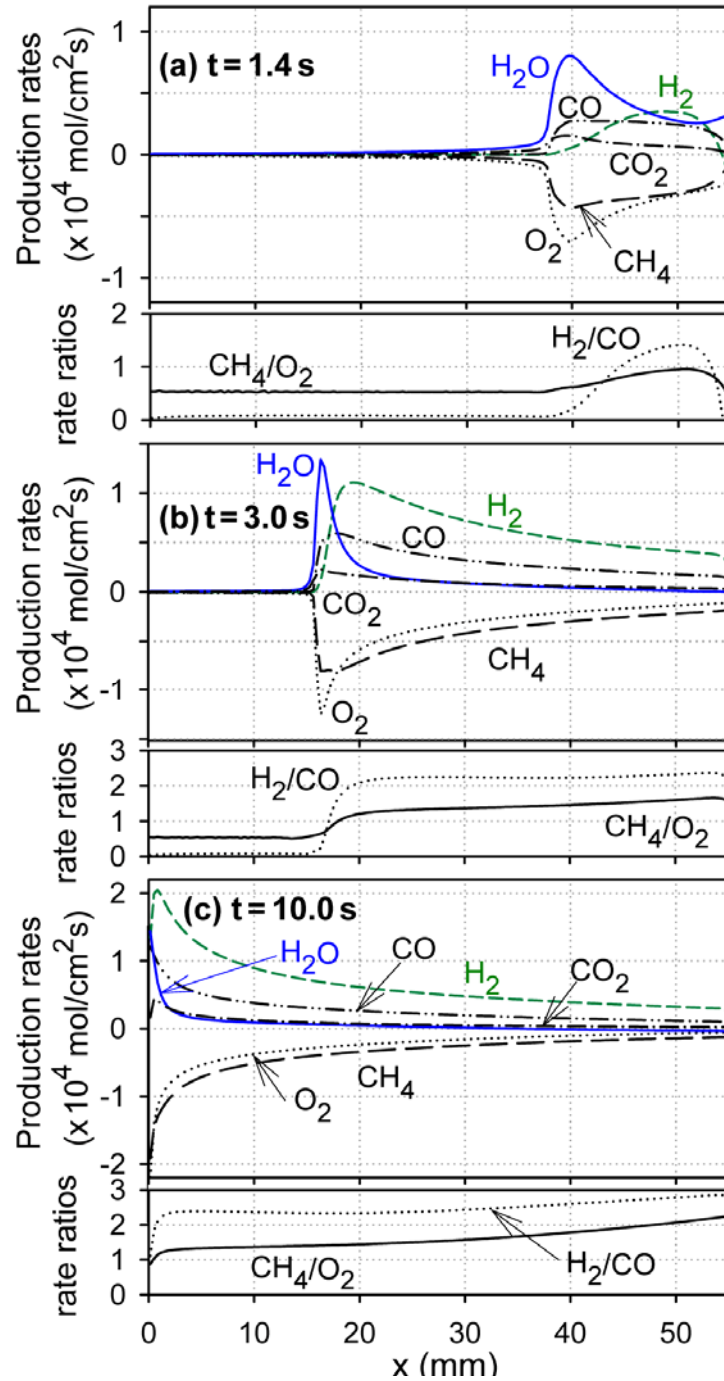
Computed axial profiles (Case 1) of species molar production rates (solid lines: H_2O, short dashed lines: H_2, double-dotted-dashed lines: CO, dotted-dashed lines: CO_2, long dashed lines: CH_4, dotted lines: O_2) and production rate-ratios (solid lines: CH_4:O_2, dotted lines: H_2/CO) at three times: (a) 1.4 s, (b) 3.0 s, and (c) 10.0 s.

Figure IV.6
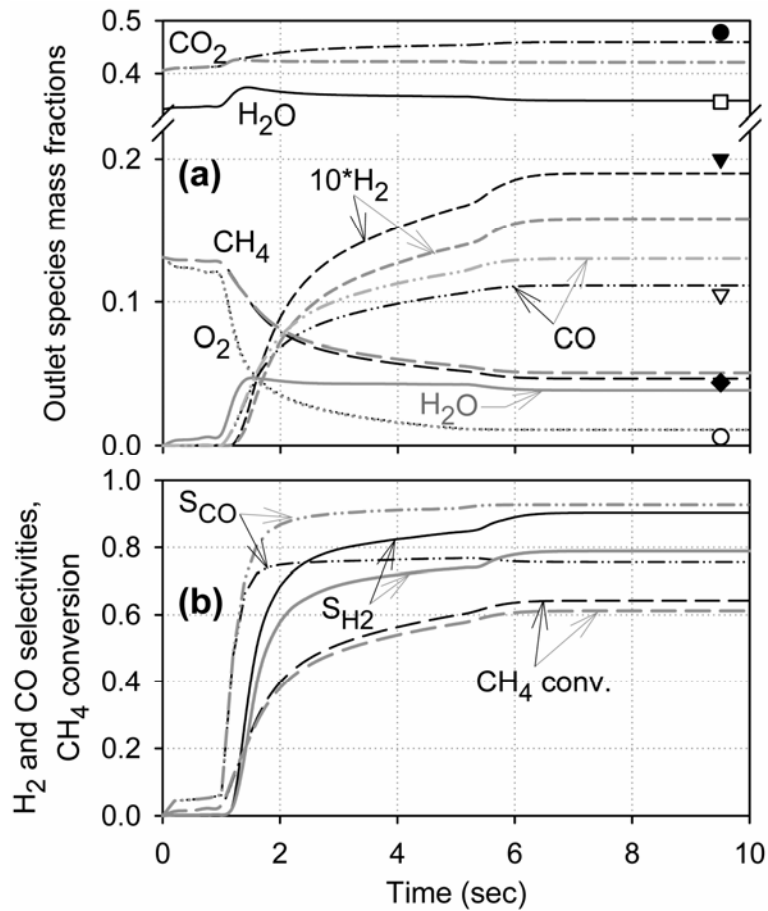
(a) Predicted mean species mass fractions at the reactor outlet ($x = 65$ mm) versus time. Black lines: Case 1, gray lines: conditions same as in Case 1 with the inlet 46.3% H_2O replaced by equal amount of chemically inert H_2O^*. The symbols denote the steady state GC measurements (CO_2: filled circle, H_2O: open square, $10 \times H_2$: filled triangle, CO: open triangle, CH_4: filled diamond, O_2: open circle), (b) predicted selectivities for H_2 and CO and fractional CH_4 conversion (the notation of the black and gray lines is the same as in (a)).

Therein, the O_2 consumption rates were too low to justify production of CO_2 via the oxidation route R1. On the other hand, the water gas shift reaction was found to be altogether insignificant in CH_4/air CPO without EGR [1, Schwiedernoch et al., 2003]. It is finally noted that at all times there was always a small amount of O_2 breakthrough at the reactor exit (Fig. IV.6).

The surface coverage for Case 1 is provided in Fig. IV.7 at two selected times. The main coverage at early times, where the temperature was low, was O(s) (Fig. IV.7(a)). The presence of O(s) inhibited ignition because high enough surface temperatures were required to

shift the adsorption/desorption equilibria of O_2 towards desorption and thus release free surface sites for methane to adsorb. Although the mechanism of $O(s)$ inhibition in catalytic ignition was the same for either fuel-lean or fuel-rich conditions [1, Schwiedernoch et al., 2003; 21, Dogwiler et al., 1999; 64, Schneider et al., 2006; 79, Deutschmann et al., 1996], it was less pronounced in the latter due to the lower O_2 content. Upon ignition, $CO(s)$ and free sites $(Rh(s))$ became the dominant surface coverage. The partial oxidation product selectivities, defined as:

$$S_{H2} = \frac{0.5\, Y_{H2}\, / W_{H2}}{(Y_{CH4,IN} - Y_{CH4,OUT})/W_{CH4}} \text{ and } S_{CO} = \frac{Y_{CO}\, / W_{CO}}{(Y_{CH4,IN} - Y_{CH4,OUT})/W_{CH4}}, \quad (16)$$

along with the fractional methane conversion at the reactor outlet are provided in Fig. IV.6(b) (black lines). The definition of S_{H2} in Eq. (16) was based on the stoichiometry of the CPO reaction and has been maintained herein, despite the added H_2 production from H_2O. At steady state, $S_{H2} = 0.91$ and $S_{CO} = 0.74$ while the methane conversion was 64%.

IV.4.2 Impact of H_2O and CO_2 dilution on catalytic ignition

Despite the added large amount of CO_2, the contribution of dry (CO_2) reforming was negligible as also shown in our previous steady-state investigation [49, Eriksson et al., 2006]. The reason was that oxy- and H_2O-reforming reactions were considerably faster than dry reforming [42, Mark and Maier, 1996] and the dominance of the former steps was further accentuated by the present short contact times. The absence of dry reforming has also been attested in CH_4/air CPO without EGR [1, Schwiedernoch et al., 2003; 73, Veser and Frauhammer, 2000]. To investigate the impact of water on the synthesis gas yields and selectivities, additional predictions have been carried out for Case 1, whereby the 46.3% H_2O feed content was replaced by a fictitious species H_2O^* that had the same thermodynamic and transport properties as H_2O but did not participate in any reaction. H_2O^* simulated only the incoming steam whereas the catalytic pathway was still allowed to create combustion-generated H_2O. Computations with H_2O^* and normal H_2O dilution are compared in Figs. IV.6 and IV.8. It is evident that the presence of water increased (decreased) the H_2 (CO) selectivity and slightly increased the methane conversion (Fig. IV.6(b)), while it moderated somewhat the surface temperatures (Fig. IV.8). This was because H_2O provided a source of surface $O(s)$ and $OH(s)$ radicals that facilitated the steps S33 and S15 against S7/S9 and S36 (see Table IV.3), respectively, as has been elaborated in earlier steady CPO studies [49, Eriksson et al., 2006]. The comparison between the black and gray H_2O lines in Fig. IV.6(a) further indicated that the added amount of H_2O facilitated steam reforming

mainly by depleting faster the water produced by total oxidation (R1) rather than by consuming the incoming steam itself (at any time, $Y_{H2O,OUT}(t) > Y_{H2O,IN}$ in Figs. IV.6(a) and IV.4). This was because the surface temperatures were moderate and the residence times too short for the slow endothermic steam reforming to dominate. Of importance in the present transient analysis, was that the chemical impact of water was already evidenced at early times (e.g. $t > 1.5$ s) as seen in Fig. IV.6. However, the effect of added water grew to larger importance at later times when a significant extent of the channel attained high temperatures.

Figure IV.7
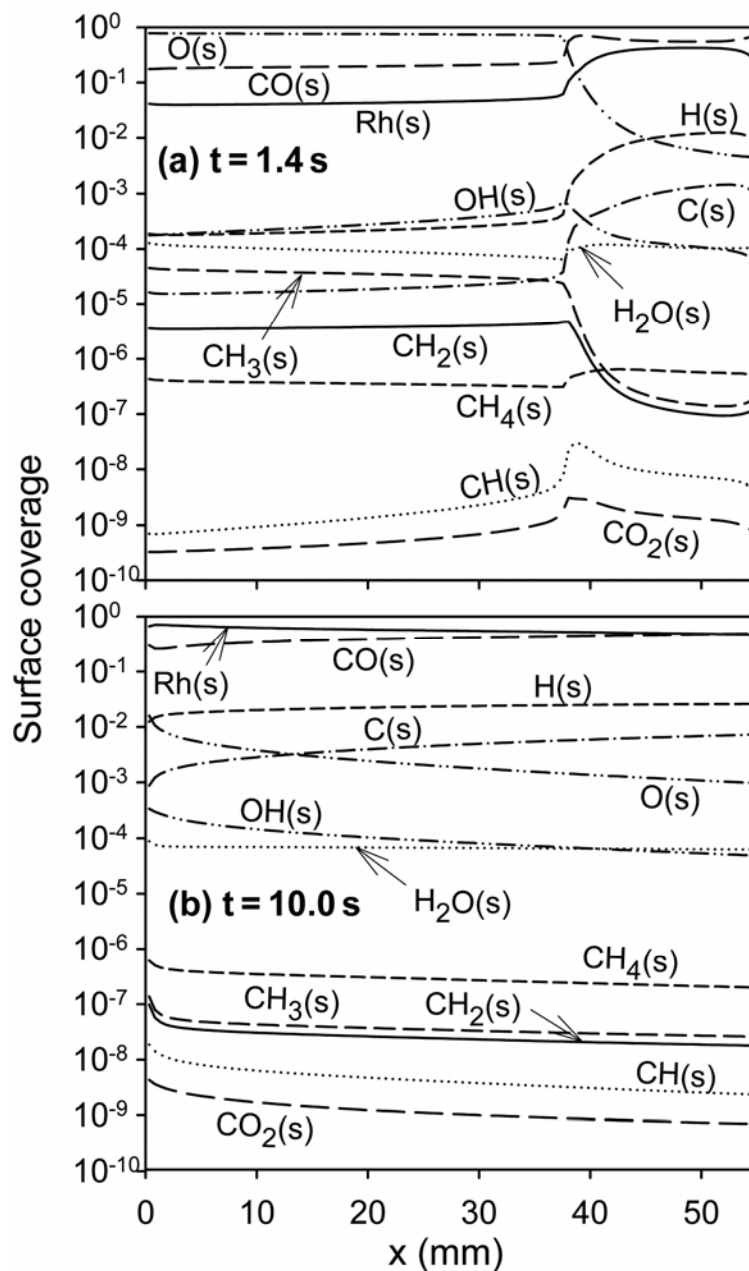
Surface coverage for Case 1 at two times: (a) 1.4 s and (b) 10 s.

Figure IV.8
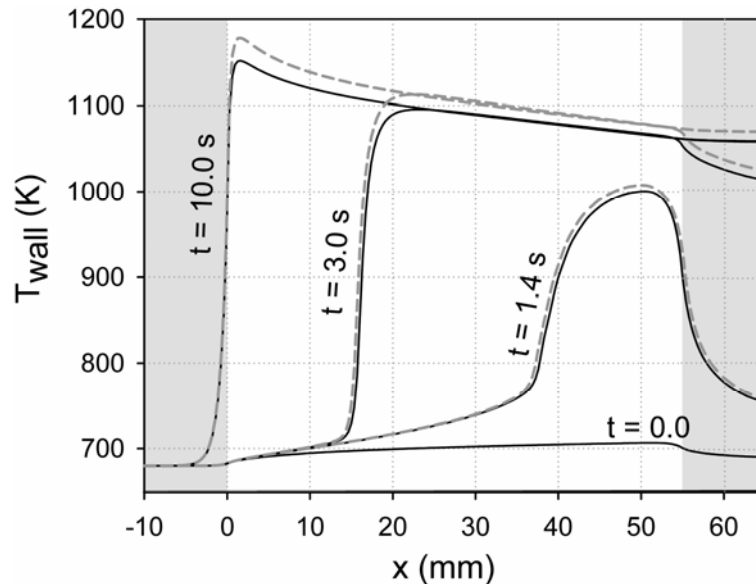
Predicted axial profiles of wall temperature at different times. Solid black lines: Case 1, dashed gray lines: conditions same as Case 1 with the inlet 46.3% H_2O replaced by equal amount of chemically inert H_2O^*. The shaded areas denote the non-catalytic part of the reactor.

Despite the chemical impact of H_2O and the associated somewhat lower surface temperatures (by as much as 26 K compared to the H_2O^* dilution, see Fig. IV.8) due to the enhanced impact of steam reforming, the times required for the onset of ignition and for the propagation of the reaction zone to the front of the catalytic section ($x = 0$) were practically the same in both H_2O and H_2O^* dilution (Fig. IV.8). To isolate reactor parameters (heat conduction in the solid, etc.) from chemical effects, ignition delay times have been computed in a batch reactor (Eqs. (12) and (13), with only surface reactions included) using $S/V = 33.3$ cm^{-1}, so as to mimic the confinement of the channel experiments. The catalytic ignition delay times, τ_{ig}, (defined as the times required to reach the 50% rise between inlet and final temperatures) were practically independent of dilution type (15.2 ms for the H_2O and 15.0 ms for the H_2O^*). The reason for this unexpected behavior is illustrated in Fig. IV.9, providing the normalized sensitivity coefficients of the ignition delay time $[=(A_i/\tau_{ig})(\partial \tau_{ig}/\partial A_i)$, with A_i the pre-exponential of the i-th reaction] for the eight most significant reactions of Table IV.3. The dominant reaction controlling catalytic ignition (in either H_2O or H_2O^* dilution) was S15, the surface oxidation of CO(s) to CO_2(s). Upon ignition, CO(s) and free sites (Rh(s)) comprised the main surface coverage (see Fig. IV.7).

During the ignition process, the rising CO(s) coverage reduced the amount of available free sites and hence inhibited ignition. An acceleration of S15 led to lower CO(s), thus promoting ignition. It is nonetheless, instructive to consider not only the chemical but also the thermal impact of S15. This reaction eventually led to the formation of CO_2, the oxidation $CO \rightarrow CO_2$ being a main exothermic heat release step. The oxidation of H_2 to H_2O was less important, since the $CO:H_2$ molar ratio over the entire induction zone was at least ten. Catalytic ignition delay times were, therefore, dominated by total oxidation reactions forming CO_2, and as such they were not critically affected by reactions forming partial oxidation products (R2 and R4). In summary, the chemical impact of H_2O dilution, although important during the time evolution of the light-off event, was minimal on the ignition delay times themselves.

IV.4.3 Effect of solid properties on catalytic ignition

To complete the picture of all processes inside the reactor, the heat balance in the solid is shown in Fig. IV.10. The heat generation ($\dot{q}_{gen}$) peaked nearly at the front of the reaction zone due to total oxidation. Radiation was altogether negligible, with only a minor net radiative heat transfer in the regions close to the front of the reaction zone. Repeating the computations with channel surfaces having $\varepsilon = 0$ or 1 reproduced essentially the same results. The negligible impact of $\dot{q}_{rad}$, even at steady-state operation where the surface temperatures were the highest, was a direct consequence of the diminished light-off distance that yielded wall temperatures at $t > 6$ s differing by less than 92 K over the extent $0 \leq x \leq 65$ mm (see Fig. IV.3). On the other hand, in fuel-lean applications the more effective blocking of the surface free sites by oxygen [21, Dogwiler et al., 1999; 76, Karagiannidis et al., 2007] could lead to appreciable (> 500 K) temperature differences along the solid wall; therein radiation exchange played an important role by transferring heat from the hotter rear channel surfaces to the colder entry, thus stabilizing combustion [76, Karagiannidis et al., 2007]. Heat conduction ($\dot{q}_{cond}$) was more important at later times when steeper spatial temperature gradients formed at the front of the reaction zone (Fig. IV.10(b,c)). Finally, heat accumulation had a dominant contribution at $t < 3$ s, while convection ($\dot{q}_{conv}$) transferred heat at early times from the gas to the rear channel solid inert section (Fig. IV.10(a)).

The impact of solid properties on the light-off has also been investigated. Increasing or decreasing the solid thermal conductivity by a factor of two did not impact the time required for the onset of ignition. The elapsed times for the rear of the solid wall to heat up by 50 K or 300 K were roughly the same, as they were primarily controlled by chemical reactivity. On the other hand, the total upstream propagation time of the reaction zone decreased with increasing thermal conductivity although not linearly due to the continuing contribution of surface reactivity in the propagation speed (e.g. the total propagation time decreased from ~6 s to ~4.9 s when $\lambda = 32$ W/mK, and increased to ~7.4 s when

Figure IV.9
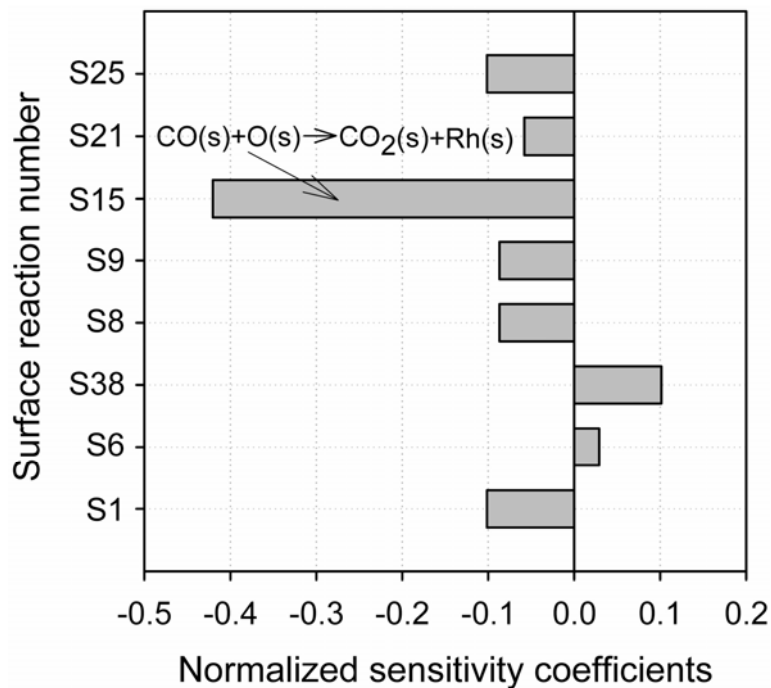
Normalized sensitivity coefficients for the eight more sensitive surface reactions on the ignition delay time (Case 1). The reaction numbering follows Table IV.3.

$\lambda = 8$ W/mK).   In practical systems, where external heat losses may also be present, higher thermal conductivities are desirable. A similar investigation has shown a stronger impact of the solid specific heat (e.g. the total propagation time decreased from ~5.8 s to ~2.2 s when the specific heat decreased from 700 to 350 J/kgK, while it increased to ~12.9 s for a specific

Figure IV.10
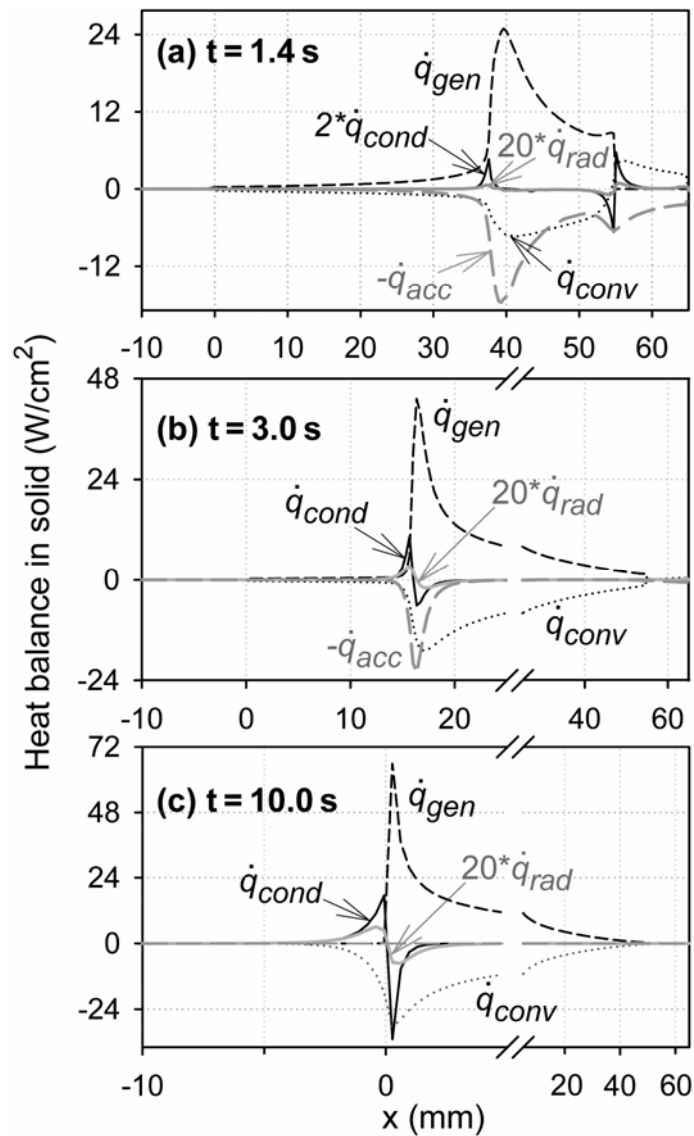
Heat balance in the solid for Case 1 at three times: (a) 1.4 s, (b) 3.0 s and (c) 10.0 s. Surface heat generation ($\dot{q}_{gen}$): dashed black lines; Convection ($\dot{q}_{conv}$): dotted black lines; Conduction ($\dot{q}_{cond}$): solid black lines; Radiation ($\dot{q}_{rad}$): solid gray lines, Negative of heat accumulation (-$\dot{q}_{acc}$): dashed gray lines. For clarity, $\dot{q}_{rad}$ has been expanded by a factor of twenty, whereas $\dot{q}_{cond}$ has been expanded in (a) by a factor of two. The term $\dot{q}_{acc}$ is practically zero in (c).

heat of 1400 J/kgK). Although thermal conductivity and heat capacity were not the only factors considered in the selection of a CPO reactor material, the high thermal conductivity of metals (an order of magnitude larger than that of ceramics) was one of their main advantages.

Figure IV.11
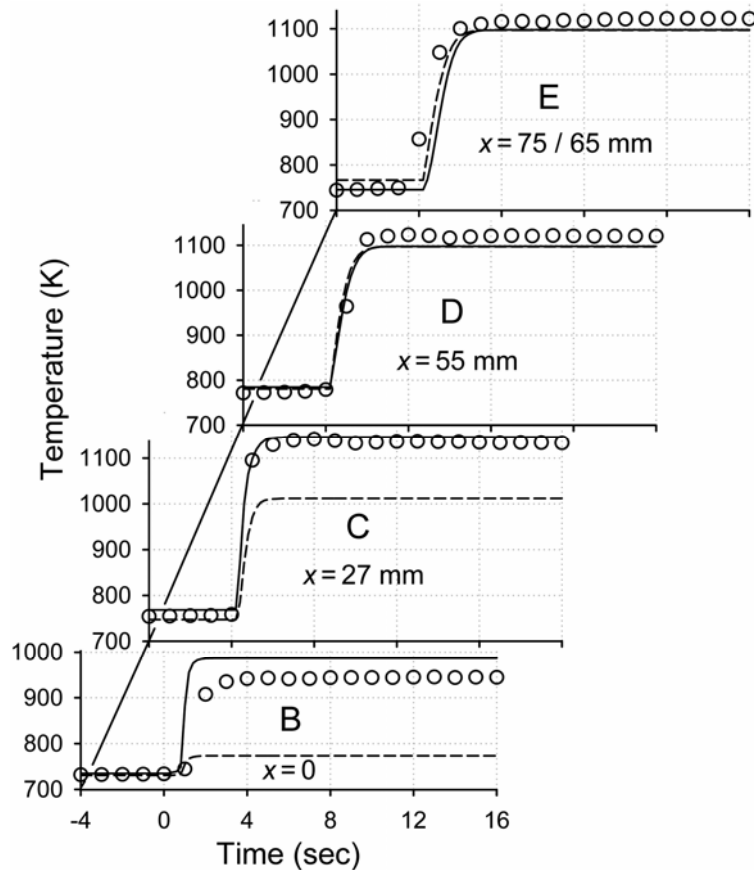
Predicted (lines) and measured (symbols) temperatures at axial positions *B* through *E* for Case 6. Predictions are provided for the wall temperature (solid lines) and mean gas temperature (dashed lines). At position *E*, the measurements refer to the mean gas temperature 10 mm downstream of the reactor exit ($x = 75$ mm), while the predictions refer to the reactor exit ($x = 65$ mm).

IV.4.4 Effect of equivalence ratio and catalyst loading on catalytic ignition

The catalytic ignition for Cases 6 and 10 is presented next, emphasizing mainly on their differences with Case 1. The Rh loading has been halved in Case 6, resulting in increased preheat requirements, with ignition attained at $T_{IN} = 730$ K. The predicted temperatures were, at all four monitoring locations, in good agreement with the measurements in terms of elapsed times for the arrival of the reaction zone and final temperatures (see Fig. IV.11). The overall

duration of the light-off event was, nevertheless, considerably shorter compared to Case 1 (~3 s, see Fig. IV.12). Of interest in Case 6 was the particular mode of reaction zone propagation. Contrary to Case 1, where the reaction front propagated upstream (Fig. IV.3), in Case 6 the reaction zone spread over most of the channel active section ($0 \leq x \leq 55$ mm) shortly after ignition ($t \sim 0.4$ s). At later times the surface temperatures increased over the entire active reactor length, as the heat accumulation in the solid diminished (plots similar to that of Fig. IV.10 revealed that $\dot{q}_{acc}$ became insignificant after 1.3 s). Therefore, light-off was mainly controlled by the surface reactivity and the solid thermal inertia ($\rho_{ZrO2} c_{ZrO2} \delta_c$), with the solid thermal conductivity playing a secondary role. Further simulations indicated that

Figure IV.12
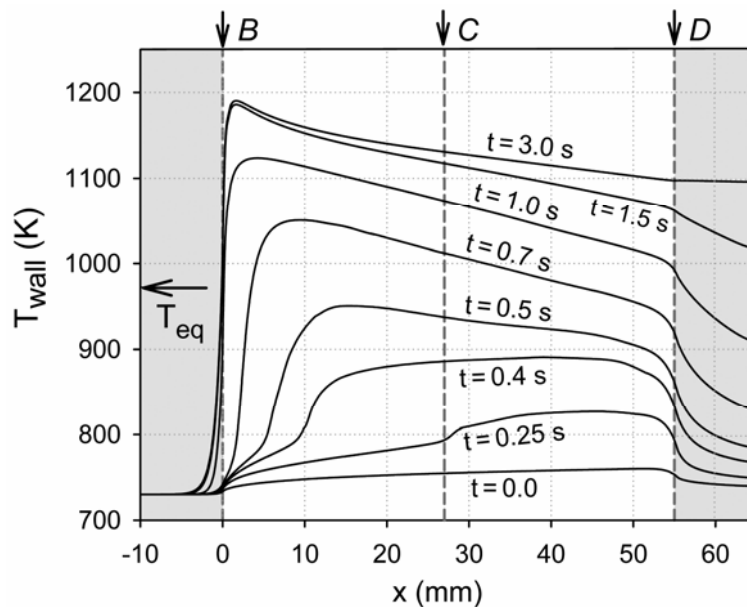
Predicted axial profiles of the wall temperature at different times for Case 6. The shaded areas denote the non-catalytic part of the reactor. The vertical arrows at *B*, *C* and *D* indicate the thermocouple locations inside the reactor, while the horizontal arrow marked T_{eq} denotes the adiabatic equilibrium temperature.

light-off could not be achieved for $T_{IN} \leq 710$ K over an integration period of 5 sec (about threefold longer than the time needed in the experiments to reach the steady wall temperature at $x \approx 0$, see Figs. IV.11 and IV.12); this result was in fair agreement with the measured light-off temperature $T_{IN} = 730$ K. It is finally worth mentioning that the only model parameter needed to capture the effect of catalyst loading was *B* (Eqs. (9), (10)), which was not arbitrarily adjusted but determined experimentally.

Figure IV.13
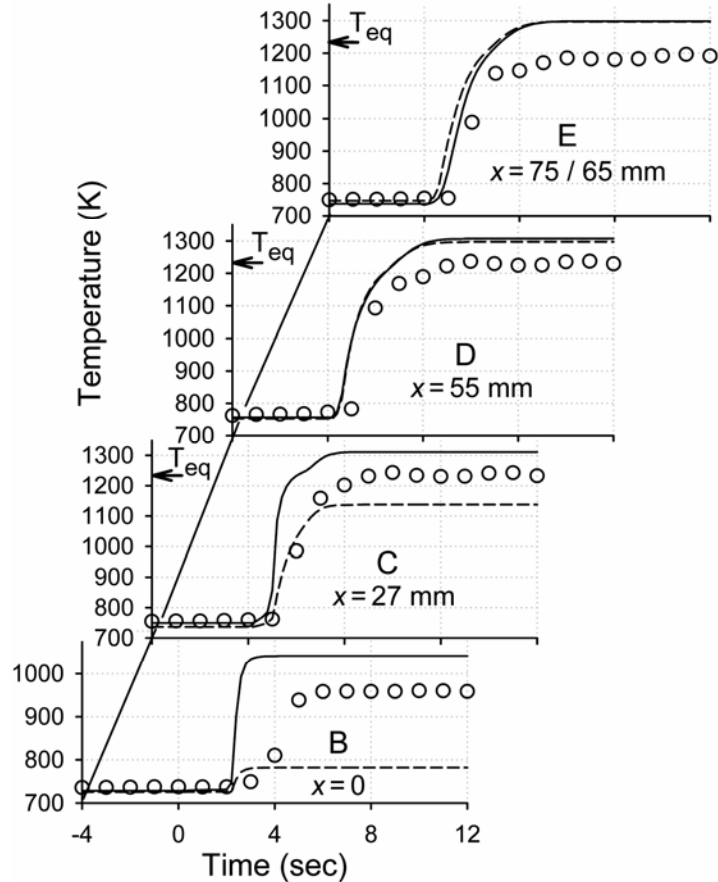
Predicted (lines) and measured (symbols) temperatures at the axial positions *B* through *E* for Case 10. Predictions are provided for the wall temperature (solid lines) and mean gas temperature (dashed lines). The horizontal arrows marked T_{eq} denote the adiabatic equilibrium temperature.

Equivalence ratios of 3.5 to 4.0 were optimal for CPO in chemical industry. In power generation applications, however, the use of even lower fuel-rich stoichiometries may be beneficial. It can be shown that, when using lower φ, the CPO outlet temperatures and compositions yielded an enhanced gas-phase reactivity that, in turn, aided the stability of the follow-up homogeneous combustion zone; details on the gas-phase reactivity of the CPO products are outside the scope of the present work. Figure IV.13 provides comparisons between predicted and measured temperatures versus time for Case 10 ($\varphi = 2.5$). The propagation mode of the reaction zone resembled that of Case 6 (Fig. IV.12) and is not shown herein.

As discussed in the previous section, the larger oxygen content inhibited catalytic ignition and this was evidenced by the higher (compared to Case 1) required inlet temperature ($T_{IN} = 725$ K). The agreement between measurements and predictions in Fig. IV.13 was fair,

however, the elapsed times for reaction zone arrival were underpredicted and the peak temperatures were overpredicted. As further seen by the comparisons of steady state species mass fractions in Fig. IV.14, the catalytic reaction scheme overpredicted (underpredicted) the H_2 (H_2O) levels. Moreover, it underpredicted (overpredicted) to an even greater extent the CO (CO_2) levels, suggesting a stronger surface oxidation of CO to CO_2. Those differences could be attributed to the fact that the surface scheme has been validated for equivalence ratios between 3.5 to 4.0 [1, Schwiedernoch et al., 2003; 63, Schneider et al., 2007] which are

Figure IV.14
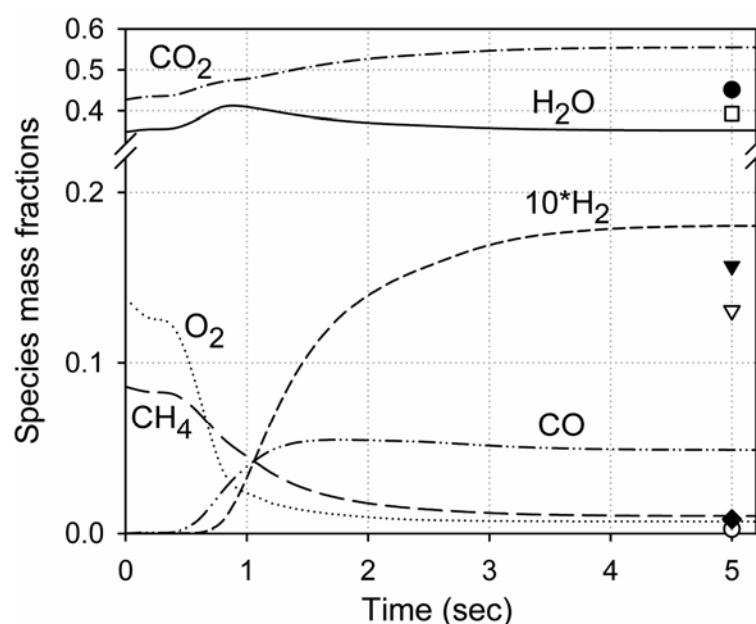
Predicted mean species mass fractions at the reactor outlet ($x = 65$ mm) versus time

for Case 10. The symbols denote the steady state GC measurements

(CO_2: filled circle, H_2O: open square, $10 \times H_2$: filled triangle,

CO: open triangle, CH_4: filled diamond, O_2: open circle).

optimal of chemical synthesis, and extension to lower φ cannot be warranted.

Despite the aforementioned discrepancies between measurements and predictions, the measured H_2 and CO yields were still high due to the elevated surface temperatures (the measured temperatures in Case 10 were up to 1250 K, i.e. ~150 K higher than those of Case 1, see Figs. IV.13 and IV.2). Such high surface temperatures could still be tolerated by the catalyst and the FeCr-alloy structure, suggesting that operation at φ as low as 2.5 could be attractive for gas turbines with EGR. The disadvantage of higher preheat requirements with decreasing φ could be alleviated by increasing the Rh loading, as discussed in the foregoing

comparisons of Cases 1 and 6. It is finally clarified that in CH_4/air CPO without EGR, φ as low as 2.5 could endanger the catalyst/reactor integrity [47, Appel et al., 2005a] due the absence of large heat capacity gases (CO_2, H_2O) that moderate the reactor temperature.

IV.4.5 Catalytic extinction

Following catalytic ignition, vigorous burning states were established in Cases 1 and 6. Subsequently, the inlet temperature was ramped down so as to establish new steady states; at those steady states (typically every $\Delta T_{IN} = 50$ K) detailed exhaust gas analysis was performed. Comparisons between predicted and measured exhaust gas compositions and temperatures for Cases 1 to 5 and Cases 6 to 9 are illustrated in Fig. IV. IV.15(a) and Fig. 15 (b), respectively. Predictions were carried out with a steady-state version of the numerical code [21, Dogwiler et al., 1999; 64, Schneider et al., 2006], whereby the steady solutions at higher inlet temperatures were used as an initial guess to obtain converged solutions at lower inlet temperatures (the lines in Fig. IV.15 were constructed by successive steady computations at steps $\Delta T_{IN} = 10$ K). The complete transient process between measured steady-states at different inlet temperatures was of no interest in the present investigation; moreover, it was computationally prohibitive to carry out transient simulations as the time span between the successive experimental steady states of Fig. IV.15 exceeded 5 min. The temperature measurements in Fig. IV.15 referred to thermocouple E and were continuous, whereas the corresponding predictions referred to the outlet ($x = 65$ mm) mean gas temperature. The accuracy in the measurements of Fig. IV.15 was particularly good: the C/H/O balances were better than 1% and the differences between inlet and outlet total enthalpies corresponded to an equivalent temperature differential of less than 15 K for all examined cases.

The lowest inlet temperature in the experiments was $T_{IN} = 473$ K, for both the 1% Rh (Fig. IV.15(a)) and the 0.5% Rh loading (Fig. 15(b)). At $T_{IN} = 450$ K steady vigorous combustion was also attained, however, water condensation at the colder solid walls of the mixing section prohibited any further reduction of the inlet temperature. For a steam partial pressure of 2.3 bar (Cases 1 through 9), thermodynamics indicated that water should start condensing at 400 K. Therefore, inlet temperatures below ca. 470 K were of no interest in practical CPO systems (e.g. gas turbines) with large EGR. Nonetheless, sustaining stable combustion at inlet temperatures as low as 470 K was of particular importance for part-load and idle turbine operation.

The resilience of CPO against extinction is explained below. When the inlet temperature decreased, there was a shift from partial to total oxidation regarding the H_2/H_2O species; this was manifested by the drop (rise) of the H_2 (H_2O) mass fraction in both experiments and predictions (Fig. IV.15). The predicted H_2 selectivity (Eq. (16)) decreased
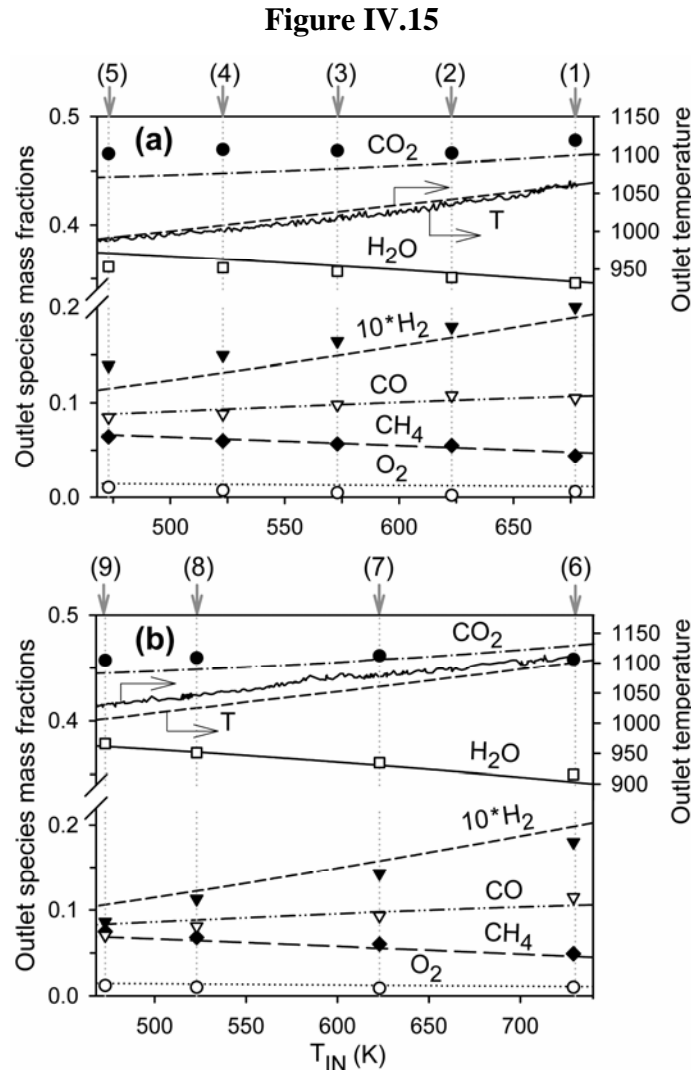
Figure IV.15

Predicted (lines) and measured (symbols) outlet species mass fractions for: (a) Cases 1 to 5 and (b) Cases 6 to 9. The symbol and line notation is the same as in Fig. IV.6. The measured outlet temperature (solid line) at position E and the predicted outlet mean gas temperature (dashed line) are also shown.

substantially from 0.91 at $T_{IN} = 680$ K to 0.70 at $T_{IN} = 473$ K. The CO and CO_2 mass fractions both decreased with decreasing inlet temperature, with the CO selectivity increasing slightly from 0.74 at $T_{IN} = 680$ K to 0.77 at $T_{IN} = 473$ K. Overall, the presence of total oxidation products was more pronounced at lower temperatures (the reason being that reforming reactions were thermodynamically favored at higher temperatures). The increased

importance of the total oxidation pathway with decreasing T_{IN} led, in turn, to higher reactor exothermicity that compensated −to a great extent− for the drop in inlet temperature. For example, the difference in exhaust gas temperatures at $T_{IN} = 473$ and 680 K (Cases 1 and 5 in Fig. IV.15(a)) was only 70 K. Alternately, the computed heat release in Case 1 amounted to 45% of the heat release calculated when considering complete oxidation of methane; the corresponding number for Case 5 was 57%. It is finally noted that the agreement between measurements and predictions in Fig. IV.15 was quite good; the predicted and measured species mass fractions were within 8% (the scarce O_2 was an exception) at $T_{IN} \geq 573$ and within 15% at $T_{IN} \leq 523$. The predicted outlet temperatures were within 12 K (Fig. IV.15(a)) and 25 K (Fig. IV.15(b)) of the measurements. At lower inlet temperatures, the model appeared to slightly overpredict (underpredict) the route to CO (CO_2).
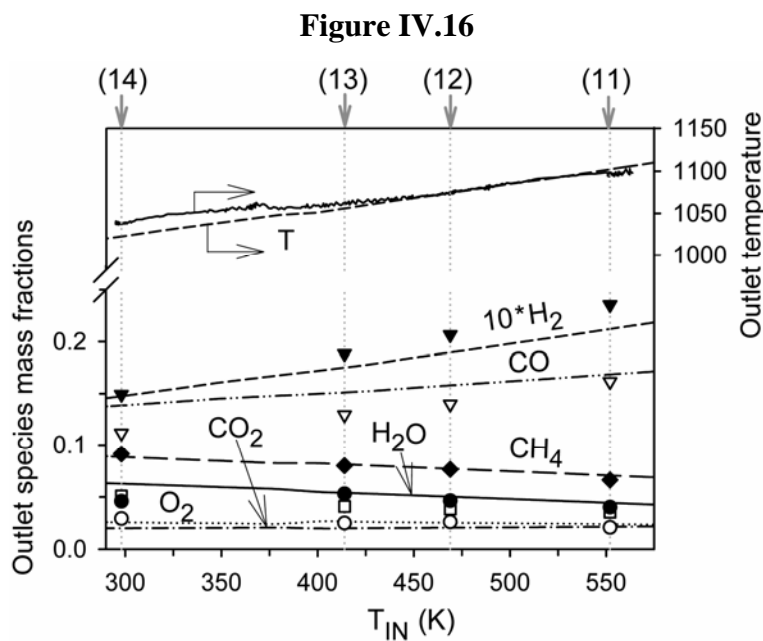
Figure IV.16

Predicted (lines) and measured (symbols) outlet species mass fractions for: (a) Cases 1 to 5 and (b) Cases 6 to 9. The symbol and line notation is the same as in Fig. IV.6. The measured outlet temperature (solid line) at position E and the predicted outlet mean gas temperature (dashed line) are also shown.

Since water condensation prohibited the investigation of potential extinction at inlet temperatures below 473 K, additional experiments were carried out with $CH_4/O_2/N_2$ compositions without EGR (Cases 11 to 14); the O_2/N_2 molar ratio in those experiments was 0.24, close to that of air. The results of Fig. IV.16 indicated that stable and vigorous combustion could be sustained even at room temperature ($T_{IN} = 298$ K). The reason for the resilience against extinction was the same as in the previous EGR-diluted cases: lower inlet

temperatures favored the total over the partial oxidation route. It is worth pointing that recent experiments in a subscale gas-turbine CPO reactor (using various fuels with air) have also attested stable operation at room inlet temperature [80, Smith et al., 2006b].

Figure IV.17
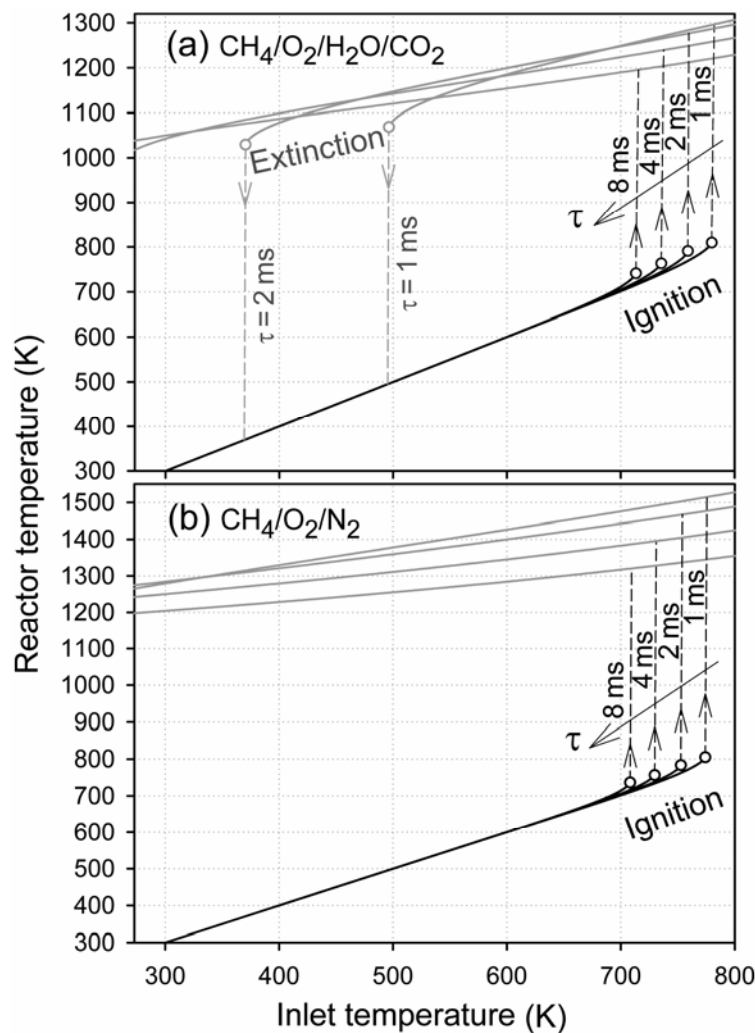
Ignition and extinction in an SPSR with a surface to volume ratio of 33.3 cm^{-1}, pressure 5 bar and various residence times: (a) CH$_4$/O$_2$ mixtures with EGR, having inlet composition as Cases 1 to 9 of Table 1, and (b) CH$_4$/O$_2$/N$_2$ mixtures without EGR, having inlet composition as Cases 11 to 14 of Table 1. The black solid lines indicate the weakly reacting branch and the gray solid lines the vigorous burning branch.

IV.4.6 Ignition-extinction characteristics and chemistry of catalytic extinction

Having established the applicability of the employed heterogeneous reaction mechanism, a rigorous numerical analysis of catalytic ignition-extinction has been carried out using the SPSR model of Eqs. (14) and (15). This analysis allowed for the investigation of residence

times lower than the ~8-10 ms of the employed honeycomb reactor. The plots of Fig. IV.17, obtained by continuation analysis, provided the ignition and extinction characteristics in terms of the stable weakly reacting and vigorous burning branches. The surface-to-volume ratio of the SPSR was 33.3 cm^{-1}and the residence times (τ) ranged from 1 to 8 ms; both CPO with EGR (Fig. IV.17(a)) and CPO without EGR (Fig. IV.17(b)) were investigated. In CPO with EGR (Fig. IV.17(a)), a reduction in residence time led to higher inlet temperature requirements for the attainment of light-off. However, upon ignition, the established vigorous burning states had higher temperatures at shorter residence times. The reason was that shorter residence times favored the exothermic oxidation reactions of methane against the slower endothermic reforming reactions. By reducing the inlet temperature, extinction was obtained only for the $\tau = 1$ and 2 ms cases. For residence times $\tau \geq 4$ ms, vigorous combustion could be sustained down to $T_{IN} = 273$ K (water condensation was not considered herein). Therefore, extinction in CPO with EGR could only be an issue at very short reactor residence times that are not relevant to power generation cycles. For CPO without EGR, combustion could not be extinguished down to $T_{IN} = 273$ K, even at residence times as short as 1 ms (Fig. IV.17(b)). The reactor temperatures were higher than those of CPO with EGR dilution, thus allowing for higher resilience against extinction.

The controlling surface chemistry during extinction in CPO with EGR was finally investigated. The normalized sensitivity coefficients of the most important reactions affecting the SPSR temperature, the methane mass fraction, and the Rh(s) coverage are provided in Fig. 18. The sensitivity analysis of Fig. IV.18 (carried out on the fly during the construction of the continuation plots) pertained to the $\tau = 2$ ms case of Fig. IV.17(a), with expanded details around the extinction temperature $T_e = 370.3$ K (the sensitivity analysis for the 1 ms residence time was qualitatively the same as for the 2 ms case). The key parameter controlling extinction was the CO(s) coverage. The main coverage at high temperatures was Rh(s) and CO(s) (see also Fig. IV.7). By decreasing the reactor temperature, CO(s) increased leading to a catalyst poisoning due to the corresponding reduction of available free sites. All reactions shown in Fig. IV.18 had a direct impact on the CO(s) coverage. Reactions S6 and S36 were the adsorption and desorption of CO; an increase (decrease) of S6 (S36) led to a drop in reactor temperature and Rh(s) coverage (Fig. IV.18(a, c)), and to a rise in methane levels (Fig. IV.18(b)), thus promoting extinction. Reaction S15 depleted CO(s) by surface oxidation to $CO_2(s)$; hence an increase in the rate of S15 stabilized combustion. The adsorption/desorption of CH_4 (S1/S38) and the surface oxidation of $CH_4(s)$ (S25) played also

Figure IV.18
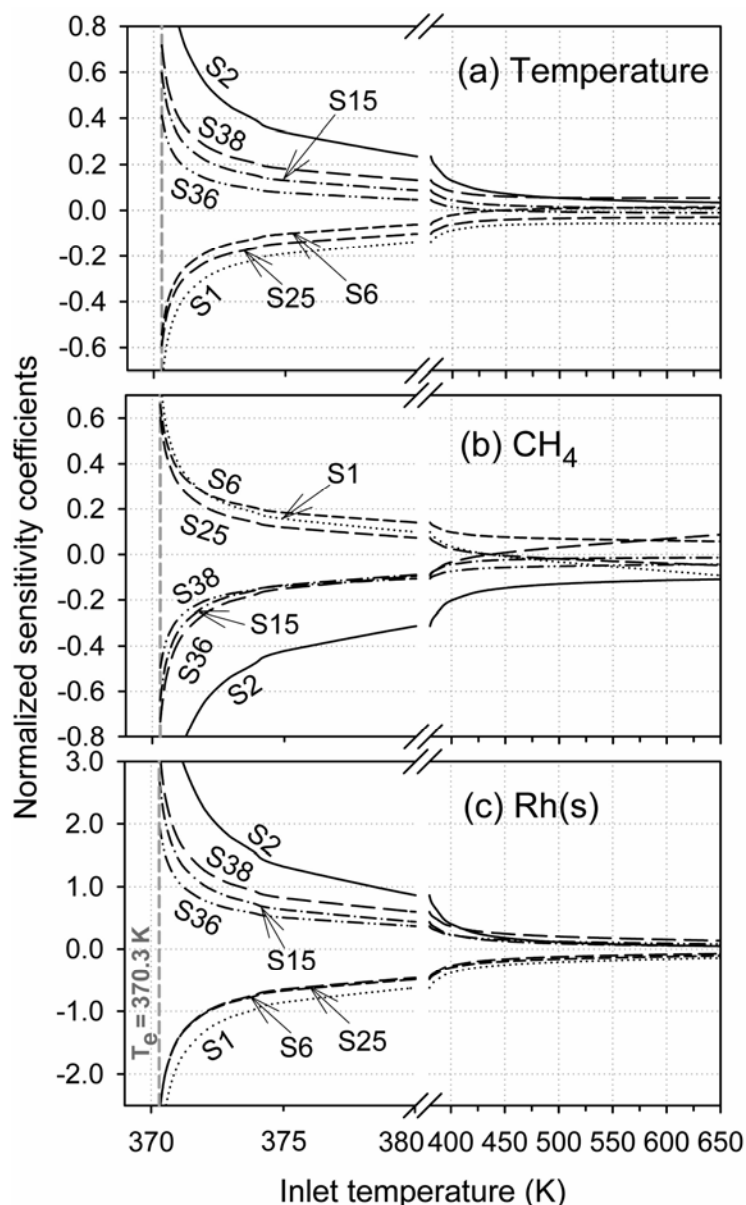
Normalized sensitivity coefficients of the most sensitive reactions on (a) reactor temperature, (b) CH_4 concentration, and (c) Rh(s) surface coverage, versus SPSR inlet temperature. SPSR surface-to-volume ratio S/V = 33.3 cm^{-1}, pressure 5 bar, and residence time τ = 2 ms. The inlet composition is the same as in Cases 1 to 9 of Table IV.1. Details are shown around the extinction point of Fig. IV.17(a) with inlet temperature 370.3 K and residence time 2 ms. The reaction numbering follows Table IV.3.

key roles since they provided the surface carbon needed to build CO(s). A reduction (increase) of the methane adsorption (desorption) extended the extinction limits; for example, a twofold decrease in the sticking coefficient of methane yielded a twofold decrease in CO(s) coverage that in turn provided stable vigorous combustion at inlet temperatures as low as 308 K. Finally, an increase in O_2 adsorption (S2) near extinction extended the combustion

stability limits since it enhanced the free site coverage Rh(s) at the expense of CO(s) by promoting the surface oxidation reaction S15. It is worth pointing that the CO chemistry, which was found important for catalytic extinction, also controlled catalytic ignition (see Fig. IV.9 and related discussion).

IV.5 Conclusions

The ignition and extinction in catalytic partial oxidation (CPO) of CH_4/O_2 mixtures with large EGR (exhaust gas recycle, comprising 46.3% H_2O and 23.1% CO_2 vol.) has been investigated experimentally and numerically at 5 bar. In addition, the extinction in CPO of $CH_4/O_2/N_2$ mixtures was studied at 3 bar. Experiments have been carried out in a Rh-coated short contact time honeycomb catalytic reactor and included thermocouple measurements of the reactor temperature and exhaust gas analysis. Numerical predictions were performed with a 2-D transient elliptic code. The following are the key conclusions of this study.

1) The employed heterogeneous reaction scheme reproduced the measured minimum inlet temperatures required for light-off, the elapsed times for the propagation of the reaction front, and the steady-state exhaust gas compositions in CPO with EGR at a fuel-to-oxygen equivalence ratio $\varphi = 4.0$. At $\varphi = 2.5$, however, only qualitative agreement was obtained and the numerical model overpredicted the synthesis gas yields.

2) The chemical impact of the added H_2O in the feed was already evident at the early stages of the transient catalytic ignition event and its importance further increased as steady state was approached. At steady state, the large H_2O dilution resulted in increased hydrogen selectivity, decreased CO selectivity and slightly increased methane conversion. The chemical impact of CO_2 dilution was minimal on both the transient event and the subsequent steady combustion.

3) Despite the significant chemical impact of H_2O dilution during the light-off process, the ignition delay times themselves were practically unaffected by its presence. The reason was that light-off times were dominated by total oxidation reactions and not by partial oxidation or reforming reactions leading to synthesis gas products. The key reaction affecting catalytic ignition was the surface oxidation of CO to CO_2, which was the main exothermic heat release step in the induction zone. The surface oxidation of H_2 to H_2O, on the other hand, was less significant due to the low amounts of H_2 formed in the induction zone.

4) Measurements and predictions indicated that vigorous combustion could be sustained at inlet temperatures as low as 473 K in CPO with EGR. In CPO without EGR, vigorous combustion was still possible with inlet temperatures as low as 298 K. The reason for the extended stability limits of CPO combustion was the shift from partial to total oxidation products –and hence to higher exothermicity– with decreasing inlet temperature.

5) Computed extinction characteristics obtained at various reactor residence times indicated that extinction in CPO with EGR was possible only at very short times (< 4 ms), which were not relevant to new power generation cycles. On the other hand, in CPO without EGR stable combustion was attained at residence times as short as 1 ms. The key parameter controlling catalytic extinction in CPO was the CO(s) coverage. Near extinction CO(s) increased, reducing the free sites and thus leading to catalyst poisoning.

6) The advantage of reactor materials with high thermal conductivity has been demonstrated for practical CPO systems. Moreover, operation at non-optimal stoichiometries ($\varphi = 2.5$) was shown to be beneficial in CPO with large EGR, due to the moderating effects of dilution on the maximum reactor temperature.

V Experimental and numerical investigation of supported rhodium catalysts for partial oxidation of methane in exhaust gas diluted reaction mixtures

A paper written by Sara Eriksson[a], Adrian Schneider, John Mantzaras, Markus Wolf[b] and Sven Järås[a]; published in Chemical Engineering Science.

[a]*Royal Institute of Technology, Chemical Technology, Teknikringen 42, SE-100 44 Stockholm, Sweden*

[b]*ALSTOM Power Technology Center, Zentralstrasse 40, 5242 Birr, Switzerland*

Abstract

The partial oxidation of methane/oxygen mixtures with large exhaust gas dilution (46.3% vol. H_2O and 23.1% vol. CO_2) has been investigated experimentally and numerically over $Rh/Ce-ZrO_2$, Rh/ZrO_2 and $Rh/\alpha-Al_2O_3$ catalysts. Experiments were carried out in a short-contact time (~8 ms) reactor at 5 bar and included exhaust gas analysis, temperature measurements along the reactor, and catalyst characterization. Additional experiments were performed in an optically accessible channel-flow reactor and involved in situ Raman measurements of major gas-phase species concentrations over the catalyst boundary layer and laser induced fluorescence (LIF) of formaldehyde. A full-elliptic two-dimensional numerical code that included elementary hetero-/homogeneous chemical reaction schemes and relevant heat transfer mechanisms in the solid was used in the simulations. The employed heterogeneous reaction mechanism, including only active Rh sites, reproduced with good accuracy the experiments. The ratio of active to geometrical surface area, deduced from hydrogen chemisorption measurements, was a single parameter needed in the numerical model to account for the effect of different supports. This indicated that water activation occurring on support sites, resulting in inverse OH spillover from the support to the noble metal sites, could be neglected under the present conditions with high water dilution. An evident relationship between noble metal dispersion and catalytic behavior, in terms of methane conversion and synthesis gas yields, could be established. Both measurements and predictions indicated that an increased Rh dispersion (in the order $Rh/Ce-ZrO_2 > Rh/ZrO_2 > Rh/\alpha-Al_2O_3$) resulted in higher methane conversions, lower surface temperatures and higher synthesis gas yields.

V.1 Introduction

The catalytic partial oxidation (CPO) of methane to synthesis gas at millisecond-long reactor residence times has attracted increased interest during the last years [1, Schwiedernoch et al., 2003; 3, Hickman and Schmidt, 1993; 4, Deutschmann and Schmidt, 1998]. Compared to the conventional steam reforming, CPO at short contact times may significantly reduce the costs for synthesis gas production and also provide a H_2/CO ratio favorable for Fischer-Tropsch synthesis. In addition to chemical synthesis, CPO of methane (the main constituent of natural gas) is intensely pursued in gas turbines of power generation systems [9, Griffin et al., 2004; 49, Eriksson et al., 2006; 64, Schneider et al., 2006]. The adopted approach, referred to as "catalytic-rich, gaseous-lean combustion", is a two-stage process. In the first stage, natural gas undergoes fuel-rich catalytic combustion (i.e. CPO) with part of the air stream. Only a fraction of the fuel is converted in the CPO reactor and the products (mainly synthesis gas and unconverted methane) are subsequently mixed with the remaining air to stabilize a follow-up fuel-lean homogeneous (gas-phase) combustion zone. In contrast to fuel-lean catalytic combustion, the lower surface oxygen coverage at fuel-rich conditions facilitates methane activation thus reducing the light-off temperature [36, Veser et al., 1999]. Furthermore, the produced hydrogen aids the stabilization of the post-catalyst flame [9, Griffin et al., 2004].

Lately, new power generation cycles have emerged to meet forthcoming emission regulations. The advanced zero emissions power concept is such an example [81, Griffin et al., 2005], aiming at mitigating both NO_x and CO_2 emissions from power plants. Therein, natural gas is combusted in pure oxygen produced by a mixed-conductive membrane that separates oxygen from air. Large exhaust gas recycle (EGR) is used, such that the reacting fuel/oxygen mixtures are heavily diluted with H_2O and CO_2 (up to 50% and 25% vol. in the feed, respectively). The "catalytic-rich, gaseous-lean combustion" methodology is also of interest for this new power cycle. The absence of nitrogen in the exhaust facilitates CO_2 separation (e.g. via water condensation). Moreover, the large amounts of steam and CO_2 can increase the hydrogen yields via reforming reactions and hence enhance the stability of the post-catalyst homogeneous combustion zone.

Catalysts for partial oxidation of methane mainly consist of supported noble metals (Rh, Ru, Pd, Pt, Ir) and supported Ni [82, York et al., 2003; 83, Tsang et al., 1995]. Nickel-based catalysts are attractive due to their high activity and relatively low cost. However, carbon deposition resulting in catalyst deactivation occurs under conditions where

synthesis gas is produced. Supported Rh catalysts exhibit high activity, synthesis gas selectivity and resistance to carbon deposition, and are thus of particular interest for CPO. The direct reaction route for the formation of synthesis gas has been reported to prevail at high temperatures and short residence times in certain noble metal catalysts [3, Hickman and Schmidt, 1993; 84, Mallens et al., 1997; 85, Heitnes-Hofstad et al., 1998]. A large number of studies supporting the indirect route (combustion followed by reforming) can also be found in the literature [31, Bruno et al., 2005; 86, Vermeiren et al., 1992; 87, Buyevskaya et al., 1994; 88, van Looij et al., 1998].

To advance the understanding of partial oxidation under turbine-relevant conditions, [63, Schneider et al., 2007] investigated the hetero-/homogeneous kinetics in CPO of methane with large EGR at pressures of 4 to 10 bar. Experiments were carried out in an optically accessible channel-flow reactor coated with Rh/ZrO_2 and included *in situ* spontaneous Raman measurements of all major gas-phase species concentrations, and laser induced fluorescence (LIF) of the trace formaldehyde. The steady performance of a subscale gas turbine honeycomb reactor, also coated with Rh/ZrO_2, and the chemical impact of large H_2O and CO_2 dilution on the synthesis gas yields and selectivities were further addressed in [64, Schneider et al., 2006] using the validated kinetic schemes from [63, Schneider et al., 2007].

The impact of different Rh-based catalyst supports in CPO of methane with large EGR has been investigated experimentally in [49, Eriksson et al., 2006]. In general, the main function of the support material is to disperse the active metal particles and prevent sintering. However, support properties such as reducibility, acidity and oxygen transport capacity may influence the activity and stability of certain catalysts. For example, an improved stability of supported Pt catalysts for partial oxidation of methane could be obtained when using a highly reducible support material, i.e. $Ce_xZr_{1-x}O_2$ [89, Passos et al., 2005]. This feature is attributed to the increased noble metal dispersion as well as to enhanced carbon removal, which is related to the high oxygen transport capacity of the support. Somewhat different results have been reported for supported Rh catalysts, when studying the effect of support reducibility on the CPO activity [40, Wang and Ruckenstein, 2000]; irreducible support materials resulted in improved catalytic activity. However, the Rh dispersion was significantly lower on the reducible supports. Furthermore, FTIR spectroscopic studies [90, Weng et al., 2003] suggested that the reaction mechanism for partial oxidation of methane can vary for different support materials: the direct formation pathway for synthesis gas is favored over Rh/SiO_2, whereas the combustion-reforming pathway prevails over $Rh/\gamma-Al_2O_3$.

The development of reliable CPO models that are applicable over different catalyst supports is of prime interest for reactor design and process optimization. Detailed heterogeneous reaction schemes for CPO of methane over Rh and Pt have been developed over the last years [1, Schwiedernoch et al., 2003; 3, Hickman and Schmidt, 1993; 29, Aghalayam et al., 2003]. The aptness of the latter mechanism in CPO of methane with large EGR under high pressures and over Rh/ZrO_2 catalysts was demonstrated in [63, Schneider et al., 2007]. The present study undertakes a combined experimental and numerical investigation of methane partial oxidation over three supported Rh catalysts (Ce-ZrO_2, ZrO_2 and α-Al_2O_3). Experiments were performed at 5 bar in a subscale gas-turbine catalytic reactor fed with $CH_4/O_2/H_2O/CO_2$ mixtures and involved exhaust gas analysis, reactor temperature measurements, and physicochemical characterization of the catalysts (BET/chemisorption and Raman microscopy). Additional experiments were carried out in an optically-accessible channel-flow reactor, and included *in situ* spontaneous Raman measurements of major gas-phase species and LIF of formaldehyde. The experiments were complemented with detailed simulations using a 2-D full elliptic numerical code for both the gas and solid phases. The main objective was to identify the key parameter(s) needed to successfully model CPO of methane with large EGR over Rh catalysts with different supports. Particular objectives were to carry out a comparative study between the different supports and to address issues of CPO process optimization.

V.2 Experimental

High-pressure experiments have been carried out in two different reactor configurations: a short contact time honeycomb reactor and an optically accessible channel-flow reactor. The former tests allowed for the investigation of the CPO processes under gas-turbine-relevant conditions and reactor geometries; the latter allowed, with the aid of in situ measurements, for the detailed investigation of the underlying heterogeneous processes.

V.2.1 Honeycomb reactor

The short contact time honeycomb catalytic reactor constituted a subscale unit of a prototype burner developed for large gas turbines of power generation systems [9, Griffin et al., 2004] and formed a liner inside a high-pressure tank (Fig. V.1(a)). The same subscale reactor geometry has also been used in earlier CH_4/air catalytic combustion studies, which included complete oxidation over Pd [45, Carroni et al., 2003] and partial oxidation over Rh/ZrO_2 [64,

Schneider et al., 2006]. It comprised a 35 mm inner-diameter and 1.5 mm thick steel tube, wherein alternating flat and corrugated 50-µm-thick FeCr-alloy foils created a honeycomb structure with individual channel hydraulic diameters of $d_h = 1.2$ mm. The reactor had a total length $L = 75$ mm and was mounted inside a well-insulated (with a 30-mm-thick fiber ceramic) cylindrical steel frame. Only the central reactor extent ($L_c = 55$ mm) was coated with a catalyst, while both end-sections with corresponding lengths $L_u = 10$ mm were catalytically inactive (see Fig. V.1(a)).

Figure V.1
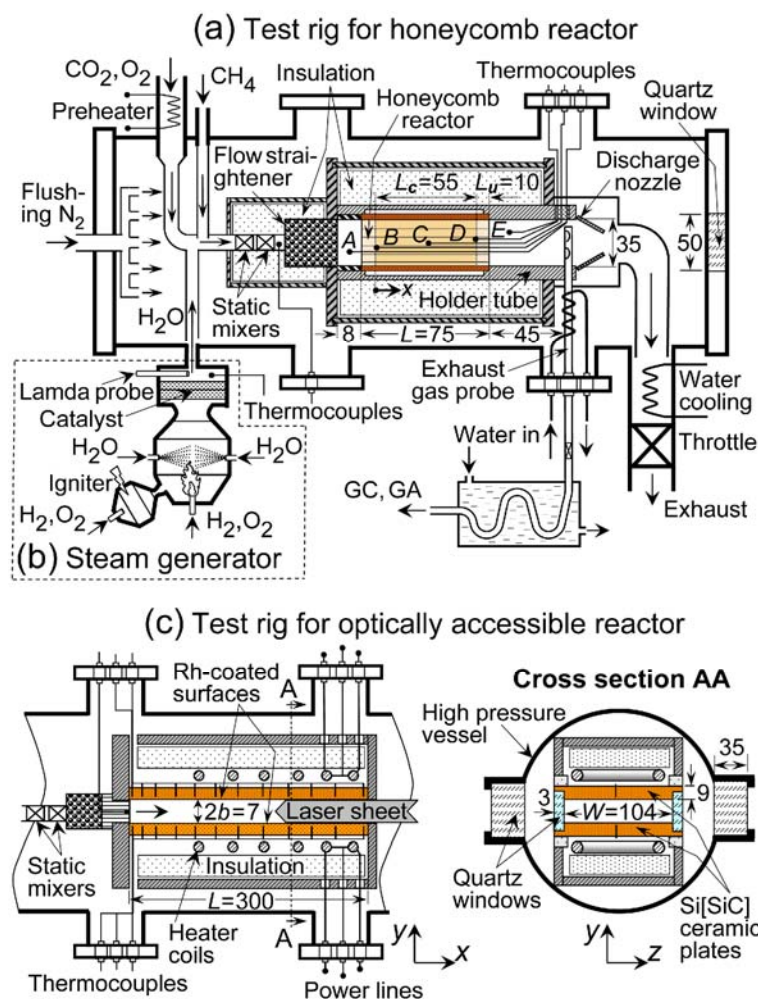
Schematics of the: (a) honeycomb catalytic reactor test rig, (b) steam generator, and (c) optically accessible channel-flow catalytic reactor test rig. All distances are in mm.

The inlet, outlet and reactor temperatures were monitored with five 50-µm-thick K-type (Ni/Cr-Ni/Al) sheathed thermocouples. The thermocouple beads were positioned at $x = -15$, 0, 27, 55 mm and 75 mm ($x = 0$ denotes the beginning of the catalytically active section). The

carrying wires of the four thermocouples A to D (Fig. V.1(a)) were driven counterflow into the reactor through four honeycomb channels. The three thermocouples inside the honeycomb structure (B, C and D) provided neither the true surface temperature nor the mean gas temperature but rather a weighted average, which was only indicative of the local temperature. Of the two measured true local gas temperatures (A, E), radiation corrections (amounting up to 8 K) have been applied to the inlet thermocouple (A) that had a direct view to the hot catalyst entry; no such corrections were required for the outlet thermocouple (E) due to the small difference between the exit gas and rear reactor wall temperature (~20°C). The absolute accuracy of the gas temperature measurements was ±10 K for the hot outlet and ±6 K for the inlet.

A dedicated steam-generator supplied superheated steam (Fig. V.1(b)). The device comprised a H_2/O_2 preburner that further ignited a main H_2/O_2 burner, the latter being operated slightly fuel-lean through the feedback control of a lambda probe. The combustion heat was in turn used to vaporize accurately-measured amounts of demineralized liquid water. A Ni/Pd catalyst positioned downstream the main burner served as a safety backup to convert any escaping hydrogen and to assure high degree of steam purity. Details of the steam generator have been provided in [64, Schneider et al., 2006].

High-pressure bottles supplied CO_2, O_2, and technical-grade CH_4 (> 99.5%). Three Brooks mass-flow controllers regulated the flows of those gases, leading to equivalence ratio accuracies better than ±0.5%. The CO_2 and O_2 flows were preheated by a 3 kW resistive heater and then mixed with superheated steam and room-temperature methane (see Fig. V.1(a)) in two sequential static mixers (Sulzer SMV). A follow-up 40-mm-long packing of 2-mm-diameter ceramic spheres straightened the flow. A K-type thermocouple positioned downstream of the static mixers monitored the gas temperature, which was then used to control the level of CO_2/O_2 preheat and the degree of steam superheat. The honeycomb was affixed 8 mm downstream of the flow straightener, and was mounted inside a 2.5 mm thick and 35 mm internal diameter holder steel tube. To further minimize heat losses, only the first and last 2 mm of the honeycomb contacted the holder tube, while in the remaining length a 1-mm-thick annular air-cushion was available. Finally, a discharge nozzle at the end of the holder tube directed the flue gases first to an exhaust pipe and then to a water-cooled outlet of the high pressure tank.

The high pressure tank that housed the reactor was a stainless-steel cylindrical structure with a length of 1.8 m and an internal diameter of 0.28 m. For safety reasons the flue gases were diluted with flushing nitrogen, which flowed continuously in the free volume between the high pressure tank and the reactor. Visual inspection of the reactor assembly was achieved via a quartz window at the rear flange of the tank (Fig. V.1(a)) and two 350 mm long quartz windows at the tank sides (discussed within the context of the optically accessible reactor in Fig. V.1(c) and also in Section V.2.3). The gas sampling probe with its associated water cooling lines (see Section V.2.2) and the thermocouple wires were driven inside the tank through high-pressure fittings mounted on four dedicated flanges.

V.2.2 Gas analysis

The exhaust gas was sampled with a water-cooled, silica-coated steel probe positioned 45 mm downstream of the honeycomb (Fig. V.1(a)). The steam of the sampled gas was condensed in a water-cooled serpentine heat exchanger outside the high pressure tank. The dried gases entered a rack of gas analyzers (GA) and the sample port of a gas chromatograph (GC). Removal of the large steam content was necessary for the proper operation of both analysis instruments. Nonetheless, the compositions of the actual wet gas products could still be determined by calculating the element balances.

The Hartmann and Braun gas analyzers Uras-10E for CO (NDIR), Magnos-6G for O_2 (paramagnetic) and Caldos-5G for H_2 (thermal-conductivity-based) were used in a continuous analysis mode. The accuracy of the GA measurements has been determined with calibration gas mixtures and was particularly good for CO (0.3% relative error for 10-14% vol. CO in the dry gas); the accuracy of O_2 was still good despite its associated low levels (20% relative error for ~1% vol. O_2). The presence of gases with thermal conductivities considerably different than that of the reference nitrogen (e.g. CH_4 and CO_2) resulted in larger inaccuracies for hydrogen (20% relative error for typical ~30% vol. H_2 in the dry gas); this effect was partly compensated by calibrating the device with simulated exhaust gas compositions. In parallel to the GA measurements, more detailed analysis was carried out in an HP-6890++ GC equipped with porous polymer and molecular sieve columns and a thermal conductivity sensor. The porous polymer column separated CO_2 before the gas entered the molecular sieve. Helium was the carrier gas, while the analysis was discontinuous with one measurement every 8 min. The GC has been tested against a selection of different calibration gas mixtures. Even though the hydrogen signals were weak due to the choice of helium as

carrier gas, for the substantial amounts of the present work (~30% vol. H_2) the accuracy was good (~4% relative error for H_2). The relative error in the GC measurements was 4-5% for CH_4, CO_2 and CO, increasing up to 50% for the scarce O_2. In the forthcoming sections only the GC measurements will be presented; the GA data have provided an additional (and successful) control mainly for the GC-measured CO and O_2 compositions.

V.2.3 Optically accessible reactor

An optically accessible channel-flow reactor was also employed to facilitate *in situ* laser-based measurements of gas-phase species over the catalyst boundary layer. The application of such techniques in catalytic systems has advanced in recent years [14, Reinke et al., 2005; 15, Reinke et al., 2004; 54, Appel et al., 2002]. Those studies demonstrated that the measurements of major species concentrations with spontaneous Raman and of trace species with LIF could provide a direct way for the assessment of the underlying heterogeneous and homogeneous processes, respectively. Using the aforementioned methodology, heterogeneous and homogeneous reaction schemes for the total oxidation [14, Reinke et al., 2005; 15, Reinke et al., 2004; 91, Reinke et al., 2005a; 92, Dogwiler et al., 1998] and partial oxidation [47, Appel et al., 2005a; 63, Schneider et al., 2007] of CH_4 over polycrystalline Pt and Rh/ZrO_2, respectively, have been validated and/or refined at industrially-relevant conditions (pressures up to 16 bar).

The channel-flow reactor (Fig. V.1(c)) was mounted inside the same high-pressure vessel used for the honeycomb reactor. The reactor comprised two non-porous Si[SiC] ceramic plates (300 mm long, 104 mm wide, 9 mm thick, placed 7 mm apart) and two 3-mm-thick quartz windows. Catalyst has been applied onto the inner Si[SiC] surfaces according to the procedure described in Section V.2.5. The surface temperatures were monitored by S-type (Pt-10%Rh/Pt) thermocouples (twelve for each plate) arranged along the *x-y* symmetry plane and embedded 0.9 mm beneath the catalyst through 8.1-mm-deep holes eroded from the outer inactive Si[SiC] surfaces. Optical access from both reactor sides was facilitated by two 350-mm-long and 35-mm-thick quartz windows positioned on the high-pressure tank (Fig. V.1(c)). Streamwise optical access was also possible with two additional quartz windows, one at the rear flange of the tank (Fig. V.1 (a)) and the other at the reactor exit. Two resistive coils positioned 2 cm away from the outer surfaces of the Si[SiC] plates provided external heat, which was necessary to sustain combustion given the large plate thermal inertia and the increased heat losses to the reactor frame. The infrastructure for the gas and steam supply was the same as in the honeycomb reactor experiments of

Section V.2.1. Details of the optically accessible reactor have been provided elsewhere [15, Reinke et al., 2004; 47, Appel et al., 2005a].

V.2.4 Laser diagnostics

The Raman/LIF set-up is depicted in Fig. V.2. The 532 nm radiation of a frequency-doubled Nd:YAG pulsed laser (Quantel YG981E20-CL, 380 mJ pulse energy, 12 ns pulse) was directed to the Raman or to the LIF set-up. In the Raman experiments, the 532 nm beam was temporally stretched to 34 ns and then focused through the tank and reactor side-windows into a vertical line (~0.3 mm thick) by an $f_1 = 150$ mm cylindrical lens. The focal line spanned the 7-mm transverse gap and was laterally offset ($z = 15$ mm) to increase the light collection angle and minimize thermal beam steering. Two $f_2 = 300$ mm spherical lenses focused the scattered light to the entrance slit of a 25 cm imaging spectrograph (Chromex-250i). The dispersed light was recorded on an intensified CCD camera (Princeton Instruments MAX-1024HQ, 1024x254 pixels). To increase the spatial resolution, only the upper channel half-height (3.5 mm) was recorded on 200 pixels, which were further binned down to 84 pixels. The spectral dispersion extended up to 4500 cm^{-1}, allowing observation of all major species. The measurement accuracy was ±3% for species compositions ≥ 10% vol. and ±10% for compositions as low as 0.5% vol.; concentrations less than 0.5% vol. entailed larger measurement uncertainties. Measurements were acquired at $14 \text{ mm} \leq x \leq 168 \text{ mm}$ by traversing axially an optical table that supported both sending and collecting optics (Fig. V.2). Raman data closer than 0.3 mm to the wall were discarded due to low signal-to-noise ratios.

To assess gas-phase combustion, formaldehyde LIF has been applied. The 532 nm radiation pumped a tunable dye laser (Quantel TDL90 NBP2UVT3, pyridine-1 dye) and its frequency-doubled radiation at 352 nm was transformed into a slightly diverging laser sheet (propagating counterflow along the x-y symmetry plane) by a telescopic system (Fig. V.2). The broadband fluorescence was collected at 90° with an intensified CCD camera (LaVision-IRO with 1392x1024 pixels, recorded with a binning of 2x2). The collection optics included achromatic lenses and filters that provided spectral detection between 410 and 480 nm. Zones of 100x7 mm^2 were recorded on a 696x44 pixel section, and the camera was traversed axially to map the entire reactor extent. Homogeneous combustion is outside the scope of this work (for details see [63, Schneider et al., 2007]), since in the foregoing short contact time honeycomb experiments gas-phase chemistry played a minimal role. The purpose of the LIF data in the present study was to delineate the extent of the channel-flow reactor that was unaffected by gas-phase chemistry and was thus suitable to study the pure

catalytic processes using the Raman technique. The Raman and LIF measuring techniques have been elaborated in [14, Reinke et al., 2005; 63, Schneider et al., 2007].

Figure V.2
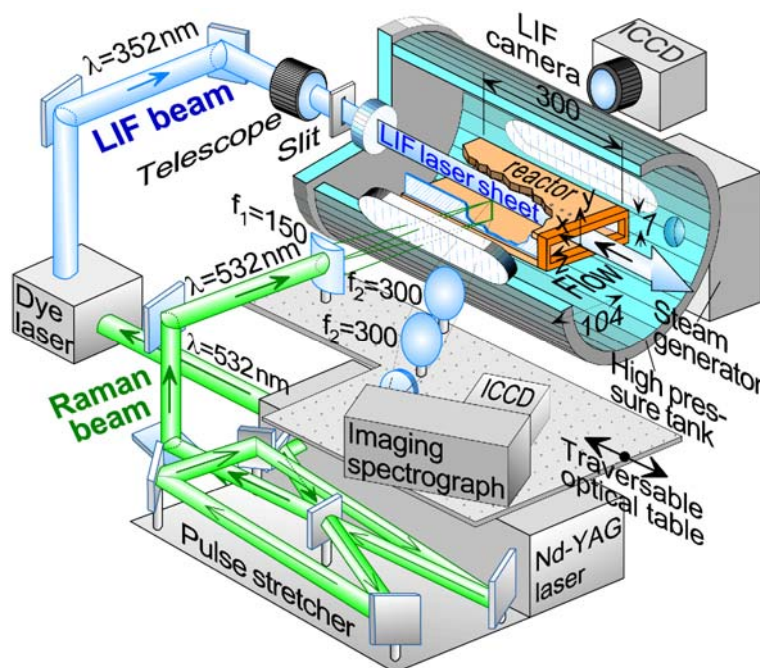
Schematic of the Raman/LIF set-up in the optically accessible channel-flow reactor. All focal lengths are in mm.

V.2.5 Catalyst preparation and characterization

Three support materials were investigated in the honeycomb reactor, Ce-ZrO$_2$ (17.5 wt% CeO$_2$), ZrO$_2$, and α-Al$_2$O$_3$; the first two were also tested in the channel-flow reactor. The supports had previously been calcined at 1373 K for 10 h (Al$_2$O$_3$) or 1073 K for 5 h (Ce-ZrO$_2$ and ZrO$_2$). The catalysts, containing 1 %wt. Rh, were prepared by incipient wetness impregnation using aqueous solutions of Rh(NO$_3$)$_3$. The impregnated supports were dried at 383 K, followed by calcination at 873 K for 5 h. A slurry, obtained by ball-milling the catalyst powder in a solvent mixture for 24 h, was sprayed on the FeCr-alloy foils of the honeycomb reactor and on the Si[SiC] plates of the channel-flow reactor; the coated structures were further calcined at 873 K for 1 h. The resulting catalyst layer had a thickness (δ_c) of 4.6 μm. Before a combustion run in either reactor configuration, the catalyst was reduced in a heated (673 K) H$_2$/N$_2$ flow for 15 min.

The total and active areas of the catalysts were measured with BET (N$_2$-physisorption) and H$_2$-chemisorption. The total surface area of fresh catalyst powder samples was

determined by nitrogen adsorption at liquid nitrogen temperature using a Micromeritics ASAP 2010 instrument. All samples were degassed at 523 K prior to analysis. The surface area was calculated according to the method of Brunauer, Emmett and Teller (BET). Hydrogen chemisorption analysis was performed on a Quantachrome Autosorb-1C to determine the noble metal dispersion of the tested catalyst samples. The samples were reduced in H_2 (50 ml/min) at 673 K for 1 h followed by evacuation (673 K for 1 h) prior to the analysis. The adsorption measurements were performed at 195 K using hydrogen and considering a H_2:Rh stoichiometry of 1:2. The adsorption temperature of 195 K was selected in order to suppress spill-over of hydrogen to the support, which has been reported to occur for ceria-containing support materials under certain conditions [93, Gatica et al., 2000]. In this respect, the present approach is an improvement to the earlier CO chemisorption analyses [64, Schneider et al., 2006]. The metal dispersion was calculated according to the dual isotherm method, i.e. after determining the first isotherm, the sample was evacuated and a second isotherm was obtained. The second isotherm represents only physisorbed H2. Thus, the difference between the two isotherms corresponds to the amount of chemisorbed hydrogen. The surface properties of the catalysts are summarized in Table V.1.

Table V.1

Textural properties of the employed catalysts[a]

Catalyst	BET surface area (m^2/g)	Active area $(m^2$ Rh/g Rh)	Rh dispersion (%)	B[b]
Rh/Ce-ZrO$_2$	44	43	11.8	10.0
Rh/ZrO$_2$	21	24	6.4	5.6
Rh/α-Al$_2$O$_3$	6	18	4.9	4.2

[a]The BET surface area was measured on fresh powder samples whereas the active area refers to tested samples.

[b]Ratio of catalytically active to geometrical surface area.

The crystal structure of the support materials was investigated with a confocal Raman microscope (Labram, DILOR) equipped with a 100 × magnification objective (laser spot size 0.1 μm) and a thermoelectrically cooled CCD detector (1152×300 pixels). The Raman spectra were obtained in a backscatter mode with the 632.8 nm line of a He-Ne laser that

yielded a power of ~4 mW at the sample surface. Raman spectra were recorded in the range from 100 to 1100 cm^{-1} using an 1800 grooves/mm grating. The lateral resolution of the Raman microscope was about 2 μm.

The measured active surface area was also a parameter needed in the numerical model (see Section V.3). Although hydrogen chemisorption tests have been carried out only on powders recovered from tested FeCr-alloy foils (testing on the large-sized coated Si[SiC] plates required their mechanical destruction), the active area of the Si[SiC] plates was considered equal to that of the FeCr foils. This was a good approximation given the non-porous nature of both FeCr and Si[SiC] surfaces; moreover, this was also supported by BET/chemisorption tests of fragmented Pt-coated Si[SiC] plates in earlier total oxidation studies [14, Reinke et al., 2005].

V.3 Numerical

A steady, two-dimensional, full elliptic laminar numerical code was used that included detailed hetero-/homogeneous chemistry and transport, as well as heat transfer mechanisms in the solid. A single-channel model has been considered for the honeycomb reactor, which was an adequate approach given the good thermal insulation and the uniform inlet properties at the entry face of the reactor (as further clarified in Section V.3.1). Each channel was modeled as an equivalent cylindrical tube with a radius $r_h = 0.6$ mm. The gas-phase governing equations have been solved in their cylindrical coordinates; those equations have been provided elsewhere [21, Dogwiler et al., 1999; 45, Carroni et al., 2003] and are not repeated here. The same numerical code was also used to simulate the channel-flow experiments; therein, Cartesian coordinates were used (see [14, Reinke et al., 2005; 54, Appel et al., 2002]) to model the reactive flow along the x-y plane of symmetry (Lx$2b$ in Fig. V.1(c)). The species diffusion velocities $\vec{V}_k$ were calculated in both reactor models using mixture-average plus thermal diffusion for the light species [51, Kee et al., 1996a]:

$$\vec{V}_k = -(D_{km} / Y_k)\nabla Y_k + (D_k^T / \rho Y_k T)\,\nabla T\,, \quad k = 1,.., K_g. \tag{1}$$

The surface species coverage equations were:

$$\frac{\partial \theta_m}{\partial t} = \sigma_m \frac{\dot{s}_m}{\Gamma}\,, \quad m = 1,.., M_s. \tag{2}$$

The left-hand side of Eqs. (2) was not a true transient term and its inclusion merely facilitated convergence to steady state. The boundary conditions and the treatment of the solid are presented separately for each reactor model in the next section.

V.3.1 Honeycomb channel

For the solid substrate of a representative honeycomb channel (solid thickness $\delta/2 + \delta_c = 29.6$ μm), a 2-D model has been used as in [64, Schneider et al., 2006] (see also Fig. V.3). Solution was obtained for the steady solid heat conduction equation:

$$\lambda_s(r)\frac{\partial^2 T_W}{\partial x^2} + \frac{1}{r}\frac{\partial}{\partial r}\left[r\lambda_s(r)\frac{\partial T_W}{\partial r}\right] = 0, \tag{3}$$

with $\lambda_s(r) = 0.4$ Wm^{-1}K^{-1} for $r_h < r \leq r_h + \delta_c$ (ZrO$_2$ porous washcoat) and $\lambda_s(r) = 16$ Wm^{-1}K^{-1} for $r_h + \delta_c < r < r_h + \delta_c + \delta/2$ (FeCr-alloy). The interfacial energy boundary condition of a representative honeycomb channel ($r = r_h$) was:

$$\dot{q}_{\text{rad}} - (\lambda_g\,\partial T_W/\partial r)_{r=r_{h-}} + (\lambda_s\,\partial T_W/\partial r)_{r=r_{h+}} + B\sum_{k=1}^{K_g}\left(\dot{s}_k h_k W_k\right)_{r=r_h} = 0. \tag{4}$$

The term $\dot{q}_{\text{rad}}$ accounted for the radiation exchange of each differential cylindrical surface element with all other differential surface elements as well as with the channel entry and outlet. The net radiation method for diffuse-gray areas [94, Siegel and Howell, 1981] was used to computed $\dot{q}_{\text{rad}}$ for each element. A surface emissivity $\varepsilon = 0.6$ was used for all coated differential surface elements, while the inlet and outlet sections were treated as black bodies ($\varepsilon = 1.0$). Finally, the radiation exchange temperatures for the entry and outlet sections were considered equal to the corresponding mean gas temperatures.

Figure V.3
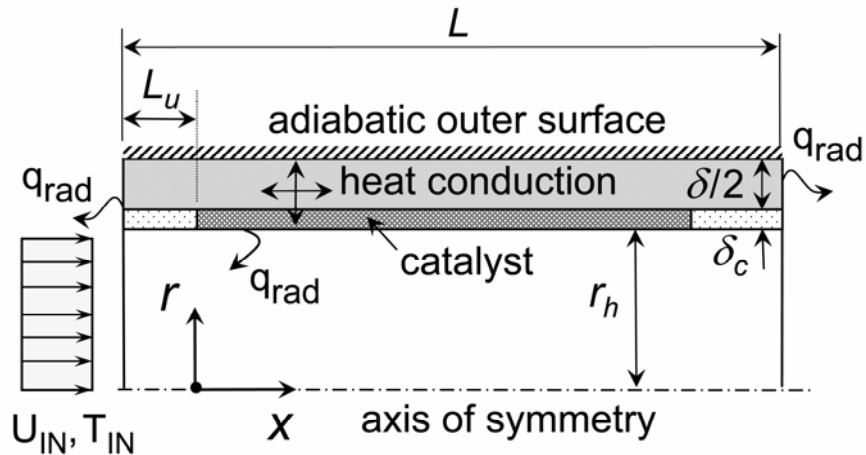
Schematic of the channel configuration used in the numerical simulations.

The gas-phase species interfacial boundary conditions were:

$$(\rho Y_k V_{k,r})_{r=r_{h-}} + B W_k \dot{s}_k = 0, \qquad k = 1,.., K_g, \qquad (5)$$

with $\dot{s}_k = 0$ over the inactive channel length. The factor B denoted the ratio of the active to the geometrical surface area and was determined by the chemisorption measurements. Those tests revealed the active area for the used catalysts; with known size, weight, and noble metal content of the analyzed samples, the active area could provide the factor B (shown in Table V.1). Intraphase species diffusion was not considered because the catalyst layer was only 4.6 μm thick and was applied on non-porous FeCr-alloy and Si[SiC] surfaces. Radiative boundary conditions were applied at the reactor inlet and outlet faces:

$$\lambda_s(r) \partial T_W / \partial x = \varepsilon \sigma \left[T_W^4(x) - T_{IN}^4 \right] \qquad \text{at } x = -L_u, \ r_h < r \le r_h + \delta_c + \delta/2$$

$$-\lambda_s(r) \partial T_W / \partial x = \varepsilon \sigma \left[T_W^4(x) - T_{rad,OUT}^4 \right] \text{ at } x = L_c + L_u, \ r_h < r \le r_h + \delta_c + \delta/2. \qquad (6)$$

The radiation exchange temperature $T_{rad,OUT}$ was taken 15 K lower than the mean gas outlet temperature, considering the somewhat colder support tube enclosure. Nonetheless, it will be shown that radiation effects were altogether minimal (Section V.4.2). Finally, the outer channel wall surfaces were treated as adiabatic ($\partial T_W / \partial r = 0$ at $r = r_h + \delta_c + \delta/2$), to account for the adjacent honeycomb channels.

Uniform profiles for the axial velocity, the species mass fractions and the temperature were specified at the inlet. The 8 mm gap between the flow straightener and the honeycomb entry face created only a very thin boundary layer (less than 0.4 mm since the Reynolds numbers in the 35 mm diameter holder tube exceeded 15000), hence justifying the consideration of a representative constant inlet velocity for all channels. Moreover, the assumption of reactor adiabaticity was affirmed by comparing the measured inlet and outlet total enthalpies (see further discussion in Section V.4.2). Apart from the good thermal insulation, the adiabatic operation was assisted by the particularly large (for laboratory-scale experiments) honeycomb diameter (35 mm) that resulted in a low external surface-to-volume ratio. At the axis of symmetry ($r = 0$) and the channel outlet ($x = L_c + L_u$) zero-Neumann boundary conditions were used for all thermoscalars and the axial velocity, while the radial velocity was set to zero. Finally, no-slip has been applied for both velocity components at $r = r_h$.

V.3.2 Channel-flow reactor

The interfacial energy boundary conditions ($y = 0$ and $y = 2b$) in the optically accessible channel-flow reactor were substantially simpler, given the direct measurement of the surface temperatures. The species and energy interfacial boundary conditions were:

$$(\rho Y_k V_{k,y})_{y=0} = B W_k (\dot{s}_k)_{y=0}, \quad -(\rho Y_k V_{k,y})_{y=2b} = B W_k (\dot{s}_k)_{y=2b} \tag{7}$$

and

$$T(x, y=0) = T_{W,L}(x), \quad T(x, y=2b) = T_{W,U}(x), \tag{8}$$

with $T_{W,U}(x)$ and $T_{W,L}(x)$ the thermocouple-measured temperature distributions of the upper and lower wall, respectively. The energy boundary conditions of Eqs. (8) have removed the need for a solid substrate model with the associated heat transfer mechanisms (heat conduction, surface radiation). This was a welcome simplification, particularly since those experiments were intended to validate kinetics. Finally, the inlet and outlet boundary conditions were of the same type as in the honeycomb channel of Section V.3.1.

V.3.3 Method of solution

A finite volume scheme was used to discretize the governing equations. The solution was obtained iteratively using a SIMPLER [52, Patankar, 1980] method for the pressure-velocity field. Details on the solution algorithm have been provided elsewhere [21, Dogwiler et al., 1999; 53, Mantzaras et al., 2000; 54, Appel et al., 2002]. For the honeycomb channel, an orthogonal staggered grid of 220x24 points in x and r, respectively, (75 mm x 0.6 mm) with finer x-spacing closer to the entry and r-spacing closer to the wall was sufficient to produce a grid-independent solution; the solid was discretized with 220x16 points (75 mm x 0.0296 mm). For the channel-flow reactor, an orthogonal staggered grid of 380x120 points (300 mm x 7 mm) was used.

V.3.4 Chemical Kinetics

The detailed heterogeneous reaction mechanism of Deutschmann [1, Schwiedernoch et al., 2003] was used for CPO of methane over rhodium (38 reactions, 12 surface and 6 gas species). Fundamental kinetic studies in the optically accessible reactor of Fig. V.1(c) have shown that this scheme reproduced the methane conversion and synthesis gas yields in CPO of CH_4/air [47, Appel et al., 2005a] and $CH_4/O_2/H_2O/CO_2$ [63, Schneider et al., 2007] over Rh/ZrO_2 catalysts. The surface site density was $\Gamma = 2.72 \times 10^{-9}$ mol/cm^2.

The C$_2$/H/O homogeneous reaction mechanism of [2, Warnatz et al., 1996] was used to assess the effect of gaseous chemistry (164 reversible reactions and 34 species). This reaction scheme has been shown to capture the onset of homogeneous ignition in the aforementioned studies [47, Appel et al., 2005a; 63, Schneider et al., 2007]. However, simulations of the present honeycomb experiments with the above hetero-/homogeneous mechanisms have shown that gas-phase chemistry was insignificant. The gaseous chemistry had also a negligible contribution over the 45-mm-long gap separating the reactor exit and the sampling probe (Fig. V.1(a)), as shown by additional plug-flow-reactor simulations. The negligible gas-phase chemistry contribution was further verified experimentally. Turning the cooling water of the sampling probe off, led to only 3% relative rise in the GC-measured hydrogen volumetric composition, even though the residence time in the visibly hot section of the probe was nearly ten times longer than that of the reactor. Therefore, the gaseous chemistry was not included in the honeycomb simulations.

The CHEMKIN database was used to evaluate transport properties [51, Kee et al., 1996a]. Thermodynamic data for the gas-phase species were included in the gas-phase chemical scheme. Finally, surface and gas-phase reaction rates were evaluated with SURFACE CHEMKIN [25, Coltrin et al., 1996] and CHEMKIN [56, Kee et al., 1996b], respectively.

V.4 Results and discussion

V.4.1 Catalyst characterization

The textural properties of the catalysts are presented in Table V.1. Doping the ZrO$_2$ support with ceria resulted in an increase of the BET surface area from 21 to 44 m^2/g. The lowest surface area (6 m^2/g) was measured for the α-Al$_2$O$_3$ supported catalyst. The noble metal dispersion decreased in the following order: Rh/Ce-ZrO$_2$ > Rh/ZrO$_2$ > Rh/α-Al$_2$O$_3$. The factor B (ratio of active to geometrical surface area) was calculated based on H$_2$ chemisorption measurements and was subsequently used in Eqs. (4), (5) and (7). The crystal structure of the support material for both fresh and tested samples of the Rh/Ce-ZrO$_2$ and Rh/ZrO$_2$ catalysts was determined by Raman spectroscopy. The spectra presented in Fig. V.4 indicated that both monoclinic and tetragonal zirconia were present in the fresh Rh/ZrO$_2$ sample, whereas only tetragonal ZrO$_2$ could be detected for fresh Rh/Ce-ZrO$_2$. The peaks corresponding to different crystal structures are indicated by dashed lines. Testing under CPO conditions resulted in the formation of a pure monoclinic phase for the Rh/ZrO$_2$ catalyst. No

phase transition occurred during reaction for the Rh/Ce-ZrO$_2$ sample, i.e. the tetragonal structure was maintained. The absence of phase transitions promoted high noble metal dispersion since encapsulation of Rh could be avoided. Stabilization of the tetragonal ZrO$_2$ phase by addition of small amounts of another dopant oxide, such as CeO$_2$ or Y$_2$O$_3$, has been reported previously [95, Hy, 1994; 96, Mastelaro et al., 2003]. Furthermore, the enhanced surface area detected for the ceria-doped catalyst could be related to the stabilization of tetragonal ZrO$_2$.

Figure V.4
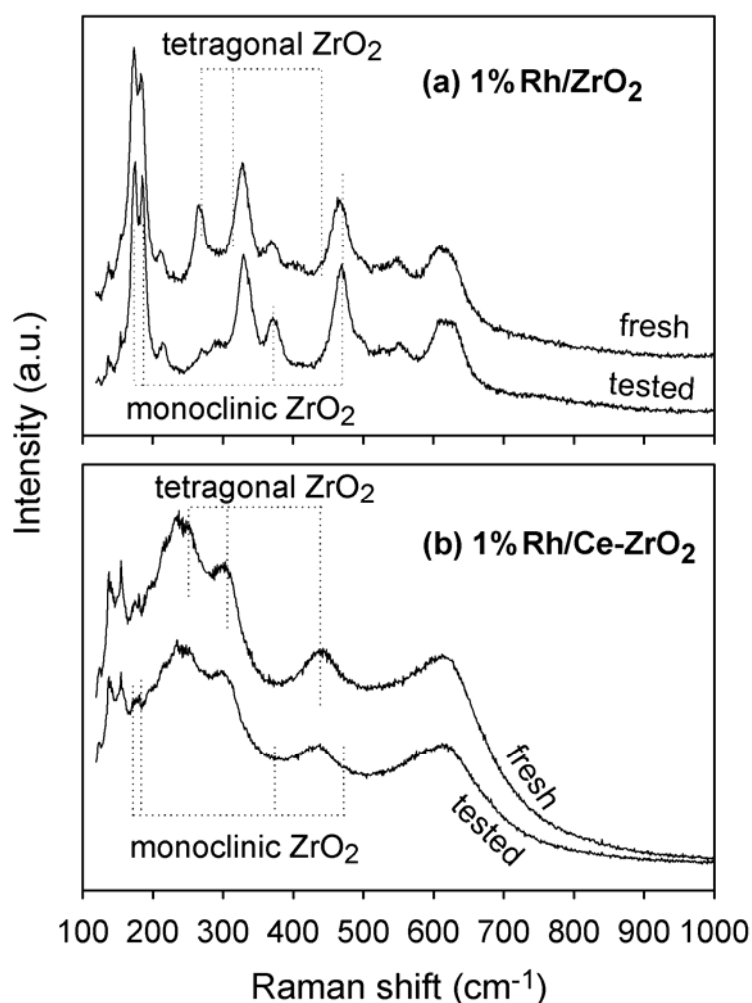
Surface Raman spectra of fresh and tested catalysts: (a) 1% Rh/ZrO$_2$ and (b) 1% Rh/Ce-ZrO$_2$.

V.4.2 Measurements and predictions in the honeycomb reactor

To facilitate performance comparisons between different catalysts, the same experimental conditions were used for the three investigated supports (see Table V.2). The pressure was 5 bar, the inlet temperatures (T_{IN}) were 623, 573 and 473 K, while the inlet velocities (U_{IN}) increased with rising T_{IN} so as to maintain the same reactor mass throughput. The flow was laminar with inlet Reynolds numbers (based on the channel hydraulic diameter) as high as 755 (see Table V.2). In all cases the gas hourly space velocity (GHSV) was 7.4×10^5 hr^{-1} and the computed residence times in the catalytic section of the reactor –accounting also for the flow acceleration due to heating– ranged from 7 ms (Cases 1, 4 and 7) to 7.8 ms (Cases 3, 6 and 9).

Table V.2

Experimental conditions in the honeycomb reactor[a]

Case	Catalyst support	p (bar)	T_{IN} (K)	U_{IN} (m/s)	Re_{IN}
1	Ce-ZrO$_2$	5	623	5.1	590
2	Ce-ZrO$_2$	5	573	4.7	637
3	Ce-ZrO$_2$	5	473	3.9	755
4	ZrO$_2$	5	623	5.1	590
5	ZrO$_2$	5	573	4.7	637
6	ZrO$_2$	5	473	3.9	755
7	α-Al$_2$O$_3$	5	623	5.1	590
8	α-Al$_2$O$_3$	5	573	4.7	637
9	α-Al$_2$O$_3$	5	473	3.9	755

[a]Pressure, inlet temperature, inlet velocity, and inlet Reynolds number. In all cases the inlet volumetric composition is 20.4% CH$_4$, 10.2% O$_2$, 46.3% H$_2$O, 23.1% CO$_2$, and the rhodium loading in the catalyst is 1 %wt.

The methane-to-oxygen equivalence ratio was $\varphi = 4.0$ and the dilution comprised 46.3% H_2O and 23.1% CO_2 per volume. The following procedure was adopted to obtain the operating conditions of Table V.2. Firstly, the desired inlet mixture composition was established at an inlet temperature of 600 K. The inlet temperature was then ramped at a rate of +10 K/min in order to reach the value required for catalytic ignition. Once light-off was achieved, the inlet temperatures were subsequently reduced to obtain the desired steady states at the three nominal temperatures of Table V.2. Although steady CPO performance was of main interest in this work, the measured light-off temperatures for the three catalysts are provided in Table V.3. The light-off temperatures increased with support type, in the order Ce-ZrO_2, ZrO_2 and α-Al_2O_3. Nonetheless, the extended ignition/extinction hysteresis in CPO [64, Schneider et al., 2006] allowed for stable combustion at inlet temperatures considerably lower than the corresponding ignition temperatures (by as much as 300 K).

To facilitate the ensuing discussion, the main reaction pathways are summarized by the following global steps:

$$CH_4 + 2O_2 = CO_2 + 2H_2O \qquad \text{(total oxidation)} \qquad \text{(R1)}$$
$$2CH_4 + O_2 = 2CO + 4H_2 \qquad \text{(partial oxidation)} \qquad \text{(R2)}$$
$$CH_4 + H_2O = CO + 3H_2 \qquad \text{(steam reforming)} \qquad \text{(R3)}$$
$$CO + H_2O = CO_2 + H_2 \qquad \text{(water gas shift)} \qquad \text{(R4)}$$
$$CH_4 + CO_2 = 2CO + 2H_2 \qquad \text{(dry reforming)} \qquad \text{(R5)}$$
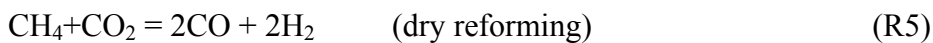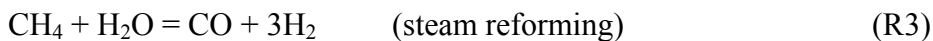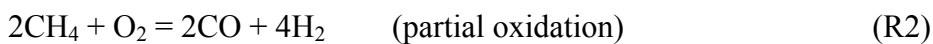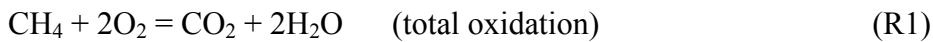
Mass rather than molar fractions will be preferably used thereafter, due to the presence of strongly non-equimolar reactions (R2, R3 and R5).

Table V.3

Catalytic ignition[a]

Catalyst	Rh (% wt.)	Support	T_{ig} (K)
1	1.0	Ce-ZrO_2	655
2	1.0	ZrO_2	670
3	1.0	α-Al_2O_3	790

[a]Ignition temperature of the employed catalysts.

Comparisons between the three different catalysts are elaborated below for $T_{IN} = 573$ K (Cases 2, 5 and 8) with the aid of Figs. V.5 to V.8. Two-dimensional color maps of all major species mass fractions and temperature (the latter for both the gas and solid phases) are provided in Fig. V.5. Steep gas-phase radial gradients can be seen in this figure, with a possible exception the fast-diffusing H_2, thus justifying the use of a 2-D model. The radial temperature differences inside the solid were particularly small, reaching near the entry up to 2.5 K over the solid thickness $\delta/2 + \delta_c = 29.6$ μm. Axial profiles of the predicted radially-averaged mass fractions of all major species are provided in Fig. V.6; the corresponding exhaust measurements are also shown in the same figure. The original mole fraction compositions deduced from the GC analysis and the measured temperatures at position E along with the accompanying numerical predictions are further summarized for all cases in Table V.4. Predicted axial profiles of the wall temperature T_W (referring to the gas-wall interface), the radially-averaged gas temperature (T_{gas}), the H_2 and CO selectivities and the CH_4 conversions are given in Fig. V.7; in the same figure, the measured temperatures at positions A through E (see Fig. V.1(a)) along with the calculated adiabatic equilibrium temperature, T_{eq}, are also shown. The wall temperatures exceeded T_{eq} by as much as 180 K, a condition typical in CPO reactors with residence times of a few milliseconds [64, Schneider et al., 2006; 73, Veser and Frauhammer, 2000]. The partial oxidation product selectivities were:

$$S_{H2} = \frac{0.5\, Y_{H2}/W_{H2}}{(Y_{CH4,IN} - Y_{CH4,OUT})/W_{CH4}} \text{ and } S_{CO} = \frac{Y_{CO}/W_{CO}}{(Y_{CH4,IN} - Y_{CH4,OUT})/W_{CH4}}. \tag{9}$$

The definition for S_{H2} in Eq. (9) was based on the stoichiometry of the CPO reaction (R2) and was maintained herein, despite the added H_2 production from H_2O.

Table V.4

Comparison between experiments and simulations[a]

Case	CH$_4$		O$_2$		H$_2$		CO		H$_2$O		CO$_2$		T(K)	
	Exp.	Sim.	Exp.	Sim.	Exp.	Sim.	Exp.	Sim.	Exp.	Sim.	Exp.	Sim.	Exp.	Sim.
1	6.0	6.4	0.1	0.8	21.0	19.9	8.8	8.6	41.4	42.0	22.7	22.3	1033	1009 1007
2	6.5	7.1	0.2	0.8	19.9	17.9	8.1	8.4	42.1	43.4	23.2	22.3	1022	995 992
3	7.4	8.6	0.2	1.0	16.8	14.3	8.2	7.7	44.2	46.0	23.2	22.4	978	966 961
4	6.8	6.9	0.5	0.8	19.4	18.7	8.3	8.2	42.1	42.8	22.9	22.6	1031	1033 1032
5	7.5	7.6	0.6	0.8	17.9	16.8	7.5	7.9	43.3	44.2	23.2	22.6	1027	1018 1015
6	8.8	9.3	0.6	1.0	14.9	12.7	6.8	7.1	45.1	47.1	23.8	22.8	994	998 994
7	7.5	7.2	0.9	0.8	18.9	18.1	7.8	8.0	42.1	43.3	22.8	22.7	1020	1046 1045
8	8.1	7.9	1.1	0.9	16.9	16.2	7.5	7.7	43.1	44.6	23.3	22.7	997	1030 1028
9	9.7	9.3	1.4	1.0	13.5	12.7	6.2	7.1	45.3	47.1	23.9	22.8	964	998 994

[a]Measured and simulated volumetric exhaust composition (%) and temperature. The temperature measurements refer to position E in Fig. V.1(a), while in the simulations refer to $x = 65$ mm. In the simulations the upper value is the wall temperature and the lower value is the mean gas temperature.

The temperature comparisons in Fig. V.7 were very favorable; the thermocouple measurements at position C and D were bounded by T_W and T_{gas}, indicating that the numerical model realistically reproduced the temperature evolution along the reactor. Finally, the molar production rates of all major species along with selected production rate ratios are provided in Fig. V.8. As seen in Table V.4, the agreement between predictions and measurements was good. The simulations consistently somewhat underpredicted (overpredicted) the H$_2$ (H$_2$O) molar compositions. For the higher inlet temperatures $T_{IN} = 623$ and 573 K and for all catalyst supports, the relative differences between measured and predicted species compositions were less than 10%, except for the scarce O$_2$. In Cases 3, 6 and 9 with $T_{IN} = 473$ K, the discrepancies were as high as 15%. The assumption of reactor adiabaticity

was also attested by comparing the inlet and outlet total enthalpies (deduced from the measurements of temperature and species mole fractions); the differences in total enthalpies corresponded to equivalent temperature differences of less than 12 K. Moreover, the C/H/O element balances in the measurements of Table V.4 were better than 1%.

Figure V.5
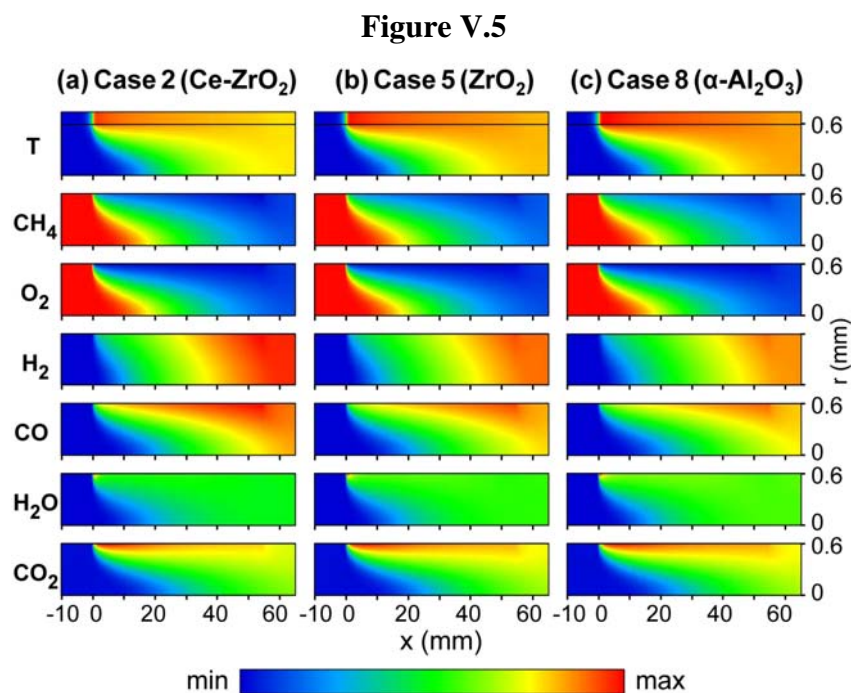
Computed 2-D distributions of temperature and species mass fractions for three cases of Table V.2 with different catalyst supports. The minimum and maximum levels of the color bar are: (a) T: 573 K to 1134 K, (b) CH4: 0.043 to 0.131, c) O2: 0.0 to 0.131, d) H2: 0.0 to 0.0172, e) CO: 0.0 to 0.124, f) H2O: 0.333 to 0.389 and g) CO2: 0.406 to 0.471. The centerline is at r = 0 and the gas-solid interface at r = 0.6 mm; the catalytically active section extends over $0 \leq x \leq 55$ mm. The temperature of the solid (0.6 mm < r < 0.629 mm) is also shown with an expanded radial scale.

Figure V.6
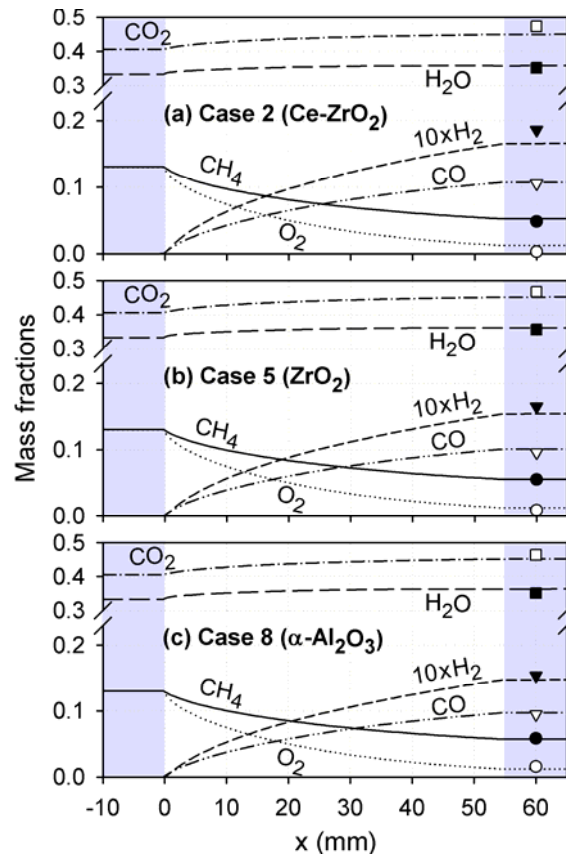
Predicted axial profiles of average species mass fractions for Cases 2, 5 and 8 of Table V.2. The measured exhaust gas composition is shown with symbols (open squares: CO_2, filled squares: H_2O, filled triangles: $10xH_2$, open triangles: CO, filled circles: CH_4, open circles: O_2). The shaded areas denote the inactive reactor length.

For the same inlet conditions, the predictions indicated that an increase in Rh dispersion ($Ce\text{-}ZrO_2 > ZrO_2 > \alpha\text{-}Al_2O_3$) led to slightly higher methane conversion and lower surface temperatures (Fig. V.7 and Table V.4), higher H_2 and CO yields and selectivities and correspondingly higher H_2O consumption (Figs. V.7, V.6 and Table V.4). The measurements in Fig. V.7 and Table V.4 supported the aforementioned trends of the predictions. A slightly higher deviation between experiments and predictions was evident for the hydrogen yields and methane conversions of the $Ce\text{-}ZrO_2$ support cases; however, those differences were mostly within the experimental uncertainty. It was thus evident that the key parameter controlling the methane conversion, synthesis gas yields and reactor temperature, at least in CPO with large EGR, was the noble metal dispersion. This issue will be further elaborated in Section V.4.4.

Figure V.7
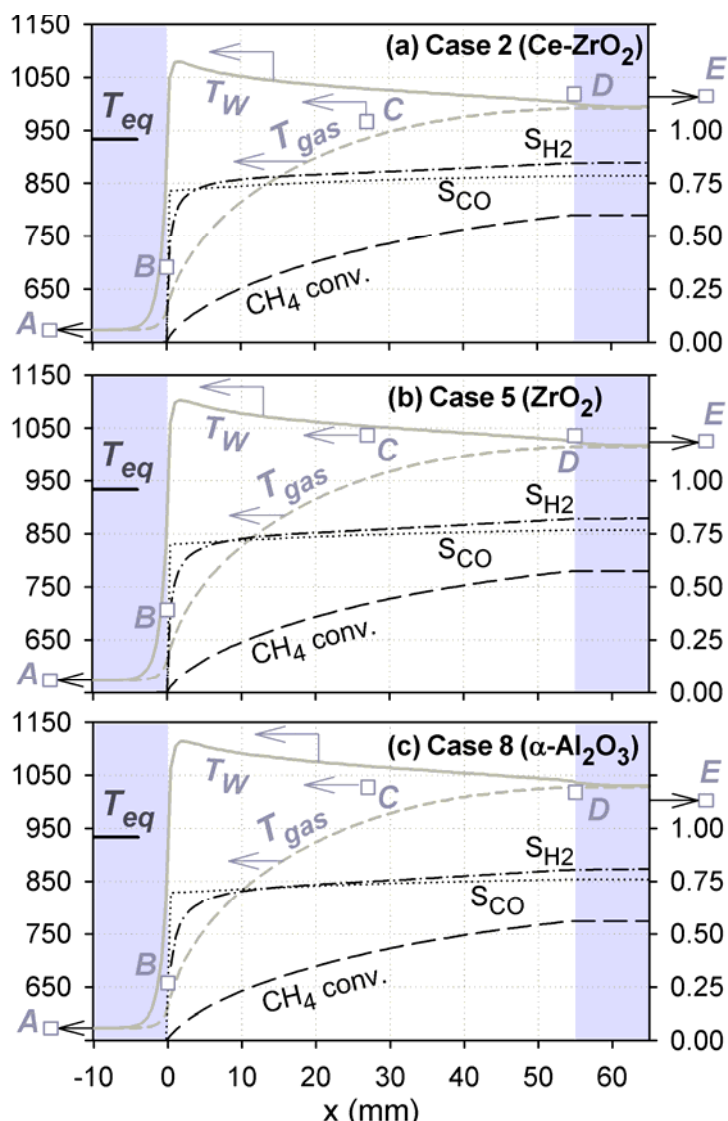
Axial profiles of temperature, H_2 and CO selectivities and CH_4 fractional conversion for Cases 2, 5 and 8 of Table V.2. Predictions: wall temperature T_W (solid gray lines), mean gas temperature T_{gas} (dashed gray lines), H_2 selectivity (dashed-dotted black lines), CO selectivity (dotted black lines), and CH_4 fractional conversion (dashed black lines). The calculated adiabatic equilibrium temperature is indicated by T_{eq}. The measured temperatures at positions A through E are shown by the square symbols. The shaded areas denote the inactive reactor length.

The contribution of the different chemical pathways along the channel is described with the aid of Fig. V.8. The peaks in the H_2O and CO_2 mass fractions and production rates at $x \approx 0$ (see Figs. V.5 and V.8) were indicative of complete oxidation (R1) at the beginning of the catalytic section. Reaction R1 was nearly mass-transport-limited already at $x \approx 0$ (manifested in Fig. V.5 by the very low levels of the deficient O_2 at $r = 0.6$), leading to high wall

temperatures at $x \approx 0$ (see Figs. V.5 and V.7). The $CH_4:O_2$ destruction ratio at $x = 0$ ranged from 0.89 to 0.97 (Fig. V.8), indicating a non-negligible partial oxidation (R2) contribution from the start of the catalyst, with CO and H_2 already formed at $x \approx 0$ (Fig. V.5).

This behavior was differentiated from previous CH_4/air CPO studies without EGR [1, Schwiedernoch et al., 2003], whereby only total oxidation was reported at the upstream reactor positions and partial oxidation products formed farther downstream. Over the length 2 mm $< x <$ 20 mm, the $H_2:CO$ production ratio was ~2.0 and the CH_4/O_2 destruction ratio was ~1.0-1.3 (Fig. V.8) pointing to the significance of both R1 and R2; therein enough oxygen was available (Fig. V.5) to accommodate both oxidation reactions. At $x >$ 48 mm, where O_2 was largely depleted (Figs. V.5 and V.6), there was a shift from production to destruction of H_2O (Fig. V.8) in all three cases. Therein, steam reforming (R3) was considerable, as also manifested by the increase of the $H_2:CO$ production ratio to ~2.5 at the rear part of the reactor; the continuous drop of the wall temperature along the reactor (Figs. V.5 and V.7) concurred the importance of this endothermic step. Water gas shift (R4) was marginally important at the rear of the channel; at $x >$ 50 it enhanced somewhat the $H_2:CO$ ratio and maintained a small production of CO_2 (Fig. V.8). Even though the presence of large steam dilution has been shown to enhance the CH_4 consumption and the H_2 selectivity [64, Schneider et al., 2006] there was always a net production of H_2O in the reactor (see Fig. V.6). The added amount of H_2O facilitated steam reforming mainly by depleting faster the water produced by total oxidation (R1) rather than by consuming the incoming steam itself, (for all catalysts, $Y_{H2O,OUT} > Y_{H2O,IN}$ in Fig. V.6). This was because the surface temperatures were moderate and the residence times too short for the slow endothermic steam reforming to dominate.

The aforementioned reactor response with increasing factor B (drop in temperature, increase in H_2 and CO yields) was due to the acceleration of the steam reforming and partial oxidation reactions; the total oxidation, which was responsible for the peak wall temperatures, did not benefit by the increase in B since it was close to the mass-transport limit as stated in the previous paragraph. Finally, despite the added amount of CO_2, the contribution of dry (CO_2) reforming was negligible as also shown in previous Rh/ZrO_2 investigation [64, Schneider et al., 2006]. The reason was that oxy- or H_2O-reforming reactions were considerably faster than dry reforming [42, Mark and Maier, 1996]. A typical surface coverage profile is finally illustrated in Fig. V.8 for Case 2 (Ce-ZrO_2 support); free sites and CO(s) constituted the main surface species for all examined cases.

Figure V.8
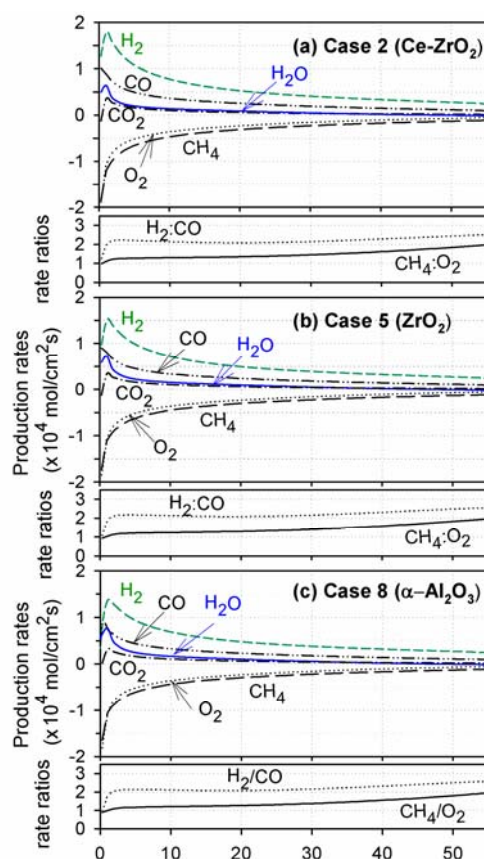
Computed axial profiles of species catalytic molar production rates and rate-ratios of $CH_4:O_2$ and $H_2:CO$. Cases 2, 5 and 8 of Table V.2 are shown. Solid lines: H_2O, short dashed lines: H_2, double-dotted-dashed lines: CO, dotted-dashed lines: CO_2, long dashed lines: CH_4, dotted lines: O_2. Production rate-ratios: solid lines: $CH_4:O_2$, dotted lines:

Figure V.9
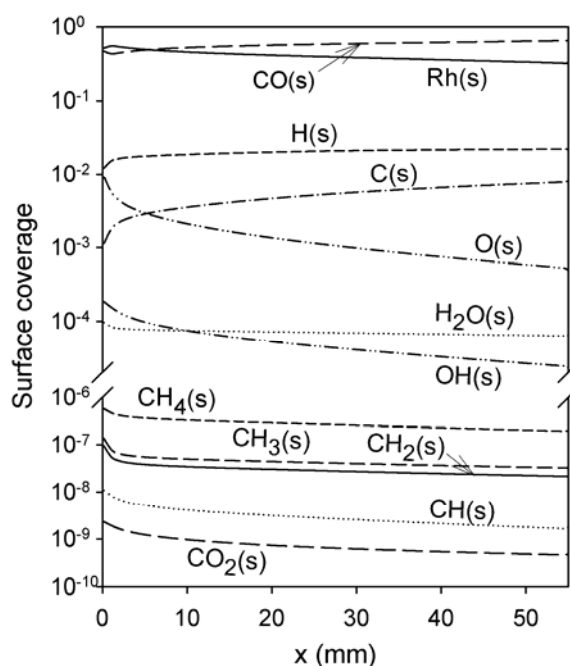
Surface coverage for Case 2 of Table V.2.

To complete the picture of the in-channel processes, the heat balance in each incremental slice $\Delta x \times (\delta/2 + \delta_c)$ of the solid is provided in Fig. V.10 for Case 2 (Ce-ZrO$_2$). The heat generation ($\dot{q}_{gen}$) peaked at $x \approx 0$ due to total oxidation. Radiation was altogether negligible, with only a minor net radiative heat transfer in the regions close to $x = 0$ (computations with $\varepsilon = 0$ or 1 for the channel surfaces reproduced essentially the same results). The negligible impact of $\dot{q}_{rad}$ was a direct consequence of the diminished light-off distance that yielded wall temperatures differing by less than 85 K over the extent $0 \leq x \leq 65$ mm (see Fig. V.7(a)). On the other hand, in fuel-lean applications the more effective blocking of the surface free sites by oxygen [21, Dogwiler et al., 1999] could lead to appreciable (> 500 K) temperature differences along the solid wall; therein, radiation exchange played an important role by transferring heat from the hotter rear channel surfaces to the colder entry, thus stabilizing combustion [76, Karagiannidis et al., 2007]. Heat conduction ($\dot{q}_{cond}$) was also important at $x \approx 0$, where the temperature gradients were the steepest.

Figure V.10
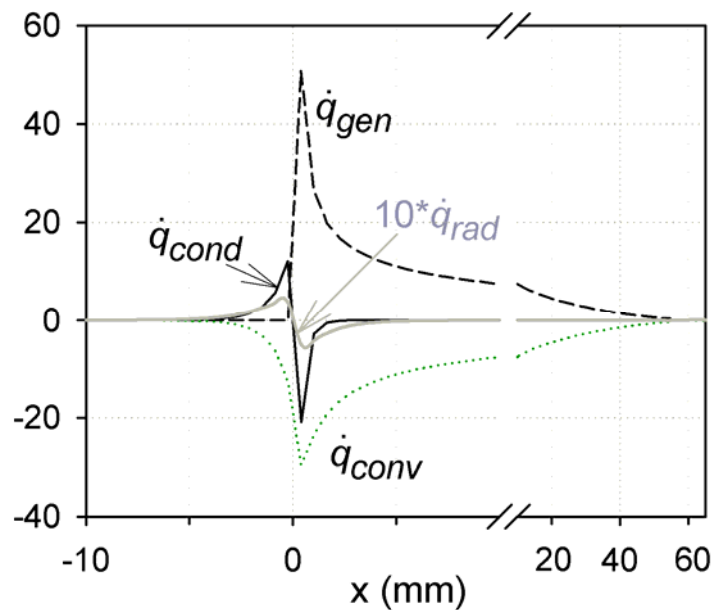
Heat balance in the solid for Case 2 of Table V.2. Surface heat generation: dashed lines; convection: dotted lines; conduction: solid lines; radiation: gray solid lines. For clarity, the radiation term is multiplied by ten.

V.4.3 In situ gas-phase Raman measurements

The foregoing analysis in the honeycomb reactor has revealed the key impact of active surface area on the synthesis gas yields and selectivities of rhodium catalysts with different

supports. To further ensure that this single parameter, when used in conjunction with the employed surface reaction mechanism, could capture the underlying CPO processes, local comparisons of Raman-measured and numerically predicted transverse profiles of gas-phase species mole fractions in the channel-flow reactor are presented in Figs. V.11 and V.12 for the Ce-ZrO_2 and ZrO_2 supports, respectively; the operating conditions are provided in the figure legends. The pressure was 6 bar as opposed to the 5 bar used in the honeycomb reactor; nonetheless, the effect of pressure on CH_4 conversion and synthesis gas selectivities was minimal over the pressure range 4 to 10 bar [63, Schneider et al., 2007] and the same also applied over the lower pressure range 1.5 to 5.5 bar [27, Dietz and Schmidt, 1995]. For clarity, up to twenty measuring points are shown over the experimentally resolvable range $0 \leq y \leq 3.2$ mm, which corresponds to the upper channel half-height. The bending of the species profiles in the vicinity of the upper wall ($y = 3.5$ mm) was directly linked to the catalytic reactivity and hence to the local wall temperature. The measured upper-wall surface temperature distributions are provided in Fig. V.13. The upper wall temperatures did not exceed 1125 K, and they differed by less than ± 15 K from the corresponding lower-wall temperatures (not shown).

To delineate the reactor extent with negligible gas-phase chemistry contribution, LIF-measured and predicted formaldehyde 2-D distributions are compared for both cases in Fig. V.14. The homogeneous ignition distances (x_{ig}) in Fig. V.14 were determined, in both experiments and predictions, by the inflection points of the axial profiles of the integrated (transversely) formaldehyde levels. Even though the measured formaldehyde zones ahead of the flame were broader than the predicted ones, an effect well-established in the literature and also elaborated in [63, Schneider et al., 2007], the key issue in the present study was the onset of homogeneous ignition. The predicted homogeneous ignition distances were in good agreement with the measurements, indicating that the employed gas-phase reaction mechanism captured the homogeneous processes and the hetero-/homogeneous chemistry coupling. Having established the aptness of the employed gas-phase mechanism, streamwise profiles of the computed catalytic and gas-phase species production rates (the latter integrated over the 7 mm channel-height) and of the measured surface temperatures are provided in Fig. V.15 for the Ce-ZrO_2 supported case of Fig. V.11; direct comparisons of the Ce-ZrO_2 and ZrO_2 cases are not meaningful due to the different operating conditions. As seen in Fig. V.15, the onset of appreciable gas-phase chemistry contribution (defined as the position where the homogeneous pathway amounted to less than 3% of the corresponding catalytic methane conversion rate) was $x_a = 130$ mm. The onset of homogeneous ignition (x_{ig}) was located

Figure V.11
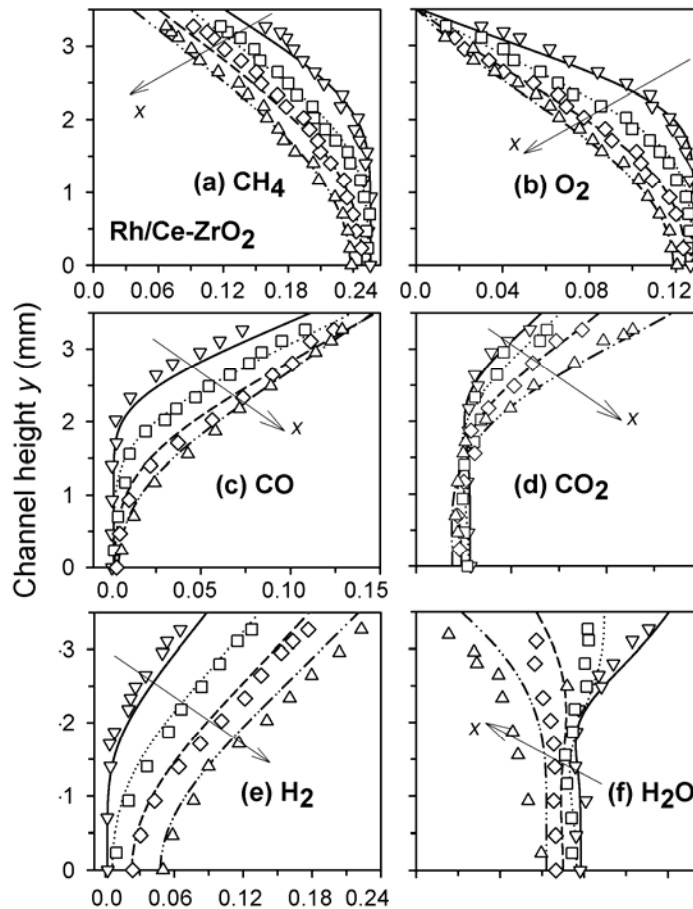
Predicted (lines) and measured (symbols) profiles of species mole-fraction for CPO on Rh/Ce-ZrO$_2$ at four axial positions: $x = 14$ mm (solid-lines, lower-triangles), $x = 48$ mm (dotted-lines, squares), $x = 88$ mm (dashed-lines, diamonds), $x = 128$ mm (double-dotted-dashed lines, upper-triangles). The upper wall is located at $y = 3.5$ mm and the symmetry plane at $y = 0$. Operating conditions: $p = 6$ bar, $U_{IN} = 1.48$ m/s, $T_{IN} = 522$ K, inlet vol. composition: CH$_4$: 25.8%, O$_2$: 12.9%, H$_2$O: 45.1%, CO$_2$: 16.2% ($\varphi = 4.0$).

~20 mm downstream of x_a. All profiles in Fig. V.11 referred to $0 < x < x_a$, therefore, the comparisons could directly reveal the aptness of the catalytic reaction scheme. It is emphasized that simulations with or without the inclusion of gas-phase chemistry have also attested that the predicted profiles of Fig. V.11 were unaffected by the homogeneous reaction pathway. The same also applied for the predicted profiles of Fig. V.12.

The relative differences between measured and predicted CH$_4$ and O$_2$ mole fractions in Figs. V.11 (a,b) and V.12 (a,b) were up to 4%, i.e. within the experimental uncertainty. At the two farthermost downstream positions the partial oxidation products, particularly hydrogen, were somewhat underpredicted (Figs. V.11 (c,e), 12(c,e)) and the total oxidation

products slightly overpredicted (Figs. V.11(d,f), V.12(d,f)). Hence, the catalytic reaction scheme at the longer residence times of the channel-flow reactor (~100 ms), favored slightly the total over the partial oxidation route, in agreement with earlier CPO studies on Rh/ZrO_2 catalysts [63, Schneider et al., 2007] and with the previous honeycomb results of Table V.4.

Figure V.12
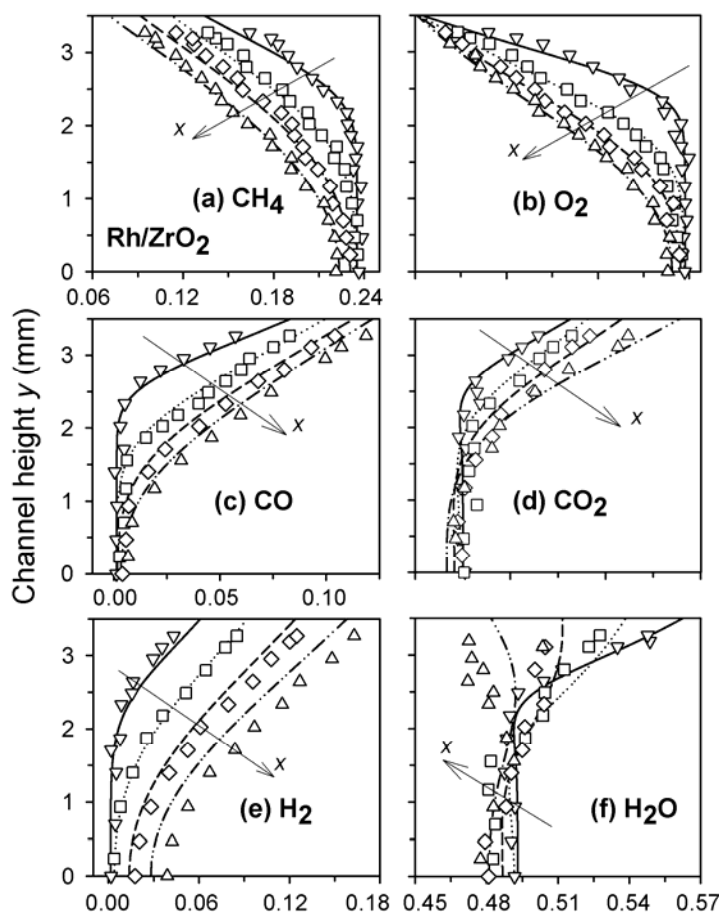
Predicted (lines) and measured (symbols) profiles of species mole-fraction in CPO over Rh/ZrO_2, at four axial positions. The line and symbol notation is as in Fig. V.10. The upper wall is located at $y = 3.5$ mm and the symmetry plane at $y = 0$. Operating conditions: $p = 6$ bar, $U_{IN} = 1.74$ m/s, $T_{IN} = 565$ K, inlet vol. composition: CH_4: 23.6%, O_2: 11.8%, H_2O: 49.4%, CO_2: 15.2%, ($\varphi = 4.0$).

The in-channel processes are summarized with the aid of Fig. V.15, in a fashion similar to that of Fig. V.8 for the honeycomb reactor studies. Total oxidation and partial oxidation dominated at early stages ($x < 10$ mm) manifested by the 0.5–1.1 value of CH_4:O_2 destruction ratio. Steam reforming was more pronounced at $x > 50$ mm, wherein the production rate of H_2O turned from positive to negative (Fig. 15(a)) and the H_2:CO production ratio reached a value around three (Fig. V.15(b)). At 70 mm $< x <$ 128 mm, water gas shift was also

important as evidenced by the further increase in the H_2:CO ratio (Fig. V.15(b)) and the corresponding rise in CO_2 production (Fig. V.15(a)). It is important that the Raman measurements directly affirmed the foregoing evolution of the chemical processes along the reactor via the absolute species mole fraction measurements and via the sign of the transverse gradients near the upper wall. In conclusion, notwithstanding the small differences in the comparisons of Figs. V.11 and V.12, the model predictions were equally successful for the Ce-ZrO$_2$ and ZrO$_2$ catalysts. Therefore, the chemical impact of ceria addition appeared to be of secondary importance for the present CPO with large EGR.

Figure V.13
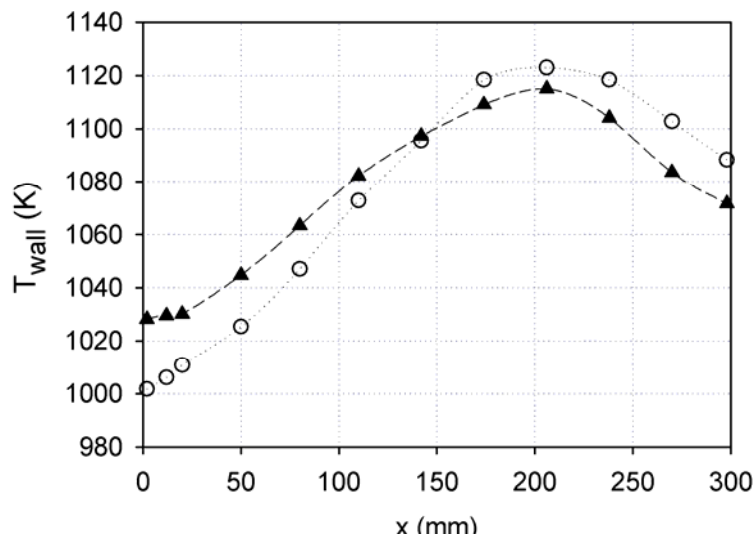
Thermocouple measurements (symbols) of the upper-wall surface temperature profiles, in the channel-flow reactor of Fig. V.1(c). Solid triangles: Rh/ZrO$_2$ case of Fig. V.11. Open circles: Rh/Ce-ZrO$_2$ case of Fig. V.10.

Figure V.14
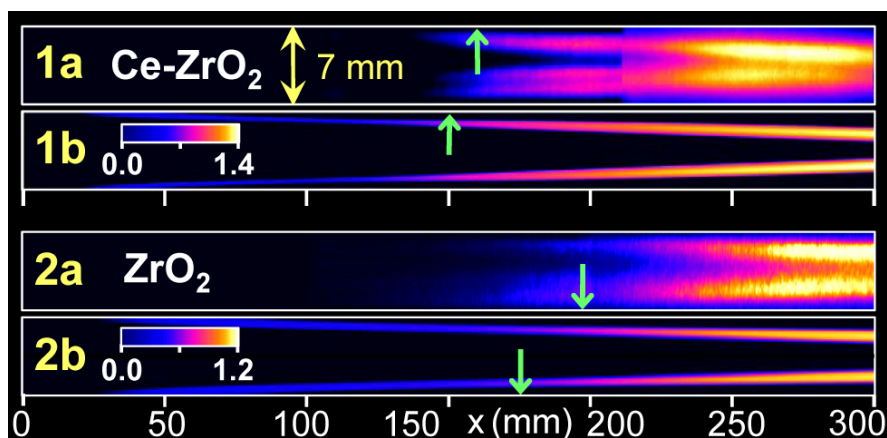
LIF-measured and predicted distributions of formaldehyde for: (a) the Rh/Ce-ZrO$_2$ case of Fig. V.10, and (b) the Rh/ZrO$_2$ case of Fig. V.11. The arrows mark the onset of homogeneous ignition (x_{ig}). The color bars provide concentrations in ppmv x 10^{-3}.

Figure V.15
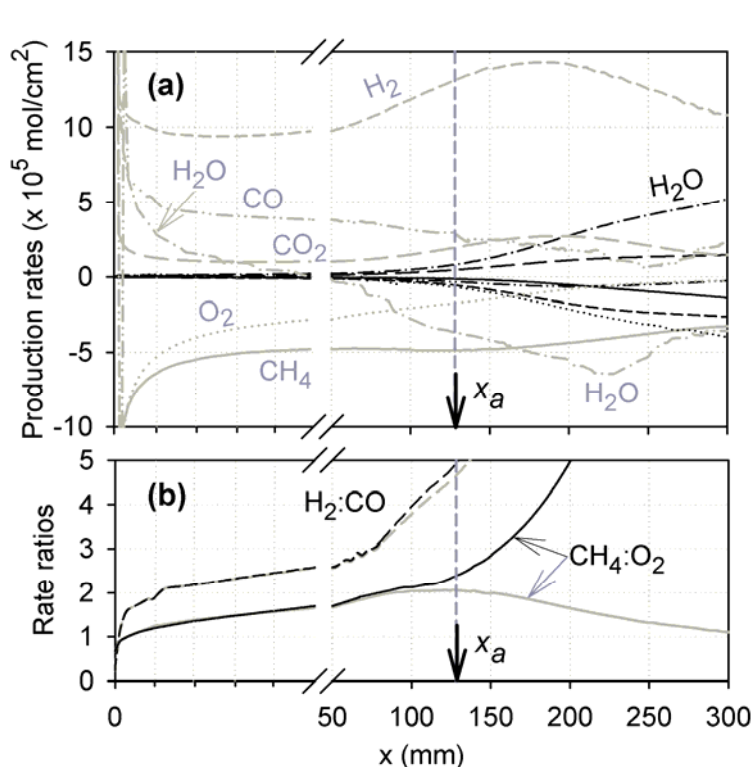
(a) Predicted axial profiles of catalytic (gray lines) and gas-phase (black lines) species molar production rates, and (b) ratios of the CH$_4$:O$_2$ and H$_2$:CO molar production rates, with gray lines referring to the catalytic contribution and black lines to the combined catalytic and gas-phase contribution. The catalyst is Rh/Ce-ZrO$_2$ and operating conditions are the same as in Fig. V.10. The arrow marked x_a denotes the onset of appreciable gas-phase contribution.

V.4.4 Effect of support

The reasons for the validity of the employed heterogeneous reaction scheme in Rh catalysts with different supports are elaborated below. Methane activation is generally considered to occur on the metal sites (Rh, Ni, Pt etc.) of supported catalysts for partial oxidation of methane, steam reforming, and carbon dioxide reforming (dry reforming) [3, Hickman and Schmidt, 1993; 84, Mallens et al., 1997; 87, Buyevskaya et al., 1994; 97, Hu and Ruckenstein, 1995]. The main function of the support is to disperse the noble metal particles and prevent sintering. However, CeO_2 is also known for its oxygen storage capacity and ability to stabilize the support. Studies have shown that the oxygen transport properties of CeO_2 make it suitable for direct oxidation of methane to synthesis gas in the absence of gaseous oxygen [98, Otsuka et al., 1998]. This process occurs in two steps, first methane reacts with CeO_2, producing H_2 and CO. In the second step, ceria is re-oxidized by CO_2 or water. The activation of methane on CeO_2 is, however, insignificant in the presence of a noble metal. Pulse studies [99, Fathi et al., 2000] have shown that methane decomposition occurs on the noble metal sites for $Rh/CeO_2/\gamma\text{-}Al_2O_3$. Therefore, any interaction of CH_4 with the support is most likely negligible for the catalysts in the present study.

Different reaction mechanisms for the reforming of methane over supported catalysts have been proposed. In steam reforming over a $Ni/MgAl_2O_4$ catalyst, [100, Xu and Froment, 1989] presented a reaction mechanism where both CH_4 and H_2O adsorbed dissociatively on surface Ni atoms. Other researchers proposed a Mars-van Krevelen type mechanism where the support played an active role [101, Stagg et al., 1998; 102, Dong et al., 2002]. Methane was activated on the metal sites producing H_2 and carbon, whereas the co-reactant (CO_2 or H_2O) dissociated on reduced support sites. The adsorbed oxygen species then reacted with the carbon deposits at the support-metal interface.

The reaction mechanism involving active support sites has especially been reported for ceria-based catalysts [103, Laosiripojana et al., 2005; 104, Laosiripojana and Assabumrungrat, 2005a; 105, Kurungot and Yamaguchi, 2004]. The high oxygen transport capacity of ceria, which is related to the ability of ceria to shift between Ce^{3+} and Ce^{4+}, facilitates oxygen transport from the support to the metal sites. Studies have shown that the activity and stability of Ni/Al_2O_3 catalysts for dry reforming could be improved by adding CeO_2 [103, Laosiripojana et al., 2005]. Those improvements were attributed to the redox properties of ceria, resulting in continuous removal of carbonaceous deposits by reaction with lattice oxygen forming CeO_{2-x}. The reduced ceria was then re-oxidized by CO_2. When

studying steam reforming, Ni/Ce-ZrO$_2$ catalysts were found to be more stable than Ni/Al$_2$O$_3$ [104, Laosiripojana and Assabumrungrat, 2005a]. However, no increase in activity was evident for this reaction when changing support to Ce-ZrO$_2$. Similar results, showing improved stability, have been reported for partial oxidation of methane over Pt/Ce$_x$Zr$_{1-x}$O$_2$ catalysts [89, Passos et al., 2005].

In general, the addition of ceria has shown positive effects on activity and stability for the catalysts used in the reactions discussed above, which often is related to the redox properties of CeO$_2$. However, ceria is also known for its ability to increase the metal dispersion on the support. Unfortunately, correlations between activity and noble metal dispersion on different supports are often lacking.

The elementary steps involved in steam and CO$_2$ reforming of methane have been investigated by [106, Wei and Iglesia, 2004]. Different noble metals (Rh, Ir, Pt, Ru) and support materials (ZrO$_2$, γ-Al$_2$O$_3$, ZrO$_2$-CeO$_2$) were studied. The results showed that the reforming rates were limited by C-H bond activation and that co-reactant activation was kinetically irrelevant. Furthermore, turnover rates were found to increase with increasing noble metal dispersion. This was related to the presence of coordinatively unsaturated surface metal atoms in catalysts of high metal dispersion, which were more active for C-H bond activation. The support material did not affect turnover rates, except indirectly by influencing the metal dispersion. These conclusions were also valid for CH$_4$-O$_2$ reactions, which were found to occur according to the combustion-reforming pathway [107, Iglesia, 2006].

[108, Wang et al., 1996] investigated the elementary reaction steps in partial oxidation of methane over Rh/Al$_2$O$_3$ catalysts. In contrast to the heterogeneous reaction mechanism of Deutschmann used in the present study, a surface reaction scheme including active Al$_2$O$_3$ sites for water adsorption was proposed. Inverse spillover of hydroxyls from the support to the metal sites could then occur. The OH spillover effect is, however, dependent on the specific experimental conditions and is expected to be less important at higher temperatures (> 1023 K for alumina) and when high amounts of water are present in the gas phase. Furthermore, it has been shown that dehydroxylation of ZrO$_2$ is complete at temperatures above 993 K [109, Stoppek-Langner et al., 1995]. In the present study, with high amounts of water in the gas phase and catalyst temperatures of 970-1045 K, OH spillover from the support to the metal sites can be considered of minor importance.

In conclusion, the redox properties of ceria appear to be important for certain catalytic systems that are easily deactivated by carbon deposition, which is generally the case for Ni-based catalysts. However, when using Rh this effect should be less significant; the main

impact of ceria is to increase the noble metal dispersion, which is in agreement with results of [106, Wei and Iglesia, 2004]. The numerical predictions presented in the foregoing sections, where no active support sites were included in the surface reaction mechanism, agree well with the experimental results. This indicates that inverse OH spillover from the support can be neglected for most cases studied in the present work. The somewhat worse agreement in H_2 production observed for the catalysts of high Rh dispersion at lower inlet temperature ($T_{IN} = 473$ K) could potentially be related to water dissociation on support sites. This lower inlet temperature case is, however, not relevant for gas turbine applications where typically $T_{IN} > 600$ K. It is finally noted that, in practical systems, the impact of catalyst dispersion is strong since transport limitations do not usually arise for all involved pathways R1 to R5.

V.4.5 CPO process optimization

For the two-stage combustion process of interest in gas-turbines, control of the outlet properties of the first (CPO) stage is crucial for the stability of the following homogeneous flame. The results presented in Section V.4.2 indicated that catalyst properties (i.e. noble metal dispersion) and operating conditions (T_{IN}) could influence the reactor outlet gas composition and temperature significantly. Additional simulations were performed in the honeycomb reactor to explore issues of CPO process optimization.

The effect of Rh dispersion on the methane conversion, synthesis gas selectivity and outlet temperature is illustrated in Table V.5. Increasing the noble metal dispersion led to higher methane conversions and H_2 and CO selectivities, and lower outlet temperatures. The effect of Rh dispersion was, however, more evident at the lower dispersion range (dispersions above 50% had a less pronounced impact). It would, therefore, appear that efforts in catalyst development should be focused on maintaining a moderately high dispersion (~20 %) for longer periods of operation.

Decreasing the linear gas velocity, while maintaining the inlet temperature at 623 K, led to higher CH_4 conversions and H_2 selectivities as shown in Table V.6. However, no effect on the CO selectivity was observed. Similar trends were observed when the inlet temperature increased, with the addition that higher outlet temperatures were obtained. High methane conversion (87%) and H_2 selectivity (81%) could thus be achieved at lower inlet velocities and higher inlet temperatures. Those values corresponded to an outlet H_2 composition of 29 vol.%. Nonetheless, care should be exercized when maximizing the methane conversion and hydrogen production by increasing the inlet temperature, since the resulting higher catalyst surface temperatures may cause catalyst deactivation and/or reactor meltdown.

Alternative catalyst preparation routes may provide a suitable solution. The observed decrease in catalyst outlet temperature with increased CH_4 conversions and H_2 outlet compositions suggested additional reforming activity when decreasing the linear velocity or when using catalysts of higher Rh dispersion. This was due to the increased residence times that, in turn, favored the slow methane reforming reactions. The reforming reactions were also favored at higher temperatures, as also shown by simulations at higher inlet temperatures.

Table V.5

Computed influence of Rh dispersion[a]

Dispersion (%)	B	CH_4 conversion (%)	S_{H2} (%)	S_{CO} (%)	H_2/CO	T_{OUT} (K)
5	4.2	65	68	60	2.3	1045
12	10	69	71	61	2.3	1007
20	28	73	72	63	2.3	970
50	70	75	73	64	2.3	941
100	140	77	74	65	2.3	912

[a]Active to geometrical area ratio (B), methane conversion, H_2 and CO selectivities, H_2/CO molar ratio and outlet temperature. Inlet conditions: $T_{IN} = 623$ K and volumetric composition: 20.4% CH_4, 10.2% O_2, 46.3% H_2O, 23.1% CO_2.

V.5 Conclusions

The partial oxidation of methane/oxygen mixtures diluted with large exhaust gas (46.3% vol. H_2O and 23.1% vol. CO_2) has been investigated experimentally and numerically over $Rh/Ce-ZrO_2$, Rh/ZrO_2 and $Rh/\alpha-Al_2O_3$ catalysts. Experiments were carried out in a short-contact time (~8 ms) honeycomb reactor at 5 bar and in an optically accessible channel-flow reactor at 6 bar. Exhaust gas analysis and temperature measurements in a honeycomb reactor provided the methane conversion and synthesis gas yields for the various catalyst supports. In situ, spatially resolved measurements of major gas-phase species concentrations over the catalyst boundary layer of a channel-flow reactor provided information on the spatial evolution of the underlying chemical processes. Physicochemical characterization of catalyst samples yielded the noble metal dispersion, total surface area and crystal structure of the support material. A detailed numerical model simulated both reactor experiments. The key conclusions of this work are the following.

1) The Rh dispersion increased in the order $Rh/\alpha-Al_2O_3$, Rh/ZrO_2 and $Rh/Ce-ZrO_2$. The $Rh/Ce-ZrO_2$ catalyst exhibited nearly twice as high dispersion as the Rh/ZrO_2 catalyst. On the other hand, the dispersion of Rh/ZrO_2 was only mildly higher (by 23%) than that of $Rh/\alpha-Al_2O_3$.

2) The heterogeneous reaction mechanism employed in this study, including only active Rh sites, was able to reproduce with good accuracy experimental results of CPO in exhaust gas-diluted mixtures. The ratio of active to geometrical surface area, deduced from chemisorption analysis, was the single parameter needed in the numerical model to account for the different supports. This indicated that water activation occurring on support sites, resulting in inverse OH spillover from the support to the noble metal sites, could be neglected under the present conditions with high water dilution.

3) An evident relationship between noble metal dispersion and catalytic behavior, in terms of methane conversion and synthesis gas yields, could be established. Both measurements and predictions indicated that an increased Rh dispersion resulted in slightly higher methane conversions, lower surface temperatures and higher synthesis gas yields. It was thus shown that the support material mainly had an indirect effect on the catalytic performance by influencing the noble metal dispersion. The redox properties of ceria, which could prevent catalyst deactivation by carbon deposition, were considered of less

importance for Rh-based catalysts and could be excluded in the numerical model, at least under the present conditions with large H_2O dilutions.

4) Comparisons between Raman-measured and numerically predicted transverse profiles of major gas-phase species concentrations, at selected reactor axial positions, were favorable for both the Rh/Ce-ZrO_2 and Rh/ZrO_2 catalysts. This allowed for identifying the spatial extent of the underlying chemical processes, which included total and partial oxidation, steam reforming and water gas shift reactions. It was shown that both total and partial oxidation reactions were present already at the beginning of the reactor (therefore suggesting a combination of direct/indirect routes for synthesis gas formation) with steam reforming becoming important farther downstream. On the other hand, dry reforming was altogether negligible.

Appendix

A References

[1]   Schwiedernoch, R., Tischer, S., Correa, C. and Deutschmann, O., Experimental and numerical study on the transient behavior of partial oxidation of methane in a catalytic monolith, *Chemical Engineering Science* 58 (2003) 633-642.

[2]   Warnatz, J., Dibble, R. W. and Maas, U., *Combustion, Physical and Chemical Fundamentals, Modeling and Simulation*, Springer-Verlag, New York, 1996.

[3]   Hickman, D. A. and Schmidt, L. D., Steps in CH_4 oxidation on Pt and Rh surfaces: high-temperature reactor simulations, *AIChE* 39 (1993) 1164-1177.

[4]   Deutschmann, O. and Schmidt, L. D., Modeling the partial oxidation of methane in a short-contact-time reactor, *AIChE* 44 (1998) 2465-2477.

[5]   Chaniotis, A. K. and Poulikakos, D., Modeling and optimization of catalytic partial oxidation methane reforming for fuel cells, *Journal of Power Sources* 142 (2004) 184-193.

[6]   Allgeier, T., Klenk, M., Landenfeld, T., Conte, E., Boulouchos, K. and Czerwinski, J., Advanced emission and fuel economy concept using combined injection of gasoline and hydrogen in SI-engines, *SAE* (2004) Paper 2004-2001-1270.

[7]   Castaldi, M. J., Etemed, S., Pfefferle, W. C., Khanna, V. and Smith, K. O., Rich-catalytic lean-burn combustion for low-single-digit NO_x gas turbines, *Journal of Engineering for Gas Turbines and Power-Transactions of the ASME* 127 (2005) 27-35.

[8]   Appel, C., Mantzaras, J., Schaeren, R., Bombach, R., Inauen, A., Tylli, N., Wolf, M., Griffin, T., Winkler, D. and Carroni, R., Partial catalytic oxidation of methane to synthesis gas over rhodium: in situ Raman measurements and detailed simulations, *Proc. Combust. Inst.* 30 (2005) 2509-2517.

[9]   Griffin, T., Winkler, D., Wolf, M., Appel, C. and Mantzaras, J., "Staged catalytic combustion method for the advanced zero emissions gas turbine power plant", ASME 2004-54101, 2004.

[10]   Bharadwaj, S. S. and Schmidt, L. D., Synthesis gas formation by catalytic oxidation of methane in fluidized bed reactors, *J. Catalysis* 146 (1994) 11-21.

[11]   Appel, C., *Katalytisch stabilisierte Verbrennung von Wasserstoff-Luft-Gemischen über Platin in laminaren und turbulenten Kanalströmungen*, Dissertation, ETH Zürich, Nr. 14642, 2002.

[12]   Deluga, G. A., Salge, J. R., Schmidt, L. D. and Verykios, X. E., Renewable hydrogen from athanol by autothermal reforming, *Science* 303 (2004) 993-997.

[13]   Dreyer, B. J., Lee, I. C., Krumenacher, J. J. and Schmidt, L. D., "Effect of steam addition on the catalytic partial oxidation of higher hydrocarbons and JP-8", IWCC6, Ischia, Italy, 2005.

[14]   Reinke, M., Mantzaras, J., Bombach, R., Schenker, S. and Inauen, A., Gas phase chemistry in catalytic combustion of methane/air mixtures over platinum at pressures of 1 bar to 16 bar, *Combust. Flame* 141 (2005) 448-468.

[15]   Reinke, M., Mantzaras, J., Schaeren, R., Bombach, R., Inauen, A. and Schenker, S., High-pressure catalytic combustion of methane over platinum: In situ experiments and detailed numerical predictions, *Combust. Flame* 136 (2004) 217-240.

[16]   Appel, C., Mantzaras, J., Schaeren, R., Bombach, R., Inauen, A., Kaeppeli, B., Hemmerling, B. and Stampanoni, A., An experimental and numerical investigation of homogeneous ignition in catalytically stabilized combustion of hydrogen/air mixtures over platinum, *Combustion and Flame* 128 (2002) 340-368.

[17]   Steiner, B., *Raman spectroscopic investigation of turbulent premixed flames*, Dissertation, University of Stuttgart, 2002.

[18]   Eisenberg, S., *Raman Spectroscopy in a jet flame*, Diploma Thesis, University of Goettingen, 1995.

[19]   Schaefer, M., Ketterle, W. and Wolfrum, J., Saturated 2D-LIF of OH and 2D Determination of Effective Collisional Lifetimes in Atmospheric Pressure Flames, *Appl. Phys. B* 52 (1991) 341-346.

[20]   Kang, W., Fujita, O. and Ito, K., Visualization of formaldehyde distribution above platinum plate by using LIF method, *ASME* 118 (1996) 82-87.

[21]   Dogwiler, U., Benz, P. and Mantzaras, J., Two-dimensional modelling for catalytically stabilized combustion of a lean methane-air mixture with elementary homogeneous and heterogeneous chemical reactions, *Combustion and Flame* 116 (1999) 243-258.

[22]   Deutschmann, O., Maier, L. I., Riedel, U., Stroemman, A. H. and Dibble, R. W., Hydrogen assisted catalytic combustion of methane on platinum, *Catalysis Today* 59 (2000) 141-150.

[23]   Kee, R. J., Dixon-Lewis, G., Warnatz, J., Coltrin, M. E. and Miller, J. A., *A Fortran computer code package for the evaluation of gas-phase multicomponent transport properties*, Report No. SAND86-8246, Sandia National Laboratories, 1996.

[24]   Kee, R. J., Rupley, F. M. and Miller, J. A., *Chemkin II: A Fortran chemical kinetics package for the analysis of gas-phase chemical kinetics*, Report No. SAND89-8009B, Sandia National Laboratories, 1996.

[25]   Coltrin, M. E., Kee, R. J. and Rupley, F. M., *Surface Chemkin: A Fortran package for analyzing heterogeneous chemical kinetics at the solid surface-gas phase interface*, Report No. SAND90-8003C, Sandia National Laboratories, 1996.

[26]   Appel, C., Mantzaras, J., Schaeren, R., Bombach, R. and Inauen, A., Turbulent catalytically stabilized combustion of hydrogen/air mixtures in entry channel flows, *Combustion and Flame* 140 (2005) 70-92.

[27]   Dietz, A. G. and Schmidt, L. D., Effect of Pressure on 3 Catalytic Partial Oxidation Reactions at Millisecond Contact Times, *Catal. Lett.* 33 (1995) 15-29.

[28]   Shin, D. I., Dreier, T. and Wolfrum, J., Spatially resolved absolute concentration and fluorescence-lifetime determination of H_2CO in atmospheric-pressure CH_4/air flames, *Appl. Phys. B* 72 (2001) 257-261.

[29]   Aghalayam, P., Park, Y. K., Fernandes, N., Papavassiliou, V., Mhadeshwar, A. B. and Vlachos, D. G., A C1 mechanism for methane oxidation on platinum, *Journal of Catalysis* 213 (2003) 23-38.

[30]   Bodke, A. S., Bharadwaj, S. S. and Schmidt, L. D., The effect of ceramic supports on partial oxidation of hydrocarbons over noble metal coated monoliths, *Journal of Catalysis* 179 (1998) 138-149.

[31]   Bruno, T., Beretta, A., Groppi, G., Roderi, M. and Forzatti, P., A study of methane partial oxidation in annular reactor: activity of Rh/α-Al$_2$O$_3$ and Rh/ZrO$_2$ catalysts, *Catalysis Today* 99 (2005) 89-98.

[32]   Goralski Jr, C. T. and Schmidt, L. D., Modeling heterogeneous and homogeneous reactions in the high-temperature catalytic combustion of methane, *Chemical Engineering Science* 54 (1999) 5791-5807.

[33]   Norton, D. G. and Vlachos, D. G., Hydrogen assisted self ignition of propane/air mixtures in catalytic microburners, *Proceedings of the Combustion Institute* 30 (2005) 2473-2480.

[34]   Carroni, R., Schmidt, V. and Griffin, T., Catalytic combustion for power generation, *Catalysis Today* 75 (2002) 287-295.

[35]   Beebe, K. W., Cairns, K. D., Pareek, V. K., Nickolas, S. G., Schlatter, J. C. and Tsuchiya, T., Development of catalytic combustion technology for single-digit emissions from industrial gas turbines, *Catalysis Today* 59 (2000) 95-115.

[36]   Veser, G., Ziauddin, M. and Schmidt, L. D., Ignition in alkane oxidation on noble-metal catalysts, *Catalysis Today* 47 (1999) 219-228.

[37]   Klein, J., Lettmann, C. and Maier, W. F., Thermally stable, silica-based amorphous porous mixed oxides prepared by sol-gel procedures, *J. Non-Cryst. Solids* 282 (2001) 203-220.

[38]   Bitter, J. H., Seshan, K. and Lercher, J. A., Mono and bifunctional pathways of CO2(CH4 reforming over Pt and Rh based catalysts., *Journal of Catalysis* 176 (1998) 93-101.

[39]   Ferreira-Aparicio, P., Guerrero-Ruiz, A. and Rodriguez-Ramos, I., Comparative study at low an dmedium reaction temperatures of syngas production by methane reformnig with carbon dioxide over silica and alumina supported catalysts, *Applied Catalysis A: General* 170 (1998) 177-187.

[40]   Wang, H. Y. and Ruckenstein, E., Carbon dioxide reforming of methane to synthesis gas over supported rhodium catalysts: the effect of support, *Applied Catalysis A: General* 204 (2000) 143-152.

[41]   Efstathiou, A. M., Kladi, A., Tsipouriari, V. A. and Verykios, X. E., Reforming of methane with carbon dioxide to synthesis gas over supported rhodium catalysts, *Journal of Catalysis* 158 (1996) 64-75.

[42]   Mark, M. F. and Maier, W. F., CO2-reforming of methane on supported Rh and Ir catalysts, *Journal of Catalysis* 164 (1996) 122-130.

[43]   Richardson, J. T., Garrait, M. and Hung, J.-K., Carbon dioxide reforming with Rh and Pt-Re catalysts dispersed on ceramic foam supports, *Applied Catalysis A: General* 255 (2003) 69-82.

[44]   Basile, F., Fornasari, G., Poluzzi, E. and Vaccari, A., Catalytic partial oxidation and CO2-reforming on Rh-based catalysts obtained from hydrotalcite-type precursors, *Applied Clay Science* 13 (1998) 329-345.

[45] Carroni, R., Griffin, T., Mantzaras, J. and Reinke, M., High-pressure experiments and modeling of methane/air catalytic combustion for power generation applications, *Catalysis Today* 83 (2003) 157-170.

[46] Reinke, M., Mantzaras, J., Schaeren, R., Bombach, R., Kreutner, W. and Inauen, A., Homogeneous ignition in high-pressure combustion of methane/air over platinum: Comparison of measurements and detailed numerical predictions, *Proc. Combust. Instit.* 29 (2002) 1021-1029.

[47] Appel, C., Mantzaras, J., Schaeren, R., Bombach, R., Inauen, A., Tylli, N., Wolf, M., Griffin, T., Winkler, D. and Carroni, R., Partial catalytic oxidation of methane to synthesis gas over rhodium: in situ Raman experiments and detailed simulations, *Procedings of the Combustion Institute* 30 (2005a) 2509-2517.

[48] Beer, S. and Willms, H., *Control of an H_2/O_2 steam generator*, Report No. DLR-FB 93-02, Deutsches Zentrum für Luft- und Raumfahrt (DLR), 1993.

[49] Eriksson, S., Wolf, M., Schneider, A., Mantzaras, J., Raimondi, F., Boutonnet, M. and Järas, S., Fuel-rich catalytic combustion of methane in zero emissions power generation processes, *Catalysis Today* 117 (2006) 447-453.

[50] Shah, R. K. and London, A. L., *Laminar Flow Forced Convection in Ducts*, Academic Press, New York, 1978.

[51] Kee, R. J., Dixon-Lewis, G., Warnatz, J., Coltrin, M. E. and Miller, J. A., *A Fortran computer code package for the evaluation of gas-phase multicomponent transport properties*, Report No. SAND86-8246, Sandia National Laboratories, 1996a.

[52] Patankar, S. V., in: Hemisphere Publ. Corp., New York, 1980.

[53] Mantzaras, J., Appel, C., Benz, P. and Dogwiler, U., Numerical modelling of turbulent catalytically stabilized channel flow combustion, *Catalysis Today* 53 (2000) 3-17.

[54] Appel, C., Mantzaras, J., Schaeren, R., Bombach, R., Inauen, A., Kaeppeli, B., Hemmerling, B. and Stampanoni, A., An experimental and numerical investigation of homogeneous ignition in catalytically stabilized combustion of hydrogen/air mixtures over platinum, *Combustion and Flame* 128 (2002) 340-368.

[55] Mantzaras, J., Appel, C. and Benz, P., Catalytic combustion of methane/air mixtures over platinum: homogeneous ignition distances in channel flow configurations, *Proceedings of the Combustion Institute* 28 (2000) 1349-1357.

[56] Kee, R. J., Rupley, F. M. and Miller, J. A., *Chemkin II: A Fortran chemical kinetics package for the analysis of gas-phase chemical kinetics*, Report No. SAND89-8009B, Sandia National Laboratories, 1996b.

[57] Pfefferle, W. C. and Pfefferle, L. D., Catalytically Stabilized Combustion, *Prog. Energy Combustion Sci.* 12 (1986) 25-41.

[58] Appel, C., Mantzaras, J., Schaeren, R., Bombach, R. and Inauen, A., Turbulent catalytically stabilized combustion of hydrogen/air mixtures in entry channel flows, *Combustion and Flame* 140 (2005b) 70-92.

[59] Mhadeshwar, A. B., Wang, H. and Vlachos, D. G., Thermodynamic consistency in microkinetic development of surface reaction mechanisms, *American Chemical Society* 226 (2003) U530 011-Fuel.

[60] Moffat, H. K., Kee, R. J., Grcar, J. F. and Miller, J. A., *Surface PSR: A Fortran program for modeling well-stirred reactors with gas and surface reactions*, Report No. SAND91-8001, Sandia National Laboratories, 1993.

[61] Karim, H., Lyle, K., Etemad, S., Smith, L., Pfefferle, W. C., Dutta, P. and Smith, K., "Advanced Catalytic Pilot for Low NOx Industrial Gas Turbines", Proceedings of ASME TURBO EXPO, Amsterdam, 2002.

[62] Griffin, T., Sundkvist, S. G., Asen, K. I. and Bruun, T., Advanced zero emission gas turbine power plant, *J. Eng. Gas Turbines and Power* 127 (2005) 81-85.

[63] Schneider, A., Mantzaras, J., Bombach, R., Schenker, S., Tylli, N. and Jansohn, P., Laser induced fluorescence of formaldehyde and Raman measurements of major species during catalytic partial oxidation of methane with large H2O and CO2 dilution at pressures up to 10 bar *Proc. Combust. Inst.* 31 (2007)
This paper is chapter II of this thesis.

[64] Schneider, A., Mantzaras, J. and Jansohn, P., Experimental and numerical investigation of the catalytic partial oxidation of CH4/O2 mixtures diluted with H2O and CO2 in a short contact time reactor, *Chem. Eng. Sci.* 61 (2006) 4634-4646.
This paper is chapter III of this thesis.

[65] Smith, L. L., Karim, H., Castaldi, M. J., Etemad, S. and Pfefferle, W. C., Rich-catalytic lean-burn combustion for fuel-flexible operation with ultra-low emissions, *Catal. Today* 117 (2006a) 438-446.

[66] Imbihl, R. and Ertl, G., Oscillatory kinetics in heterogeneous catalysis, *Chemical Reviews* 95 (1995) 697-733.

[67] Sinha, N., Bruno, C. and Bracco, F. V., Two-Dimensional, Transient Catalytic Combustion of Co-Air on Platinum, *Physicochemical Hydrodynamics* 6 (1985) 373-391.

[68] Hayes, R. E. and Kolaczkowski, S. T., *Introduction into Catalytic Combustion*, Gordon and Breach Science Publisher, Amsterdam, 1997.

[69] Schwiedernoch, R., Tischer, S., Correa, C., Deutschmann, O. and Warnatz, J., "Experimental and numerical investigation of the ignition of methane combustion in a platinum-coated honeycomb monolith", Proceedings of the Combustion Institute, Pittsburgh, 2002.

[70] Zygourakis, K. and Aris, R., "Heat transfer in the array passages of a monolith reactor", AIChE 75th Annual Meeting, 1983.

[71] Kramer, J. F., Reihani, S. A. S. and Jackson, G. S., Low temperature combustion of hydrogen on supported Pd catalysts, *Proc. Combust. Instit.* 29 (2002) 989-996.

[72] Mantzaras, J., Understanding and modeling of thermofluidic processes in catalytic combustion, *Catalysis Today* 117 (2006) 394-406.

[73] Veser, G. and Frauhammer, J., Modelling steady state and ignition during catalytic methane oxidation in a monolith reactor, *Chemical Engineering Science* 55 (2000) 2271-2286.

[74] Touloukian, Y. S., Powell, R. W., Ho, C. Y. and Klemens, P. G., in: Y. S. Touloukian and C. Y. Ho, *Thermophysical properties of matter*, the TPRC Data Series, Plenum, New York, 1970.

[75]   Siegel, R. and Howell, J. R., *Thermal radiation heat transfer*, Hemisphere, New York, p. 271, 1981.

[76]   Karagiannidis, S., Mantzaras, J., Jackson, G. S. and Boulouchos, K., Hetero-/homogeneous combustion and stability maps of methane-fueled catalytic microreactors, *Proc. Combust. Inst.* 31 (2007)

[77]   Ferziger, J. H. and Petric, M., *Computational methods for fluid dynamics*, Springer Verlag, New York, p.142, 1999.

[78]   Lutz, A. E., Kee, R. J. and Miller, J. A., *SENKIN: A Fortran program for predicting homogeneous gas phase chemical kinetics with sensitivity analysis*, Report No. SAND87-8248, Sandia National Laboratories, 1996.

[79]   Deutschmann, O., Schmidt, R., Behrendt, F. and Warnatz, J., Numerical modeling of catalytic ignition, *Proc. Combust. Instit.* 26 (1996) 1747-1754.

[80]   Smith, L. L., Karim, H., Castaldi, M. J., Etemad, S. and Pfefferle, W. C., "Fuel-flexible fuel-rich catalytic combustion with ultra-low emissions", Proceedings, Sixth International Workshop on Catalytic Combustion (IWCC6), Ischia, Italy, pp. 55-60., 2006b.

[81]   Griffin, T., Sundkvist, S. G., Asen, K. I. and Bruun, T., Advanced zero emission gas turbine power plant, *Journal of Engineering for Gas Turbines and Power* 127 (2005) 81-85.

[82]   York, A. P. E., Xiao, T. and Green, M. L. H., Brief overview of the partial oxidation of methane to synthesis gas, *Topics in Catalysis* 22 (2003) 345-358.

[83]   Tsang, S. C., Claridge, J. B. and Green, M. L. H., Recent advances in the conversion of methane to synthesis gas, *Catalysis Today* 23 (1995) 3-15.

[84]   Mallens, E. P. J., Hoebink, J. H. B. J. and Marin, G. B., The reaction mechanism of the partial oxidation of methane to synthesis gas: A transient kinetic study over rhodium and a comparison with platinum, *J. Catal.* 167 (1997) 43-56.

[85]   Heitnes-Hofstad, K., Hoebink, J. H. B. J., Holmen, A. and Marin, G. B., Partial oxidation of methane to synthesis gas over rhodium catalysts, *Catalysis Today* 40 (1998) 157-170.

[86]   Vermeiren, W. J. M., Blomsma, E. and Jacobs, P. A., Catalytic and thermodynamic approach of the oxyreforming reaction of methane, *Catalysis Today* 13 (1992) 427-436.

[87]   Buyevskaya, O. V., Wolf, D. and Baerns, M., Rhodium-catalyzed partial oxidation of methane to CO and H_2 – transient studies on its mechanism, *Catalysis Letters* 29 (1994) 249-260.

[88]   van Looij, F., Stobbe, E. R. and Geus, J. W., Mechanism of the partial oxidation of methane to synthesis gas over Pd, *Catalysis Letters* 50 (1998) 59-67.

[89]   Passos, F. B., de Oliveira, E. R., Mattos, L. V. and Noronha, F. B., Partial oxidation of methane to synthesis gas on $Pt/Ce_xZr_{x-1}O_2$ catalysts: the effect of the support reducibility and of the metal dispersion on stability of the catalysts, *Catal. Today* 101 (2005) 23-30.

[90]   Weng, W. Z., Luo, C. R., Huang, J. J., Liao, Y. Y. and Wan, H. L., Comparative study on the mechanisms of partial oxidation of methane to syngas over rhodium supported on SiO_2 and $\gamma-Al_2O_3$, *Topics in Catalysis* 22 (2003) 87-93.

[91] Reinke, M., Mantzaras, J., Schaeren, R., Bombach, R., Inauen, A. and Schenker, S., Homogeneous ignition of CH_4/air and H_2O- and CO_2-diluted CH_4/O_2 mixtures over platinum; an experimental and numerical investigation at pressures up to 16 bar, *Proc. Combust. Instit.* 30 (2005a) 2519-2527.

[92] Dogwiler, U., Mantzaras, J., Benz, P., Kaeppeli, B., Bombach, R. and Arnold, A., Homogeneous ignition of Methane/Air mixtures over platinum: Comparison of measurements and detailed numerical predictions, *Proc. Combust. Instit.* 27 (1998) 2275-2282.

[93] Gatica, J. M., Baker, R. T., Fornasiero, P., Bernal, S., Blanco, G. and Kaspar, J., Rhodium dispersion in a $Rh/Ce_{0.68}Zr_{0.32}O_2$ catalyst investigated by HRTEM and H_2 chemisorption, *Journal of Physical Chemistry B* 104 (2000) 4667-4672.

[94] Siegel, R. and Howell, J. R., *Thermal Radiation Heat Transfer*, Hemisphere, New York, p. 271, 1981.

[95] Hy, Z., $CeO_{1.5}$-stabilized tetragonal ZrO_2, *Journal of Materials Science* 29 (1994) 4351-4356.

[96] Mastelaro, V. R., Briois, V., de Souza, D. P. F. and Silva, C. L., Structural studies of a ZrO_2-CeO_2 doped system, *Journal of the European Ceramic Society* 23 (2003) 273-282.

[97] Hu, Y. H. and Ruckenstein, E., Pulse-MS study of the partial oxidation of methane over Ni/La2O3 catalyst, *Catalysis Letters* 34 (1995) 41-50.

[98] Otsuka, K., Wang, Y., Sunada, E. and Yamanaka, I., Direct partial oxidation of methane to synthesis gas by cerium oxide, *Journal of Catalysis* 175 (1998)

[99] Fathi, M., Bjorgum, E., Viig, T. and Rokstad, O. A., Partial oxidation of methane to synthesis gas: elimination of gas phase oxygen, *Catalysis Today* 63 (2000) 489-497.

[100] Xu, J. G. and Froment, G. F., Methane steam reforming, methanation and water-gas shift: I. Intrinsic kinetics, *AIChE Journal* 35 (1989) 88-96.

[101] Stagg, S. M., Romeo, E., Padro, C. and Resasco, D. E., Effect of promotion with Sn on supported Pt catalysts for CO_2 reforming of CH_4, *Journal of Catalysis* 178 (1998) 137-145.

[102] Dong, W. S., Roh, H. S., Jun, K. W., Park, S. E. and Oh, Y. S., Methane reforming over Ni/Ce-ZrO2 catalysts: effect of nickel content, *Applied Catalysis A* 226 (2002) 63-72.

[103] Laosiripojana, N., Sutthisripok, W. and Assabumrungrat, S., Synthesis gas production from dry reforming of methane over CeO_2-doped Ni/Al_2O_3: influence of the doping ceria on the resistance toward carbon formation, *Chemical Engineering Journal* 112 (2005) 13-22.

[104] Laosiripojana, N. and Assabumrungrat, S., Methane steam reforming over Ni/Ce-ZrO_2 catalyst: influence of Ce-ZrO_2 support on reactivity, resistance towrad carbon formation, and intrinsic reaction kinetics, *Appl. Catal. A* 290 (2005a) 200-211.

[105] Kurungot, S. and Yamaguchi, T., Stability improvement of Rh/γ-Al_2O_3 catalyst layer by ceria doping for steam reforming in an integrated catalytic membrane recator system, *Catalysis Letters* 92 (2004) 181-187.

[106] Wei, J. and Iglesia, E., Mechanism and site requirements for activation and chemical conversion of methanon supported Pt clusters and turnover rate comparisons among noble metals, *Journal of Physical Chemistry B* 108 (2004) 4094-4103.

[107] Iglesia, E., Kinetic coupling and methane activation on supported metal clusters: structural requirements and reaction pathway, *12th Nordic Symposium on Catalysis, Trondheim, Norway* (2006)

[108] Wang, D., Dewaele, O., De Groote, A. M. and Froment, G. F., Reaction mechanism and role of the support in the partial oxidation of methane on Rh/Al$_2$O$_3$, *Journal of Catalysis* 159 (1996) 418-426.

[109] Stoppek-Langner, K., Goldwasser, J., Houalla, M. and Hercules, D. M., Infrared and carbon-dioxide chemisorption study of Mo/ZrO$_2$ catalysts, *Catalysis Letters* 32 (1995) 263-271.

B Surface reaction mechanism

The surface reaction mechanism by Deutschmann et. al. in CHEMKIN format as used for computations [1, Schwiedernoch et al., 2003]:

```
REACTIONS    JOULES/MOLE
!****************************************************************
!**** 1. ADSORPTION
!****************************************************************
H2    +Rh(s) +Rh(s) =>H(s)  +H(s)    0.010E-00 0.0    0.0
                      STICK
O2    +Rh(s) +Rh(s) =>O(s)  +O(s)    0.010E-00 0.0    0.0
                      STICK
CH4   +Rh(s)       =>CH4(s)          8.000E-03 0.0    0.0
                      STICK
H2O   +Rh(s) =>H2O(s)                1.000E-01 0.0    0.0
                      STICK
CO2   +Rh(s) =>CO2(s)                1.000E-05 0.0    0.0
                      STICK
CO    +Rh(s) =>CO(s)                 5.000E-01 0.0    0.0
                      STICK
!****************************************************************
!**** 2. DESORPTION
!****************************************************************
H(s)  +H(s)  =>Rh(s) +Rh(s) +H2     3.000E+21 0.0    77800
O(s)  +O(s)  =>Rh(s) +Rh(s) +O2     1.300E+22 0.0    355200
                COV/O(s)   0.0 0.0  -280000/
H2O(s)       =>H2O   +Rh(s)         3.000E+13 0.0    45000
CO(s)        =>CO    +Rh(s)         3.500E+13 0.0    133400
                COV/CO(s)  0.0 0.0  -15000/
CO2(s)       =>CO2   +Rh(s)         1.000E+13 0.0    21700
CH4(s)       =>CH4   +Rh(s)         1.000E+13 0.0    25100
!****************************************************************
!**** 3. SURFACE REACTIONS
!****************************************************************
H(s)  +O(s)  =>OH(s)  +Rh(s)        5.000E+22 0.0    83700
OH(s) +Rh(s) =>H(s)   +O(s)         3.000E+20 0.0    37700
H(s)  +OH(s) =>H2O(s) +Rh(s)        3.000E+20 0.0    33500
H2O(s) +Rh(s) =>H(s)  +OH(s)        5.000E+22 0.0    106400
OH(s) +OH(s) =>H2O(s) +O(s)         3.000E+21 0.0    100800
H2O(s) +O(s) =>OH(s)  +OH(s)        3.000E+21 0.0    224200
C(s)  +O(s)  =>CO(s)  +Rh(s)        3.000E+22 0.0    97900
CO(s) +Rh(s) =>C(s)   +O(s)         2.500E+21 0.0    169000
CO(s) +O(s)  =>CO2(s) +Rh(s)        1.400E+20 0.0    121600
CO2(s) +Rh(s) =>CO(s) +O(s)         3.000E+21 0.0    115300
!****************************************************************
CH4(s) +Rh(s) =>CH3(s) +H(s)        3.700E+21 0.0    61000
CH3(s) +H(s)  =>CH4(s) +Rh(s)       3.700E+21 0.0    51000
CH3(s) +Rh(s) =>CH2(s) +H(s)        3.700E+24 0.0    103000
CH2(s) +H(s)  =>CH3(s) +Rh(s)       3.700E+21 0.0    44000
CH2(s) +Rh(s) =>CH(s)  +H(s)        3.700E+24 0.0    100000
CH(s)  +H(s)  =>CH2(s) +Rh(s)       3.700E+21 0.0    68000
CH(s)  +Rh(s) =>C(s)   +H(s)        3.700E+21 0.0    21000
C(s)   +H(s)  =>CH(s)  +Rh(s)       3.700E+21 0.0    172800
!****************************************************************
CH4(s) +O(s)  =>CH3(s) +OH(s)       1.700E+24 0.0    80300
CH3(s) +OH(s) =>CH4(s) +O(s)        3.700E+21 0.0    24300
CH3(s) +O(s)  =>CH2(s) +OH(s)       3.700E+24 0.0    120300
```

```
CH2(s) +OH(s) =>CH3(s) +O(s)       3.700E+21 0.0    15100
CH2(s) +O(s)  =>CH(s)  +OH(s)      3.700E+24 0.0    158400
CH(s)  +OH(s) =>CH2(s) +O(s)       3.700E+21 0.0    36800
CH(s)  +O(s)  =>C(s)   +OH(s)      3.700E+21 0.0    30100
C(s)   +OH(s) =>CH(s)  +O(s)       3.700E+21 0.0    145500
!************************************************************
END
```

C   Gas-phase reaction mechanism

The gas-phase reaction mechanism by Warnatz et. al. in CHEMKIN format as used for computations [2, Warnatz et al., 1996]:

```
REACTIONS    JOULES/MOLE
!****************************************
!***   01.  H2-O2 React. (no HO2, H2O2)
!****************************************
O2   +H    =OH   +O          8.700E+13 0.0    60300.
H2   +O    =OH   +H          5.060E+04 2.670  26300.
H2   +OH   =H2O  +H          1.000E+08 1.600  13800.
OH   +OH   =H2O  +O          1.500E+09 1.140  420.
!****************************************
!***   02.  Recombination Reactions
!****************************************
H    +H    +M   =H2   +M     1.800E+18 -1.000  0.000
  H2/1.0/ H2O/6.5/ O2/0.40/ N2/0.4/ CO/0.75/ CO2/1.50/ CH4/3.0/
O    +O    +M   =O2   +M     2.900E+17 -1.000  0.0
  H2/1.0/ H2O/6.5/ O2/0.40/ N2/0.4/ CO/0.75/ CO2/1.50/ CH4/3.0/
H    +OH   +M   =H2O  +M     2.200E+22 -2.000  0.000
  H2/1.0/ H2O/6.5/ O2/0.40/ N2/0.4/ CO/0.75/ CO2/1.50/ CH4/3.0/
!****************************************
!***   03.  HO2 Formation/Consumption
!****************************************
H    +O2   +M   =HO2  +M     2.300E+18 -0.800  0.0
  H2/1.0/ H2O/6.5/ O2/0.40/ N2/0.4/ CO/0.75/ CO2/1.50/ CH4/3.0/
HO2  +H    =OH   +OH         1.500E+14 0.0    4200.
HO2  +H    =H2   +O2         2.500E+13 0.0    2900.
HO2  +H    =H2O  +O          3.000E+13 0.0    7200.
HO2  +O    =OH   +O2         1.800E+13 0.0    -1700.
HO2  +OH   =H2O  +O2         6.000E+13 0.0    0.0
!****************************************
!***   04.  H2O2 Formation/Consumption
!****************************************
HO2  +HO2  =H2O2  +O2        2.500E+11 0.0    -5200.
OH   +OH   +M   =H2O2  +M    3.250E+22 -2.000  0.0
  H2/1.0/ H2O/6.5/ O2/0.40/ N2/0.4/ CO/0.75/ CO2/1.50/ CH4/3.0/
H2O2  +H    =H2   +HO2       1.700E+12 0.0    15700
H2O2  +H    =H2O  +OH        1.000E+13 0.0    15000
H2O2  +O    =OH   +HO2       2.803E+13 0.0    26800
H2O2  +OH   =H2O  +HO2       5.400E+12 0.0    4200
!****************************************
!***   05.  CO Reactions
!****************************************
CO   +OH   =CO2  +H          4.760E+07 1.230  290
CO   +HO2  =CO2  +OH         1.500E+14 0.0    98700
CO   +O    +M   =CO2  +M     7.100E+13 0.0    -19000
  H2/1.0/ H2O/6.5/ O2/0.40/ N2/0.4/ CO/0.75/ CO2/1.50/ CH4/3.0/
CO   +O2   =CO2  +O          2.500E+12 0.0    200000
!****************************************
```

!***   10. CH Reactions
!**
CH   +O   =CO   +H   4.000E+13 0.0   0.0
CH   +O2   =CHO   +O   3.000E+13 0.0   0.0
CH   +CO2   =CHO   +CO   3.400E+12 0.0   2900
CH   +OH   =CHO   +H   3.000E+13 0.0   0.0
CH   +H2O   =CH2O   +H   4.560E+12 0.0   -3200
CH   +H2O   =CH2   +OH   1.140E+12 0.0   -3200
!**
!***   11. CHO REACTIONS
!**
CHO   +M   =CO   +H   +M   7.100E+14 0.0   70300
   H2/1.0/ H2O/6.5/ O2/0.40/ N2/0.4/ CO/0.75/ CO2/1.50/ CH4/3.0/
CHO   +H   =CO   +H2   9.000E+13 0.0   0.0
CHO   +O   =CO   +OH   3.000E+13 0.0   0.0
CHO   +O   =CO2   +H   3.000E+13 0.0   0.0
CHO   +OH   =CO   +H2O   1.000E+14 0.0   0.0
CHO   +O2   =CO   +HO2   3.000E+12 0.0   0.0
CHO   +CHO   =CH2O   +CO   3.000E+13 0.0   0.0
!**
!***   12. CH2 Reactions
!**
CH2   +H   =CH   +H2   6.000E+12 0.0   -7500
CH2   +O   =>CO   +H   +H   8.400E+12 0.0   0.0
CH2   +CH2   =C2H2   +H2   1.200E+13 0.0   3400.
CH2   +CH2   =C2H2   +H   +H   1.100E+14 0.0   3400.
CH2   +CH3   =C2H4   +H   4.200E+13 0.0   0.0
CH2   +O2   =CO   +OH   +H   1.300E+13 0.0   6200.
CH2   +O2   =CO2   +H2   1.200E+13 0.0   6200.
CH2(S) +M   =CH2   +M   1.200E+13 0.0   0.0
   H2/1.0/ H2O/6.5/ O2/0.40/ N2/0.4/ CO/0.75/ CO2/1.50/ CH4/3.0/
CH2(S) +O2   =CO   +OH   +H   3.100E+13 0.0   0.0
CH2(S) +H2   =CH3   +H   7.200E+13 0.0   0.0
CH2(S) +H2O   =>CH3   +OH   7.900E+13 0.0   0.0
CH2(S) +CH3   =C2H4   +H   1.600E+13 0.00   -2380.
!**
!***   13. CH2O Reactions
!**
CH2O +M   =CHO   +H   +M   5.000E+16 0.0   320000.
   H2/1.0/ H2O/6.5/ O2/0.40/ N2/0.4/ CO/0.75/ CO2/1.50/ CH4/3.0/
CH2O +H   =CHO   +H2   2.300E+10 1.05   13700.
CH2O +O   =CHO   +OH   4.150E+11 0.57   11600.
CH2O +OH   =CHO   +H2O   3.400E+09 1.2   -1900.
CH2O +HO2   =CHO   +H2O2   3.000E+12 0.0   54700.
CH2O +CH3   =CHO   +CH4   1.000E+11 0.0   25500.
CH2O +O2   =CHO   +HO2   6.000E+13 0.0   170700.
!**
!***   14. CH3 Reactions
!**
CH3   +M   =CH2   +H   +M   1.000E+16 0.0   379000.
   H2/1.0/ H2O/6.5/ O2/0.40/ N2/0.4/ CO/0.75/ CO2/1.50/ CH4/3.0/
CH3   +O   =CH2O   +H   8.430E+13 0.0   0.0
!   HIGH PRESSURE OPTIONS
!--- Next value obtained from Kassel formalism at p = 0.0253 bar
!--- CH3   +H   =CH4   3.770E+35 -7.30   36000.
!--- Next value obtained from Kassel formalism at p = 0.1200 bar
!--- CH3   +H   =CH4   1.260E+36 -7.30   36690.
!--- Next value obtained from Kassel formalism at p = 1.0000 bar
!--- CH3   +H   =CH4   1.930E+36 -7.00   38000.
!--- Next value obtained from Kassel formalism at p = 3.0000 bar

```
CH3    +H     =CH4            4.590E+35 -6.70 39300.
!--- Next value obtained from Kassel formalism at p = 9.0000 bar
!--- CH3    +H     =CH4            8.340E+33 -6.10  38020.
!--- Next value obtained from Kassel formalism at p = 20.000 bar
!--- CH3    +H     =CH4            2.500E+32 -5.60  36520.
!--- Next value obtained from Kassel formalism at p = 50.000 bar
!--- CH3    +H     =CH4            1.390E+30 -4.90  32810.
CH3    +OH    =>CH3O  +H         2.260E+14 0.0 64800.
CH3O   +H     =>CH3   +OH         4.750E+16 -0.13 88000.
CH3    +O2    =>CH2O   +OH        3.300E+11 0.0   37400.
CH3    +HO2   =CH3O   +OH         1.800E+13 0.0     0.0
CH3    +HO2   =CH4   +O2          3.600E+12 0.0     0.0
CH3    +CH3   =>C2H4   +H2        1.000E+16 0.0 134000.
! HIGH PRESSURE OPTIONS
!--- Next value obtained from Kassel formalism at p = 0.0253 bar
!--- CH3    +CH3    =C2H6         3.230E+58 -14.0 77790.
!--- Next value obtained from Kassel formalism at p = 0.1200 bar
!--- CH3    +CH3    =C2H6         2.630E+57 -13.5  80790.
!--- Next value obtained from Kassel formalism at p = 1.0000 bar
!--- CH3    +CH3    =C2H6         1.690E+53 -12.0   81240.
!--- Next value obtained from Kassel formalism at p = 3.0000 bar
CH3    +CH3    =C2H6         1.320E+49 -10.7   75680.
!--- Next value obtained from Kassel formalism at p = 9.0000 bar
!--- CH3    +CH3    =C2H6         8.320E+43 -9.1 67000.
!--- Next value obtained from Kassel formalism at p = 20.000 bar
!--- CH3    +CH3    =C2H6         1.840E+39 -7.7 57840.
!--- Next value obtained from Kassel formalism at p = 50.000 bar
!--- CH3    +CH3    =C2H6         3.370E+33 -6.0 45280.
CH3    +M     =CH   +H2    +M     6.900E+14 0.0   345030.
   H2/1.0/ H2O/6.5/ O2/0.40/ N2/0.4/ CO/0.75/ CO2/1.50/ CH4/3.0/
CH3    +OH    =>CH2(S) +H2O       2.300E+13 0.0     0.0
!**************************************
!***    15a.  CH3O Reactions
!**************************************
CH3O  +M    =CH2O  +H    +M     5.000E+13 0.0   105000.
   H2/1.0/ H2O/6.5/ O2/0.40/ N2/0.4/ CO/0.75/ CO2/1.50/ CH4/3.0/
CH3O  +H    =CH2O  +H2         1.800E+13 0.0     0.0
CH3O  +O2   =CH2O  +HO2        4.000E+10 0.0    8900.
CH2O  +CH3O  =>CH3OH  +CHO       0.600E+12 0.0    13800.
CH3OH  +CHO  =>CH2O  +CH3O       0.650E+10 0.0    57200.
CH3O  +O    =O2    +CH3         1.100E+13 0.0     0.0
CH3O  +O    =OH    +CH2O        1.400E+12 0.0     0.0
!**************************************
!***    15b.  CH2OH Reactions
!**************************************
CH2OH  +M    =CH2O  +H    +M     5.000E+13 0.0   105000.
   H2/1.0/ H2O/6.5/ O2/0.40/ N2/0.4/ CO/0.75/ CO2/1.50/ CH4/3.0/
CH2OH  +H    =CH2O  +H2         3.000E+13 0.0     0.0
CH2OH  +O2   =CH2O  +HO2        1.000E+13 0.0    30000.
!**************************************
!***    16.  CH3O2 Reactions
!**************************************
CH3O2  +M    =>CH3   +O2    +M     0.724E+17 0.0   111100.
   H2/1.0/ H2O/6.5/ O2/0.40/ N2/0.4/ CO/0.75/ CO2/1.50/ CH4/3.0/
CH3    +O2    +M    =>CH3O2 +M     0.141E+17 0.0    -4600.
   H2/1.0/ H2O/6.5/ O2/0.40/ N2/0.4/ CO/0.75/ CO2/1.50/ CH4/3.0/
CH3O2  +CH2O  =>CH3O2H +CHO       0.130E+12 0.0    37700.
CH3O2H +CHO  =>CH3O2 +CH2O       0.250E+11 0.0    42300.
CH3O2  +CH3  =>CH3O  +CH3O        0.380E+13 0.0    -5000.
CH3O   +CH3O  =>CH3O2 +CH3        0.200E+11 0.0     0.0
```

```
CH3O2  +HO2   =>CH3O2H +O2        0.460E+11 0.0   -10900.
CH3O2H +O2    =>CH3O2  +HO2        0.300E+13 0.0   163300.
CH3O2  +CH3O2 =>CH2O  +CH3OH +O2   0.180E+13 0.0     0.0
CH2O  +CH3OH +O2   =>CH3O2 +CH3O2  0.000E+00 0.0     0.0
CH3O2  +CH3O2 =>CH3O  +CH3O  +O2   0.370E+13 0.0   9200.
CH3O  +CH3O  +O2  =>CH3O2 +CH3O2   0.000E+00 0.0     0.0
!**************************************
!***    17. CH4 Reactions
!**************************************
CH4   +H   =H2   +CH3        1.300E+04 3.000  33600.
CH4   +O   =OH   +CH3        6.923E+08 1.560  35500.
CH4   +OH  =H2O  +CH3        1.600E+07 1.830  11600.
CH4   +HO2 =H2O2  +CH3        1.100E+13 0.0  103100.
CH4   +CH  =C2H4  +H        3.000E+13 0.0   -1700.
CH4   +CH2 =CH3  +CH3        1.300E+13 0.0   39900.
!**************************************
!***    18. CH3OH Reactions
!**************************************
! HIGH PRESSURE OPTIONS
!--- Next value obtained from Kassel formalism at p = 0.0253 bar
!--- CH3OH      =CH3  +OH     2.170E+24 -3.30  368000
!--- Next value obtained from Kassel formalism at p = 0.1200 bar
!--- CH3OH      =CH3  +OH     3.670E+26 -3.70  381400
!--- Next value obtained from Kassel formalism at p = 1.0000 bar
!--- CH3OH      =CH3  +OH     9.510E+29 -4.30  404100
!--- Next value obtained from Kassel formalism at p = 3.0000 bar
CH3OH      =CH3  +OH     2.330E+29 -4.00  407100
!--- Next value obtained from Kassel formalism at p = 9.0000 bar
!--- CH3OH      =CH3  +OH     8.440E+27 -3.50  406300
!--- Next value obtained from Kassel formalism at p = 20.000 bar
!--- CH3OH      =CH3  +OH     2.090E+26 -3.00  403400
!--- Next value obtained from Kassel formalism at p = 50.000 bar
!--- CH3OH      =CH3  +OH     4.790E+24 -2.50  400100
CH3OH  +H   =CH2OH  +H2     4.000E+13 0.0   25500.
CH3OH  +O   =CH2OH  +OH     1.000E+13 0.0   19600.
CH3OH  +OH  =CH2OH  +H2O     1.000E+13 0.0    7100.
CH3OH  +HO2 =>CH2OH  +H2O2     0.620E+13 0.0   81100.
CH2OH  +H2O2 =>HO2  +CH3OH     0.100E+08 1.7   47900.
CH3OH  +CH3 =CH4  +CH2OH     9.000E+12 0.0   41100.
CH3O  +CH3OH =>CH2OH  +CH3OH     0.200E+12 0.0   29300.
CH2OH  +CH3OH =>CH3O  +CH3OH     0.220E+05 1.7   45400.
CH3OH  +CH2O =>CH3O  +CH3O     0.153E+13 0.0  333200.
CH3O  +CH3O  =>CH3OH  +CH2O     0.300E+14 0.0    0.0
!**************************************
!***    19. CH3O2H Reactions
!**************************************
CH3O2H     =CH3O  +OH     4.000E+15 0.0   180500.
OH   +CH3O2H =H2O   +CH3O2     2.600E+12 0.0    0.0
!**************************
!***         *
!*** 4. C2 MECHANISM    *
!***         *
!**************************
!**************************************
!***    20. C2H Reactions
!**************************************
C2H   +O   =CO   +CH        1.000E+13 0.0    0.0
C2H   +O2  =HCCO  +O        3.000E+12 0.0    0.0
!**************************************
!***    20A.  HCCO Reactions
```

```
!***************************************
HCCO   +H    =CH2   +CO          1.500E+14 0.0    0.0
HCCO   +O    =>CO   +CO   +H      9.600E+13 0.0    0.0
HCCO   +CH2  =C2H3  +CO           3.000E+13 0.0    0.0
!***************************************
!***   21.   C2H2 Reactions
!***************************************
C2H2   +M    =C2H   +H    +M      3.600E+16 0.0   446000.
   H2/1.0/ H2O/6.5/ O2/0.40/ N2/0.4/ CO/0.75/ CO2/1.50/ CH4/3.0/
C2H2   +O2   =HCCO  +OH           2.000E+08 1.5   126000.
C2H2   +H    =C2H   +H2           6.023E+13 0.0   116400.
C2H2   +O    =CH2   +CO           2.168E+06 2.1     6570.
C2H2   +O    =HCCO  +H            5.059E+06 2.1     6570.
C2H2   +OH   =H2O   +C2H          6.000E+13 0.0    54200.
!***************************************
!***   21A.   CH2CO Reactions
!***************************************
CH2CO  +M    =CH2   +CO   +M      1.000E+16 0.0   248000.
   H2/1.0/ H2O/6.5/ O2/0.40/ N2/0.4/ CO/0.75/ CO2/1.50/ CH4/3.0/
CH2CO  +H    =CH3   +CO           3.600E+13 0.0    14100.
CH2CO  +O    =CHO   +CHO          2.300E+12 0.0     5700.
CH2CO  +OH   =CH2O  +CHO          1.000E+13 0.0      0.0
!***************************************
!***   25.   C2H3 Reactions
!***************************************
! HIGH PRESSURE OPTIONS
!--- Next value obtained from Kassel formalism at p = 0.0253 bar
!--- C2H3        =C2H2  +H          0.940E+38 -8.5  190100.
!--- Next value obtained from Kassel formalism at p = 0.1200 bar
!--- C2H3        =C2H2  +H          3.770E+38 -8.5  190290.
!--- Next value obtained from Kassel formalism at p = 1.0000 bar
!--- C2H3        =C2H2  +H          4.730E+40 -8.8  194500.
!--- Next value obtained from Kassel formalism at p = 3.0000 bar
C2H3        =C2H2  +H          1.890E+42 -9.1  199560.
!--- Next value obtained from Kassel formalism at p = 9.0000 bar
!--- C2H3        =C2H2  +H          3.630E+43 -9.3  205360.
!--- Next value obtained from Kassel formalism at p = 20.000 bar
!--- C2H3        =C2H2  +H          4.370E+43 -9.2  208300.
!--- Next value obtained from Kassel formalism at p = 50.000 bar
!--- C2H3        =C2H2  +H          0.950E+45 -9.5  219660.
C2H3   +OH   =C2H2  +H2O          5.000E+13 0.0      0.0
C2H3   +H    =C2H2  +H2           1.200E+13 0.0      0.0
C2H3   +O    =C2H2  +OH           1.000E+13 0.0      0.0
C2H3   +O    =CH3   +CO           1.000E+13 0.0      0.0
C2H3   +O    =CHO   +CH2          1.000E+13 0.0      0.0
!C2H3  +O2   =CH2O  +CHO           5.420E+12 0.0      0.0
! DUPLICATE
!C2H3  +O2   =CH2O  +CHO          -2.460E+15 -0.78  13120.
! DUPLICATE
! Replaced by a fitting accurate for T=500K-2500K
C2H3   +O2   =CH2O  +CHO           3.000E+12 -0.05   -3324.

C2H3   +O2   =CH2CHO +O            2.460E+15 -0.78  13120.
!***************************************
!***   22A.   CH3CO Reactions
!***************************************
! HIGH PRESSURE OPTIONS
!--- Next value obtained from Kassel formalism at p = 0.0253 bar
!--- CH3CO       =CH3   +CO          4.130E+23 -4.7  68500.
!--- Next value obtained from Kassel formalism at p = 0.1200 bar
```

!--- CH3CO   =CH3   +CO   3.810E+24 -4.8   69990.
!--- Next value obtained from Kassel formalism at p = 1.0000 bar
!--- CH3CO   =CH3   +CO   2.320E+26 -5.0   75120.
!--- Next value obtained from Kassel formalism at p = 3.0000 bar
CH3CO   =CH3   +CO   4.370E+27 -5.2 80940.
!--- Next value obtained from Kassel formalism at p = 9.0000 bar
!--- CH3CO   =CH3   +CO   8.790E+28 -5.4   88330.
!--- Next value obtained from Kassel formalism at p = 20.000 bar
!--- CH3CO   =CH3   +CO   2.400E+29 -5.4   92950.
!--- Next value obtained from Kassel formalism at p = 50.000 bar
!--- CH3CO   =CH3   +CO   7.320E+29 -5.4   98400.
!--- OK WA 84 NO REC CEC
CH3CO +H   =CH2CO +H2   2.000E+13 0.0   0.0
!**
!***   22B. CH2CHO Reactions
!**
CH2CHO +H   =CH2CO +H2   2.000E+13 0.0   0.0
!**
!***   23.   C2H4 Reactions
!**
C2H4 +M   =C2H2 +H2   +M   7.500E+17 0.0   332000.
  H2/1.0/ H2O/6.5/ O2/0.40/ N2/0.4/ CO/0.75/ CO2/1.50/ CH4/3.0/
C2H4 +M   =C2H3 +H   +M   0.850E+18 0.0   404000.
  H2/1.0/ H2O/6.5/ O2/0.40/ N2/0.4/ CO/0.75/ CO2/1.50/ CH4/3.0/
C2H4 +H   =C2H3 +H2   0.540E+15 0.0   62900.
C2H4 +O   =CH2CHO +H   1.020E+06 2.08   0.0
C2H4 +O   =CHO   +CH3   2.420E+06 2.08   0.0
C2H4 +OH   =C2H3 +H2O   2.200E+13 0.0   24900.
!**
!***   23A. CH3CHO Reactions
!**
CH3CHO +M   =CH3   +CHO   +M   7.000E+15 0.0   342800.
  H2/1.0/ H2O/6.5/ O2/0.40/ N2/0.4/ CO/0.75/ CO2/1.50/ CH4/3.0/
CH3CHO +H   =CH3CO +H2   2.100E+09 1.16   10100.
CH3CHO +H   =CH2CHO +H2   2.000E+09 1.16   10100.
CH3CHO +O   =CH3CO +OH   5.000E+12 0.0   7600.
CH3CHO +O   =CH2CHO +OH   8.000E+11 0.0   7600.
CH3CHO +O2   =CH3CO +HO2   4.000E+13 0.0   164300.
CH3CHO +OH   =CH3CO +H2O   2.300E+10 0.73   -4700.
CH3CHO +HO2 =CH3CO +H2O2   3.000E+12 0.0   50000.
CH3CHO +CH2 =CH3CO +CH3   2.500E+12 0.0   15900.
CH3CHO +CH3 =CH3CO +CH4   2.000E-06 5.64   10300.
!**
!***   24. C2H5 Reactions
!**
! HIGH PRESSURE OPTIONS
!--- Next value obtained from Kassel formalism at p = 0.0253 bar
!--- C2H5   =C2H4 +H   2.650E+42 -9.5 210100.
!--- Next value obtained from Kassel formalism at p = 0.1200 bar
!--- C2H5   =C2H4 +H   1.760E+43 -9.5 215050.
!--- Next value obtained from Kassel formalism at p = 1.0000 bar
!--- C2H5   =C2H4 +H   1.020E+43 -9.1 224150.
!--- Next value obtained from Kassel formalism at p = 3.0000 bar
C2H5   =C2H4 +H   6.090E+41 -8.6 226500.
!--- Next value obtained from Kassel formalism at p = 9.0000 bar
!--- C2H5   =C2H4 +H   6.670E+39 -7.9 227110.
!--- Next value obtained from Kassel formalism at p = 20.000 bar
!--- C2H5   =C2H4 +H   2.070E+37 -7.1 224180.
!--- Next value obtained from Kassel formalism at p = 50.000 bar
!--- C2H5   =C2H4 +H   1.230E+34 -6.1 219200.

```
C2H5   +H     =CH3    +CH3           3.000E+13 0.0    0.0
C2H5   +O     =CH3CHO +H             5.000E+13 0.0     0.0
C2H5   +O     =CH2O    +CH3          1.000E+13 0.0    0.0
C2H5   +O2    =C2H4    +HO2          1.100E+10 0.0    -6300.
C2H5   +CH3   =C2H4    +CH4          1.140E+12 0.0     0.0
C2H5   +C2H5  =C2H4    +C2H6         1.400E+12 0.0     0.0
!****************************************
!***   25.  C2H6 Reactions
!****************************************
C2H6   +H     =C2H5    +H2           1.400E+09 1.5    31100.
C2H6   +O     =C2H5    +OH           1.000E+09 1.5    24400.
C2H6   +OH    =C2H5    +H2O          7.200E+06 2.0     3600.
C2H6   +HO2   =C2H5    +H2O2         1.700E+13 0.0    85900.
C2H6   +O2    =C2H5    +HO2          6.000E+13 0.0   217000.
C2H6   +CH2   =C2H5    +CH3          2.200E+13 0.0    36300.
C2H6   +CH3   =C2H5    +CH4          1.500E-07 6.0    25400.
!****************************************
END
```

Curriculum vitae

Name: Adrian Schneider

Born: 28.09.1977, Osnabruck, Germany

Citizen of: Buchholterberg, Bern, Switzerland

1984 – 1990   Primary School

1990 – 1997   High school "Ratsgymnasium Osnabruck"

1997   School leaving certificate "Abitur"

1997 – 1998   Military Services, German Federal Armed Forces

1998 – 2003   Mechanical engineering studies at Swiss Federal Institute of Technology Zurich

2003   Degree in mechanical engineering "Dipl. Masch.-Ing. ETH"

2003 – 2006   Research assistant in Combustion Fundamentals Group at Paul Scherrer Institute, Villigen, Switzerland

24.04.2007   PhD examination, ETH Zurich